DYNAMIC MODELING OF SPINDLE VIBRATION AND SURFACE GENERATION IN ULTRA-PRECISION MACHINING

SHAOJIAN ZHANG

Ph.D

The Hong Kong
Polytechnic University

2012

The Hong Kong Polytechnic University

Department of Industrial and Systems Engineering

Dynamic Modeling of Spindle Vibration and Surface Generation in Ultra-precision Machining

By

Shaojian ZHANG

A thesis submitted in partial fulfillment of the requirements
for the degree of Doctor of Philosophy

May 2012

CERTIFICATE OF ORIGINALITY

I hereby declare that this thesis is my own work and that, to the best of my knowledge and belief, it reproduces no material previously published or written, nor material that has been accepted for the award of any other degree or diploma, except where due acknowledgement has been made in the text.

________________________________ (Signed)

SHAOJIAN ZHANG (Name of student)

Abstract

Abstract of thesis entitled "Dynamic Modeling of Spindle Vibration and Surface Generation in Ultra-precision Machining" submitted by Shaojian Zhang in May 2012 for a doctor of philosophy degree at The Hong Kong Polytechnic University.

Ultra-precision machining (UPM) typically includes ultra-precision diamond turning (UPDT) and ultra-precision raster milling (UPRM) for the manufacture of symmetric and non-symmetric profiles, such as spherical, aspheric and freeform components for optical, medical and telecommunication applications etc. They require extremely high geometrical accuracies in sub-micrometric form error and nanometric surface finish. In UPM, an aerostatic bearing spindle is popularly employed as only one power source to remove surface material of components due to its low friction, low heat generation, low contamination, and high accuracy. However, its vibration (spindle vibration) plays a major part among many factors that directly degrades the surface quality of fabricated components. There has been still a lack of investigation into dynamic characteristics of spindle vibration under the excitation of cutting forces in UPM and its effects on surface generation. In this regard, this study develops a theoretical dynamic model to characterize the basis mechanism of spindle vibration and sheds light on the effects of spindle vibration on surface generation.

In this thesis, the theoretical and experimental investigation is divided into two parts. In the first part, a five-degree-of-freedom dynamic model has been built up based on the linear and angular momentum principles. Newton-Euler equations for spindle vibration are developed to explore its dynamics under the excitations from continuous and intermittent cutting forces in UPDT and in UPRM, respectively. With the linearization of the Newton-Euler equations, the analytic solutions are sought to describe and characterize the spindle vibration under different machining processes. The solutions are further verified by the experimental and simulated results.

Based on the power spectral density (PSD) analysis of the acquired cutting forces and the measured surface topographies, the dynamic characteristics of spindle vibration from the proposed dynamic model are identified with that (i) the motion of spindle vibration consists of periodic, sub-harmonic, quasi-periodic and coupled-periodic components; (ii) the frequency characteristics of spindle vibration possess radial, axial and coupled tilting frequencies accounting for radial, axial and coupled-tilting motions, respectively; (iii) the coupled tilting frequencies (CTFs) are influenced by the spindle rotational frequency (SRF); (iv) the spindle vibration is determined by its inertial moments and force, and influenced by the external cutting forces and torques; and (v) the factors of spindle speed, cutting forces and contact time produce quasi-quadratic, quasi-linear and linear impact on the dynamic responses of spindle vibration, respectively.

In the second part, a surface generation model integrated with the dynamic model of spindle vibration is developed to simulate the formation of surface topographies in UPM. In the surface generation model for UPDT, the spindle vibration is considered with the effects of its damping ratio and phase shift. The periodic concentric, spiral, radial, and two-fold patterns (PCSRPs) are concluded at the simulated surface topographies, which are further confirmed by the measured surface topographies in the cutting trials. In UPRM, the aliased or lattice-like patterns, the ribbon-stripe patterns and the aliased tool loci (run-out) are evidently observed at both the simulated and measured surface topographies. The patterns are caused by the spindle-vibration-induced profiles (SVIPs), which are determined by the dynamic responses of the spindle excited by intermittent cutting forces of UPRM.

Moreover, the prediction and optimization models for surface generation of UPM are established to predict surface roughness and optimize surface quality, respectively. The theoretical and experimental results present that the phase shift of 0.5 and the half shift length are optimal to achieve the best surface quality in UPM, and surface roughness increases with depths of cut and contact time. The results also reveal that the prediction models can precisely predict surface roughness as considering spindle vibration. Especially, the optimal selection of spindle speed to minimize surface roughness in UPRM can effectually improve surface quality by avoiding the 'resonance' phenomenon induced by the intermittent cutting forces synchronously exciting the spindle.

The thesis presents an original study of spindle vibration and its effect on surface generation. It significantly contributes to (i) further understanding of dynamic characteristics of spindle vibration in the perspectives of an aerostatic bearing spindle in UPM, (ii) the predication and optimization of surface generation in UPM zeroing in on the improvement of surface quality, and (iii) the development of ultra-precision machine tools with enhanced precision to meet future demands for the manufacture of components with ever-stringent tolerance requirements.

Acknowledgements

The author would like to express his sincere thanks to everyone who has assisted in carrying out this research project.

First and foremost, the author wishes to express his sincerest gratitude to his chief supervisor, Dr. Sandy To, Associate Professor of the Department of Industrial and Systems Engineering and Associate Director of the State Key Laboratory in Ultra-precision Machining Technology, for her guidance, supervision, encouragement and support during his Ph.D. study.

The author is deeply grateful to his co-supervisors, Dr. C.F. Cheung, Associate Professor of the Department of Industrial and Systems Engineering and Associate Director of the State Key Laboratory in Ultra-precision Machining Technology, and Professor W.B. Lee, Professor of the Department of Industrial and Systems Engineering and Director of the State Key Laboratory in Ultra-precision Machining Technology, for a lot of advices, constructive comments and intelligent ideas for this project.

Many thanks are also due to The Research Grants Council (RGC) of the Hong Kong Special Administrative Region of the People's Republic of China for the financial support of the research work under the Project No. 5291/08E. The author would like to express his gratitude to Mr. K.C. Cheung, Mr. T.W. Chung, Mr. C.M. Wong, Ms May Chun and all staffs in State Key Laboratory in Ultra-precision Machining Technology for their technical support and his colleagues and friends for their kind encouragement and support during the course of the work.

Finally, the author wants to express his utmost thanks to his wife, Ms Yan Zhang, his young brothers and his parents for their altruistic love and support throughout the period of his study. Without their patience, this work would not have been completed successfully.

Publications Arising from this Study

Journal Paper

[1] **Shaojian Zhang**, Suet To, Chifai Cheung and Haitao Wang, Dynamic characteristics of an aerostatic bearing spindle and its influence on surface topography in ultra-precision diamond turning, International Journal of Machine Tools and Manufacture, 2012 (Accepted).

[2] **Shao-Jian Zhang**, Suet To, Chi-Fai Cheung and Jian-Jun Du, Novel Auto-regressive measurement of diamond tool wear in ultra-precision raster milling, International Journal of Precision Engineering and Manufacturing, 2012 (Accepted).

[3] **S.J. Zhang**, S. To and C.F. Cheung, Nonlinear dynamics of tool vibration in micro-cutting, Key Engineering Materials, 2012 (Accepted).

[4] S. To, C.Y. Chan, **S.J. Zhang**, C.F. Cheung, Y.H. Zhu and W.B. Lee, Microstructural characterization of an ultra-precision-machined surface of a Zn-Al alloy, Journal of Micromechanics and Microengineering, Vol.19, p.054005, 2009.

[5] Y.H. Zhu, S. To, W.B. Lee, **S.J. Zhang** and C.F. Cheung, Ultra-precision raster milling-induced phase decomposition and plastic deformation at the surface of a Zn-Al-based alloy, Scripta Materialia, Vol.62, pp.101-104, 2010.

[6] **S.J. Zhang**, S. To, C.F. Cheung, A theoretical and experimental investigation on five-degree-of-freedom dynamic characteristics of an aerostatic bearing spindle in ultra-precision diamond turning, IEEE/ASME Transactions on Mechatronics, 2012 (Under review).

[7] **Shaojian Zhang**, Suet To, Chifai Cheung, Haitao Wang and Sujian Wang, Dynamic modeling of an aerostatic bearing spindle with surface generation in ultra-precision raster milling, Journal of Sound and Vibration, 2012 (Under review).

[8] **S.J. Zhang**, S. To and C.F. Cheung, Dynamics of spindle vibration in micro-milling, IEEE/ASME Transactions on Mechatronics, 2012 (Under review).

[9] **S.J. Zhang** and S. To, A theoretical and experimental study of multimode-tool vibration influencing micro-topographical surface generation in ultra-precision diamond turning, Journal Applied Mechanics, 2012 (Under review).

[10] **S.J. Zhang**, S. To, C.F. Cheung and Y.H. Zhu, Micro-structural changes of Zn-Al alloy influencing surface topography, International Journal of Advanced Manufacturing Technology, 2012 (Under review).

Conference Paper

[11] Jian Jun Du, Sandy To, **Shao Jian Zhang**, Chi Fai Cheung and Yi Zhang, Study of on-position image detection algorithm for fly-cutter wear in optical ultra-precision machining, In conference: Asia Pacific Conference on Optics Manufacture (APCOM2009), Taipei, China.

[12] S. To, **S.J. Zhang**, C.F. Cheung and W.B. Lee, Effect of cutting strategy on surface microstructural changes in ultraprecision raster milling, In conference: Asian Symposium for Precision Engineering and Nanotechnology (ASPEN2009), Kokura, Japan.

[13] S. To, **S.J. Zhang**, C.F. Cheung and W.B. Lee, A Study of Cutting Strategy on Surface Microstructural Changes in Ultra-precision Raster Milling of Aluminium Alloy, In conference: The 10th International Conference of the European Society for Precision Engineering & Nanotechnology (eUSPEN2010) , Delft, Netherlands.

[14] **S.J. Zhang**, S. To, C.Y. Chan and C.F. Cheung, A study of cutting force variation influencing surface topography in ultra-precision machining, In conference: The 2nd International Conference on Nanomanufacturing 2010 (nanoMan2010), Tianjin, China.

[15] S. To, **S.J. Zhang**, H.T. Wang, S.J. Wang, Dynamic modeling of aerostatic

bearing spindle and measurement of surface topographies in ultra-precision raster milling, In conference: The 10th International Symposium of Measurement Technology and Intelligent Instruments (ISMTII 2011), Daejeon, Korea.

[16] **S.J. Zhang**, S. To, C.F. Cheung and J.J. Du, 3D measurement of tool wear with the in-process image based on a new auto-regressive calibration algorithm in ultra-precision raster milling, In conference: The 10th International Symposium of Measurement Technology and Intelligent Instruments (ISMTII 2011), Dajeon, Korea.

Table of Contents

Abstract.................... I

Acknowledgements IV

Publications Arising from this Study...V

Table of Contents VIII

Lists of Figures XIII

Lists of Tables... XXI

Chapter 1 Introduction..1

1.1 Background..1

1.2 Research Objectives and Significance...4

1.3 Organization of the Thesis..5

Chapter 2 Literature Review 7

2.1 Introduction..7

2.2 Development of the Optics Industry...7

2.3 Ultra-precision Machining...10

2.3.1 Ultra-precision Diamond Turning 12

2.3.2 Ultra-precision Raster Milling... 13

2.4 Aerostatic Bearing Spindle..15

2.4.1 Development of Aerostatic Bearing Spindle 15

2.4.2 Dynamic Characteristics of Aerostatic Bearing Spindle 18

2.4.3 Measurement of Spindle Errors 20

2.5 Surface Integrity in UPM 22

2.5.1 Factors Influencing Surface Roughness in UPDT 23
2.5.2 Factors Affecting Surface Roughness in UPRM 25
2.5.3 Effects of Diamond Tool Wear on Surface Roughness in UPM 27
2.5.4 Effects of Spindle Vibration on Surface Roughness in UPM 30
2.5.5 Effects of UPM on Surface Material Properties 30

2.6 Measurement and Estimation of Surface Roughness 32

2.6.1 Surface Roughness Estimation 32
2.6.2 Surface Roughness Measurement 34

2.7 Surface Generation in UPM 36

2.7.1 Surface Generation and Prediction in UPDT 36
2.7.2 Surface Generation and Prediction in UPRM 38

2.8 Optimization of Surface Topography in UPM 39

2.8.1 Optimization of Surface Roughness in UPDT 39
2.8.2 Optimization of Surface Roughness in UPRM 40

2.9 Summary 41

Chapter 3 Modeling of Spindle Vibration and Cutting Mechanism in UPM 43

3.1 Introduction 43

3.2 Surface Formation in UPM 43

3.2.1 Surface Formation in UPDT 43
3.2.2 Surface Formation in UPRM 45
3.2.2.1 Cutting Strategies 47
3.2.2.2 Cutting Directions 47

3.3 Fundaments of Modeling of Spindle Motions 48

3.3.1 Eulerian Angles 50
3.3.2 Newton-Euler Equations of Motion 51

3.4 Dynamic Modeling of an Aerostatic Bearing Spindle in UPDT 52

3.4.1 Dynamic System of a Spindle 53
3.4.2 Coordinate Transformations 54
3.4.3 Cutting Force Description 58

3.4.4 Establishment of Dynamic Equations 59

3.5 Dynamic Modeling of an Aerostatic Bearing Spindle in UPRM .62

3.5.1 Dynamic System of a Spindle 63
3.5.2 Cutting Force Description 65
3.5.3 Dynamic Equations of Spindle Motions... 66

3.6 Summary..68

Chapter 4 Dynamic Characteristics of Spindle Vibration in UPM.69

4.1 Introduction..69

4.2 Dynamic Characteristics of Spindle Vibration in UPDT 69

4.2.1 Solutions of Dynamic Equations 70
4.2.1.1 Solutions of Translational Equations 70
4.2.1.2 Solutions of Rotational Equations 75
4.2.2 Dynamic Responses of the Spindle 82
4.2.2.1 Spindle Responses under Air Cutting 83
4.2.2.2 Spindle Responses under Continuous Cutting..88
4.2.2.3 Spindle Responses under Intermittent Cutting 91
4.2.3 Influences of Eccentric Distances with Spindle Speeds on Vibration Amplitudes 94
4.2.4 Influences of Cutting Forces with Spindle Speed on Vibration Amplitudes 97

4.3 Dynamic Characteristics of Spindle Vibration in UPRM...........101

4.3.1 Solutions of Spindle Motion Equations... 101
4.3.2 Dynamic Responses of the Spindle under Intermittent Cutting Forces... 109
4.3.3 Influences of Intermittent Cutting Forces with Spindle Speed 109
4.3.4 Influences of Depths of Cut with Spindle Speed.............................. 112

4.4 Summary..115

Chapter 5 Prediction and Optimization of Surface Generation in UPM 117

5.1 Introduction..117

5.2 Surface Generation in UPDT..117

5.2.1 Modeling of Surface Generation 118
5.2.2 Results of Surface Generation 119
5.2.2.1 Surface Topography...121
5.2.2.2 Influences of Damping Ratios 123
5.2.2.3 Effects of Phase Shift of Vibration 125
5.2.2.4 Prediction of Vibration Effects on Surface Topography 129
5.2.2.5 Optimization of Vibration Effects on Surface Topography 130

5.3 Surface Generation in UPRM...131

5.3.1 Modeling of Surface Generation 131
5.3.2 Results of Surface Generation 135
5.3.2.1 Surface Topography...135
5.3.2.2 Shift Length of Tool Loci and Phase Shift of Vibration Influencing Surface Topography..137
5.3.2.3 Prediction of Vibration Effects on Surface Topography 138
5.3.2.4 Optimization of Vibration Effects on Surface Topography 139

5.4 Summary...140

Chapter 6 Experimental Investigation and Analysis......................142

6.1 Introduction...142

6.2 Experimental Setup in UPDT 142

6.2.1 Cutting Conditions.. 142
6.2.2 Measurement of Cutting Forces 143
6.2.3 Measurement of Surface Topographies 145

6.3 Experimental Results and Analysis in UPDT.............................147

6.3.1 Variation of Cutting Forces 147
6.3.2 Characteristics of Surface Topographies 151
6.3.3 Effects of Depths of Cut on Surface Topographies 153
6.3.4 Effects of Spindle Speeds on Surface Topographies 156

6.4 Experimental Setup in UPRM 161

6.4.1 Cutting Conditions.. 161
6.4.2 Measurement of Cutting Forces 162
6.4.3 Measurement of Surface Topography.. 163

6.5 Experimental Results and Analysis in UPRM............................165

6.5.1 Surface Characteristics 165

6.5.2 Effects of Spindle Speeds on Surface Topographies 167
6.5.3 Effects of Depths of Cut on Surface Topographies 172
6.6 Summary 176

Chapter 7 Conclusions and Suggestions for Future Studies..........178

7.1 Overall Conclusions..178

7.2 Suggestions for Future Work 181

References...185

Appendices..210

Appendix I SPDT Optoform 30 210

Appendix II UPRM Precitech Freeform 705G 212

Appendix III State Space Equations..214

Appendix IV Fast Fourier Transform..215

Appendix V Impedance Method..216

Appendix VI Transient State Solutions..218

Appendix VII Beating Phenomenon 221

Appendix VIII Power Spectral Density..223

Appendix IX Kistler 9252A 225

Appendix X Wyko 8000 Optical Profiling System..........................227

Lists of Figures

Figure 2.1 Optical components market forecast 8
Figure 2.2 (a) Roadmap for precision optical components with (b) ultra-precision machines 9
Figure 2.3 Achievable machining accuracy (Taniguchi, 1983, 1996) 11
Figure 2.4 Single-point diamond tools 11
Figure 2.5 Ultra-precision single-point diamond turning (SPDT) 13
Figure 2.6 Ultra-precision raster milling (UPRM) (Precitech Freeform 705G, Precision Inc., USA) 14
Figure 2.7 (a) Schematic structure of an aerostatic bearing spindle (Horiuchi et al., 2006) and (b) an aerostatic bearing spindle of Precision Freeform 705G (Precision Inc., USA) 15
Figure 2.8 (a) Top view of crater wear and nose profile and (b) lateral view of flank wear land and notch wear of a diamond tool 27
Figure 2.9 Framework for tool wear effects in machining 29
Figure 2.10 Metrology selection (Stedman, 1987) 35

Figure 3.1 Ultra-precision single point diamond lathe machine (Optoform 30) with a single point diamond tool 44
Figure 3.2 Schematic diagram of surface generation with (a) a tool spiral trajectory and (b) a surface profile in the radial direction 44
Figure 3.3 (a) Schematic configuration of a UPRM machine and (b) Precitech Freeform 705G 45
Figure 3.4 Schematic ultra-precision raster milling and surface topographies under (a) horizontal cutting strategy, (b) vertical cutting strategy, and (c) a machined surface topography with shift effects 46
Figure 3.5 Ultra-precision raster milling with (a) up-raster and (b) down-raster 48
Figure 3.6 Relative motions of a mass point in a rigid body 49

Figure 3.7 Definition of Eulerian angles 50

Figure 3.8 Schematic diagrams of the spindle motions (a) axial translational motion along the Z axis (the axial direction), (b) radial translational motion along the X axis or Y axis (the radial direction) and (c) tilting motion deviating away from the Z axis 52

Figure 3.9 The schematic spindle system with one workpiece referred to the reference coordinate frame $o(xyz)$ moving in the inertial coordinate frame $O(XYZ)$ 54

Figure 3.10 The coordinate transformations: (a) translational transformation and (b) rotational transformation 55

Figure 3.11 Schematic diagrams of spindle rotor motions involving (a) the axial motion, (b) the radial motion and (c) the tilting motion 63

Figure 3.12 Schematic diagram of an aerostatic bearing spindle in UPRM 63

Figure 3.13 The coordinate transformation: (a) translational transformation and (b) rotational transformation 65

Figure 3.14 Idealized cutting forces in UPRM 66

Figure 4.1 Configuration parameters of the Simulink model regarding the simulation 82

Figure 4.2 Dynamic responses of the spindle rotor under air cutting at the spindle speed of 5000rpm with the specifications of Table 4.1, involving: (a) the translational motion along the spin axis, (b) and (c) the translational motions along the radial axes, and (d) and (e) the tilting motions deviating away from the spin axis 84

Figure 4.3 PSDs of dynamic responses of the spindle rotor for Figure 4.2: (a) the translational motion along the spin axis, (b) and (c) the translational motions along the radial axes, and (d) and (e) the tilting motions deviating away from the spin axis 85

Figure 4.4 Effects of spindle speeds with eccentric distances on the vibration amplitude of (a) the translational motion along the spin axis, (b) and (c) the translation motions along the radial axes, and (d) and (e) the tilting motions deviating away from the spin axis under air cutting at the steady state 86

Figure 4.5 Effects of spindle speeds with eccentric distances on the vibration amplitude of (a) the translational motion along the spin axis, (b) and (c) the translation motions along the radial axes, and (d) and (e) the tilting motions deviating away from the spin axis under air cutting at the transient state 87

Figure 4.6 Dynamic responses of the spindle rotor with (a) the translational motion along the spin axis, (b) and (c) the translation motions along the radial axes, and (d) and (e) the tilting motions deviating away from the spin axis with the spindle speed of 5000rpm and constant cutting forces (0.05 N, 0.05 N, 0.003N) under the spindle specifications of Table 4.1 89

Figure 4.7 PSDs of dynamic responses of the spindle rotor in Figure 4.6 for (a) the translational motion along the spin axis, (b) and (c) the translation motions along the radial axes, and (d) and (e) the tilting motions around the radial axes 90

Figure 4.8 Effects of cutting force frequencies on the vibration amplitudes of (a) the translational motion along the spin axis, (b) and (c) the translation motions along the radial axes, and (d) and (e) the tilting motions deviating away from the spin axis acted by intermittent cutting forces (half-periodical pulse wave in the form of 0.05 N, 0.05 N, 0.003N) under the spindle specifications of Table 4.1 with the spindle speed of 5000rpm........ 92

Figure 4.9 Effect of eccentric distances on amplitudes of spindle vibration combining the spindle speeds with the simulation parameters of Table 4.3 at the transient state for (a) the translational motion along the spin axis, (b) and (c) the translation motions along the radial axes, and (d) and (e) the tilting motions deviating away from the spin axis under air cutting........ 95

Figure 4.10 Effects of eccentric distances on amplitudes of spindle vibration combining the spindle speeds with the simulation parameters of Table 4.3 at the steady state for (a) the translational motion along the spin axis, (b) and (c) the translation motions along the radial axes, and (d) and (e) tilting motions deviating away from the spin axis 96

Figure 4.11 Effect of cutting forces (Fm=0.025 Fr=0.0015 Ft=0.025) on amplitude of spindle vibration combining the spindle speed with the simulation parameters of Table 4.4 at the transient state for (a) the translational motion along the spin axis, (b) and (c) the translation motions along the radial axes, and (d) and (e) the tilting motions deviating away from the spin axis 99

Figure 4.12 Effect of cutting forces (Fm=0.025 Fr=0.0015 Ft=0.025) on amplitude of spindle vibration combining the spindle speed with the simulation parameters of Table 4.4 at the steady state for (a) the translational motion along the spin axis, (b) and (c) the translation motions along the radial axes, and (d) and (e) the tilting motions deviating away from the spin axis 100

Figure 4.13 Dynamic responses of the spindle applied by intermittent cutting forces of Table 4.5 under the spindle specifications of Table 4.5 and the cutting conditions of Table 4.6: (a1) the axial motion along the *Y*-axis, (a2) the radial motion along the *X*-axis, (a3) the radial motion along the *Z*-axis, (a4) the tilting motion around the *x*-axis and (a5) the tilting motion around the *z*-axis 108

Figure 4.14 Vibration amplitudes of the spindle at different spindle speeds with different cutting forces k (Fm=0.025, Ft=0.025 and Fr=0.0015) with damping (a) along the *Y*-axis, (b) along the *X*-axis, (c) along the *Z*-axis, (d) around the *x*-axis and (e) around the *z*-axis 110

Figure 4.15 Vibration amplitudes in contact time at different spindle speeds with different cutting forces k (Fm=0.025, Ft=0.025 and Fr=0.0015) with damping (a) along the *Y*-axis, (b) along the *X*-axis, (c) along the *Z*-axis, (d) around the *x*-axis and (e) around the *z*-axis 111

Figure 4.16 Vibration amplitudes of spindle at different spindle speeds with different depths of cut (a) along the *Y*-axis, (b) along the *X*-axis, (c) along the

Z-axis, (d) around the *x*-axis and (e) around the *z*-axis 113

Figure 4.17 Vibration amplitudes in contact time at different spindle speeds with different depths of cut (a) along the *Y*-axis, (b) along the *X*-axis, (c) along the *Z*-axis, (d) around the *x*-axis and (e) around the *z*-axis 114

Figure 5.1 Schematic diagram of surface generation (a) a tool spiral trajectory and (b) a surface profile in the radial direction.. 119

Figure 5.2 Simulated surface topography at the sample center without vibration under the cutting conditions of Table 5.1 120

Figure 5.3 Simulated surface topography at the sample center under the cutting conditions of Table 5.1 with the vibration at the frequency of 1098.3 and the amplitude of 8nm.. 120

Figure 5.4 Simulated surface topography at the sample center under the cutting conditions of Table 5.1 with the vibration at the frequency of 1098.3Hz and the amplitude of 8nm and at the SRF of 50Hz and the amplitude of 8nm.. 121

Figure 5.5 Simulated surface topography away from the surface center under the cutting conditions of Table 5.1 without vibration.................................. 122

Figure 5.6 Simulated surface topographies at 3mm away from the sample center under the cutting conditions of Table 5.1 at the CTFs of 2001Hz and 1953Hz and the amplitudes of 8nm (a) in the feed direction and (b) in the cutting direction.. 123

Figure 5.7 Simulated surface topographies away from the sample center under the cutting conditions of Table 5.1 with the vibration at the frequencies of 2001Hz, 1953Hz and 50Hz corresponding to the amplitudes of 8nm (a) in the feed direction and (b) in the cutting direction 123

Figure 5.8 Simulated surface topography at the sample center under the cutting conditions of Table 5.1 with the vibration at the axial frequency of 1098.3Hz and its derivative frequency of 1096.9Hz with the amplitudes of 8nm.. 124

Figure 5.9 Simulated surface topography at the surface center under the cutting conditions of Table 5.1 at the axial frequency of 1098.3Hz, its derivative frequency of 1096.9Hz and the SRF of 50Hz with the same amplitudes of 8nm 124

Figure 5.10 Graphical illustrations of ideal cutting profiles with vibration in the feed direction (a) without the phase shift (b) with the half phase shift 126

Figure 5.11 Simulated surface topographies generated at the place of 3mm away from the surface center under the cutting conditions of Table 5.2 with the tilting vibration at the frequencies of Table 5.4 with the same amplitudes of 8nm under the spindle speeds of (a) 2000, (b) 3000, (c) 4000, (d) 5000, (e) 6000, (f) 7000 and (g) 8000rpm 127

Figure 5.12 Simulated surface topographies generated at the place of 3mm away from the surface center under the cutting conditions of Table 5.3 with the tilting vibration at the frequencies of Table 5.4 with the same amplitudes of 8nm under the spindle speeds of (a) 2000, (b) 3000, (c) 4000, (d) 5000, (e) 6000, (f) 7000 and (g) 8000rpm 128

Figure 5.13 Schematic diagram of surface generation in vertical cutting (a) a vertical surface profile and (b) a horizontal surface profile 132

Figure 5.14 A framework for the whole simulation system 133

Figure 5.15 Simulated surface topographies under horizontal cutting (a) with the uniform phase shift of zero and (b) with the phase shift of 0.5 135

Figure 5.16 Simulated surface topographies under vertical cutting (a) with the random phase shift and (b) with the phase shift of 0.5 135

Figure 5.17 Schematic milled profiles (a) in the feed direction with a shift length, (b) in the raster direction with a shift length, (c) in the feed direction without a shift length and (d) in the raster direction without a shift length........ 137

Figure 6.1 A Kistler 9252A 3-component force sensor 144

Figure 6.2 Configuration of the cutting force measurement system in UPDT.......... 145

Figure 6.3 Schematic diagram of the cutting force measurement in the cutting process

.... 145
Figure 6.4 Wyko NT8000 Optical Profiling System 146
Figure 6.5 A series of the thrust cutting forces measured in order (a1)-(l1) and their corresponding PSDs (a2)-(l2) as the tool was moving from the outside to the machined surface center under the cutting conditions of Table 6.2 (the tool radius of 0.762mm, the spindle speed of 3000rpm and the depth of cut of 5μm) 148
Figure 6.6 Measured surface topography of the sample center generated under the cutting conditions (the tool radius of 0.762mm, the spindle speed of 3000rpm, the feed rate of 0.005mm/rev., the depth of cut of 5μm) in Table 6.1 151
Figure 6.7 Measured surface topography at the place of 3mm away from the center generated under the cutting conditions (the tool radius of 0.762mm, the spindle speed of 3000rpm, the feed rate of 0.005mm/rev., the depth of cut of 5μm) 153
Figure 6.8 Measured surface topographies at the place of 3mm away from the center generated under the cutting conditions: Tool radius of 0.762mm, spindle speed of 3000rpm, feed rate of 0.005mm/rev., depths of cut of (a) 1, (b) 5 and (c) 25μm 154
Figure 6.9 Corresponding PSDs of the measured surface topographies in Figure 6.8(a)-(b).. 155
Figure 6.10 Measurend and predicted surface roughness only considering the spindle vibration under various depths of cut 155
Figure 6.11 Measured surface topographies at the place of 3mm away from the center generated under the cutting conditions: the tool radius of 0.128mm, the feed rate of 0.005mm/rev., the depth of cut of 5μm, the spindle speeds of (a) 2000rpm, (b) 3000rpm, (c) 4000rpm, (d) 5000rpm and (e) 6000rpm 158
Figure 6.12 PSD plots of the measured surface topographies in Figure 6.11(a)-(e) . 159
Figure 6.13 A surface profile of Figure 6.11(b).. 159

Figure 6.14 Measurend and predicted surface roughness under different spindle speeds 160

Figure 6.15 Configuration of the cutting force measurement system in UPRM....... 162

Figure 6.16 Measured surface topographies under horizontal cutting (a) with uniform patterns and (b) with random patterns 163

Figure 6.17 Measured surface topographies under vertical cutting (a) with uniform patterns and (b) with random patterns 164

Figure 6.18 Measured surface roughness (a) Ra, (b) Rq, (c) Rz and (d) Rt of Table 6.4 166

Figure 6.19 Measured and predicted surface roughness Rt under the cutting conditions: the spindle speeds of 4000rpm-4900rpm at the interval of 20rpm, the depth of cut of 5µm and others tabulated in Table 6.3 167

Figure 6.20 Measured surface topography and its profiles milled under the cutting conditions: the spindle speeds of 4900rpm, the depth of cut of 5µm and others tabulated in Table 6.3 168

Figure 6.21 Measured and predicted surface roughness Rt/ Rz under the cutting conditions: the spindle speeds of 4000rpm-4900rpm at the interval of 20rpm, the depth of cut of 5µm and others tabulated in Table 6.3........ 172

Figure 6.22 Measured surface roughness (a) Ra, (b) Rq, (c) Rz and (d) Rt generated under the cutting conditions of Table 6.3 173

Figure 6.23 Measured and predicted surface roughness Rz and Rt under the cutting conditions of Table 6.3 with the depths of cut of (a) 5µm, (b) 10µm and (c) 20µm 174

Figure 6.24 Measured and modified-predicted surface roughness Rz and Rt under the cutting conditions of Table 6.3 with the depths of cut of (a) 5µm, (b) 10µm and (c) 20µm 175

Lists of Tables

Table 4.1 Spindle performance specifications of UPDT Opto30 70

Table 4.2 Natural frequencies of the spindle rotor in the spindle system.................... 86

Table 4.3 Spindle performance specifications with cutting forces for simulation 93

Table 4.4 Spindle performance specifications with cutting forces in UPDT 98

Table 4.5 Spindle performance specifications with cutting forces in UPRM 107

Table 4.6 Cutting conditions of UPRM... 107

Table 5.1 Cutting conditions in UPDT 119

Table 5.2 Cutting conditions with the tool radius of 0.762 in UPDT........................ 126

Table 5.3 Cutting conditions with the tool radius of 0.128mm in UPDT.................. 126

Table 5.4 Spindle speeds with its corresponding CTFs for the tilting motions of the spindle rotor under the spindle specifications tabulated in Table 4.1........ 126

Table 5.5 Cutting conditions for surface generation in UPRM 134

Table 5.6 Spindle performance specifications with the cutting forces of UPRM 134

Table 6.1 Cutting conditions of diamond turning... 143

Table 6.2 Natural frequencies of the spindle rotor with the spindle speed of 3000rpm under the spindle specifications tabulated in Table 4.1 148

Table 6.3 Cutting conditions of raster milling.. 161

Table 6.4 Measured surface topographies being milled under the cutting conditions: the spindle speeds of 4000rpm-4900rpm at the interval of 20rpm, the depth of cut of 5μm and others tabulated in Table 6.3 168

Chapter 1 Introduction

1.1 Background

Ultra-precision machining (UPM), typically including ultra-precision diamond turning (UPDT) and ultra-precision raster milling (UPRM), with a single point diamond tool possessing nanometric edge sharpness, wear resistance and high stiffness, is an advanced machining process directly allowing manufacturing high precision components with a nano-metric surface roughness and within a sub-micrometric form error without the need for any subsequent polishing. Due to fast growing demands from manufacturing industries, the aerospace industry and the military for high-quality products, UPM is frequently used to produce super-mirror-like surfaces such as spherical and aspheric lenses, freeform lenses, micro-lens arrays, and F-theta lenses with a surface roughness of less than 10 nanometers and a surface form tolerance of less than sub-micrometers. Surface roughness is a crucial feature parameter to estimate machined surface quality, since it determines a product's functional performance (Ikawa et al., 1987, 1985, 1991) and affects its lifecycle. It is primarily influenced by many factors such as cutting conditions of tool tip radius, depth of cut, spindle speed and feed rate, material pile-up, material swelling and recovery, crystal orientation and micro-structural changes, tool vibration, spindle vibration, slide vibration, and tool wear. These factors can be classified into process factors, dynamic factors and material factors.

UPDT is widely utilized to fabricate high precision rotational symmetric components, such as spherical and aspheric components, with a nanometric surface roughness and with sub-micrometric form errors (Cheung and Lee, 2000). And surface topography/surface roughness is mainly determined by the following factors: cutting conditions (Lee and Cheung, 2001, Kim et al., 2002, Lee et al., 2007), such as tool tip geometry, spindle speed, depth of cut and feed rate; material pile-up (Liu and Melkote, 2006); material swelling and recovery (To, 2000, To et al., 2001, Kong, 2006, Kong et al., 2006); crystal orientation (Yuan et al., 1994, Cheung et al., 2002, Chen, 2008); the relative vibration between tool and work-piece (Kim et al., 2002, Cheung and Lee, 2000a, Zhu and Cheng, 2009); material-induced vibration (Lee et al., 1999); tool tip vibration (Wang et al., 2010, Ostasevicius et al., 2010, Zhang et al., 2010) and tool shank vibration (Zhang et al., 2010); and tool wear (Wada et al., 1980, Ge et al., 2009). Although attempts have been made in UPDT, most of them focused on the synthesis of surface generation based on static, kinematics or quasi-dynamics. However, the effects of spindle vibration under the excitation of cutting forces on surface generation in UPDT have been little studied. Therefore, there is a vital need to take account of spindle vibration in surface generation of UPDT.

UPRM is an ultra-precision machining technique for fabricating non-rotational freeform surfaces with a nanometric surface roughness and sub-micrometric form accuracy. Owing to the complex cutting process of UPRM, there has been a lot of interest in studying the factors influencing surface topography. A framework of a model-based simulation system for prediction of surface generation in UPRM of freeform surfaces was presented by Cheung et al. (Cheng, et al., 2004), and a model-based simulation system for prediction of form accuracy in the UPRM of optical freeform surfaces (Cheung, et al., 2006) was developed to take account of the cutting mechanics, the cutting strategies and the kinematics of the cutting process. Cheng et al. (2005, 2007, 2008) proposed a theoretical model to predict surface roughness and optimize cutting conditions (tool tip geometry, spindle speed, depth of cut, feed rate, swing distance, and step distance) and cutting strategies (horizontal cutting and vertical cutting) in UPRM. A theoretical dynamics model in UPRM for surface generation was employed (Kong, et al., 2008), and the factors influencing surface generation of UPRM were discussed (Kong, 2009). The results show that cutting conditions, tool geometry, cutting strategies and tool wear have a major impact on surface roughness, while cutting strategies, tool path generation, and kinematic errors of sliders are the main influences on the form accuracy of freeform surfaces. Wang (2010) investigated material swelling and recovery for different materials using the second order differential and studied the effects of shift length ratios on surface topographies in UPRM. In most of the prior studies of surface generation in UPRM, the effects of cutting mechanism and material factors on surface generation have been overemphasized, whereas spindle vibration in surface generation of UPRM has been overlooked. Moreover, little attention has been paid to studying the spindle vibration under the excitation of intermittent cutting forces in UPRM and its influence on surface generation. Therefore, a better understanding of the dynamic characteristics of an aerostatic bearing spindle excited by intermittent cutting forces in UPRM is needed.

Only a few studies have been reported on the effects of spindle dynamics on surface profiles/topographies in UPM. After investigating spindle errors, surface finish and form errors of machined parts, Martin et al. (1995) proposed that spindle vibration influenced the surface topography of machined parts; Marsh et al. (2005) suggested that the topographical patterns of the flat surfaces in precision fly-cutting were caused by spindle dynamics; and An et al. (2010) identified that the tilting motion of an aerostatic bearing spindle influenced the machined surface topography in ultra-precision fly cutting. However, there is insufficient experimental and theoretical knowledge to provide a better understanding of the entire cutting mechanism along with spindle dynamics under cutting forces in UPDT and in UPRM.

With regard to the behaviors of an aerostatic bearing spindle, many researchers have conducted simulations and taken measurements to study axial, radial and tilting motions of spindle. Generally, these motions are the synthesis of dynamic and static behaviors. Spindle vibration is regarded as the dynamic behavior of spindle. It has been reported that the spindle vibration is induced by unbalanced mass and eccentric moments of spindle (Lund, 1967, Ni, 1985). The spindle vibration, such as periodic (Ehrich, 1966), sub-harmonic (Ehrich, 1966, Li and Taylor, 1987, Zhao et al., 1994, Adiletta et al., 1997a, 1997b), quasi-periodic (Zhao et al., 1994, Adiletta et al., 1997a, 1997b) and chaotic motions (Adiletta et al., 1997a, 1997b, Wang and Yau, 2010), has been theoretically and experimentally verified, but most of the research has focused on two-degree-of-freedom spindle vibration without the external excitation under the ideal assumption of a spindle considered as a short shaft system. The spindle error motion measured through displace sensors using different methods (Bryan, 1967, Burdekin, 1972, Donaldson, 1972, Kakino, 1977, Mitsui, 1982, Tu et al., 1997, Marsh and Grejda, 2000, Grejda et al., 2005, Marsh et al., 2006, Yang et al., 2004, Kim et al., 2007, Okuyama et al., 2007, Chang and Chen, 2009) is only regarded as the static motion, since spindle-vibration-induced motion makes a small contribution to spindle error motion after damping. Therefore, the measured spindle error motion is only the static but not dynamic behavior of spindle. The existence of the gap is in the study of the five-degree-of-freedom motions of aerostatic bearing spindle and its dynamic characteristics under its inertial moments and external cutting forces in UPM, where the spindle is considered as a long shaft spindle system.

A better understanding of dynamic characteristics of an aerostatic bearing spindle excited by different kinds of cutting forces in UPM is thus needed, and an investigation into the effects of spindle vibration on surface roughness/surface topography is becoming increasingly important for practical applications of UPM.

1.2 Research Objectives and Significance

To address the key issues mentioned above, this study develops a five-degree-of-freedom dynamic model for an aerostatic bearing spindle under the external excitation of cutting forces in UPM. It further studies dynamic responses of the spindle under cutting forces, discusses the effects of spindle vibration on surface topography, and develops an optimization model and a prediction model for surface generation based on the selection of optimal cutting conditions in order to improve surface quality in UPM. The objectives of the study include:

(1) Developing a dynamic model of the aerostatic bearing spindle excited by cutting forces of UPM, based on the linear momentum principle of Newton and the angular momentum principle of Euler;

(2) Deriving the analytic solutions for the dynamic model by linearizing the Newton-Euler equations to elaborate the dynamic responses of the spindle vibration with rigorous mathematical expressions;

(3) Establishing a surface generation model to discuss the effects of the spindle vibration on surface topography in UPDT and UPRM; and

(4) Developing a prediction model and an optimization model for surface generation in UPM using the proposed analytic solutions.

In order to achieve higher productivity and better surface integrity effectively under the optimal machining conditions and cutting strategies in UPM, spindle vibration is of paramount importance and one of the dominant, dynamic and in-process factors. This research adopts a multi-disciplinary approach from the perspectives of mechanics, materials science, surface characterization, and mathematics. The study elucidates the basic mechanism of spindle vibration inducing surface topographical patterns in UPM, provides practical and optimal cutting conditions to fabricate surfaces with the assistance of the prediction and optimization models of surface generation, and offers better control for manufacturing precision components with the highest surface stability, productivity and efficiency.

1.3 Organization of the Thesis

The thesis comprises seven chapters. Chapter 1 presents the background of the study, problem formulation, and objectives and significance of the research. In Chapter 2, a literature review of the relevant topics for supporting the study is introduced, consisting of the development of optics, ultra-precision machining, aerostatic bearing spindles, surface generation mechanisms, simulation and measurement of aerostatic bearing spindles, the factors influencing surface topography/surface roughness, surface generation techniques, and prediction and optimization models in UPM.

In Chapter 3, cutting mechanisms for surface generation in UPM are introduced, and a five-degree-of-freedom dynamic model of an aerostatic bearing spindle excited by cutting forces of UPM is establish with the linearization of Newton-Euler equations of motion, based on the linear momentum principle of Newton and the angular momentum principle of Euler.

In Chapter 4, the analytic solutions for the linearized Newton-Euler equations of Chapter 3 are derived to present the dynamic motions of the spindle vibration under the cutting process, which are identified by the numerical simulation for the Newton-Euler equations. The frequency characteristics of spindle vibration are proposed, and the effects of external parameters, such as cutting forces, on dynamics responses of the spindle vibration are discussed in this chapter.

In Chapter 5, a surface generation model is built to study the effects of spindle vibration on surface topographies in UPM. And, based on the results in Chapter 4, the prediction and optimization models for surface generation of UPM are developed.

In Chapter 6, the results from a series of experiments are analyzed to identify the previously proposed theoretical results through the dynamic characteristics of the measured cutting forces and the measured surface topographies. Simultaneously, the prediction and optimization models are confirmed by the experiments.

Finally, Chapter 7 provides overall conclusions for the study and some suggestions for future research.

Chapter 2 Literature Review

2.1 Introduction

Ultra-precision machining (UPM) is a growing technology with a fine single point diamond tool to fabricate high-precision products, such as spherical and aspheric lenses, freeform lenses, micro-lens arrays and F-theta lenses within a nanometric surface roughness and a surface form accuracy of less than 0.5 micrometers. It is widely employed for manufacturing consumer products due to its low cost and high precision.

2.2 Development of the Optics Industry

Over the last few decades, the optics industry has grown from a skilled manual-based industry to one based on advanced optical manufacturing with UPM. As shown in Figure 2.1, the optical components market was worth $3.8 billion in 2008 and is expected to reach $11.3 billion by 2015 (Winter Green Research, Inc., Optical Component Worldwide Strategies, Market Shares and Forecasts, 2009 to 2015, Sep 2009). Integrated optical components include amplifiers, lasers, receivers, transmitters, and transceivers and transponders, and the markets comprise transceivers, optical amplifiers, and passive and active optical component technology ranging from contact lenses to giant mirrors. Typical products contain laser printers, hand-held scanners, tube TV compensators, phase modulation mirrors, LCD backlights, broadband optical fibre connectors and laser rangefinders (Ruckman et al., 1999). Using UPM to produce high-quality surfaces with a nanometric surface finish and within a sub-micrometric form error is a growing trend in the optics industry.

In recent years, optical products have become more specialized, functionalized and complicated in order to meet the ever-growing demands of customers. The more high-value-added part of the products has promoted the design and complex fabrication of surfaces with features and functional requirements, which are crucial to the development of complex and micro-optical-electro-mechanical devices used in many photonics and telecommunication products and systems. The applications cover lighting, telecommunications, medical facilities, automotives, military, and aerospace. Figure 2.2(a) shows the development and applications of optical components from relatively simple spherical/aspheric components, F-theta lenses and micro-lens arrays, to micro-grooving and freeform components, which are based on UPM having developed from two-axis machining to multi-axis machining. The ultra-precision two-axis machine is used to fabricate aspheric/spherical components, the ultra-precision two-axis machine with fast tool servo is employed to produce micro-lens arrays, and the five-axis machine is utilized to fabricate micro-grooving and freeform surfaces, as shown in Figure 2.2(b).

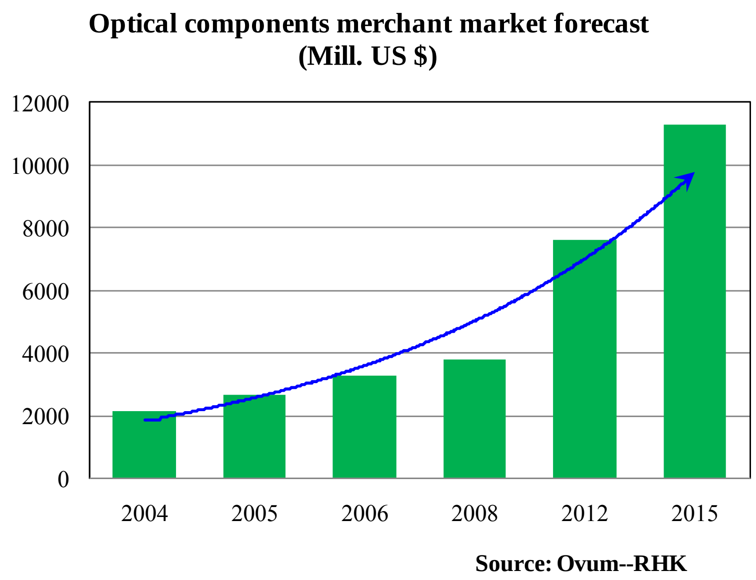

Figure 2.1 Optical components market forecast

Freeform optical components are new in the world of optics and have large-scale surfaces with shapes generally possessing non-rotational symmetry. Freeform surfaces are more flexible when designing components with functional, aesthetic and ergonomic surfaces, but it is difficult for two-axis machining to manufacture such functional surfaces; five-axis machining has been proven to be the most efficient tool where manufacturing is relatively more complex than that for aspheric/spherical surfaces. According to Kurgano et al. (2002), it is difficult and time consuming to generate a freeform surface to such a high degree of accuracy and is also information intensive and prone to errors. Moreover, the manufacture of high-quality freeform optics demands advanced machining technology having a capable and comprehensive solution for fabricating the freeform surface with a surface finish Ra of less than 10 nanometers and a form error of less than 0.2 micrometers, which are the demands of precision aspheric/spherical or rotational symmetric surfaces produced by two-axis ultra-precision machines. Since many factors influence a component's surface quality, researchers have studied surface generation and material property change under various cutting conditions in UPM. However, the studies only focused on static factors, not on the key dynamic factor of spindle vibration in UPM, especially in ultra-precision raster milling.

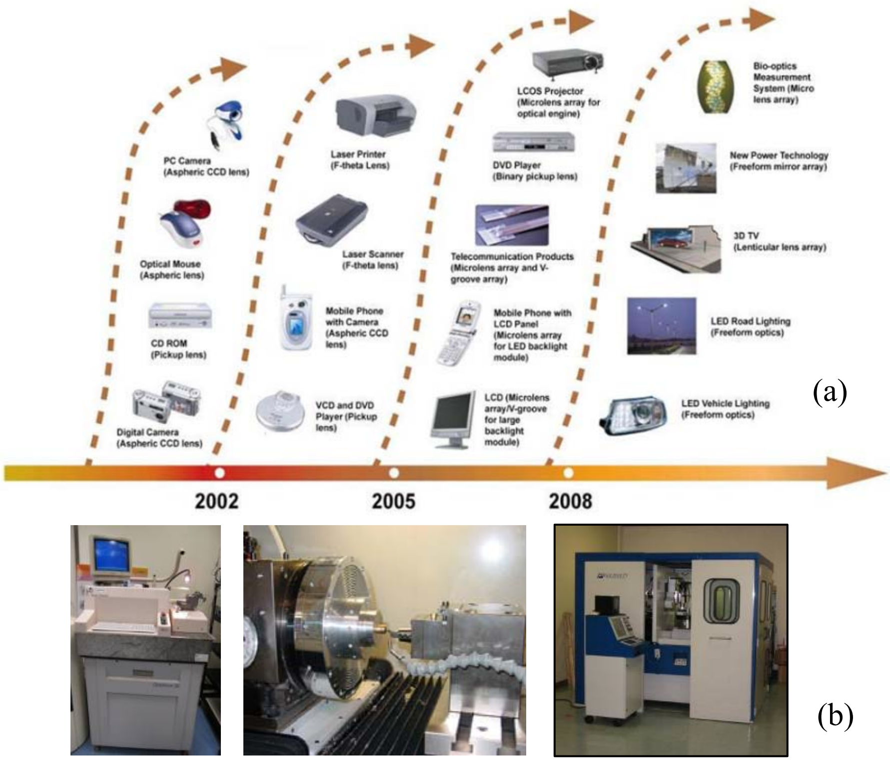

Figure 2.2 (a) Roadmap for precision optical components with (b) ultra-precision machines

2.3 Ultra-precision Machining

Ultra-precision machining (UPM) is an ultra-precision machining technique for fabricating high precision surfaces with nanometric surface roughness and sub-micrometric form accuracy, without the need for any subsequent polishing. It was pioneered at the Lawrence Livermore National Laboratory (LLNL) by Bryan et al. in the early 1960s (Bryan et al., 1967; Bryan, 1979) when UPM was first developed for manufacturing military products (Ikawa et al., 1991). It was not until the 1970's that it was used to fabricate high precision components to meet the demands of the computer, electronics and defense industries (Corbett et al., 2000). As a result of that demand and of the experience gained, the 80's and 90s saw the wider development of highly advanced machine tools and of reliable high quality diamond tools for fabricating rotational symmetric components. Due to the great advances in science and technology made at the beginning of the 21st century, multi-axis ultra-precision machining is now widely used to serve the demands for freeform surface products.

In terms of machining accuracy, the machining process can be classified into conventional machining, precision machining, ultra-precision machining, and nano-machining. The machining accuracy for UPM is 100 times greater in form error and 1000 times greater in surface finish than for conventional machining. Conventional machining nowadays was once regarded as precision machining in the past. In Figure 2.3, the well-known *Taniguchi-curves* plot the development of machining accuracy over the last sixty years (Taniguchi, 1983, 1996; Cheung and Lee, 2003). It shows that the machining accuracy of UPM has achieved the nanometer level and hints the trend for machining accuracy. Commonly, precision machining can produce precision components with form accuracy in the range of 1 to 0.1μm and surface roughness in the range of 25~100nm, whereas UPM can fabricate components with form accuracy of less than 100nm and surface roughness of less than 25nm. UPM is also known as micro-machining.

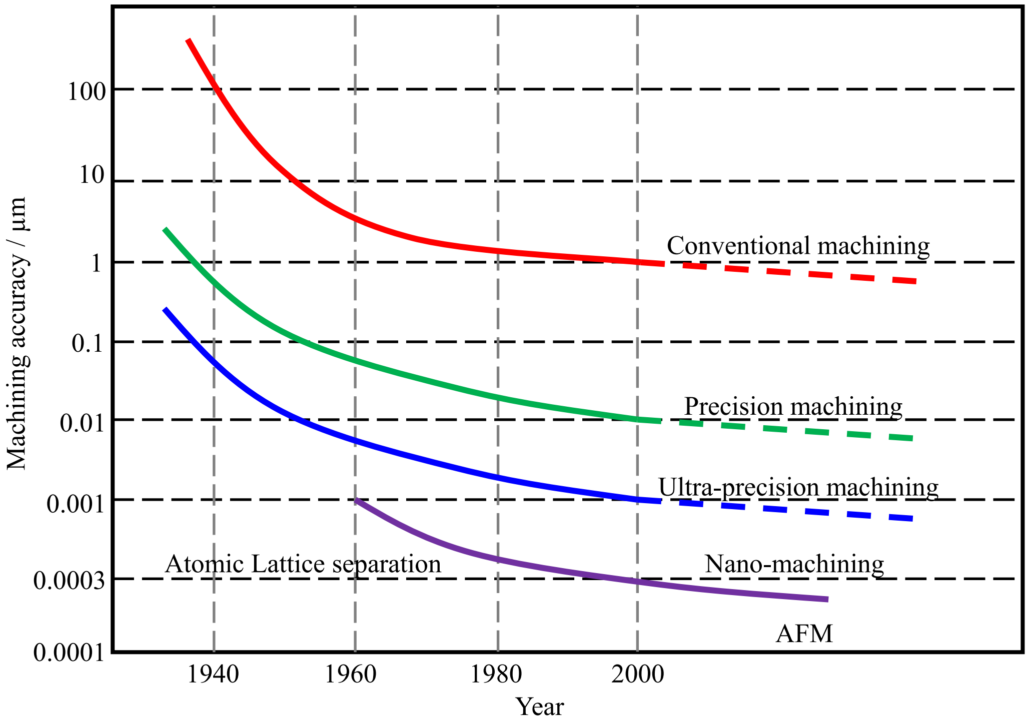

Figure 2.3 Achievable machining accuracy (Taniguchi, 1983, 1996)

Figure 2.4 Single-point diamond tools

In UPM, single point diamond tools/cutters (as shown in Figure 2.4) play an important role. The tools are employed to machine non-ferrous metals, such as copper and aluminum, since the diamond tools possess a nanometric edge radius less than

10nm, good form reproducibility, high stiffness and low wear resistance (Zhang, 1996). Therefore, diamond tools provide a comprehensive solution for UPM to manufacture precision parts and optics of mirror-like surface finish.

UPM typically based on single-point diamond turning (SPDT) and ultra-precision raster milling (UPRM) is a powerful technique for producing high precision components within a surface roughness of a few nanometers and a form error tolerance in the sub-micrometric range (Cheung and Lee, 2003). The development of UPM has become essential to the fast growing demand for crucial optical components for high-value photonics and telecommunications.

2.3.1 Ultra-precision Diamond Turning

Ultra-precision diamond turning (UPDT), also known as single-point diamond turning (SPDT), makes use of a diamond tool to fabricate high precision rotational symmetric components, such as aspheric/spherical surfaces, with a nanometric surface roughness and sub-micrometric form errors. Whitten and Lewis (1966) reported that in the 1950's, SPDT was successfully used to machine some soft metals, such as aluminum and copper. Through the 1970's, SPDT was widely employed for computer, electronics and defense applications (Mckeown, 1987). The achievable machining accuracy was a nanometric surface roughness and a surface form error of about 10nm (Taniguchi, 1983). Figure 2.5 depicts the process of diamond turning of copper alloy, which is capable of producing components with sub-micrometric to micrometric form accuracy and surface roughness in the nanometric range (Cheung and Lee, 2000, 2001). Non-ferrous materials, such as aluminum, copper alloy, silver, gold, electroless nickel, and acrylic plastic workpieces, can be directly machined to optical quality without subsequent post-polishing (Cheung and Lee, 2000, 2001, 2002).

SPDT can finish some 'infrared' materials, such as silicon and germanium, to a surface roughness of a few tens of nanometers (Nakasuji et al., 1990) and it can also machine brittle materials like glass (Puttick et al., 1989). In recent years, hundreds of thousands of ultra-precision components have been developed in the fields of optics, ophthalmic, consumer electronics, computers, communications, medicine and aerospace. In some fields, like automotive and diesel engine fabrication, traditional manufacturing industries have been actively pursuing the development of low cost ultra-precision machining systems. With the development of fast tool servo (FTS) (Ku et al., 1998; To et al., 2006), SPDT can be utilized to produce structural surfaces, such as micro-lens arrays and pyramid arrays. In summary, since SPDT produces a superior surface finish and high-precision form accuracy, the technology has been widely adopted for the manufacture of a variety of precision mechanical and optical parts. Applications have been developed in the manufacture of inserts for injection-moulded plastic camera lenses, scanner mirrors, photoconductor drums in photocopiers, and substrates for memory disks.

Figure 2.5 Ultra-precision single-point diamond turning (SPDT)

2.3.2 Ultra-precision Raster Milling

Ultra-precision raster milling (UPRM) is an emerging ultra-precision machining technology making use of a single crystal diamond tool for fabricating non-rotational freeform surfaces with a surface roughness of a few nanometers and a sub-micrometric form tolerance, without the need for any subsequent post-polishing (Cheung et al., 2004; Cheng, et al., 2007; Wang et al., 2010). It is widely employed for the manufacture of high-precision mechanical components. The milling process is complex (Cheung et al., 2004; Kong, 2009), since it possesses multiple axes, which allow the technology to generate freeform surfaces. It is also time consuming (low efficiency), information intensive, and prone to errors (Cheung et al., 2004).

Figure 2.6 Ultra-precision raster milling (UPRM) (Precitech Freeform 705G, Precision Inc., USA)

The process can be simply considered as face milling the top of a flat surface with a diamond cutter. Figure 2.6 depicts a five-axis ultra-precision raster milling machine, which is an ultra-precision machining technique allowing the production of non-rotational freeform optical surfaces of form accuracy in the sub-micrometric range and surface finish in a ten-nanometric range due to its five-axis motions involving three linear axes and two rotational axes. It is frequently utilized for machining soft ductile materials such as aluminum and copper.

2.4 Aerostatic Bearing Spindle

2.4.1 Development of Aerostatic Bearing Spindle

Generally, an aerostatic bearing spindle comprises a rotary shaft (the spindle rotor/spin), two journal bearings that support the spindle rotor in the radial directions, a pair of thrust bearings that support the spindle rotor in the axial direction, a driving AC servomotor, a spindle house/seal, and a rotary encoder for detecting the spindle speed as illustrated in Figure 2.7. The spindle rotor is flowed by the air bearings without contacting the spindle house though the constant pressure of an air film (named radial clearance) at several micrometric thicknesses (Grassam and Powell, 1964). The constant pressure is generally distributed around the spindle rotor, which is regarded as a rigid body. The motor and the rotary encoder are also non-contact types. Because the spindle rotor is flowed by the pressurized air, the frictional resistance on the spindle rotor is tiny, which allows a very accurate control of the rotary motion of the spindle rotor. In addition to the fundamental structure proposed above, for any other aerostatic bearing spindle for precision machines, the spindle needs to incorporate a bearing arrangement for high spindle rigidity with a high-torque motor offering the torque necessary for the machining process.

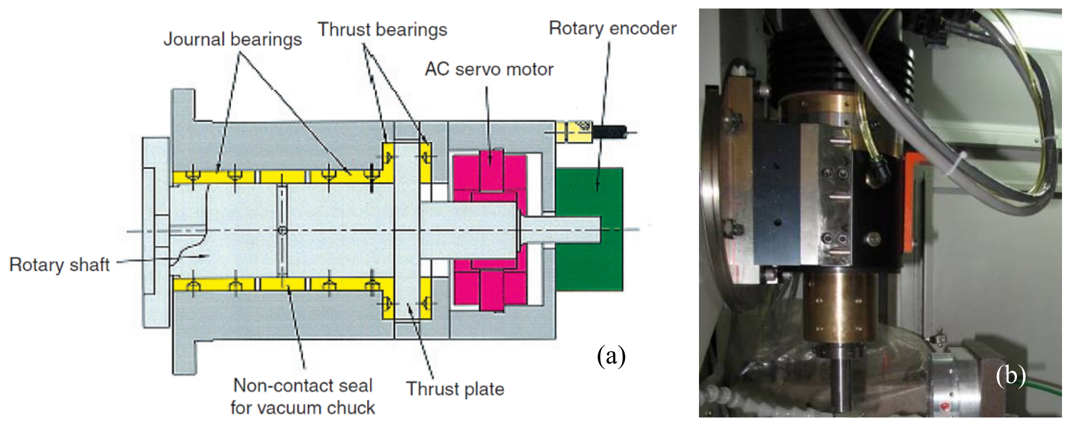

Figure 2.7 (a) Schematic structure of an aerostatic bearing spindle (Horiuchi et al., 2006) and (b) an aerostatic bearing spindle of Precision Freeform 705G (Precision Inc., USA)

The development and study of gas lubricated bearings can be traced back to the early 19th century (Willis, 1828), the middle 19th century (Hirn, 1854) and the late 19th century (Kingsbury, 1897). After the first 50 years of twentieth, with the development of the ultra-precision machining technology, gas lubricated bearings were applied to the air bearing spindle (Gross and Zachmanaglou, 1961; Gross, 1962; Larson and Richardson, 1962; Grassam and Powell, 1964; Taniguchi, 1967; Fuller, 1969). In the mid-1980s, Stout and Sweeney (1984) presented the design of aerostatic thrust bearings which used pocketed orifice restrictors.

In the last twenty years, advances in science and technology have allowed designers of the air bearing spindle to increase its stability by improving stiffness and spindle speed. Kim et al. (1990) designed a hybrid gas bearing spindle and analyzed its stability. As part of a PhD study, Ahuja (1996) designed an aerostatic–aerodynamic, as well as hydrostatic–hydrodynamic conical journal bearing, where rigidity increased with an increase of conical bearing number and supply pressure. Cho et al. (1997) designed and manufactured a hybrid one-piece drive shaft composed of carbon fiber epoxy composite and aluminum tube by co-curing the carbon fiber on the aluminum tube. A high-speed aerostatic spindle using high modulus carbon fiber–epoxy composite material was first proposed by Lee and Choi (2000) in order to increase dynamic stiffness and performance; they developed the composite spindle and the method of joining it to steel sleeves for the aerostatic bearing mounting. Carbon fiber-epoxy composite material has excellent properties for structures due to its high specific modulus, high damping and low thermal expansion, which improve the vibrational and thermal characteristics of the high-speed air bearing spindle (Lee et al., 1985; Choi and Lee, 1997; Lee and Choi, 2000). Bang and Lee (2002a, 2002b) designed the air supply part of a thrust air bearing for a high-speed composite air spindle taking account of its axial stiffness and load capability and considering the static and dynamic characteristics under an axial load and the centrifugal force during high-speed rotation. They also contributed to the design of a high speed air spindle composed of a carbon fiber epoxy shaft and two steel flanges for maximum critical speed considering both the deflection due to bending load, radial expansion, centrifugal force and temperature rise during high-speed rotation. Belforte et al. (2006) designed a high-speed rotor spindle using air bearings and tested its dynamic characteristics.

Due to their advantages of low friction and low heat generation, aerostatic/air bearing spindle systems are widely used in many fields where high precision and high speed are required. However, their advantages are also their disadvantages in that spindle vibration is not damped due to the low viscosity of air. Therefore, some researchers have made great efforts to decrease the effects of spindle vibration on the rotation precision by designing an automatically controlled restrictor and an active inherent restrictor. The former is a passive control method and the latter is an active control method. The passive control method has been the subject of many studies (Mizumoto et al., 1989, 1990; Brzeski and Kazimierski, 1979, 1992; Kazimierski et al., 1992; Yokota et al., 1992) using different approaches. Horikawa and Shimokobe (1990) used the active control method to control the bearing clearance of an air spindle with a piezo actuator, while Mizumoto et al. (1996, 2008, 2010, 2011) used the active control by designing an active inherent restrictor for air bearing spindles. Air-magnetic bearing has been studied to improve spindle precision by many scholars (Ma et al., 1995; Dexter et al., 1998; Li et al., 2002).

The spindle rotation precision or the spindle roundness error is achievable at a few nanometers using different means. These high precision aerostatic bearing spindles are widely used in ultra-precision machines by: LLNL of USA; Rank Taylor Hobson Ltd. of UK; Precitech Inc. of USA; Moore Nanotech of USA; Cranfield Precision of UK; KUGLER Company of Germany; Fanuc Ltd. of Japan; Nachi-Fujikoshi Corp. of Japan; and Matech Industrial Co. Ltd. of Taiwan. The machines include the following large optics diamond turning machines: PERL II, POGAL and DTM 3 (LLNL, 2001); Nanofrom and Freeform series (Precitech, 2011); DeltaTurn40 and OGM 2000 (Cranfield, 2011); KUGLER Microgantry nano3/5X (Kugler, 2011); Nanotech series (Moore, 2011); FANUC ROBONANO α-0iB (Fanuc, 2011); ASP series (Nachi, 2011); and Matech UPT-2000 (Matech, 2011). Despite the widespread use of these machines, spindle vibration still remains an issue.

2.4.2 Dynamic Characteristics of Aerostatic Bearing Spindle

Since gas bearings have less heat generation, lower noise contamination, higher accuracy, and frictional losses close to zero (Gross, 1962; Grassam and Powell, 1964; Frew and Scheffer, 2008), the gas bearing spindle system is employed for high-speed/high-precision electrical spindles. However, the disadvantages of gas bearings are that they become nonlinear under high spindle speed, their low stability often limits the range of applications, and the achievable machining accuracy in UPM is majorly determined by the overall loop rigidity of the system. Furthermore, because it is less stiff than the overall loop stiffness of the machining system, the spindle characteristics considerably affect the machined surface.

Because of the advantages and disadvantages of air bearing spindle characteristics, many researchers have conducted dynamic simulations and measurements of aerostatic/air bearing spindle motions to study its radial, axial and tilting motions. The dynamic motions are known as spindle vibration, which is induced by an unbalanced mass and eccentric moments (Lund, 1967; Ni, 1985). In the early 1960s, Gross (1961) gave perturbation solutions for steady, self-acting, infinitely long journal and plane wedge films. The method was valid for all ranges of geometrical parameters and yielded excellent accuracy. A few years later, linearized Reynolds equations of self-acting bearings were solved by Ausman (1963) to analyze the stability of the static equilibrium position of the shaft. Castelli and Elrod (1965) later proposed a method where a complete set of nonlinear equations were integrated numerically to obtain the rotor center orbits corresponding to any state of geometrical, operating and initial conditions to solve the stability problem. In the mid 60s, Ehrich (1966) identified a sub-harmonic vibration phenomenon in dynamic rotor systems, while near the end of the 60s Marsh (1969) obtained the stability and gave equations of conical motion with and without gyroscopic effect using a linearized theory. In the subsequent decade, Botman (1976) reported non-synchronous vibrations when speeds were in excess of twice the system critical speed on a high-speed rigid rotor-damper system, aperiodic behavior in journal bearings was reported (Holmes et al., 1978), and

Nikolajsen and Holmes (1979) observed non-synchronous vibrations in a flexible, symmetric rotor on two identical plain journal bearings supported by centralized squeeze film dampers.

It was not until the late 80s that sub-harmonic motion in rotor-bearing systems was reported by Li and Taylor's (1987) and Sykes and Holmes (1990) experimentally observed the subharmonic motion in squeeze film bearings and linked this to possible precursors of chaotic motion. In the mid 90s, Brown (1994) developed a simple model of a rigid and hydrodynamically supported journal bearing, using short bearing theory, to analyze the journal's chaotic behavior when the rotating unbalance force exceeded its gravitational load; and Zhao et al. (1994) discussed the sub-harmonic and quasi-periodic motions of an eccentric squeeze film damper-mounted rigid rotor system and noted that for large values of unbalance and static misalignment, the sub-harmonic and quasi-periodic motions in excess of twice the critical speed were bifurcated from the unstable harmonic solution. Theoretical and experimental investigations, in which a rigid rotor supported by short bearings behaved with sub-harmonic, quasi-periodic and chaotic motion for suitable values of system parameters, were subsequently reported by Adiletta et al. (1997a, 1997b); and in the final year of the twentieth century Jang and Kim (1999) calculated dynamic coefficients in a herringbone-grooved journal bearing and thrust bearing, considering five degrees of freedom for a general rotor-bearing system.

Throughout the first decade of the 21st century, Wang (2001, 2004, 2006, 2007, 2008) analyzed the dynamic and nonlinear behavior of a flexible rotor supported by a relative short herringbone-grooved gas journal bearing system, comprised of periodic and quasi-periodic response and varying with bearing number and rotor mass. Most recently, Wang and Yau (2010) studied the behaviors of the high speed air bearing spindle system combining the differential transformation method and the finite difference method to analyze complex dynamic behaviors with periodic, sub-harmonic and quasi-periodic responses.

Above, the periodic, sub-harmonic quasi-periodic and chaotic motions have been proposed. Nonlinear elements are common in structural and mechanical applications because of material hysteresis properties, structural joints, clearances, external air pressure, journal bearings, seals, fractional forces, and the suspension of structure. There has been limited research into the five-degree-of-freedom motions of the spindle regarded as a long shaft and its dynamic characteristics induced by its inertial moments and external forces. The challenges connected with the complex dynamics of the spindle remain formidable.

2.4.3 Measurement of Spindle Errors

As spindle technology develops and demands and expectations of spindle performance increases, it becomes clear that it is necessary to measure and estimate spindle error or vibration. Many machine tool testing methods were adopted in international standards such as ANSI (ANSI/ASME B5.54, 1992; ANSI/ASME B5.57, 1998) and ISO (ISO230 Part3, 2001). ANSI especially drew up the standard (ANSI/ASME B89.3.4, 2010) for the test of a spindle. Many scholars have made a huge contribution to the standards and employed various methods based on separating measured signals.

In the late 60s, Bryan (1967) introduced a fixed sensitive direction method, but it wasn't until the early 70s that Burdekin (1972) proposed a spindle measurement system to measure spindle accuracy and Donaldson (1972) developed a simple method for separating the master ball's error to obtain the spindle error. In the late 70's, Kakino et al. (1977) used two probes to measure the spindle axis error motion for the case of a rotating sensitive direction. Five years later, Mitsui (1982) used a three-probe method at three different angles to observe the roundness shape of the reference arbor and the two-dimensional spindle error motion simultaneously. In the mid 80s, a probe to inspect the spindle axis error motion for the case of a fixed sensitive direction was reported by Su (1985) but it wasn't until the mid 90s that spindle vibration was measured through a laser ball bar rather than a capacitance gauge (Srinivasa et al., 1996). In the following year, Zhang et al. (1997) mounted four probes to measure and estimate the radial error motion of the spindle, and Tu et al.

(1997) proposed an exact model and error analysis for measuring the spindle error motion using the conventional three-probe method.

In the first decade of the 21st century a lot of related research was carried out. Marsh and/or his cooperators measuring the spindle error motion in the radial and axial directions (Marsh and Grejda, 2000; Grejda et al., 2005; Marsh et al., 2006); Yang et al. (2004) developed a ball bar system, as a replacement for the conventional capacitance sensor system, to measure spindle thermal errors in a machine tool; Kim et al. (2007) used three translations and two tilt motions of a rotating stage with high precision capacitive sensors to obtain the radial error motion from T.I.R (Total Indicated Reading) in a radial direction using Donaldson's reversal technique, and the axial components of the spindle tilt error motion from the axial direction outputs of sensors by using the Estler face motion reversal technique; Okuyama et al. (2007) employed a three-point method based on inverse filtering to obtain the radial motion, and calculated the optimal sensor setting angle based on the transfer function, which was applied to the radial motion measurement of a spindle for hard disk inspection in the high revolution range of 4000–10,000rpm; and Chang and Chen (2009) utilized spectral analysis techniques to monitor the vibration of spindle by a piezoelectric transducer.

Further, Gao and his cooperators have made a great contribution to spindle measurement through different developed methods. Firstly, they developed a new multiprobe method for roundness measurements, called the mixed method. This method could eliminate the effect of the spindle error and completely separate the roundness error and the spindle error, as compared to the traditional 3-point method (Gao et al., 1996). Based on the mixed method, a new error separation method for accurate roundness measurement, using one displacement probe and one angle probe to separate roundness error from spindle error, was developed in 1997 (Gao et al., 1997). In 2002, a system integrated with three two-dimensional surface slope sensors was proposed to measure spindle error and roundness. Using this method, the two-directional components of the spindle angular error motion could be obtained accurately (Gao et al., 2002). In the same year, an angular three-probe method was utilized for the radial error motion and angular error motion of the spindle, and the angle probes were calibrated through an in-situ self-calibration method without extra angle references. Comparing with the conventional displacement three-probe method, the angular three-probe method was more suitable for monitoring the multi-degree-of-freedom components of spindle error and roundness (2002a). In 2007, they successfully applied the spindle measurement method for the compensation of error motions in ultra-precision diamond turning to improve surface quality of sinusoidal microstructures on a flat workpiece (Gao et al., 2007).

In summary, the error motions of a spindle can be classified into axial, radial and tilting error motion, majorly measured by displacement sensors, such as piezoelectric transducers, capacitive sensors and laser vibrometry sensors. Although the error motions have been observed by experiments, they have not been sufficiently explored in theory and not enough theoretical work has been done to support spindle error measurements. The challenge is to efficiently separate measurement errors and motion errors from measured signals, because measured signals are observed in one coordinate system (the inertial system) and the motion error is in another coordinate system (the fixed-body system). The measured errors should be regarded as the synthesis of the static errors with the spindle-vibration-induced errors (dynamic errors), not only the static errors.

2.5 Surface Integrity in UPM

UPM is a newly developed manufacturing technique that has shown its comprehensive applicability in the production of components for optics, photonics and telecommunication products. Surface roughness, form accuracy and surface material property changes play an extremely important role in the estimation of a component's surface integrity when using UPM, which are directly related to a component's quality, life and stability. The machined topographical surface is divided into three sizes, depending on the scale of the features: macro, micro and nano. These topographical sizes are primarily determined by factors such as the cutting conditions of tool tip radius, depth of cut and feed rate; material properties of pile-up, swelling and recovery, crystal orientation, and micro-structural change; and relative vibrations such as tool vibration, spindle vibration and slide vibration. Simultaneously, these factors change the properties of machined surface material.

2.5.1 Factors Influencing Surface Roughness in UPDT

Because of many factors affecting topographical surfaces of UPM, there has been a plethora of research on the relationship between surface generation and factors. Geometric surface finish in single-point turning is majorly influenced by cutting speed, feed rate and tool nose radius (Mehta and Mital, 1988; Boothroyd and Knight, 1989).

The depth of cut (i.e. minimum cutting thickness) in precision machining has been studied in different ways by researchers. Basuray et al. (1997) analyzed the transition from ploughing to cutting during machining when using a blunt tool. Ikawa et al. (1985) estimated the edge radius of a diamond tool using SEM and proved experimentally that a continuous chip could be generated at a nanometer order depth of cut. Lucca and Seo (1993) estimated the thinnest cutting thickness with a continuous chip from the observation of the cutting force in a study on energy dissipation in UPM. A simple analytical expression was defined by Yuan et al. (1996) for the minimum cutting thickness derived from relationships between tool sharpness, cutting force and the friction coefficients. Son et al. (2005) derived an equation for the minimum cutting thickness by considering the friction coefficient between a tool and a workpiece, and demonstrated its validity experimentally. The effect of vibration cutting on the minimum cutting thickness was evaluated by Son et al. (2006).

Regarding material properties, Yuan et al. (1994) proposed that the crystallographic orientation of work-piece material exerted a great influence on cutting force and surface roughness and they built a micro-plasticity model to analyze cutting force variation induced by crystallographic nature. Cheung et al. (2002) investigated the effect of crystallographic orientation and process parameters on the surface roughness of brittle silicon single crystals in UPM; their experimental results indicated that anisotropy in surface finish occurred when the cutting direction relative to the crystal orientation varied, where a periodic variation of surface roughness per workpiece revolution existed, which was closely related to the crystallographic orientation of the crystals being cut. Chen (2008) employed a wavelet and fractal method to analyze and evaluate the 3D surface topography of KDP crystal, the results of which presented fractal analysis for the influence of machining method on the surface topography from the disturbance of the material factor, and obtained the microscale waviness information among other spatial frequencies decomposed from the machined KDP crystal surface. Zhao et al. (2009) investigated surface roughness on different crystal planes and reported that on different crystal planes the average surface roughness, as well as variation amplitude, was different.

Concerning material flow in micro-cutting process, Sata (1964) reported the existence of material swelling caused greater tool marks due to tool-nose geometry and resulted in higher surface roughness than in the theoretical case. Effects of material swelling and recovery on surface roughness of ultra-precision diamond turning for different materials under the same cutting conditions have also been studied (To et al., 2001; Kong et al., 2006). Simoneau et al. (2006) proposed that surface micro-defects, such as dimples occurring at a hard-soft grain boundary, influenced surface roughness during micro-scale cutting. Liu and Melkote (2006) presented a model for predicting surface roughness in micro-turning, taking into consideration the effects of material pile-up. To et al. (2009) studied the effect of coolant and dry cutting on surface roughness in UPDT.

Vibration plays a principle role in the micro-cutting process. Material induced vibration had its origin in the variation of micro-cutting forces caused by changing the crystallographic orientation of the material being cut, and its captioned vibration resulted in a local variation of surface roughness of a diamond turned surface (Lee et al., 1999, 2001, 2002). Kim et al. (2002) discussed the effects of tool vibration on surface profiles at the microscopic level. After analyzing the features on a diamond turned surface by the multi-spectrum analysis of its surface roughness profiles measured at a finite number of radial sections of the turned surface, Cheung and Lee

(2000a) presented that the feed rate, the spindle speed, the tool geometry, the material properties, as well as the relative tool-work vibration, were not the only dominant components contributing to the generation of surface roughness. Zhou and Cheng (2009) elaborated that in the nano/micro cutting process, the surface quality was heavily dependent on all the dynamic factors, including those from the material, tooling, process parameters, servo accuracy, mechanical structural stiffness, and non-linear factors. The influence of tool-tip vibration on surface generation in UPDT has been discussed (Ostasevicius et al., 2010; Wang et al., 2010).

In summary, surface topography in UPDT is primarily influenced by: cutting conditions (Lee et al., 2007; Kim et al., 2002; Lee and Cheung, 2001), such as tool tip geometry, spindle speed, depth of cut and feed rate; material pile-up; material swelling and recovery; crystal orientation; the relative vibration (Zhu and Cheng, 2009); material induced vibration and tool vibration. However, spindle vibration and its influence on surface generation in UPDT have been relatively little discussed.

2.5.2 Factors Affecting Surface Roughness in UPRM

Ultra-precision raster milling (UPRM) with a single crystal diamond tool is a new advanced manufacturing technique providing a satisfactory solution for high precision, functional, aesthetic and ergonomic freeform parts within a sub-micrometric form error and a dozen nanometric surface finish. The surface quality depends largely on the selection of cutting conditions and cutting strategies, such as whether to cut along only one direction or both, or whether to cut under only one cutting strategy, or both, or whether to perform spiral cuts.

In conventional milling, factors affecting surface roughness are much more than that in turning, owing to its complex machining mechanism and the multiple selections of cutting operations. Run-out effects are a common problem. A literature review of several previous run-out studies was conducted by Schmitz et al. (2007) who pointed out that the run-out was induced by spindle vibration. The problems associated with radial run-out in end milling operations and the importance of the relationship between the run-out and chip load on surface finish were reported by Kline and DeVor (1983). The identification of cutting force coefficients in the presence of run-out (Yun and Cho, 2001; Ko et al., 2002; Wang and Zheng, 2003) and efforts focused on in-process monitoring and rejection of run-out contributions to the cutting force have been described by many researchers (Liang and Wang, 1994; Stevens and Liang, 1995; Yan et al., 1995; Hekman and Liang, 1997). Moreover, the run-out effects in a chatter suppression scheme for end milling have also been illustrated (Altintas and Chan, 1992). Chen et al. (2003) conducted experimental research into the dynamic characteristics of the cutting temperature in high-speed milling, which presented an inverse heat-transfer model considering three-dimensional transient heat conduction to calculate the heat flux and the temperature distribution on the tool-workpiece interface in the high speed milling process. Peigne et al. (2004) studied the effects of the cutting vibratory phenomenon and its impact on the surface roughness of milled surfaces.

Some researchers have focused on studying the influence of variable cutting operations on surface topographies in UPRM. Kong et al. (2006a) elucidated that material swelling was significant in UPRM, especially when copper alloys machined in the up-cutting direction. By using the surface characterization system in various cutting experiments on different kinds of materials in UPRM, Kong (2006) successfully identified and delineated different swelling responses. Cheng et al. (2005, 2007, 2008) discussed the factors on surface quality in UPRM involving cutting conditions, tool geometry, cutting strategies, cutting directions. Cheng (2006) established the relationship of surface roughness to the factors in order to explore how the factors influenced surface roughness and firstly reported that the run-out phenomenon appeared in UPRM. Kong et al. (2009) investigated the factors influencing surface generation in UPRM and reported that cutting conditions, tool geometry, cutting strategies and tool wear have a major impact on surface roughness, and that cutting strategies, tool path generation and kinematic errors of sliders principally influence the form accuracy of freeform surfaces. Kong (2009) discussed the factors such as the cutting mechanics, surface generation mechanisms and cutting strategies influencing surface roughness, while Wang (2010) discussed material swelling and recovery on different materials in UPRM and the effects of shift length ratio on surface topographies. Although some researchers have studied surface generation in UPRM, the influence of spindle vibration on the surface generation of UPRM has not been considered as a crucial factor.

2.5.3 Effects of Diamond Tool Wear on Surface Roughness in UPM

The single crystal diamond tool has been employed for UPM, and micro-wear of its cutting edge has a larger influence on surface roughness (Wada et al., 1980). A lot of researchers have focused their studies on acoustic emission (AE), cutting force, vibration (acceleration), and SEM pictures to detect diamond tool wear features and to investigate the relationship between diamond tool wear and surface roughness, mainly based on Fourier transform and wavelet transform in UPM. The major types of tool wear include nose wear, flank wear, crater wear, and notch wear as shown in Figure 2.8(a) and (b). Most of studies on tool condition monitoring (TCM) or tool wear detection in the past focused on flank wear and crater wear. This is because the ISO 3685 (ISO 3682, 1993) standard identified flank wear and crater wear as the criteria of tool life.

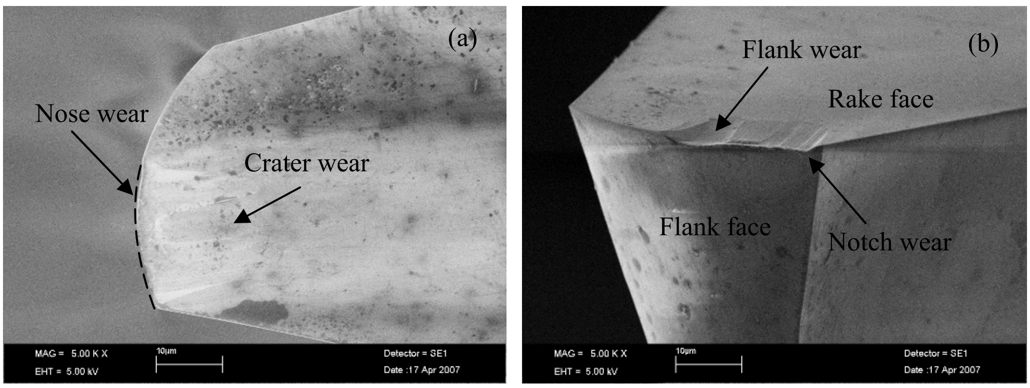

Figure 2.8 (a) Top view of crater wear and nose profile and (b) lateral view of flank wear land and notch wear of a diamond tool

Wada et al. (1980) investigated a relationship of wear to various crystal orientations as well as to surface roughness in cutting Aluminum alloy and Nylon with the diamond tool. The results obtained by observation under a scanning electron microscope (SEM) was that, with the progress of cutting, the wear lands grew in stepped geometry corresponding to the feed rate but were hardly influenced with regard to surface roughness. Syn et al. (1986) proposed multi-methods including Talystep measurement of an root-mean-square amplitude of feed-marks versus cumulative cutting distance, representative examples of shape changes for feed-mark profiles, SEM and optical micrographics of tool rake and flank face wear zones, and measurements of cutting edge profiles and an edge recession distance by a tool-nose replication technique to analyze tool wear and its effects on cutting electroless nickel.

For the purpose of monitoring the progress of the machining state to assure machining accuracy and surface quality, Choi et al. (1999) used a frequency response of multi-sensors signal by acquiring cutting force and acceleration, which included the wear state of the tool in terms of energy within a specific frequency band, to monitor machining states of a diamond tool under face-cutting. They proposed that an increase in cutting velocity and feed for machining with high productivity was generally restricted by elevated cutting temperatures, which caused rapid tool failure in precision machining that impaired dimensional and form accuracy of the product, as well as affecting surface integrity by inducing tensile residual stresses and surface and subsurface cracks. Dhar et al. (2002) suggested that cryogenic cooling by liquid nitrogen jet is an environmentally friendly clean technology for desirable control of cutting temperature to reduce tool wear in turning AISI 4140 steel. Uddlin et al. (2004) investigated tool wear on nano-scale ductile cutting of silicon using an ultra-precision lathe with single crystal diamond tools and reported that gradual wear mainly occurred on the flank face of a tool, and for all the crystallographic orientations studied in diamond tools, gradual tool flank wear had no significant effect on surface roughness of machined silicon work material.

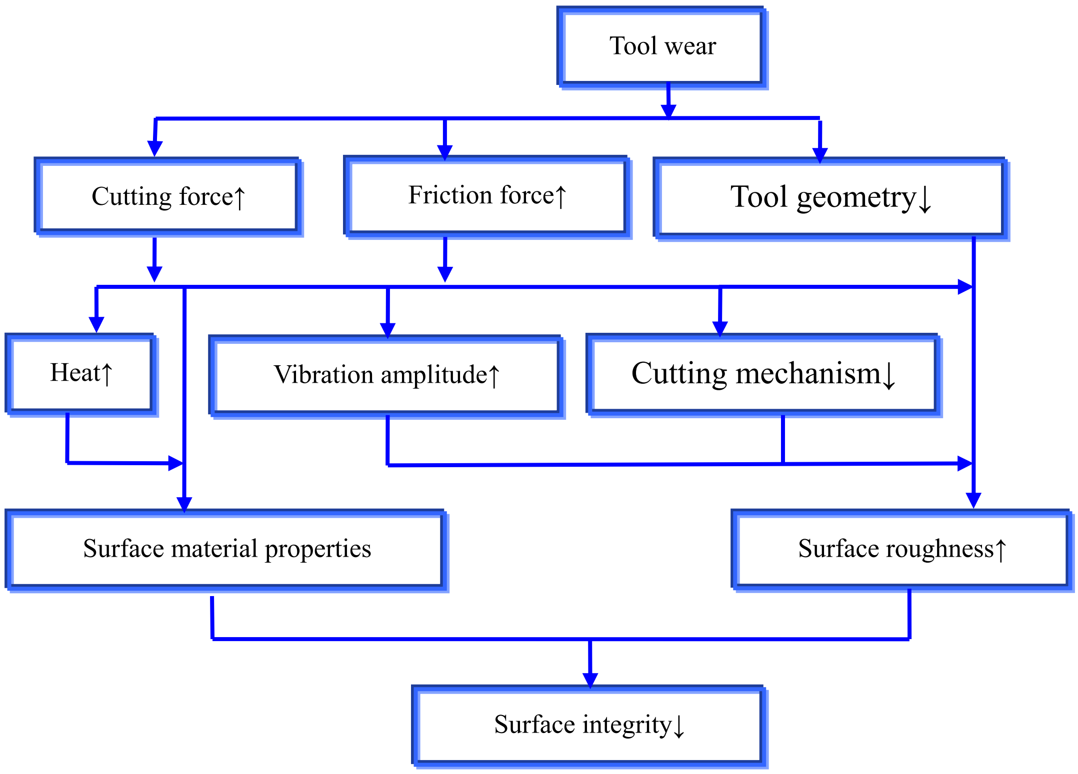

Figure 2.9 Framework for effects of tool wear in machining

In 2006, a wear criterion was chosen as the technological criterion of diamond tool cutting wedge clearance face wear, criterion of temperature rise, and criterion of cut surface deterioration (Grabchenko et al., 2006). Ge et al. (2009) experimentally and theoretically investigated wear pattern and its mechanisms of single crystal diamond (SCD) and polycrystalline diamond (PCD) tools during UPDT of SiCp/2009Al matrix composite under wet machining conditions. The results were as follow: (1) microwear, chipping, cleavage, abrasive wear and chemical wear were principle wear patterns of SCD tools were observed; (2) the SCD tool with the crystal orientation of (rake face 1 1 0-flank 1 0 0) had the best cutting performance among the three types of tools; (3) the PCD tool had a steady and favorable cutting performance and could produce acceptable surface quality after a long cutting distance; (4) adhesive wear on the rake face and abrasive wear on the flank gradually increased with increase of cutting distance; (5) for all three types of tool, with increase of cutting distance, the rate of machining induced defects such as craters and scratches also increased; and (6) when cutting distance was long enough to cause severe tool wear, material swelling was severe due to the plastic side flow.

Overall, tool wear is dynamic and uncontrollable in the metal cutting process, which will induce a poor surface integrity if the tool is worn severely. Tool wear can affect surface integrity either directly or indirectly through others. The summary of tool wear effects in machining is shown Figure 2.9. As shown in Figure 2.9, tool wear causes cutting forces to increase, and those forces promote spindle vibration in the cutting process, which further worsens surface integrity. Hence, it is necessary to establish the relationship between cutting forces and spindle vibration.

2.5.4 Effects of Spindle Vibration on Surface Roughness in UPM

A few researchers have studied the influence of spindle dynamics on surface profiles/topographies in UPM and obtained some primary results. Martin et al. (1995) proposed that spindle vibration influenced surface topographies of machined parts through examining spindle errors, surface finish and form errors of machined parts. Marsh et al. (2005) discussed the effects of spindle dynamics on the topography of flat surfaces in precision fly-cutting, and An et al. (2010) experimentally and theoretically identified the tilting motions of an aerostatic bearing spindle influencing the surface topography of ultra-precision fly cutting. Although some research has been preliminarily conducted on spindle vibration and its effects on surface generation in UPM, it is needed to provide a thorough understanding of the entire cutting mechanism along with the spindle dynamics under cutting forces in UPM.

2.5.5 Effects of UPM on Surface Material Properties

The geometric properties of ultra-precision machined surfaces are determined by many factors, including the cutting tool, cutting parameters and cutting strategies, as well as the surface metallurgical properties before and after machining. The manner and sequence in which cutting takes place will not only affect the machining efficiency of the UPM process but also affect the physical and mechanical properties of the machined surface. The stability of the machined surface not only depends on surface quality, such as surface roughness and form error, but also on surface material properties and change characteristics during the creation of the new surface.

To (2000) produced a doctoral thesis studying the effect of crystallographic orientation on material behavior in UPDT of single crystals and developing a microplasticity model to predict the shear angle and cutting force variation that takes into consideration the Taylor factor, the number of slip systems and the texture softening factor of the material. The theoretical findings accompanied by a detailed microstructure analysis showed how the shear plane forms under different circumstances, depending largely on the orientation of the slip system with respect to the cutting direction (To et al., 1999). The importance of plastic deformation mechanisms at a dislocation level was demonstrated by crystallographic texture analysis, which was used to probe the deformation mode of the machined layer behind the advanced diamond tool (To et al., 2003).

Some research has been conducted on surface material property changes induced by UPM, such as phase decomposition, micro-structural change, phase precipitation, and hardness change. To et al. (2002, 2005, 2006a) discussed the phase transformation in UPDT and the effects of the machining parameters, such as cutting speed and depth of cut, on phase decomposition. In 2008, To et al. studied the effects of UPRM on phase decomposition and hardness of the surface of Zn-Al alloy under various operating conditions (To et al., 2008). Later, To et al. (2009) investigated the characterization of the surface of a furnace-cooled Zn–Al-based alloy ultra-precision machined both with and without a coolant using the data dependent system and power spectral techniques. To et al. (2009a) further proposed that the effect of down-cutting strategy on surface micro-structural changes was stronger than that of up-cutting strategy and that the up-cutting strategy could be used to reduce the effect on surface microstructure in UPRM. Wang et al. (2010) presented ultra-precision raster milling-induced heating effect based on the study of the time–temperature-dependent precipitation of 6061 aluminum alloy under different depths of cut by using a scanning electron microscope (SEM) to reveal the temperature on the raster-milled surface. Zhu et al. (2010) proposed that UPRM resulted in plastic deformation and phase decomposition on the surface layer of the alloy at a thickness of about 250 nm, and discussed the effects of UPRM on surface material properties.

Above all, component's surface integrity consists of surface quality (surface roughness and form error) and surface material property changes, which are directly relevant to component's quality, life and stability. Geometric properties of ultra-precision machined surfaces are determined by many factors, including tool geometry, cutting parameters, cutting strategies and tool wear principally influencing surface roughness, and cutting strategies, tool path generation and kinematic errors of sliders making a major impact on form accuracy as well as metallurgical properties of the surface layer before and after machining. The manner and sequence in machining will not only affect the machining efficiency of the cutting process, but also affect the surface integrity of the machined surface. Unfortunately, the spindle vibration being an extremely important role in UPM has not been substantially studied.

2.6 Measurement and Estimation of Surface Roughness

2.6.1 Surface Roughness Estimation

Surface roughness, synonymously referred to as surface finish, is a key parameter for estimating the quality of a wide variety of engineering components. Perhaps, the most demanding applications are in the optics industry because surface roughness results in scattering and stray light in optical systems and degrades the sharpness and contrast of optical images. In general, the smoother the surface the better a component's function will be.

Surface roughness is employed to evaluate the irregularities on a surface left after manufacturing. These irregularities are inherent in the material removal process as opposed to waviness owing to the poor performance of an individual machine (Whitehouse, 1994). The most commonly used surface roughness parameters are:

(a) Arithmetic Roughness (R_a / S_a);

(b) Root-Mean-Square Roughness (R_q / S_q);

(c) Maximum Peak-to-Valley Height (R_t / S_t); and

(d) Average Maximum Peak-to-Valley Height (R_z / S_z).

Arithmetic Roughness

The arithmetic roughness (R_a / S_a) is the arithmetic average of the absolute deviations from the mean. Surface profile is defined mathematically as (Whitehouse, 1994, ISO 4287:1997):

$$R_a = \bar{z} = \frac{1}{N}\sum_{i=1}^{N}|z_i| \tag{2-1}$$

where the variable z_i is the value deviating away from the mean and N is the number of the sampling points in a measured surface profile. A 3D surface is denoted by (ISO 25178:2009):

$$S_a = \frac{1}{NM}\sum_{i=1}^{N}\sum_{j=1}^{M}|z_{i,j}| \tag{2-2}$$

where, the variable $z_{i,j}$ is the value deviating away from the mean, and N and M are the numbers of the sampling points within a measured 3D surface along two orthogonal directions, respectively.

Root-Mean-Square Roughness

The Root-Mean-Square (RMS) Roughness (R_q / S_q) is the root mean square height of a surface from the mean, called the standard of deviation of the height distribution. The surface profile is defined as (ISO 4287:1997):

$$R_q = \sqrt{\frac{1}{N}\sum_{i=1}^{N} z_i^2} \tag{2-3}$$

where the variable z_i is the value deviating away from the mean and N is the number of the sampling points in a measured surface profile. A 3D surface is defined as (ISO 25178:2009):

$$S_q = \sqrt{\frac{1}{NM}\sum_{i=1}^{N}\sum_{j=1}^{M} z_{i,j}^2} \tag{2-4}$$

where, the variable $z_{i,j}$ is the value deviating away from the mean, and N and M are the numbers of the sampling points in a measured 3D surface along two orthogonal directions, respectively.

Maximum Peak-to-Valley Height

The peak-to-valley height of surface roughness (R_t / S_t) is the distance between the highest peak and the deepest valley within a sampling surface. For the surface profile, the maximum peak-to-valley height (R_t) is the total roughness at the distance from the deepest valley to the highest peak within the sampling length (ISO 4287:1997). For a 2D surface, the maximum peak-to-valley height (S_t) is the total roughness in the sum of the distance from the deepest valley to the highest peak within the sampling surface (ISO 25178:2009).

Average Maximum Peak-to-Valley Height

The Average Maximum Peak-to-Valley Height (R_z / S_z) is the mean of the distances between the 5 highest peaks and the 5 deepest valleys within a sampling surface. For the surface profile, the average maximum peak-to-valley height is the distance between the average value of the sum of the 5 highest values and that of the 5 deepest values within the sampling length (ISO 4287:1997). For a 3D surface, the average maximum peak-to-valley height is the distance between the average value of the sum of the 5 highest values and that of the 5 deepest values within the sampling surface (ISO 25178:2009).

2.6.2 Surface Roughness Measurement

Surface roughness measurement instruments can be classified into conventional instruments and unconventional instruments (Whitehouse, 1994). The conventional instruments mainly comprise contact instruments such as the measurement mechanism of a stylus laser interferometer (Lee et al., 2005) and the Talysurf series (Hu et al, 2009; Taylor Hobson, 2011), and non-contact instruments such as the Zygo series (Zygo, 2011) and the Wyko NT series (Veeco, 2011). Unconventional instruments include the Atomic Force Microscope (Panasonic, 2011). The measuring scale of these instruments is shown in Figure 2.10 (Stedman, 1987). Technique for surface roughness measurement is highly developed.

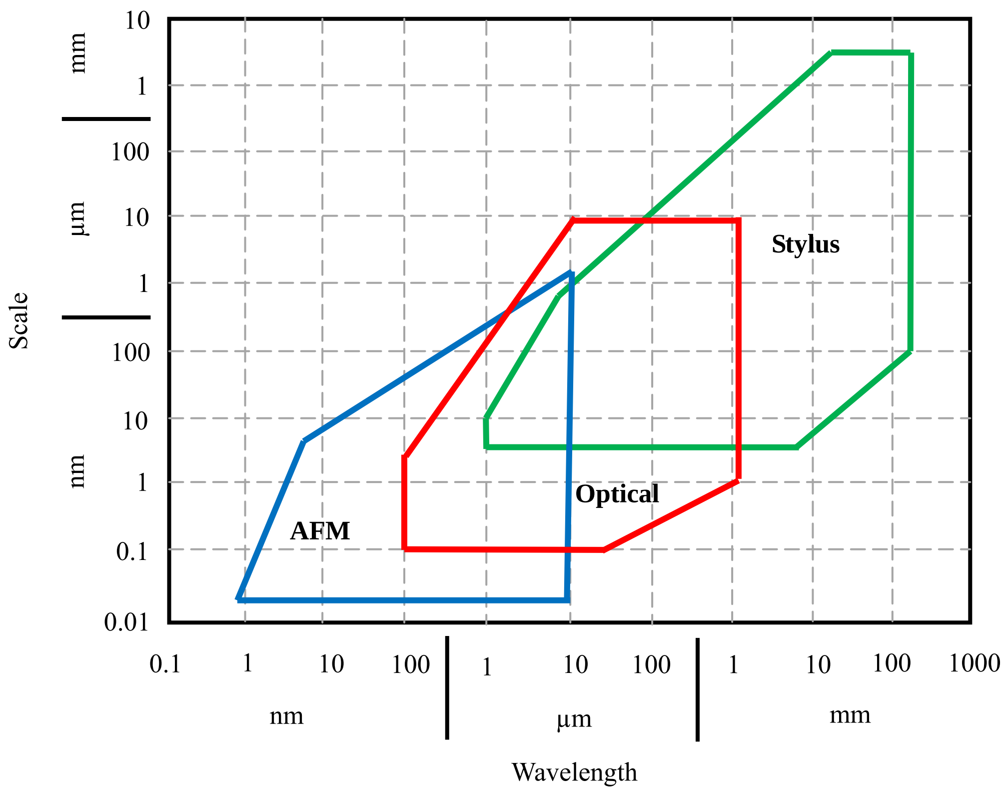

Figure 2.10 Metrology selection (Stedman, 1987)

In stylus measurement instrumentation, a spherical tip linked to a probe is employed to measure surface form and surface roughness, based on the laser interferometer with high precision at a nanometer or even sub-nanometer scale. In 1929, a first stylus instrument was developed by Schmalz (1929, 1936). In 1940, a Talysurf with a stylus was firstly made in Britain to measure surface roughness (Sherwood and Crookall, 1968). Up to the present, the measurement range is increased to 12.5mm and the measurement resolution is to 0.2nm. Although it usually prefers for measuring large surface form, the stylus potentially damages the measured surface to influence the measured surface roughness.

Optical measurement is an efficient means to avoiding damaging the measured surface. The principle is based on the interferometric optical methods. The light projected onto the workpiece surface and reflected into the system is mixed with the standard light from the reference source together. Then, the interferometric stripes are formed and sensed by CCD. Its advantages are that it can measure soft surface with a high resolution and 3D surface topography is easily obtained. Its disadvantage is that its measurement results are influenced by the material color (Gasvik, 1995) and the measuring area is largely limited by the slope of the measured surface. Typical optical instruments include Wyko NT series (Veeco, 2011) and Zygo series (Zygo, 2011).

Atomic force microscopy (AFM) is widely utilized in nanoscience and nanoengineering (Rützel et al., 2003). The developed technique has the tremendous capacity at the atomic scale to test surface properties (electronics, magnetism, friction, adhesion, surface topography, nanohardness, modulus, DNA characterization, etc.) through a tip attached to a soft elastic cantilever, using one of three open-loop modes (non-contact mode, contact mode and tapping mode) (Jalili and Laxminarayana, 2004). The first AFM was invented by Binning, Quate and Gerber in 1986 (Binning et al., 1986), and the first commercial AFM, the Digital Instruments NanoScope® was introduced in 1989 (Park Systems, 2012). Many suppliers manufacture an atomic force microscope, including Agilent Technologies (2012), Angstrom Advanced Inc. (2012), NanoScience Technologies (2012) and Park Systems (2012). Typical AFM instruments include Agilent 6000ILM Atomic Force Microscope (Agilent Technologies, 2012), Angstrom Advanced AA2000 Atomic Force Microscope (Angstrom Advanced Inc., 2012), NanoScience Nanosurf EasyScan 2 FlexAFM (NanoScience Technologies, 2012) and Park Systems XE-Bio (Park Systems, 2012). AFM disadvantages are majorly the single scan image size of the order of 150×150μm and the relatively long scan time.

2.7 Surface Generation in UPM

2.7.1 Surface Generation and Prediction in UPDT

In ultra-precision diamond turning (UPDT), many researchers have focused on building/developing simulation models for surface topography generation, which is governed by the relative movement between a tool and a workpiece depending on the controllability of machine tool to predict surface roughness. Most surface roughness modeling studies have assumed that geometric surface finish in single point turning is influenced by the cutting speed, feed rate and tool nose radius (Mehta and Mital, 1988; Boothroyd and Knight, 1989). Cheung and Lee (2000b, 2000c) proposed a surface roughness simulation model and contended that the process factors involving cutting conditions, tool geometry, relative tool-work vibration and material factors referred to material anisotropy, material swelling and crystallographic orientation of work materials, which are related to the surface topography characteristics in UPDT. An effective fourth order response surface model was further interfaced with a developed genetic algorithm to optimize cutting conditions for desired surface roughness thereby reducing the surface roughness value in the mould cavity from 0.412μm to 0.374μm, representing a 10% improvement (Öktem et al., 2005). Empirical models were developed to correlate the machining parameters with surface roughness, and the influence of cutting parameters on surface roughness parameters such as Ra, Rt, Rq and Rz in turning of glass fiber reinforced composite materials was presented by Palanikumar et al. (2008).

Lin and Chang (1998) suggested that the vibration frequency ratio was a more important vibration parameter than a vibration frequency on the characterization of the surface finish profile. A framework of a model-based simulation system was proposed to determine quantitatively the magnitude of the vibration and its effects on the surface topography of a diamond-turned surface (Lee and Cheung, 2001). A cutting force model was developed to predict the effect of crystallographic orientation on surface quality in UPDT (Lee et al., 1999; Cheung, 2003). Abouelatta and Mádl (2001) focused on building up a relationship between surface roughness and cutting vibrations in turning, and derived mathematical surface models for the predicted roughness parameters based on both cutting parameters and machined tool vibrations. Yurkevich (2006) conducted an experimental study of cutting tool vibrations during turning and discussed their effect on the surface roughness of an article being machined. In diamond turning for the manufacture of optical surfaces, a certain degree of relative vibration was inevitably encountered between tool and work-piece, deteriorating the surface quality and affecting the surface profiles at the microscopic level (Kim et al., 2002). Recently, Salgado et al. (2009) proposed an in-process surface roughness estimation procedure for turning process based on least-squares support vector machines. Thus, the work of Zhu and Cheng (2009) bridged the gap between the cutting process and surface topography/texture generation by proposing an integrated simulation-based approach involving the dynamic cutting process control/drive system, and surface generation.

In summary, most of the research work has focused only on surface generation (Kim et al., 2002; Abouelatta and Mádl, 2001; Lee and Cheung, 2001) based on kinetics and quasi-dynamics affecting surface topography in UPDT to predict surface roughness. However, spindle dynamics of UPDT have not been taken into consideration.

2.7.2 Surface Generation and Prediction in UPRM

Ultra-precision raster milling (UPRM) supports a satisfactory solution for fabricating non-rotational freeform surfaces with nanometric surface roughness and sub-micrometric form accuracy without the need for any subsequent polishing. Surface topography generation is an efficient approach to understanding cutting mechanism of UPRM, as compared with UPDT and conventional milling. Some researchers have studied surface generation and prediction.

Cheung et al. (2004) presented a framework of a model-based simulation system for the prediction of surface generation in ultra-precision multi-axis raster milling of freeform surfaces. Two years later, Cheung et al (2006) developed a model-based simulation system for prediction of form accuracy in UPRM of optical freeform surfaces, which majorly took into consideration the cutting mechanism, cutting strategies and the kinematics of the cutting process. Cheng et al. (2007, 2008) proposed a theoretical model to predict surface roughness and utilized the model to optimize cutting conditions (tool tip geometry, spindle speed, depth of cut, feed rate, swing distance, and step distance) and cutting strategies (horizontal cutting and vertical cutting) in UPRM. Kong et al. (2008) employed a theoretical dynamics model in UPRM for surface generation. Kong (2009) built various surface roughness models based on the cutting mechanics, surface generation mechanisms and cutting strategies to predict and optimize surface generation in UPRM, and Wang (2010) developed a three-dimensional holistic kinematic model for surface generation considering the effects of cutting strategies on surface generation in UPRM. Although some studies have focused on surface generation to understand UPRM's cutting mechanism and predict surface topography, the spindle vibration excited by intermittent cutting forces in UPRM has not been discussed.

To summarize this section, many scholars have attempted to develop various models to predict surface generation of UPM using empirical methods, geometric/mathematical methods, artificial neural networks, cutting force models, and micro-plasticity models. However, there has not been a comprehensive investigation of spindle vibration affecting surface topographies in UPM.

2.8 Optimization of Surface Topography in UPM

2.8.1 Optimization of Surface Roughness in UPDT

The surface generation technique has led to the optimization of machining operations (depth of cut, feed rate, and spindle speed) to achieve good surface quality. To increase machining efficiency, the optimization criteria are majorly considered in minimizing surface roughness, machining time and the number of tool paths.

In conventional turning, Taylor (1907) reported that an optimum value for the cutting speed can be achieved by maximizing the material removal rate in turning. Various technological and practical constraints have been taken into consideration, such as computer software, machine specifications, computing programming, and machining response time. A review by Aggarwal and Singh (2005) showed that the optimization techniques include fuzzy logic, scatter search technique, genetic algorithm, Taguchi technique, and response surface methodology. In addition to these, tool path generation is another important factor influencing both machining efficiency and surface quality in machining (Yan et al., 1997; Yan, 1998; Monreal and

Rodriguez, 2003; Boujelbene et al., 2004; Klaus et al., 2006; Alberti et al. 2007; Zhang et al., 2009), but it does not have to be considered since the tool path is simply determined by two-axis motions of turning. Additionally, some researchers have taken into consideration the acceleration and deceleration effect (Yan et al., 1999; Kim et al., 2002; Heo et al., 2003; Heo et al., 2006). These approaches have been implanted into UPM. Concerning the optimization of surface generation influenced by spindle vibration in UPDT, relatively little quantitative work has been reported.

2.8.2 Optimization of Surface Roughness in UPRM

A significant amount of the literature presented in the above section relates to the optimization of conventional turning, whose approaches can be used into the optimization of conventional milling. In conventional milling, the optimization depends on the use of computer programming, cutting operations (Draghici and Paltinea, 1974; Kruglov and Darymov, 1978; Hough and Goforth, 1981; Ostafiev et al., 1984; Eskicioglu and Eskicioglu, 1992; Alauddin et al., 1997; Baek et al., 2001; Tandon et al., 2002; Chen et al., 2005; Zain et al., 2010) and multiple selections of tool paths (Yan et al., 1997; Yan, 1998; Monreal and Rodriguez, 2003; Boujelbene et al., 2004; Klaus et al., 2006; Alberti et al., 2007).

These methods can be also utilized in UPRM. Since the selection of cutting conditions and cutting strategies in UPRM is multifarious, which largely contributes to surface quality, several researchers have carried out studies on this topic. Cheng et al. (2005, 2007, 2008) developed a theoretical model to predict surface roughness and to optimize cutting conditions (tool tip geometry, spindle speed, depth of cut, feed rate, swing distance, and step distance) and cutting strategies (horizontal cutting and vertical cutting) in UPRM. Kong (2009) built various surface roughness models based on cutting mechanics, surface generation mechanisms and cutting strategies to predict and optimize surface generation in UPRM. And Wang (2010) proposed quality-optimal and time-optimal strategies for UPRM, not only considering the geometry of freeform surfaces but also the cutting mechanics and surface generation mechanism of raster milling; the study found that when the shift length ratio is 0.5, the surface quality is the best one. Although some significant results have been obtained from UPRM studies, the optimization considering the effects of spindle vibration acted on by intermittent cutting forces on surface topography in UPRM is noticeably absent.

2.9 Summary

Along with the development of UPM, there is a huge market for high-precision components like symmetric components, asymmetric and freeform products, which are widely applied in the industry of photonics, telecommunications, illumination systems, etc. Ultra-precision machining technology provides a satisfactory solution for the stringent demands on high quality optical parts widely used in civilian products. In this chapter, the major findings are summarized as below:

(i) The literature review has revealed that the surface quality of these ultra-precision machined products is influenced by many factors. Although relatively fewer studies in UPM have been conducted and some preliminary results have been obtained, the research work is not sufficient for a better understanding of spindle dynamics of UPM with the surface generation mechanism.

(ii) Many studies have focused on developing dynamic models for analyzing the dynamics of spindle motions. However, since the spindle has been regarded as a short rotor, angular perturbation of a spindle has not been considered and no study on the dynamics of angular vibration has been reported in the review.

(iii) Concerning the measurement of spindle errors, the radial, axial and tilting motion errors have been investigated by many scholars with the assistance of displacement sensors, but the measured spindle errors are considered static rather than dynamic, i.e. the spindle vibration cannot be effectively measured due to damping. In the meanwhile, the inertial coordinate system where the spindle motion errors are measured coincides with the coordinate system (namely the fixed-body system) where the spindle moves. There is still a lack of approach efficiently separating static motion errors and dynamic motion errors from the measured signals backed up with a theoretical support. Thus, there is a need for investigation of the dynamics of spindle system under cutting forces in UPM.

(iv) In addition to the contributions made by researchers to the area of UPM, the research on surface generation and optimization and prediction of surface quality has made significant progress. However, the factor of spindle vibration with cutting forces of UPM has not been taken into consideration. No researcher has placed an essential emphasis on the optimization of surface generation relating to the effects of spindle dynamics under the excitation of different cutting forces in UPM.

(v) Consequently, this study investigates dynamic modeling of five-degree-of-freedom vibration of aerostatic bearing spindle under the excitation of cutting forces, and discusses the prediction and optimization of surface generation influenced by spindle vibration.

Chapter 3 Modeling of Spindle Vibration and Cutting Mechanism in UPM

3.1 Introduction

UPM is high precision surface generation through material removal based on precise controllability and measurement of ultra-precision machine tools. Since surface quality is vital for the functional performance and life of product and it is influenced by factors such as cutting operations, material properties and vibration, it attracts much attention.

This chapter focuses on introducing the cutting mechanism for surface formation in ultra-precision diamond turning (UPDT) and ultra-precision raster milling (UPRM), and on the development of a five-degree-of-freedom dynamic model of an aerostatic bearing spindle excited by different types of cutting forces in UPDT and UPRM.

3.2 Surface Formation in UPM

3.2.1 Surface Formation in UPDT

Ultra-precision diamond turning (UPDT) is a high precision technology widely used for manufacturing rotational symmetric surfaces with a few nano-metric surface roughness and sub-micrometric form accuracy, and is performed on ultra-precision single point diamond lathe machines (Optoform 30, Taylor Hobson Pneumo Co., UK, see Appendix I). Figure 3.1 depicts the two-axis CNC ultra-precision lathe. X represents the cutting force direction, Y is the feed direction, and Z is the thrust cutting force direction (depth of cut direction) corresponding to the spindle rotation axis.

During turning of a surface, a workpiece is clamped so that it rotates with the spindle around the Z axis and moves along the Z slide, and a diamond tool is mounted on the Y slide and moves along the Y-axis. Hence, the cutting geometry of single point diamond turning in face-cutting can be represented as that of a tool trajectory with its shape generated at a being-machined surface around the spindle rotation axis Z at the interval of feed rate (f_r). As schematically shown in Figure 3.2(a) and (b), the formed surface topography can be ideally separated into two parts, one is a spiral path of a tool arc center rotating along the spindle rotation axis Z, and the other is a surface profile along the radial direction formed by a series of tool arcs.

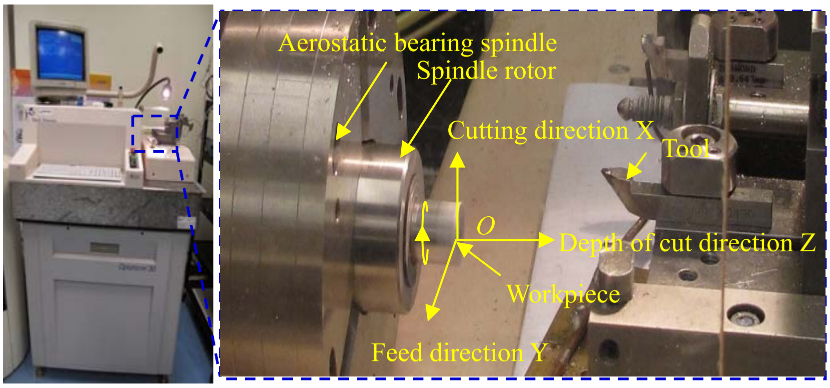

Figure 3.1 Ultra-precision single point diamond lathe machine (Optoform 30) with a single point diamond tool

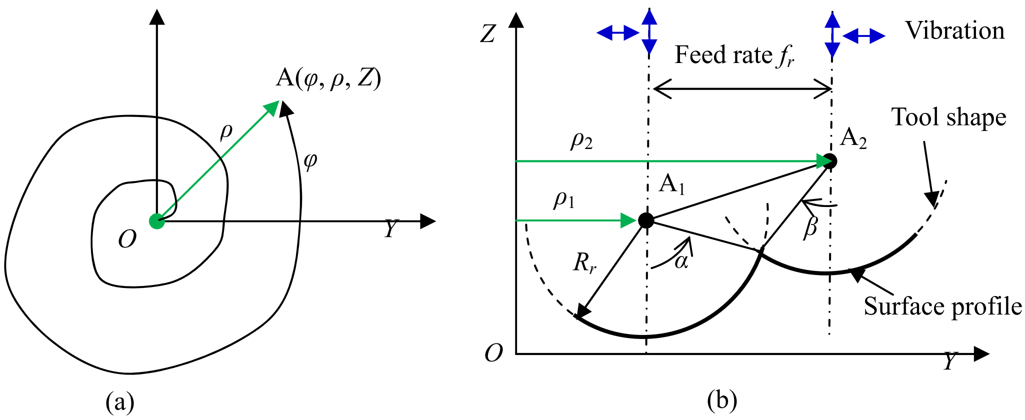

Figure 3.2 Schematic diagram of surface generation with (a) a tool spiral trajectory and (b) a surface profile in the radial direction

3.2.2 Surface Formation in UPRM

Ultra-precision raster milling (UPRM) is an enabling technology widely used for manufacturing non-rotational symmetric freeform surfaces with nano-metric surface roughness and sub-micrometric form accuracy and in this study is performed on an ultra-precision raster milling machine (Precitech Freeform 705G, Precision Inc., USA, see Appendix II). As shown in Figure 3.3, the five-axis ultra-precision freeform machine system possesses three linear axes (X, Y and Z) and two rotational axes (B and C), a diamond tool is set up on the spindle and the work-piece is installed on the B axis rotation table. Since it has multiple axial motions, the material-removing process is complex.

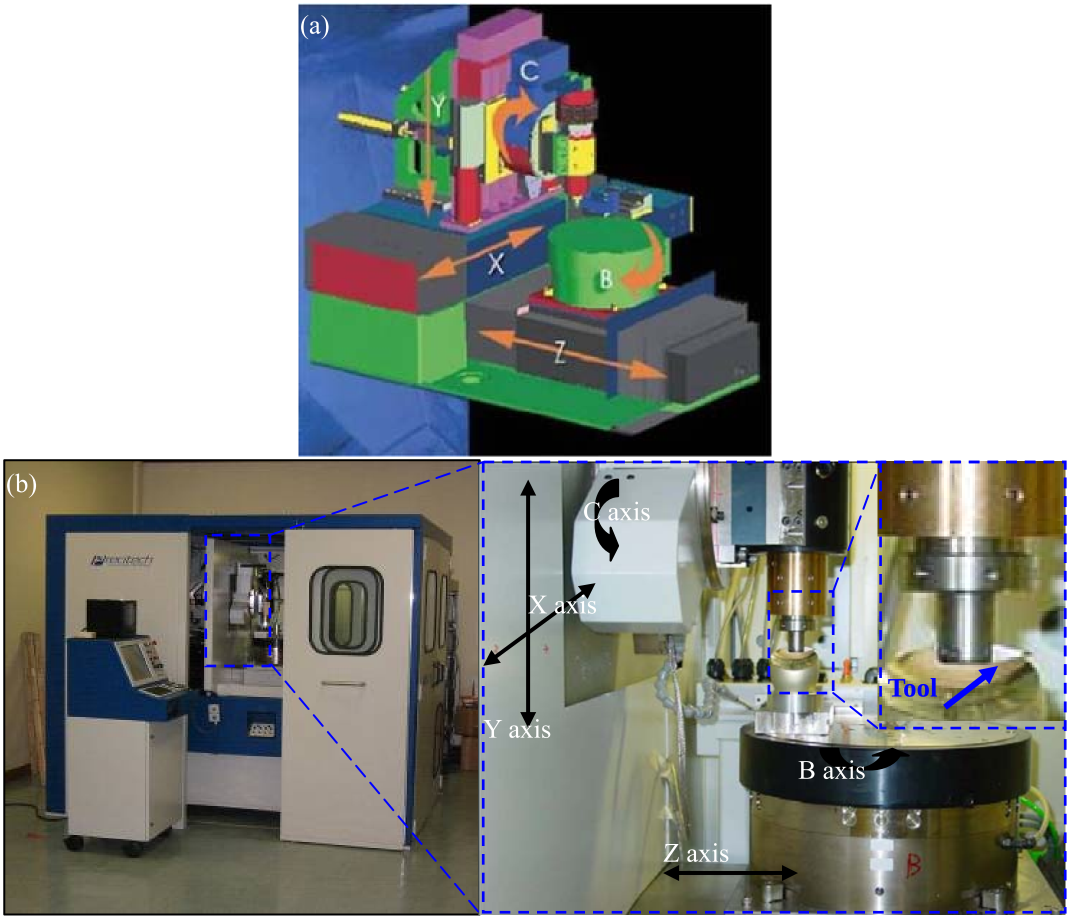

Figure 3.3 (a) Schematic configuration of a UPRM machine and (b) Precitech Freeform 705G

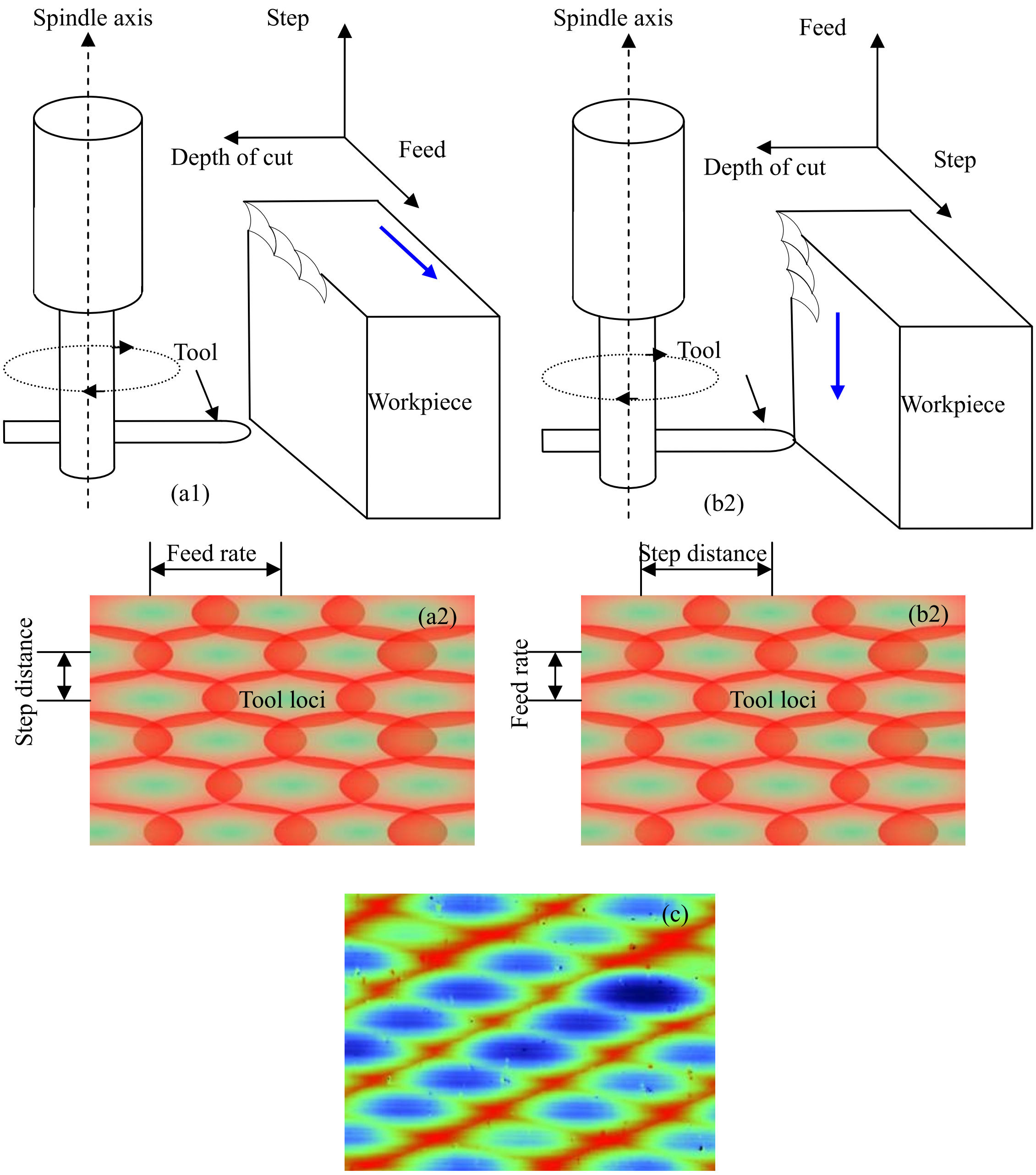

Figure 3.4 Schematic ultra-precision raster milling and surface topographies under (a) horizontal cutting strategy, (b) vertical cutting strategy, and (c) a machined surface topography with shift effects

In UPRM, the surface profile along the tool feed direction of a work-piece is determined by tool geometry, swing distance (d_1), and feed rate (f_r), whilst the surface profile along the raster direction is formed by tool geometry and step distance (s_r). As shown in Figure 3.4 and Figure 3.5, the surface profiles under ideal conditions are formed by the repetition of the tool tip profile at intervals of feed per revolution of the spindle and step distance, and the tool geometry in the feed and raster directions under two cutting strategies with two cutting directions.

3.2.2.1 Cutting Strategies

Horizontal Cutting

Figure 3.4(a) depicts the cutting geometry for horizontal cutting from a three-dimensional view. Feed, raster and spindle rotation directions are moved along the X-axis, Y-axis and Z-axis. The surface profile for the milled surface is formed by the repetition of the tool tip profile at intervals of the tool feed rate along the feed direction and intervals of step distance along the raster direction under ideal cutting conditions.

Vertical Cutting

Figure 3.4(b) shows a three-dimensional view of cutting geometry of the vertical cutting. Feed, raster and spindle rotation directions are moved along the Y-axis, X-axis and B-axis, respectively. The formation of the surface profile under ideal cutting conditions for the machined surface in vertical cutting is similar to that in horizontal cutting.

3.2.2.2 Cutting Directions

Figure 3.5 illustrates the geometry of cutting directions for up-raster milling (up-cutting) and down-raster milling (down-cutting) in horizontal cutting. In up-raster milling, the chip thickness starts at zero and increases to a maximum at the exit per each raster, just as shown in Figure 3.5(a), such that the cutting force direction is along the dashed circle A-B-C. In down-raster milling, the chip thickness starts at maximum and decreases to zero at the exit per each raster, as shown in Figure 3.5(b), such that the cutting force direction is along the dashed circle C-B-A.

The discrepancy between them is that the arc A-B is longer than the arc B-C but twice shorter, according to the rate between the spindle speed ω and the feed rate

f_r and the swing distance d_1. In up-cutting, the cutting time acting the work-piece from the compression force is twice less than that the tensile force, while in down-cutting it is completely reversed.

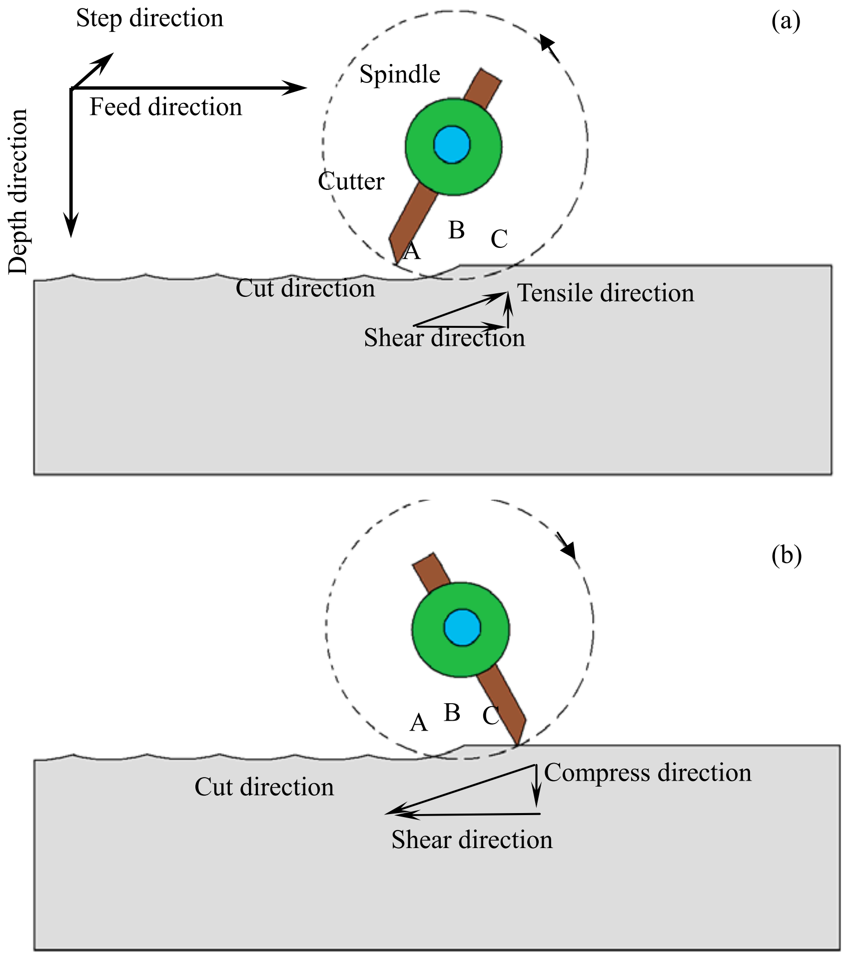

Figure 3.5 Ultra-precision raster milling with (a) up-cutting and (b) down-cutting

3.3 Fundaments of Modeling of Spindle Motions

The concept "a rigid body" is an artificially given one, because all objectives deform after forces or torques are applied to them. Nevertheless, it is very important to analyze rigid motion of an objective as ignoring itself flexural deformation/motion, if the objective is considered as a rigid body when its shape changes relatively little. The forces and torques are referred to as constraints. This hypothesis is quite helpful to build up greatly simplified kinematical and dynamic motions of an objective (Ginsberg, 2008).

In Figure 3.6, a rigid body moves with pure translations in the inertial system O_{XYZ}, and Figure 3.7 describes pure rotations with the reference system O'_{xyz}. The reference system is also defined as a body-fixed system, which cannot move relative to the rigid body. Hence, the velocity and acceleration of one mass point A of the rigid body are described as below:

$$\vec{v}_A = \vec{v}_{O'} + \vec{\omega} \times \vec{r}_{O'A} \tag{3-1}$$

$$\vec{a}_A = \vec{a}_{O'} + \vec{\alpha} \times \vec{r}_{O'A} + \vec{\omega} \times (\vec{\omega} \times \vec{r}_{O'A}) \tag{3-2}$$

where the arrow → over one character represents the vector in a three dimensional space. $\vec{v}$ is the velocity, $\vec{\omega}$ denotes the angular velocity, $\vec{a}$ is the acceleration, $\vec{\alpha}$ is the angular acceleration, $\vec{r}$ is the distance and the cross × denotes the cross product between two vectors.

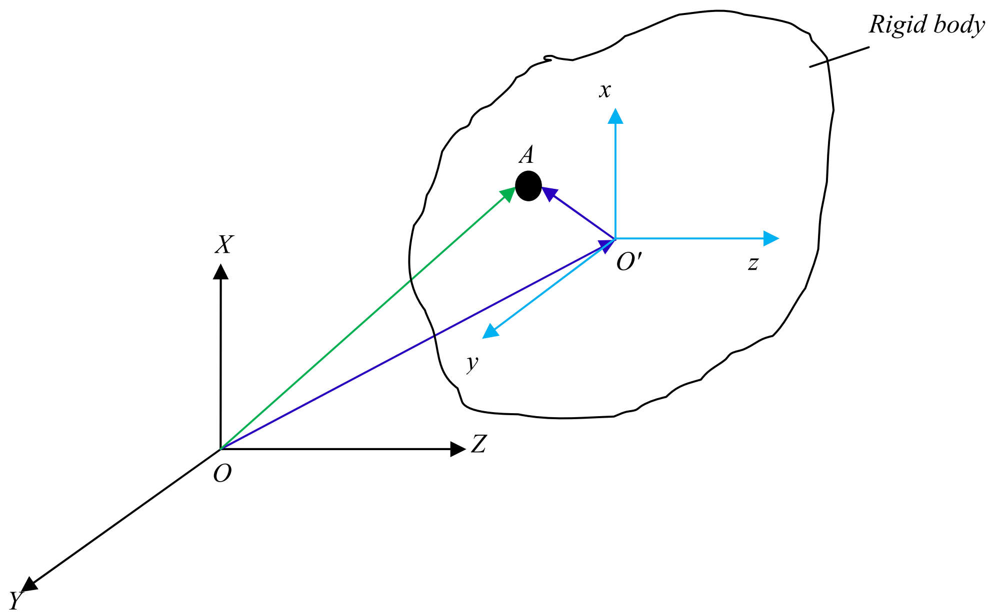

Figure 3.6 Relative motions of a mass point in a rigid body

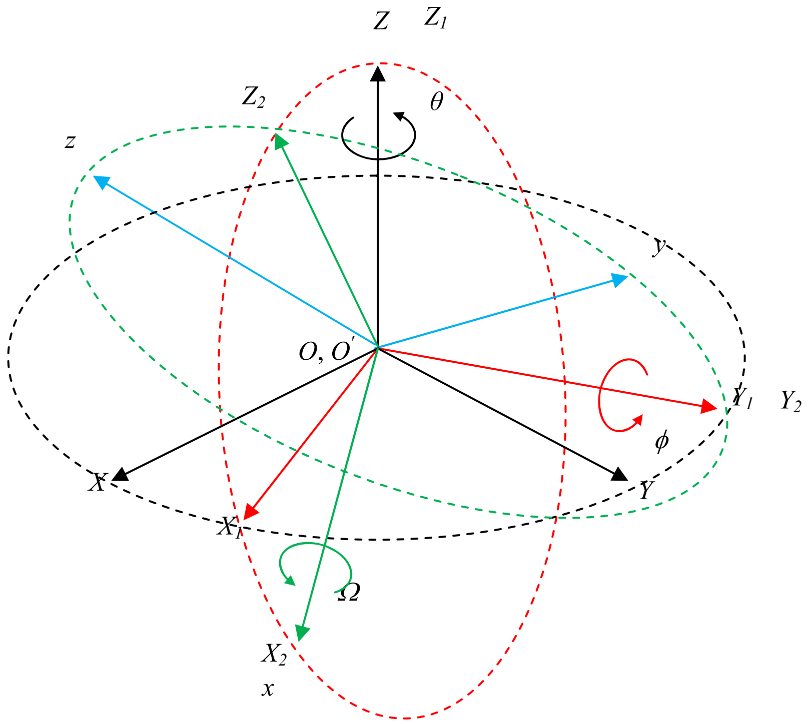

Figure 3.7 Definition of Eulerian angles

3.3.1 Eulerian Angles

In a system, Eulerian angles (Meirovitch, 1970) present the orientation of a rigid body at a sequent set of three independent direction angles. Figure 3.7 shows that the body-fixed system O_{xyz} sequentially rotates in the inertial system O_{XYZ} at the angles, θ, ϕ and Ω, respectively, and O/O' is the rotation center.

The first rotation is named the precession. The orientation of the moving system is denoted as $O_{X_1Y_1Z_1}$ rotated away from the inertial system O_{XYZ} around the fixed Z axis at the angle of θ, as shown in Figure 3.7. Specifically, the transformation of Point A is:

$$\begin{bmatrix} A_{X1} \\ A_{Y1} \\ A_{Z1} \end{bmatrix} = \begin{bmatrix} \cos\theta & -\sin\theta & 0 \\ \sin\theta & \cos\theta & 0 \\ 0 & 0 & 1 \end{bmatrix} \begin{bmatrix} A_X \\ A_Y \\ A_Z \end{bmatrix} \tag{3-3}$$

The second rotation is named the nutation. The orientation of the moving system is denoted as $O_{X_2Y_2Z_2}$ rotated away from the initial system $O_{X_1Y_1Z_1}$ around the fixed Y_1 axis at the angle of ϕ. Specifically, the transformation of Point A is:

$$\begin{bmatrix} A_{X2} \\ A_{Y2} \\ A_{Z2} \end{bmatrix} = \begin{bmatrix} \cos\phi & 0 & -\sin\phi \\ 0 & 1 & 0 \\ \sin\phi & 0 & \cos\phi \end{bmatrix} \begin{bmatrix} A_{X1} \\ A_{Y1} \\ A_{Z1} \end{bmatrix} \tag{3-4}$$

The last rotation is named the spin. The orientation of the moving system is denoted as O_{xyz} rotated away from the initial system $O_{X_2Y_2Z_2}$ around the fixed X_1 axis at the angle of Ω. Specifically, the transformation of Point A is:

$$\begin{bmatrix} A_x \\ A_y \\ A_z \end{bmatrix} = \begin{bmatrix} 1 & 0 & 0 \\ 0 & \cos\Omega & -\sin\Omega \\ 0 & \sin\Omega & \cos\Omega \end{bmatrix} \begin{bmatrix} A_{X2} \\ A_{Y2} \\ A_{Z2} \end{bmatrix} \tag{3-5}$$

Therefore, the angular velocity Eq.3-1 and the angular acceleration Eq.3-2 are readily expressed by adding the precession, nutation and spin rate around the respective axes.

3.3.2 Newton-Euler Equations of Motion

Newton-Euler equations of motion are based on the linear principle of Newton and the angular momentum principle of Euler. These principles represent the translational and rotational motions of a rigid body.

According to Newton's second law stating that the resultant force acting on a particle is proportional to the acceleration of the particle, called the linear momentum principle of Newton, the mass is the factor of proportionality, and the formula can be written as:

$$\vec{F} = m\vec{a}_A \tag{3-6}$$

According to Euler's second law stating that the resultant moment of the external forces acting on a particle is equal to the rate of change of the total angular momentum of the particle, called the angular momentum principle of Euler, the formula can be written as:

$$\vec{M} = \vec{r} \times \vec{F} = \dot{\vec{H}} = J \cdot \dot{\vec{\omega}} + \vec{\omega} \times (J \cdot \vec{\omega}) \tag{3-7}$$

where the dot · over one character represents the derivative or between two characters means the dot product, the arrow → denotes the vector, H is the angular momentum, M means the moment and $\vec{\omega}$ denotes the angular velocity.

3.4 Dynamic Modeling of an Aerostatic Bearing Spindle in UPDT

An aerostatic bearing spindle, schematically shown in Figure 2.7(a) of Chapter 2, comprises a spindle shaft/rotor, two journal air bearings supporting the spindle rotor in the radial direction, one pair of thrust air bearings supporting the spindle rotor in the axial direction, and an AC servomotor driving the spindle rotor. The spindle rotor is floated by a constant pressurized air film at several micrometric thicknesses through these bearings. The aerostatic bearings are equivalently considered as springs to support the spindle rotor, since they are stable. The spindle vibration consists of the radial, axial and tilting motions (see Figure 3.8). It is modeled to characterize its dynamic characteristics, and the dynamic formulas are described by Newton-Euler equations of motion, including three translational motions and three rotational motions in a three-dimensional space.

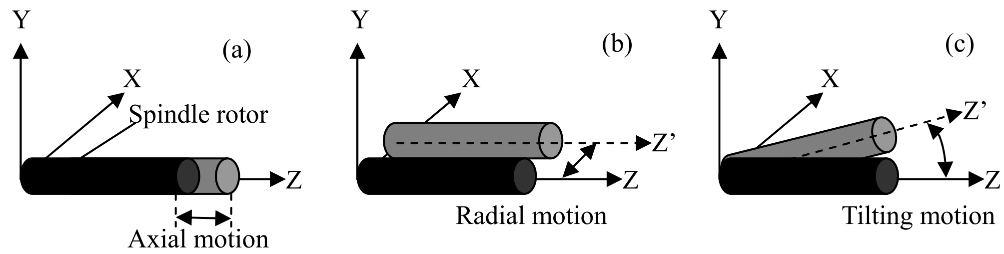

Figure 3.8 Schematic diagrams of the spindle motions (a) axial translational motion along the Z axis (the axial direction), (b) radial translational motion along the X axis or Y axis (the radial direction) and (c) tilting motion deviating away from the Z axis

3.4.1 Dynamic System of a Spindle

When considering a synchronous unbalance rotor supported by two pairs of external pressurized air journal and thrust bearings, the following assumptions should be made:

(1) The stiffness of the aerostatic bearings is independent of spindle speed, constant and stable at small values of eccentricity ratio, because the spindle speed is less than 10000rpm, i.e., the bearing stiffness is regarded as a constant value.

(2) The flexural stiffness of the rotor is further higher than the aerostatic bearing stiffness, i.e. the rotor is considered as a rigid body.

(3) The static displacement of a rotor due to its weight is neglected, because the rotor is in static equilibrium.

(4) The damping ratio in the bearings is independent of speed, because of the spindle speed less than 10000rpm.

Based on these assumptions, to model the radial, axial and tilting motions (Figure 3.8) of the aerostatic bearing spindle in ultra-precision diamond turning (UPDT), the spindle system is simply idealized as a multi-degree-of-freedom spring-mass-damper system, as schematically shown in Figure 3.9. The spindle rotor is regarded as a rigid body, which mass is generally distributed, but for a simple analysis, it is approximated and represented by a single point mass with an eccentric distance. Thus, the spindle rotor is supported by a constant pressurized air film denoted by a series of springs in the axial and radial directions, whose stiffness distribution along the journal length is considered as a stable and constant value. In Figure 3.9, the spindle rotor mass is replaced by a mass point m, x, y and z express translational displacements of the spindle rotor, c represents viscous damper and k stands for stiffness of springs, e represents an eccentric distance, θ and ϕ mean tilting angles of the spindle rotor deviating away from the initial spin axis, respectively, and ω is the angular velocity of the spindle rotation equal to spindle speed.

In Figure 3.9, the springs support the spindle rotor in the radial and axial directions, and the spindle rotor is referred to a reference system *o*(*xyz*) (namely a body-fixed system) moving in the inertial coordinate system *O*(*XYZ*) with the rotor's eccentric mass *m*. Therefore, its motions consist of the rotations of the inertial coordinate system *O*(*XYZ*) around the *x*, *y* and *z*-axis with the variable angles (θ, ϕ and Ω) of the reference coordinate system *o*(*xyz*) as shown in Figure 3.10(a) and the translations of the inertial coordinate system *O*(*XYZ*) along the *X*, *Y* and *Z*-axis with the variable displacements (*x*, *y* and *z*, respectively) of the inertial coordinate system *O*(*XYZ*) as shown in Figure 3.10(b). Then, the dynamic equilibrium of the spindle rotor in the spindle system can be presented by Newton-Euler equations of motion, which includes three translational motions and three rotational motions in a three-dimensional space.

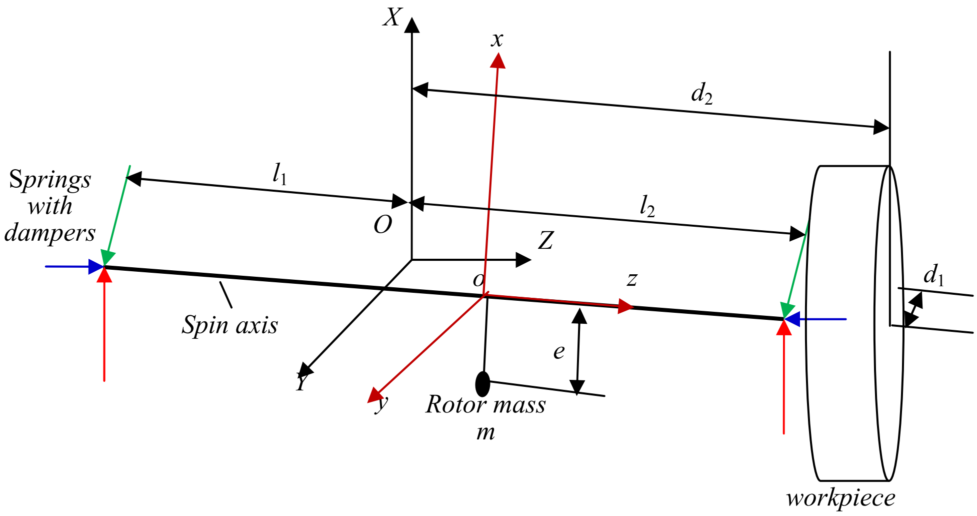

Figure 3.9 The schematic spindle system with one workpiece referred to the reference coordinate frame *o*(*xyz*) moving in the inertial coordinate frame *O*(*XYZ*)

3.4.2 Coordinate Transformations

Figure 3.9 schematically shows that the springs support the spindle rotor in the radial and axial directions and a reference system *o*(*xyz*) attached to the spindle rotor is built up and moving in the inertial coordinate system *O*(*XYZ*) with the rotor's eccentric mass *m*. The moving reference system *o*(*xyz*) is named the body-fixed system. To follow the rotations of the axes, *O*(*XYZ*) is the original orientation of the body-fixed system *o*(*xyz*) prior to the initiation of motion. Because a translation transformation accounts for the motions of the origin of *o*(*xyz*), the *O*(*XYZ*) coincides with the origin of *o*(*xyz*). For rotation of the rigid body, to avoid ambiguity, the right-hand rule is employed to define the positive sense of rotation. Specially, one curls the fingers of the right hand in the sense of the rotation. If the extended thumb of that hands points in the positive sense of the rotations axis, the rotation angle is positive.

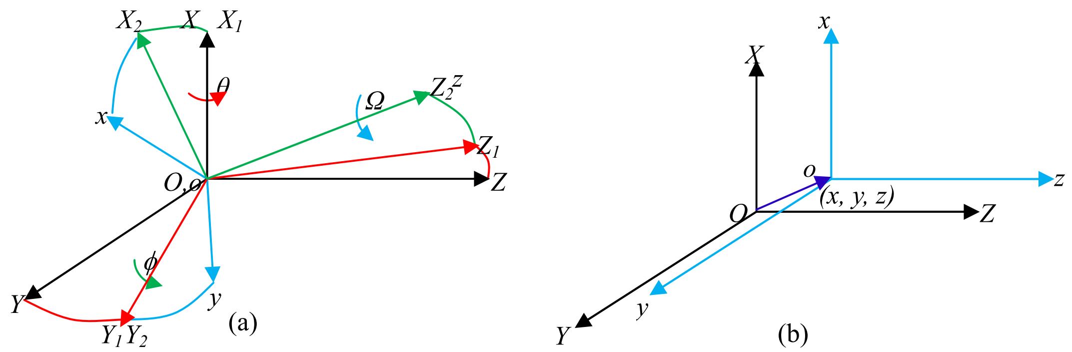

Figure 3.10 The coordinate transformations: (a) translational transformation and (b) rotational transformation

In Figure 3.10, the motions are comprised of the rotations of the inertial coordinate system *O*(*XYZ*) around the *x*, *y* and *z*-axis with the rotation angles (θ, ϕ and Ω) of the reference coordinate system *o*(*xyz*), where the corresponding first order derivatives of the rotation angles are the angular velocity $\dot{\theta}$, $\dot{\phi}$ and $\dot{\Omega}$, and the corresponding second order derivatives of rotation angles are the angular acceleration $\ddot{\theta}$, $\ddot{\phi}$ and $\ddot{\Omega}$, and of the translations of the inertial coordinate system *O*(*XYZ*) along the *x*, *y* and *z*-axis with the displacements (*x*, *y* and *z*, respectively) of the reference coordinate system *o*(*xyz*), where the corresponding first order derivatives of the displacements are the velocity $\dot{x}$, $\dot{y}$ and $\dot{z}$, and the corresponding second order derivatives of the displacements are the acceleration $\ddot{x}$, $\ddot{y}$ and $\ddot{z}$, as below:

(1) Translation along the *X*-axis, *x*;

(2) Translation along the *Y*-axis, *y*;

(3) Translation along the *Z*-axis, *z* ;

(4) Rotation around the *X*-axis, θ, called the precession angle;

(5) Rotation around the Y_1-axis, ϕ, called the nutation angle; and

(6) Rotation around the *z*-axis (the spin axis), Ω, called the spin angle, which are known as Eulerian transformation.

For the two-axis CNC ultra-precision lathe, *X* represents the main cutting force direction, *Y* is the feed direction, and *Z* is the thrust cutting force direction, corresponding to the initial spin axis. *l* is the position of the mass center relative to the spindle bearing on two sides along the *Z*-axis. d_1 means the distance between the tool tip and the spindle axis along the *Y*-axis and d_2 is the distance from the machined workpiece surface to the equilibrium center of the spindle rotor along the *Z*-axis, when cutting. It is shown in Figure 3.1.

For the previous Eulerian transformation of the spindle system as shown in Figure 3.10(a), according to Eq.3-3, Eq.3-4 and Eq.3-5, the mathematic transformation metrics are described below.

Firstly, from $O(XYZ)$ to $O_1(X_1Y_1Z_1)$ around the X/X_1-axis with the angle θ, the rotation transformation is described as:

$$C_{OO_1} = \begin{bmatrix} 1 & 0 & 0 \\ 0 & \cos\theta & -\sin\theta \\ 0 & \sin\theta & \cos\theta \end{bmatrix} \approx \begin{bmatrix} 1 & 0 & 0 \\ 0 & 1 & -\theta \\ 0 & \theta & 1 \end{bmatrix} \tag{3-8}$$

Secondly, from $O_1(X_1Y_1Z_1)$ to $O_2(X_2Y_2Z_2)$ around the Y_1/ Y_2-axis with the angle ϕ, the rotation transformation is expressed as:

$$C_{O_1O_2} = \begin{bmatrix} \cos\phi & 0 & -\sin\phi \\ 0 & 1 & 0 \\ \sin\phi & 0 & \cos\phi \end{bmatrix} \approx \begin{bmatrix} 1 & 0 & -\phi \\ 0 & 1 & 0 \\ \phi & 0 & 1 \end{bmatrix} \tag{3-9}$$

Thirdly, from $O_2(X_2Y_2Z_2)$ to $o(xyz)$ around the Z_2/z-axis with the angle Ω

(corresponding to the spindle rotation angle), the rotation transformation is written as:

$$C_{O_2 o} = \begin{bmatrix} \cos\Omega & -\sin\Omega & 0 \\ \sin\Omega & \cos\Omega & 0 \\ 0 & 0 & 1 \end{bmatrix} \tag{3-10}$$

Hence, from $O(XYZ)$ to $o(xyz)$, the whole rotation transformation is given by

$$C_{Oo} = \begin{bmatrix} \cos\Omega & -\sin\Omega & -\phi \\ \sin\Omega & \cos\Omega & -\theta \\ \phi\cos\Omega + \theta\sin\Omega & -\phi\sin\Omega + \theta\cos\Omega & 1 \end{bmatrix} \tag{3-11}$$

where $\sin\phi \approx \phi$, $\sin\theta \approx \theta$, $\phi\sin\phi \approx 0$, $\theta\sin\theta \approx 0$, $\phi\sin\theta \approx 0$, $\theta\sin\phi \approx 0$, $\cos\phi \approx 1$ and $\cos\theta \approx 1$. Since these perturbation angles are extremely tiny because of the micrometric bearing clearance, these variables are defined as one linear small quantity, their products are one quadratic small quantity, which can be neglected in the system transformation, and the products between linear small quantity with its deviation are still not taken account of, i.e., $\theta\dot{\theta} \approx 0$, $\theta\dot{\phi} \approx 0$, $\phi\dot{\phi} \approx 0$ and $\phi\dot{\theta} \approx 0$.

From O (XYZ) to o (xyz), the angular velocity of the spindle spin rotation is:

$$\dot{\vec{\theta}} + \dot{\vec{\phi}} + \vec{\omega} \tag{3-12}$$

Then, in o (xyz), the angular velocity is:

$$\omega_o = \begin{bmatrix} \overline{\omega}_x \\ \overline{\omega}_y \\ \overline{\omega}_z \end{bmatrix} = C_{O_1 o} \begin{bmatrix} 0 \\ \dot{\phi} \\ \omega \end{bmatrix} + C_{Oo} \begin{bmatrix} \dot{\theta} \\ 0 \\ 0 \end{bmatrix} \tag{3-13}$$

where Ω is equal to ωt, in which ω is the angular velocity of the spindle rotation corresponding to spindle speed and t is time. The angular velocity is simplified as:

$$\omega_o = \begin{bmatrix} \overline{\omega}_x \\ \overline{\omega}_y \\ \overline{\omega}_z \end{bmatrix} = \begin{bmatrix} -\dot{\phi}\omega + \dot{\theta}\cos\omega t \\ \dot{\phi} - \dot{\theta}\sin\omega t \\ \omega \end{bmatrix} \tag{3-14}$$

where the product between linear small quantity with its deviation is unevaluated, $\overline{\omega}_x$, $\overline{\omega}_y$ and $\overline{\omega}_z$ stands for the angular velocities in $o(xyz)$.

The mass center coordinate $\vec{e}$ in $o(xyz)$ (as shown in Figure 3.9) is expressed as:

$$\vec{e} = \begin{bmatrix} e_x \\ e_y \\ e_z \end{bmatrix} = \begin{bmatrix} 0 \\ e \\ 0 \end{bmatrix}. \qquad (3\text{-}15)$$

Since the spindle rotor is symmetric, the inertial tensor (moment of inertia) in $o(xyz)$ is displayed as:

$$J = \begin{bmatrix} J_x & -J_{xy} & -J_{xz} \\ -J_{yx} & J_y & -J_{yz} \\ -J_{zx} & -J_{zy} & J_z \end{bmatrix} = \begin{bmatrix} J_x & 0 & -me(l_1 - l_2) \\ 0 & J_y & -me(l_1 - l_2) \\ -me(l_1 - l_2) & -me(l_1 - l_2) & J_z \end{bmatrix} \qquad (3\text{-}16)$$

3.4.3 Cutting Force Description

In the cutting process of diamond turning, the cutting forces are indirectly applied to the spindle rotor through the workpiece. When the cutting velocity ($2\pi d_1 \omega$) is greater than the vibration velocity, the cutting process is a continuous cutting mode, but as the d_1 is very small, i.e. the cutting speed is less than the vibration velocity, the cutting process is an intermittent cutting mode. Whereas, in the center, the cutting process is regarded as intermittent cutting, otherwise the cutting process is considered as constantly continuous cutting, i.e. the cutting forces are invariable. In practice, when moving to the centre, the spindle velocity is zero, so the intermittent cutting appears due to the spindle vibration, but the cutting time is negligibly short. Therefore, in this study the cutting process of diamond turning is regarded as the continuous cutting mode, i.e. the cutting forces are constant.

In the cutting process, the spindle rotor and the workpiece are considered as a whole body, and the cutting forces are regarded as the inputs for the system. Dynamic responses of the spindle rotor will play a significant role in the cutting process, since this kind of spindle vibration is directly relevant to the cutting force variation, and it simultaneously influences surface micro-topography or surface roughness.

3.4.4 Establishment of Dynamic Equations

To present dynamic responses of the spindle rotor, Newton-Euler equations based on the linear and angular momentum principles of Newton and Euler are employed. Since external forces and a centrifugal force in the system *O*(*XYZ*) and external torques and inertial moments in the *o*(*xyz*) excite the spindle rotor, the spindle rotor is moving with the translational motions and the rotational motions.

In the system *O* (*XYZ*), the external forces are expressed as:

Cutting forces: $\begin{bmatrix} F_m \\ F_r \\ F_t \end{bmatrix}$.

Frictional forces: $\begin{bmatrix} c_x \dot{x} \\ c_y \dot{y} \\ c_z \dot{z} \end{bmatrix}$, where c_is are linear viscous dampers of air.

Constraint forces from the air bearings: $\begin{bmatrix} k_2 x \\ k_3 y \\ k_1 z \end{bmatrix} + C_{Oo}^T \begin{bmatrix} k_2(l_1 - l_2)\theta \\ k_3(l_1 - l_2)\phi \\ k_1(l_1 - l_2)\cos\sqrt{\theta^2 + \phi^2} \end{bmatrix}$, where k_2 and k_3 are the radial stiffness in the *X*-axis and *Y*-axis, respectively, and k_1 is the axial stiffness in the *Z*-axis.

In the *o* (*xyz*), external torques contains:

Frictional torques: $\begin{bmatrix} d_x \dot{\theta} \\ d_y \dot{\phi} \\ d_z \omega \end{bmatrix}$, where d_is are angular viscous dampers of air.

Torques from the air bearings: $\begin{bmatrix} ((k_2 + k_3)(l_1^2 + l_2^2) + k_1 R^2)\theta \\ ((k_2 + k_3)(l_1^2 - l_2^2) + k_1 R^2)\phi \\ 0 \end{bmatrix}$.

Driving torque from the AC driver: $\begin{bmatrix} 0 \\ 0 \\ M \end{bmatrix}$.

Cutting force torques:

$$
\begin{aligned}
& C_{Oo}\begin{bmatrix} F_r d_2 + F_t d_1 \\ F_m d_2 \\ F_m d_1 \end{bmatrix} \\
&= \begin{bmatrix} (F_r d_2 + F_t d_1)\cos\Omega - F_m d_2 \sin\Omega - \Phi F_m d_1 \\ (F_r d_2 + F_t d_1)\sin\Omega + F_m d_2 \cos\Omega - \theta F_m d_1 \\ (F_r d_2 + F_t d_1)(\phi\cos\Omega + \theta\sin\Omega) + F_m d_2(-\Phi\sin\Omega + \theta\cos\Omega) + F_m d_1 \end{bmatrix}. \\
&\approx \begin{bmatrix} (F_r d_2 + F_t d_1)\cos\Omega - F_m d_2 \sin\Omega \\ (F_r d_2 + F_t d_1)\sin\Omega + F_m d_2 \cos\Omega \\ F_m d_1 \end{bmatrix}
\end{aligned}
$$

Base on the linear momentum principle of Newton, the corresponding equations of the spindle translational motion in the O (XYZ) are:

$$[\vec{a}_o + \dot{\vec{\omega}}_o \times \vec{e} + \vec{\omega}_o \times (\vec{\omega}_o \times \vec{e})]m = \vec{F} \tag{3-17}$$

i.e.:

$$
\begin{aligned}
& m\begin{bmatrix} \ddot{x} \\ \ddot{y} \\ \ddot{z} \end{bmatrix} + \begin{bmatrix} c_x\dot{x} \\ c_y\dot{y} \\ c_z\dot{z} \end{bmatrix} + \begin{bmatrix} k_2 x \\ k_3 y \\ k_1 z \end{bmatrix} = C_{Oo}^T \begin{bmatrix} k_2(l_1 - l_2)\theta \\ k_3(l_1 - l_2)\phi \\ k_1(l_1 - l_2)\cos\sqrt{\theta^2 + \phi^2} \end{bmatrix} \\
& + C_{Oo}^T \begin{bmatrix} 0 & -\dot{\varpi}_z & \dot{\varpi}_y \\ \dot{\varpi}_z & 0 & \dot{\varpi}_x \\ -\dot{\varpi}_y & -\dot{\varpi}_x & 0 \end{bmatrix} \begin{bmatrix} e_x \\ e_y \\ e_z \end{bmatrix} m \\
& + C_{Oo}^T \begin{bmatrix} 0 & -\overline{\omega}_z & \overline{\omega}_y \\ \overline{\omega}_z & 0 & -\overline{\omega}_x \\ -\overline{\omega}_y & \overline{\omega}_x & 0 \end{bmatrix} \begin{bmatrix} 0 & -\overline{\omega}_z & \overline{\omega}_y \\ \overline{\omega}_z & 0 & -\overline{\omega}_x \\ -\overline{\omega}_y & \overline{\omega}_x & 0 \end{bmatrix} \begin{bmatrix} e_x \\ e_y \\ e_z \end{bmatrix} m + \begin{bmatrix} F_m \\ F_r \\ F_t \end{bmatrix}
\end{aligned} \tag{3-18}
$$

Base on the angular momentum principle of Euler, the corresponding equations of the spindle rotational motion in the o (xyz) are:

$$J \cdot \dot{\vec{\omega}}_o + \vec{\omega}_o \times (J \cdot \vec{\omega}_o) = \vec{F} \times \vec{r} + M \tag{3-19}$$

i.e.:

$$
\begin{aligned}
&J\begin{bmatrix}\dot{\overline{\omega}}_x\\ \dot{\overline{\omega}}_y\\ \dot{\overline{\omega}}_z\end{bmatrix}+\begin{bmatrix}0 & -\overline{\omega}_z & \overline{\omega}_y\\ \overline{\omega}_z & 0 & -\overline{\omega}_x\\ -\overline{\omega}_y & \overline{\omega}_x & 0\end{bmatrix}J\begin{bmatrix}\overline{\omega}_x\\ \overline{\omega}_y\\ \overline{\omega}_z\end{bmatrix}\\
&=-\begin{bmatrix}d_x\dot{\theta}\\ d_y\dot{\phi}\\ d_z\omega\end{bmatrix}-\begin{bmatrix}((k_2+k_3)(l_1^2+l_2^2)+k_1R^2)\theta\\ ((k_3+k_2)(l_1^2+l_2^2)+k_1R^2)\phi\\ M\end{bmatrix}+C_{Oo}\begin{bmatrix}F_rd_2+F_td_1\\ F_md_2\\ F_md_1\end{bmatrix}\\
&=-\begin{bmatrix}d_x\dot{\theta}\\ d_y\dot{\phi}\\ d_z\omega\end{bmatrix}-\begin{bmatrix}((k_2+k_3)(l_1^2+l_2^2)+k_1R^2)\theta\\ ((k_3+k_2)(l_1^2+l_2^2)+k_1R^2)\phi\\ M\end{bmatrix}+\begin{bmatrix}(F_rd_2+F_td_1)\cos\Omega-F_md_2\sin\Omega\\ (F_rd_2+F_td_1)\sin\Omega+F_md_2\cos\Omega\\ F_md_1\end{bmatrix}
\end{aligned}
\tag{3-20}
$$

where, M is the AC servomotor torque.

Finally, considering linear and quadratic small quantity, the previous corresponding equations Eq.3-18 of the translational motions of the spindle rotor in the $O(XYZ)$ are linearized as:

$$
\begin{cases}
m\ddot{z}+c_z\dot{z}+k_1z=F_t\\
m\ddot{y}+c_y\dot{y}+k_3y=me\omega^2\sin\omega t+F_r\\
m\ddot{x}+c_x\dot{x}+k_2x=me\omega^2\cos\omega t+F_m
\end{cases}
\tag{3-21}
$$

And the previous corresponding equations Eq.3-20 of tilting motions of the spindle rotor in the $o(xyz)$ are simplified as:

$$
\begin{cases}
J_x\ddot{\theta}-(J_y-J_z)\omega\dot{\phi}+d_x\dot{\theta}=-(k_2+k_3)(l_1^{\,2}+l_2^{\,2})\theta\\
\quad -k_1R^2\theta+\{(F_rd_2+F_td_1)\cos\Omega-F_md_2\sin\Omega\}\\
J_y\ddot{\phi}+(J_x-J_z)\omega\dot{\theta}+d_y\dot{\phi}=-(k_2+k_3)(l_1^{\,2}+l_2^{\,2})\phi\\
-k_1R^2\phi+me\omega^2(l_1-l_2)+\{(F_rd_2+F_td_1)\sin\Omega+F_md_2\cos\Omega\}
\end{cases}
\tag{3-22}
$$

where R is the radius of the spindle rotor/shaft, $-(k_2+k_3)(l_1^2+l_2^2)\theta-k_1R^2\theta$ and $-(k_2+k_3)(l_1^2+l_2^2)\phi-k_1R^2\phi$ are represented as rotational torques of the pressurized air film around the x-axis and the y-axis, respectively, $me\omega(l_1-l_2)$ is the inertia moment of the spindle rotor, F_r is the feed cutting force in the Y-axial direction, F_t is the thrust cutting force in the Z-axial direction and F_m is the main cutting force in the X-axial direction. The above procedure is called linearization. For the aerostatic spindle system of the ultra-precision diamond turning machine, as the linear damping ratio of the pressurized air film is further tiny less than 0.05 and the angular damping ratio is negligibly tiny less than 1×10^{-4} (Frew and Scheffer, 2008), the resistance and the drag torques are totally taken account of. For Eq.3-21, the system is subjected to external cutting forces, damping forces and inertial forces, and for Eq.3-22, the harmonic torques are applied to the system with frictional torques. The responses of the system applied by harmonic excitation are called forced damped harmonic responses.

3.5 Dynamic Modeling of an Aerostatic Bearing Spindle in UPRM

According to the proposed methodology in Section 3.4 above, for modeling of aerostatic bearing spindle motions, the proposed dynamic model of the spindle rotor in UPT can directly be used for the spindle system in UPRM. The approach is extremely similar, but there are some discrepancies as explained as below:

(1) Cutting forces excite the spindle rotor intermittently, which can be idealized as the rectangular wave in form, since the contact time that cutting forces are applied to the spindle rotor is very short, as compared with the cycle period corresponding to the spindle speed.

(2) The spindle rotor is balanced, i.e.: the eccentric distance $\vec{e} = 0$. In practical machining, a spindle rotor would be balanced. Hence, the spindle rotor is considered without an eccentric distance after balancing.

(3) Effects of spindle vibration on surface topography are intermittent but not continuous like that in UPDT, i.e. surface topography is geometrically formed by one tiny part of the profile of the spindle vibration.

(4) Since the duration time of cutting forces is extremely short and periodical, the external torques is idealized as constant values, not harmonic excitation.

To model the system of a spindle rotor in UPRM, some assumptions are made as mentioned in Section 3.4.1.

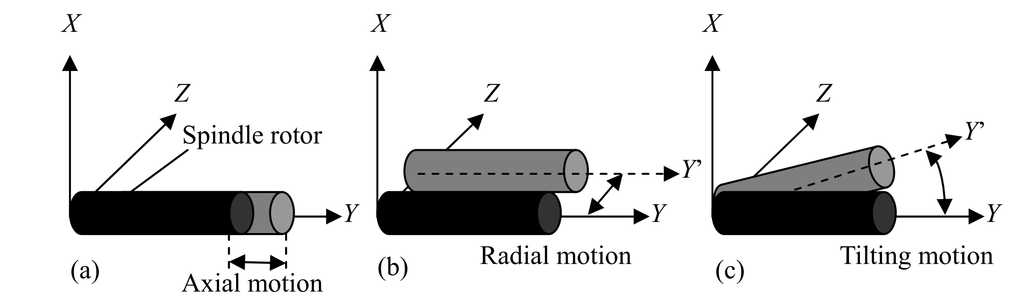

Figure 3.11 Schematic diagrams of spindle rotor motions involving (a) the axial motion, (b) the radial motion and (c) the tilting motion

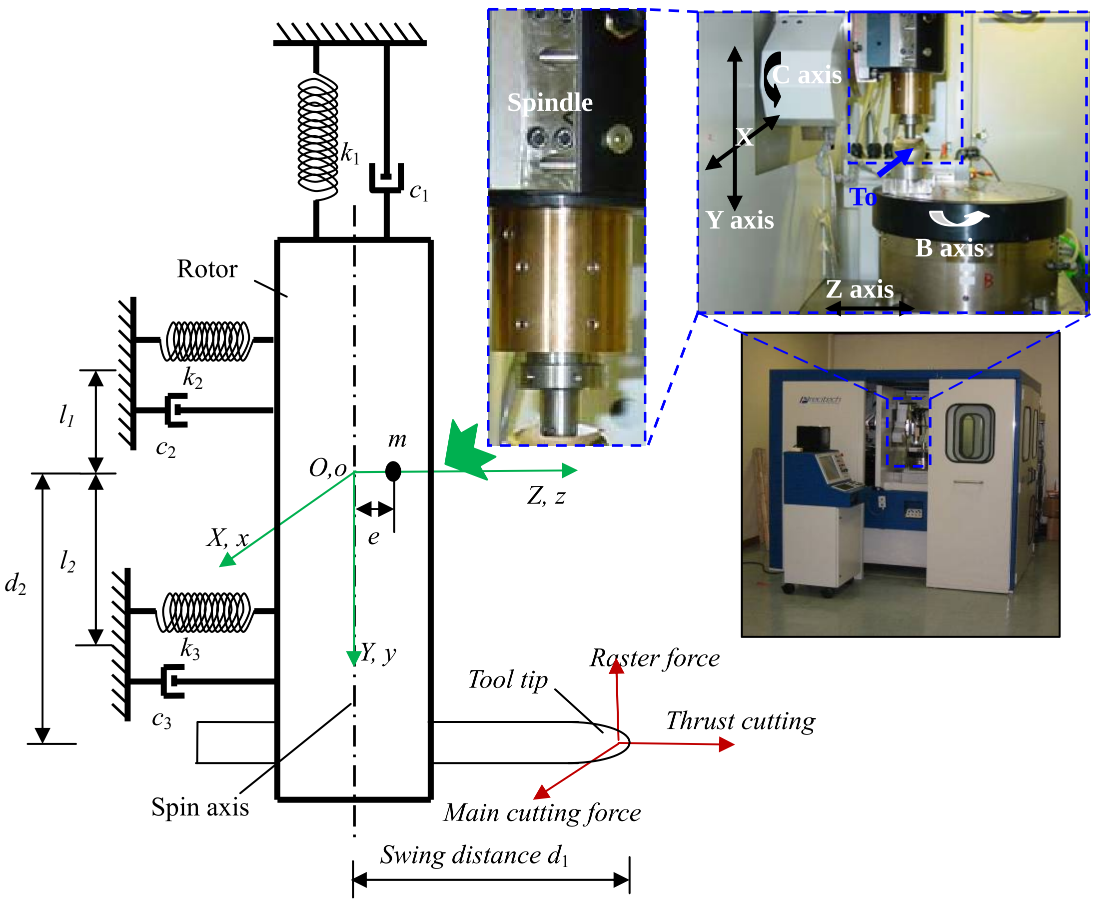

Figure 3.12 Schematic diagram of an aerostatic bearing spindle in UPRM

3.5.1 Dynamic System of a Spindle

Since the coordinate system in UPRM is different with that in UPDT, the whole process for modeling of an aerostatic bearing spindle is re-described. The motions of an aerostatic bearing spindle in UPRM involve radial, axial and tilting motions, as shown in Figure 3.11 above. The spindle system is modeled as a multiple-degree-of-freedom spring-mass-damper system. The spindle rotor is regarded as a rigid body supported by an air film represented by a series of springs in the axial and radial directions. The spring stiffness distribution along the journal length is considered as a constant value. Its schematic diagram is shown in Figure 3.12. The spindle rotor is replaced by m, x, y and z express translational displacements of its spindle rotor, c represents viscous dampers and k denotes stiffness of springs, e represents an eccentric distance, and θ and Φ mean tilting angles of the spindle rotor around the radial axis, respectively.

The dynamic motion is described by Netow-Euler equations of motion, involving three translational motions and three rotational motions in a three-dimensional space. Figure 3.13 shows that the spindle rotor is referred to and fixed with a reference system $o(xyz)$ moving in an inertial coordinate system $O(XYZ)$ with the rotor's eccentric mass m. Its motions can be represented by the rotations of the inertial coordinate system $O(XYZ)$ around the z, x and y-axis with the angles (θ, Φ and Ω) of the reference system $o(xyz)$ as shown in Figure 3.13(a), where the corresponding first order derivatives of the rotation angles are the angular velocity $\dot{\theta}$, $\dot{\phi}$ and $\dot{\Omega}$, and the corresponding second order derivatives of the rotation angles are the angular acceleration $\ddot{\theta}$, $\ddot{\phi}$ and $\ddot{\Omega}$, and by the translations of the inertial coordinate system $O(XYZ)$ along the x, y and z-axis with the displacements (x, y and z, respectively) of the reference system $o(xyz)$ as shown in Figure 3.13(b), where the corresponding first order derivatives of the displacements are the velocity $\dot{x}$, $\dot{y}$ and $\dot{z}$, and the corresponding second order derivatives of the displacements are the acceleration $\ddot{x}$, $\ddot{y}$ and $\ddot{z}$, i.e.:

(1) Translation along the x-axis, x;

(2) Translation along the y-axis, y;

(3) Translation along the z-axis, z;

(4) Rotation around the Z-axis, θ;

(5) Rotation around the X_1-axis, ϕ; and

(6) Rotation around the y-axis, Ω (Ω is equal to ωt, in which ω is the spindle speed and t is time).

For the five-axis CNC ultra-precision milling machine, X, Y and Z in the spindle system are parallel to the X, Y and Z axes in the machine system, respectively, where Y is corresponding to the initial spin axis. F_r, F_t and F_m represent the intermittent raster cutting force, the intermittent thrust cutting force and the intermittent main cutting force direction, respectively. l is the position of the mass center relative to the spindle bearing on two sides along the Y-axis. d_1 means the swing distance between the tool tip and the spindle axis along the Z-axis and d_2 is the tilting distance from the tool to the equilibrium center of the spindle rotor along the Y-axis, when raster milling. It is shown in Figure 3.12 above.

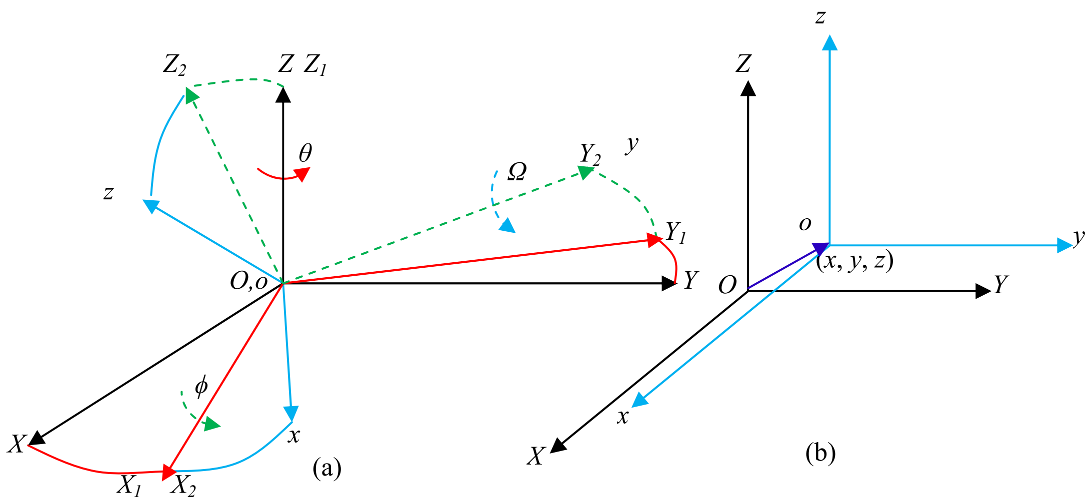

Figure 3.13 The coordinate transformation: (a) translational transformation and (b) rotational transformation

3.5.2 Cutting Force Description

In the UPRM cutting process that is different to UPT, since the cutting process is intermittent, the cutting forces, acting over a very short interval, are applied to the spindle rotor intermittently, which are regarded as the pulse waves in form with a short duration. The shape of the pulse wave is defined by a duty cycle τ, which is the ratio between the pulse duration known as the contact time and the period *T*. The duty cycle can be modulated for a more dynamic timbre, also known as the rectangular wave. The cutting forces are idealized as a rectangular wave in form, shown in Figure 3.14. In URPM, the duration of cutting forces can be modulated according to $60 \times \arccos((d_1 - d_0)/d_1)/\pi/\omega$ as the period is T=60/ω corresponding to spindle speed. Accordingly, the cutting forces are applied to the spindle rotor with periodic pulse excitation.

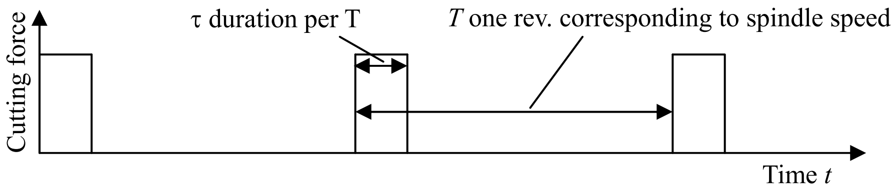

Figure 3.14 Idealized cutting forces in UPRM

3.5.3 Dynamic Equations of Spindle Motions

In the spindle system of UPRM, after balancing, the mass center coordinate $\vec{e}$ in $o(xyz)$ is expressed as:

$$\vec{e} = \begin{bmatrix} e_x \\ e_y \\ e_z \end{bmatrix} = \begin{bmatrix} 0 \\ 0 \\ 0 \end{bmatrix}. \tag{3-23}$$

Since the spindle rotor is symmetric, the inertial tensor in $o(xyz)$ is displayed as:

$$J = \begin{bmatrix} J_x & -J_{xy} & -J_{xz} \\ -J_{yx} & J_y & -J_{yz} \\ -J_{zx} & -J_{zy} & J_z \end{bmatrix} = \begin{bmatrix} J_x & 0 & 0 \\ 0 & J_y & 0 \\ 0 & 0 & J_z \end{bmatrix}. \tag{3-24}$$

Due to the contact time being very short, the cutting forces and corresponding torques are denoted as:

$$F = \begin{bmatrix} -F_m \\ -F_r \\ -F_t \end{bmatrix} \text{ and } \vec{M} = \begin{bmatrix} F_r d_1 - F_t d_2 \\ M \\ F_m d_2 \end{bmatrix}. \tag{3-25}$$

Similarly, the dynamic model of the spindle in UPRM can be expressed by Newton-Euler Equations. Since these perturbation angles are extremely tiny due to the micrometric bearing clearance, $\sin\phi \approx \phi$, $\sin\theta \approx \theta$, $\cos\phi \approx 1$ and $\cos\theta \approx 1$ (linear small quantity) and $\theta\dot{\theta} \approx 0$, $\theta\dot{\phi} \approx 0$, $\phi\dot{\phi} \approx 0$, $\phi\dot{\theta} \approx 0$, $\phi\sin\phi \approx 0$, $\theta\sin\theta \approx 0$, $\phi\sin\theta \approx 0$ and $\theta\sin\phi \approx 0$ (quadratic small quantity). After being linearized, the corresponding equations of the spindle motions are:

$$\begin{cases} m\ddot{y} + c_1\dot{y} + k_1 y = \{-F_r\} \\ m\ddot{x} + c_2\dot{x} + k_2 x = \{-F_m\} \\ m\ddot{z} + c_3\dot{z} + k_3 z = \{-F_t\} \\ J_z\ddot{\theta} - (J_x - J_y)\omega\dot{\phi} + d_z\dot{\theta} = -(k_2 + k_3)(l_1^2 + l_2^2)\theta - k_1 R^2\theta + \{+F_m d_2\} \\ J_x\ddot{\phi} + (J_z - J_y)\omega\dot{\theta} + d_x\dot{\phi} = -(k_2 + k_3)(l_1^2 + l_2^2)\phi - k_1 R^2\phi + \{+F_r d_1 - F_t d_2\} \end{cases} \tag{3-26}$$

where R is the radius of the spindle rotor, $-(k_2 + k_3)(l_1^2 + l_2^2)\theta - k_1 R^2\theta$ and $-(k_2 + k_3)(l_1^2 + l_2^2)\phi - k_1 R^2\phi$ are represented as the rotational torques of the air film around the *x*-axial direction and the *z*-axial direction, respectively, $me\omega^2(l_1 - l_2)$ is the inertia moment of the spindle rotor of zero since $\vec{e} = 0$, the frequency of the cutting forces is the spindle rotational frequency (SRF) and the corresponding contact time is about $60 \times \arccos((d_1 - d_0)/d_1)/\pi/\omega$. As the damping ratio of the pressure air film is tiny, the resistance and the drag torques are negligible. For Eq.3-26, the system is subjected to the intermittent cutting forces, the damping forces and the inertial forces, and the intermittent torques are applied to the system with frictional torques. The responses of the system applied by such excitation are called pulsed damped responses.

The numerical solutions of these equations before being linearized were done with Matlab Simulink using the Dormand-Prince method.

3.6 Summary

In this chapter, the mechanism of surface formation and the development of motions of a rigid body are presented in detail. It is majorly summarized as below:

(i) In UPDT, the surface is formed by a spiral path of a tool arc center rotating along the spindle rotation axis with tool shape.

(ii) In UPRM, the surface under ideal conditions is formed by the repetition of the tool tip profile at intervals of feed per revolution of the spindle and step distance, and the tool geometry in the feed and raster directions under two cutting strategies with two cutting directions.

(iii) After the basic motions of a rigid body with pure translations and rotations, Euler transformation and Newton-Euler equations of motion are proposed, a five-degree-of-freedom dynamic model of an aerostatic bearing spindle excited by cutting forces in UPM is developed based on the linear momentum principle of Newton and the angular momentum principle of Euler.

(iv) The developed Newton-Euler equations are linearized in this chapter. This is prepared for the following chapters that study the dynamic characteristics of spindle vibration with the excitation of cutting forces of UPM and its influence on surface generation in UPM.

Chapter 4 Dynamic Characteristics of Spindle Vibration in UPM

4.1 Introduction

In UPM, the aerostatic bearing spindle is one crucial part. Its dynamics directly influence surface quality, since its stiffness is a vital part of whole loop rigidity of ultra-precision machine tool. Investigation into the dynamic characteristics of aerostatic bearing spindle of UPM is placed essential emphasis upon in this chapter.

In this study, the analytic solutions for dynamic responses of the aerostatic bearing spindle in UPM with cutting force action are derived from the linearized dynamic model developed in Chapter 3. Frequency characteristics of the aerostatic bearing spindle are also provided. Finally, the effects of external parameters such as cutting forces, eccentric distances of the spindle rotor, depths of cut, and spindle speed on dynamic responses of the spindle are discussed based on the dynamic model using Matlab Simulink.

4.2 Dynamic Characteristics of Spindle Vibration in UPDT

Eq.3-21 and Eq.3-22 represent the dynamic responses of a spindle rotor supported by a pressured air film. They include the titling motions, the radial motions and the axial motion induced by spindle speed relative to inertia force and the inertia moment, and cutting forces and cutting force torques and dissipated by frictional forces and frictional torques in UPDT. By solving these equations, the solutions can be obtained to analyze the dynamic characterization of spindle, such as the transient characterization and the steady characterization. The spindle in UPDT Opto30 (See Appendix I) is employed and the spindle performance specifications provided by the machine tool manufactures are tabulated in Table 4.1.

Table 4.1 Spindle performance specifications of UPDT Opto30

Spindle rotor mass (m) (kg)	0.5
Radial stiffness (k_2/ k_3) (N/µm)	20
Axial stiffness (k_1) (N/µm)	25
Eccentric position of the mass imbalance away from the rotor axis (e) (µm)	1
Position of the centre of mass center relative to its equilibrium along the z-axis (l_1/ l_2) (mm)	50+5e / 50-5e
Radius of spindle rotor (R) (mm)	25
Inertial tensor around y-axis (J_z) (gm^2)	0.05
Inertial tensor around z/x-axis (J_x/J_y) (gm^2)	1.4
The distance of tilting center of spindle rotor to the tool tip (d_2) (mm)	60
The distance of tool tip away from the spindle axis in cutting (d_1) (mm)	3
Linear damping ratio μ	<0.05
Angular damping ratio ξ	$<1\times10^{-4}$

4.2.1 Solutions of Dynamic Equations

The spindle rotor motions described by Eq.3-21 and Eq.3-22 in the previous chapter are the forced damped motions of a multi-degree-of-freedom system subjected to forcing functions, which are time-dependent. To obtain the basic dynamic characteristics of the system, the state-space representation (see Appendix III) for the system is employed.

4.2.1.1 Solutions of Translational Equations

For Eq.3-21, its corresponding state-space model with its characteristic equations is expressed as:

$$
\begin{cases}
\begin{bmatrix} \ddot{z} \\ \dot{z} \end{bmatrix} = \begin{bmatrix} -\dfrac{c_z}{m} & -\dfrac{k_1}{m} \\ 1 & 0 \end{bmatrix} \begin{bmatrix} \dot{z} \\ z \end{bmatrix} + \begin{bmatrix} 1 \\ 0 \end{bmatrix} \left[F_t \right] \\
\begin{bmatrix} \ddot{y} \\ \dot{y} \end{bmatrix} = \begin{bmatrix} -\dfrac{c_y}{m} & -\dfrac{k_3}{m} \\ 1 & 0 \end{bmatrix} \begin{bmatrix} \dot{y} \\ y \end{bmatrix} + \begin{bmatrix} 1 \\ 0 \end{bmatrix} \left[me\omega^2 \sin \omega t + F_r \right] \\
\begin{bmatrix} \ddot{x} \\ \dot{x} \end{bmatrix} = \begin{bmatrix} -\dfrac{c_x}{m} & -\dfrac{k_2}{m} \\ 1 & 0 \end{bmatrix} \begin{bmatrix} \dot{x} \\ x \end{bmatrix} + \begin{bmatrix} 1 \\ 0 \end{bmatrix} \left[me\omega^2 \cos \omega t + F_m \right]
\end{cases} \tag{4-1}
$$

$$
\begin{cases}
\det(\begin{bmatrix} -\dfrac{c_z}{m} & -\dfrac{k_1}{m} \\ 1 & 0 \end{bmatrix} - \lambda I) = 0 \\
\det(\begin{bmatrix} -\dfrac{c_y}{m} & -\dfrac{k_3}{m} \\ 1 & 0 \end{bmatrix} - \lambda I) = 0 \\
\det(\begin{bmatrix} -\dfrac{c_x}{m} & -\dfrac{k_2}{m} \\ 1 & 0 \end{bmatrix} - \lambda I) = 0
\end{cases} \tag{4-2}
$$

Eq.4-1 is a linear time-invariant system described by the differential equations with constant coefficients. By solving the characteristic equations of the above state-space model, the eigenvalues of the characteristic matrices Eq.4-2 in each sub-system of Eq.4-1 can be achieved as λ_{x1}, λ_{x2}, λ_{y1}, λ_{y2} and λ_{z1}, λ_{z2}, which are the complex conjugate roots. Then, the undamped natural angular frequencies $\omega_i^{'}$ through their modulus can be calculated and expressed as Eq.4-3.

$$
\omega_i^{'} = \sqrt{\lambda_{i1}\lambda_{i2}} = \sqrt{\frac{k_j}{m}} \qquad (i=x, y, z \text{ and } j=2, 3, 1) \tag{4-3}
$$

where λ_{i1} and λ_{i2} are a pair of the complex conjugate roots for the spindle system. Eq.4-3 also means that the spindle possesses the axial and radial natural frequencies.

From the above equations, the damped natural angular frequencies of the system with dampers can be derived, and the damped natural angular frequencies ω_i determined by their imaginary parts can be calculated by using Eq.4-4, where the dampers are variable and are calculated by using Eq.4-5.

$$\omega_i = \left| \frac{(\lambda_{i1} - \lambda_{i2})}{2} \right| = \frac{\sqrt{4k_j m - c_i^2}}{2m} \qquad (i{=}x, y, z \text{ and } j{=}2, 3, 1) \qquad (4\text{-}4)$$

$$c_i = 2\mu_i \sqrt{k_j m} \qquad (i{=}x, y, z \text{ and } j{=}2, 3, 1) \qquad (4\text{-}5)$$

where c_i is a viscous damper of air in the spindle system and μ_i is a damping ratio of air less than 0.05, set at 0.025, for the spindle system. In this system, k_i and m are known parameters as shown in Table 4.1, but these linear dampers will affect the natural frequencies. This implies that, when the linear damper is changing, the damped natural frequencies will fluctuate away from the principle characteristic frequencies (PCFs) (i.e. the natural frequencies of the spindle), named the derivative characteristic frequencies (DCFs), which mean that multi-derivative characteristic frequencies (MDCFs) are close to the PCFs.

Since viscous damping on the forced vibration of a linear oscillation (the spindle system) makes the system energy dissipate, the system develops from a transient equilibrium into a stable equilibrium, where the steady state response exists after the transient state response dies out. For the system of Eq.3-21, using the mechanical impedance method (See Appendix V), the corresponding steady-state solutions are expressed as:

$$\begin{cases} z_{steady-state} = \dfrac{F_t}{k_1} \\ y_{steady-state} = \dfrac{F_r}{k_3} + \dfrac{\omega^2}{(\frac{k_3}{m} - \omega^2)^2 + 4\mu^2\omega^2 \frac{k_3}{m}} e \sin(\omega t - \arctan(\dfrac{2\mu\omega\sqrt{k_3 m}}{k_3 - m\omega^2})) \\ x_{steady-state} = \dfrac{F_m}{k_2} + \dfrac{\omega^2}{(\frac{k_2}{m} - \omega^2)^2 + 4\mu^2\omega^2 \frac{k_2}{m}} e \cos(\omega t - \arctan(\dfrac{2\mu\omega\sqrt{k_2 m}}{k_2 - m\omega^2})) \end{cases} \qquad (4\text{-}6)$$

And the transient-state solutions referred to Appendix VI are:

$$\begin{cases} z(t)=\begin{cases} -\dfrac{F_t}{k_1}\dfrac{e^{-\mu\sqrt{\frac{k_1}{m}}t}}{\sqrt{1-\mu^2}}\sqrt{1-\mu^2}\cos(\sqrt{\dfrac{k_1}{m}}\sqrt{1-\mu^2}\,t) \\ +\dfrac{F_t}{k_1}\dfrac{e^{-\mu\sqrt{\frac{k_1}{m}}t}}{\sqrt{1-\mu^2}}\mu\sin(\sqrt{\dfrac{k_1}{m}}\sqrt{1-\mu^2}\,t) \end{cases} \\ y(t)=\begin{cases} -\dfrac{F_r}{k_3}\dfrac{e^{-\mu\sqrt{\frac{k_3}{m}}t}}{\sqrt{1-\mu^2}}(\sqrt{1-\mu^2}\cos(\sqrt{\dfrac{k_3}{m}}\sqrt{1-\mu^2}\,t)+\mu\sin(\sqrt{\dfrac{k_3}{m}}\sqrt{1-\mu^2}\,t)) \\ +A_y e^{-\mu\sqrt{\frac{k_3}{m}}t}\sin(\sqrt{1-\mu^2}\sqrt{\dfrac{k_3}{m}}t+\alpha_y) \end{cases} \\ x(t)=\begin{cases} -\dfrac{F_m}{k_2}\dfrac{e^{-\mu\sqrt{\frac{k_2}{m}}t}}{\sqrt{1-\mu^2}}(\sqrt{1-\mu^2}\cos(\sqrt{\dfrac{k_2}{m}}\sqrt{1-\mu^2}\,t)+\mu\sin(\sqrt{\dfrac{k_2}{m}}\sqrt{1-\mu^2}\,t)) \\ +A_x e^{-\mu\sqrt{\frac{k_2}{m}}t}\sin(\sqrt{1-\mu^2}\sqrt{\dfrac{k_2}{m}}t+\alpha_x) \end{cases} \end{cases} \tag{4-7}$$

where.
$$\begin{cases} A_y=\dfrac{1}{\sqrt{4\mu^2\dfrac{k_3}{m}\omega^2+\left(\dfrac{k_3}{m}-\omega^2\right)^2}}\dfrac{e\omega^3}{\sqrt{\dfrac{k_3}{m}(1-\mu^2)}} \\ A_x=\dfrac{1}{\sqrt{\dfrac{k_2}{m}(1-\mu^2)}}\dfrac{e\omega^2\sqrt{\dfrac{k_2}{m}}}{\sqrt{4\mu^2\dfrac{k_2}{m}\omega^2+\left(\dfrac{k_2}{m}-\omega^2\right)^2}} \end{cases}$$

and
$$\begin{cases} \alpha_y=\arctan\dfrac{-2\mu\dfrac{k_3}{m}\sqrt{(1-\mu^2)}}{\dfrac{k_3}{m}-\omega^2} \\ \alpha_x=-\arctan\dfrac{\sqrt{(1-\mu^2)}}{\mu}-\arctan\dfrac{2\mu\sqrt{(1-\mu^2)}\dfrac{k_2}{m}}{\dfrac{k_2}{m}-\omega^2} \end{cases}.$$

Then, combining Eq.4-6 and Eq.4-7, the general solutions for the linear equations of Eq.3-21 are:

$$
\left\{
\begin{aligned}
z(t) &= \left\{
\begin{aligned}
&\frac{F_t}{k_1} \\
&-\frac{F_t}{k_1}\frac{e^{-\mu\sqrt{\frac{k_1}{m}}t}}{\sqrt{1-\mu^2}}\sqrt{1-\mu^2}\cos\left(\sqrt{\frac{k_1}{m}}\sqrt{1-\mu^2}\,t\right) \\
&+\frac{F_t}{k_1}\frac{e^{-\mu\sqrt{\frac{k_1}{m}}t}}{\sqrt{1-\mu^2}}\mu\sin\left(\sqrt{\frac{k_1}{m}}\sqrt{1-\mu^2}\,t\right)
\end{aligned}
\right. \\
y(t) &= \left\{
\begin{aligned}
&\frac{F_r}{k_3}\left(1-\frac{e^{-\mu\sqrt{\frac{k_3}{m}}t}}{\sqrt{1-\mu^2}}\left(\sqrt{1-\mu^2}\cos\left(\sqrt{\frac{k_3}{m}}\sqrt{1-\mu^2}\,t\right)+\mu\sin\left(\sqrt{\frac{k_3}{m}}\sqrt{1-\mu^2}\,t\right)\right)\right) \\
&+A_y e^{-\mu\sqrt{\frac{k_3}{m}}t}\sin\left(\sqrt{1-\mu^2}\sqrt{\frac{k_3}{m}}t+\alpha_y\right) \\
&+\frac{e\omega^2}{\left(\frac{k_3}{m}-\omega^2\right)^2+4\mu^2\omega^2\frac{k_3}{m}}\left(\left(\frac{k_3}{m}-\omega^2\right)\sin\omega t-2\mu\omega\sqrt{\frac{k_3}{m}}\cos\omega t\right)
\end{aligned}
\right. \\
x(t) &= \left\{
\begin{aligned}
&\frac{F_m}{k_2}\left(1-\frac{e^{-\mu\sqrt{\frac{k_2}{m}}t}}{\sqrt{1-\mu^2}}\left(\sqrt{1-\mu^2}\cos\left(\sqrt{\frac{k_2}{m}}\sqrt{1-\mu^2}\,t\right)+\mu\sin\left(\sqrt{\frac{k_2}{m}}\sqrt{1-\mu^2}\,t\right)\right)\right) \\
&+A_x e^{-\mu\sqrt{\frac{k_2}{m}}t}\sin\left(\sqrt{1-\mu^2}\sqrt{\frac{k_2}{m}}t+\alpha_x\right) \\
&+\frac{e\omega^2}{\left(\frac{k_2}{m}-\omega^2\right)^2+4\mu^2\omega^2\frac{k_2}{m}}\left(\left(\frac{k_2}{m}-\omega^2\right)\cos\omega t+2\mu\omega\sqrt{\frac{k_2}{m}}\sin\omega t\right)
\end{aligned}
\right.
\end{aligned}
\right. \tag{4-8}
$$

where the initial conditions, such as the velocity and the displacement, are zeros.

From the above equations, it can be inferred that due to the radial translational vibration induced by the inertia/centrifugal force, concave will take place at the center of the machined surface. Based on Section 3.4.3 in Chapter 3, as the tool tip is moving close to the center of the machined surface in turning, the cutting process is developing from continuous cutting in the steady state to uncontinuous/intermittent cutting in the transient state. In intermittent cutting, the cutting forces excite the spindle rotor intermittently, so radial patterns are produced by the axial translational vibration, whose number is equal to the quotient between the frequency in the axial direction and the spindle rotational frequency (SRF) that corresponds to the spindle speed. To ascertain the inferred results, the simulated and experimental surface topography generation is proposed in the next sections.

4.2.1.2 Solutions of Rotational Equations

For Eq.3-22, where the differential equations are mutually coupled, describing the system of the tilting motions of the spindle rotor subjected to harmonically varying torques, the corresponding state-space model with its characteristic equations is expressed as:

$$
\begin{bmatrix} \ddot{\theta} \\ \dot{\theta} \\ \ddot{\phi} \\ \dot{\phi} \end{bmatrix} =
\begin{bmatrix} \frac{(F_r d_2 + F_t d_1)}{J_x}\cos\Omega + \frac{-F_m d_2}{J_x}\sin\Omega \\ 0 \\ \frac{(F_r d_2 + F_t d_1)}{J_y}\sin\Omega + \frac{F_m d_2}{J_y}\cos\Omega \\ 0 \end{bmatrix}
+ \begin{bmatrix} -\frac{d_x}{J_x} & \frac{-(k_2+k_3)(l_1{}^2+l_2{}^2)}{J_x} + \frac{-k_1 R^2}{J_x} & \frac{(J_y - J_z)\omega}{J_x} & 0 \\ 1 & 0 & 0 & 0 \\ -\frac{(J_x - J_z)\omega}{J_y} & 0 & -\frac{d_y}{J_y} & \frac{-(k_2+k_3)(l_1{}^2+l_2{}^2)}{J_y} + \frac{-k_1 R^2}{J_y} \\ 0 & 0 & 1 & 0 \end{bmatrix}
\begin{bmatrix} \dot{\theta} \\ \theta \\ \dot{\phi} \\ \phi \end{bmatrix}
\tag{4-9}
$$

$$\det\begin{bmatrix} -\dfrac{d_x}{J_x}-\lambda & \dfrac{-(k_2+k_3)(l_1{}^2+l_2{}^2)}{J_x}+\dfrac{-k_1R^2}{J_x} & \dfrac{(J_y-J_z)\omega}{J_x} & 0 \\ 1 & 0-\lambda & 0 & 0 \\ -\dfrac{(J_x-J_z)\omega}{J_y} & 0 & -\dfrac{d_y}{J_y}-\lambda & \dfrac{-(k_2+k_3)(l_1{}^2+l_2{}^2)}{J_y}+\dfrac{-k_1R^2}{J_y} \\ 0 & 0 & 1 & 0-\lambda \end{bmatrix}=0 \quad (4\text{-}10)$$

By solving the characteristic equations of the above state-space model, the eigenvalues of Eq.4-10 can be achieved as $\lambda_{\theta 1}$, $\lambda_{\theta 2}$, $\lambda_{\phi 1}$ and $\lambda_{\phi 2}$, which are the respective complex conjugate roots. The angular damping ratio of air is negligible, which is set at zero. Therefore, the undamped natural angular frequencies with dampers (equal to 0) calculated by their modulus are equal to the damped natural angular frequencies ω calculated by their imaginary parts, which can be expressed by Eq.4-11 below.

$$\omega_i=\sqrt{\lambda_{i1}\lambda_{i2}}=\left|\frac{(\lambda_{i1}-\lambda_{i2})}{2}\right| \qquad (i=\theta,\ \phi) \qquad (4\text{-}11)$$

Then, according to the above equation (Eq.4-11), the angular frequencies of the tilting motions are expressed as Eq.4-12 and Eq.4-13.

$$\omega_\theta=\sqrt{\frac{\omega_1^2+\omega_2^2+\frac{J_y-J_z}{J_x}\omega\frac{J_x-J_z}{J_y}\omega}{2}+\sqrt{\frac{(\omega_1^2+\omega_2^2+\frac{J_y-J_z}{J_x}\omega\frac{J_x-J_z}{J_y}\omega)^2-4(\omega_1\omega_2)^2}{2}}} \qquad (4\text{-}12)$$

$$\omega_\phi=\sqrt{\frac{\omega_1^2+\omega_2^2+\frac{J_y-J_z}{J_x}\omega\frac{J_x-J_z}{J_y}\omega}{2}-\sqrt{\frac{(\omega_1^2+\omega_2^2+\frac{J_y-J_z}{J_x}\omega\frac{J_x-J_z}{J_y}\omega)^2-4(\omega_1\omega_2)^2}{2}}} \qquad (4\text{-}13)$$

where $\omega_1=\sqrt{\dfrac{k}{J_x}}$, $\omega_2=\sqrt{\dfrac{k}{J_y}}$, $k=(k_2+k_3)(l_1{}^2+l_2{}^2)+k_1R^2$. The two kinds of angular tilting frequencies are called angular coupled tilting frequencies (ACTFs), which will produce the "beating" phenomena (see Appendix VII). The ACTFs are influenced by the SRF. Eq.4-11 implies that two coupled principle characteristic frequencies (CPCFs) occur with multiple derivative coupled characteristic frequencies (MCDCFs) produced by variably damping in UPM. Eq.4-12 means that the spindle also possesses coupled tilting natural frequencies (CTFs) influenced by the SRF.

To solve the coupled equations of Eq.4-22, it can be represented as:

$$\begin{cases} \ddot{\theta} - \dfrac{(J_y - J_z)\omega}{J_x}\dot{\phi} + \dfrac{d_x}{J_x}\dot{\theta} = \dfrac{-(k_2+k_3)(l_1^{\,2}+l_2^{\,2})\theta - k_1 R^2\theta}{J_x} \\ + \dfrac{\{(F_r d_2 + F_t d_1)\cos\Omega - F_m d_2 \sin\Omega\}}{J_x} \\ \ddot{\phi} + \dfrac{(J_x - J_z)\omega}{J_y}\dot{\theta} + \dfrac{d_y}{J_y}\dot{\phi} = \dfrac{-(k_2+k_3)(l_1^{\,2}+l_2^{\,2})\phi - k_1 R^2\phi}{J_y} \\ + \dfrac{me\omega^2(l_1 - l_2)}{J_y} + \dfrac{\{(F_r d_2 + F_t d_1)\sin\Omega + F_m d_2 \cos\Omega\}}{J_y} \end{cases} \tag{4-14}$$

i.e.:

$$\begin{cases} \ddot{\theta} - C_x\dot{\phi} = -\omega_1^2\theta + S_1\cos\Omega - S_2\sin\Omega \\ \ddot{\phi} + C_y\dot{\theta} = -\omega_2^2\phi + S_0 + S_1\sin\Omega + S_2\cos\Omega \end{cases} \tag{4-15}$$

where, $$\begin{cases} C_y = \dfrac{(J_x - J_z)\omega}{J_y} \\ \omega_2^2 = \dfrac{((k_2+k_3)(l_1^{\,2}+l_2^{\,2}) + k_1R^2)}{J_y} \\ S_0 = \dfrac{me\omega^2(l_1 - l_2)}{J_y} \\ C_x = \dfrac{(J_y - J_z)\omega}{J_x} \\ \omega_1^2 = \dfrac{((k_2+k_3)(l_1^{\,2}+l_2^{\,2}) + k_1R^2)}{J_x} \\ S_1 = \dfrac{\{(F_r d_2 + F_t d_1)\}}{J_x} \\ S_2 = \dfrac{\{F_m d_2\}}{J_x} \\ d_x = 2\xi\omega_1 = d_y = 2\xi\omega_2 = 0 \end{cases}.$$

The solution of Eq.4-15 includes two parts: a homogeneous solution and a particular solution. The complete solution is the sum of two parts. In order to obtain its particular solution, noting that the exciting torques are harmonic, the particular solution is also harmonic and has the same frequency. Thus, the particular solution (See Appendix V) can be set in the form below:

$$\begin{aligned} \theta_{parti}(t) &= \theta_1 \cos\omega t - \theta_2 \sin\omega t \\ \phi_{parti}(t) &= \phi_0 + \phi_1 \sin\omega t + \phi_2 \cos\omega t \end{aligned} \tag{4-16}$$

Substituting Eq.4-16 with its first order of differential equations Eq.4-17 and second order of differential equations Eq.4-18 into Eq.4-15, we can obtain Eq.4-19, which is an identity equation, not relevant to the time *t*. Then, the corresponding linear system of equations we obtain is Eq.4-20.

$$\begin{aligned} \dot{\theta}_{parti}(t) &= -\theta_1\omega \sin\omega t - \theta_2\omega \cos\omega t \\ \dot{\phi}_{parti}(t) &= \phi_1\omega \cos\omega t - \phi_2\omega \sin\omega t \end{aligned} \tag{4-17}$$

$$\begin{aligned} \ddot{\theta}_{parti}(t) &= -\theta_1\omega^2 \cos\omega t + \theta_2\omega^2 \sin\omega t \\ \ddot{\phi}_{parti}(t) &= -\phi_1\omega^2 \sin\omega t - \phi_2\omega^2 \cos\omega t \end{aligned} \tag{4-18}$$

$$\begin{cases} -\theta_1\omega^2 \cos\omega t + \theta_2\omega^2 \sin\omega t - C_x(\phi_1\omega \cos\omega t - \phi_2\omega \sin\omega t) \\ = -\omega_1^2(\theta_1 \cos\omega t - \theta_2 \sin\omega t) + S_1\cos\Omega - S_2 \sin\Omega \\ -\phi_1\omega^2 \sin\omega t - \phi_2\omega^2 \cos\omega t + C_y(-\theta_1\omega \sin\omega t - \theta_2\omega \cos\omega t) \\ = -\omega_2^2(\phi_0 + \phi_1 \sin\omega t + \phi_2 \cos\omega t) + S_0 + S_1 \sin\Omega + S_2 \cos\Omega \end{cases} \tag{4-19}$$

$$\begin{cases} -\theta_1\omega^2 - C_x\phi_1\omega = -\omega_1^2\theta_1 + S_1 \\ \theta_2\omega^2 + C_x\phi_2\omega = \omega_1^2\theta_2 - S_2 \\ -\phi_1\omega^2 - C_y\theta_1\omega = -\omega_2^2\phi_1 + S_1 \\ -\phi_2\omega^2 + C_y\theta_2\omega = -\omega_2^2\phi_2 + S_2 \\ \omega_2^2\phi_0 = S_0 \end{cases} \tag{4-20}$$

The constant coefficients of Eq.4-16 are expressed as Eq.4-21.

$$\begin{cases} \theta_1 = \dfrac{S_1(C_x\omega + (\omega_2^2 - \omega^2))}{((\omega_2^2 - \omega^2)(\omega_1^2 - \omega^2) - C_xC_y\omega^2)} \\ \theta_2 = \dfrac{S_2(C_x\omega + (\omega_2^2 - \omega^2))}{((\omega_2^2 - \omega^2)(\omega_1^2 - \omega^2) + C_yC_x\omega^2)} \\ \phi_1 = \dfrac{S_1((\omega_1^2 - \omega^2) + C_y\omega)}{((\omega_2^2 - \omega^2)(\omega_1^2 - \omega^2) - C_xC_y\omega^2)} \\ \phi_2 = \dfrac{S_2((\omega_1^2 - \omega^2) - C_y\omega)}{((\omega_2^2 - \omega^2)(\omega_1^2 - \omega^2) + C_yC_x\omega^2)} \\ \phi_0 = \dfrac{S_0}{\omega_2^2} \end{cases} \tag{4-21}$$

Then, the particular solution is:

$$
\begin{aligned}
\theta_{parti}(t) &= \frac{S_1(C_x\omega+(\omega_2^2-\omega^2))}{((\omega_2^2-\omega^2)(\omega_1^2-\omega^2)-C_xC_y\omega^2)}\cos\omega t \\
&-\frac{S_2(C_x\omega+(\omega_2^2-\omega^2))}{((\omega_2^2-\omega^2)(\omega_1^2-\omega^2)+C_yC_x\omega^2)}\sin\omega t \\
\phi_{parti}(t) &= \frac{S_0}{\omega_2^2}+\frac{S_1((\omega_1^2-\omega^2)+C_y\omega)}{((\omega_2^2-\omega^2)(\omega_1^2-\omega^2)-C_xC_y\omega^2)}\sin\omega t \\
&+\frac{S_2((\omega_1^2-\omega^2)-C_y\omega)}{((\omega_2^2-\omega^2)(\omega_1^2-\omega^2)+C_yC_x\omega^2)}\cos\omega t
\end{aligned}
\tag{4-22}
$$

Next, the homogeneous solution (See Appendix VI) for Eq.4-15 can be set in the form below:

$$
\begin{cases}
\phi_{\text{hom}}(t) = A_1\sin\omega_\theta t + A_2\cos\omega_\theta t + A_3\sin\omega_\phi t + A_4\cos\omega_\phi t \\
\theta_{\text{hom}}(t) = B_1\cos\omega_\theta t + B_2\sin\omega_\theta t + B_3\cos\omega_\phi t + B_4\sin\omega_\phi
\end{cases}
\tag{4-23}
$$

The solution Eq.4-24 for the homogeneous equations of Eq.4-15 with its corresponding first order of the differential equations Eq.4-25 and the corresponding second order of the differential equations Eq.4-26 is expressed as:

$$
\begin{cases}
\phi = A_1\sin\omega_\theta t + A_2\cos\omega_\theta t + A_3\sin\omega_\phi t + A_4\cos\omega_\phi t \\
\theta = B_1\cos\omega_\theta t + B_2\sin\omega_\theta t + B_3\cos\omega_\phi t + B_4\sin\omega_\phi t
\end{cases}
\tag{4-24}
$$

$$
\begin{cases}
\dot\phi = A_1\omega_\theta\cos\omega_\theta t - A_2\omega_\theta\sin\omega_\theta t + A_3\omega_\phi\cos\omega_\phi t - A_4\omega_\phi\sin\omega_\phi t \\
\dot\theta = -B_1\omega_\theta\sin\omega_\theta t + B_2\omega_\theta\cos\omega_\theta t - B_3\omega_\phi\sin\omega_\phi t + B_4\omega_\phi\cos\omega_\phi t
\end{cases}
\tag{4-25}
$$

$$
\begin{cases}
\ddot\phi = -A_1\omega_\theta^2\sin\omega_\theta t - A_2\omega_\theta^2\cos\omega_\theta t - A_3\omega_\phi^2\sin\omega_\phi t - A_4\omega_\phi^2\cos\omega_\phi t \\
\ddot\theta = -B_1\omega_\theta^2\cos\omega_\theta t - B_2\omega_\theta^2\sin\omega_\theta t - B_3\omega_\phi^2\cos\omega_\phi t - B_4\omega_\phi^2\sin\omega_\phi t
\end{cases}
\tag{4-26}
$$

Substituting Eq.4-24, Eq.4-25 and Eq.4-26 into Eq.4-15, we obtain Eq.4-27.

$$
\begin{aligned}
&(-A_1\omega_\theta^2\sin\omega_\theta t - A_2\omega_\theta^2\cos\omega_\theta t - A_3\omega_\phi^2\sin\omega_\phi t - A_4\omega_\phi^2\cos\omega_\phi t) + \\
&C_y(-B_1\omega_\theta\sin\omega_\theta t + B_2\omega_\theta\cos\omega_\theta t - B_3\omega_\phi\sin\omega_\phi t + B_4\omega_2\cos\omega_\phi t) + \\
&\omega_2^2(A_1\sin\omega_\theta t + A_2\cos\omega_\theta t + A_3\sin\omega_\phi t + A_4\cos\omega_\phi t) = 0 \\
&(-B_1\omega_\theta^2\cos\omega_\theta t - B_2\omega_\theta^2\sin\omega_\theta t - B_3\omega_\phi^2\cos\omega_2 t + B_4\omega_\phi^2\sin\omega_2 t) + \\
&C_x(A_1\omega_\theta\cos\omega_\theta t - A_2\omega_\theta\sin\omega_\theta t + A_3\omega_\phi\cos\omega_\phi t - A_4\omega_\phi\sin\omega_\phi t) + \\
&\omega_1^2(B_1\cos\omega_\theta t + B_2\sin\omega_\theta t + B_3\cos\omega_\phi t + B_4\sin\omega_\phi t) = 0
\end{aligned}
\tag{4-27}
$$

Eq.4-27 is also an identity equation, not relevant to time *t*, so another linear system of equations we can obtain is Eq.4-28 or Eq.4-29.

$$\begin{cases} -(\omega_\theta^2 - \omega_2^2)A_1 = C_y B_1 \omega_\theta \\ -A_2(\omega_\theta^2 - \omega_2^2) = -C_y B_2 \omega_\theta \\ -A_3(\omega_\phi^2 - \omega_2^2) = C_y B_3 \omega_\phi \\ -A_4(\omega_\phi^2 - \omega_2^2) = -C_y B_4 \omega_\phi \end{cases} \tag{4-28}$$

$$\begin{cases} -B_1(\omega_\theta^2 - \omega_1^2) = -C_x A_1 \omega_\theta \\ -B_2(\omega_\theta^2 - \omega_1^2) = C_x A_2 \omega_\theta \\ -B_3(\omega_\phi^2 - \omega_1^2) = -C_x A_3 \omega_\phi \\ -B_4(\omega_\phi^2 - \omega_1^2) = C_x A_4 \omega_\phi \end{cases} \tag{4-29}$$

The initial conditions of the system are:

$$\begin{cases} \phi(t=0) = A_2 + A_4 + \dfrac{S_0}{\omega_2^2} + \dfrac{S_2((\omega_1^2 - \omega^2) - C_y\omega)}{((\omega_2^2 - \omega^2)(\omega_1^2 - \omega^2) + C_y C_x \omega^2)} = 0 \\ \theta(t=0) = B_1 + B_3 + \dfrac{S_1(C_x\omega + (\omega_2^2 - \omega^2))}{((\omega_2^2 - \omega^2)(\omega_1^2 - \omega^2) - C_x C_y \omega^2)} = 0 \end{cases} \tag{4-30}$$

$$\begin{cases} \dot{\phi}(t=0) = A_1\omega_\theta + A_3\omega_\phi = \dfrac{S_1((\omega_1^2 - \omega^2) + C_y\omega)}{((\omega_2^2 - \omega^2)(\omega_1^2 - \omega^2) - C_x C_y \omega^2)}\omega \\ \dot{\theta}(t=0) = B_2\omega_\theta + B_4\omega_\phi = -\dfrac{S_2(C_x\omega + (\omega_2^2 - \omega^2))}{((\omega_2^2 - \omega^2)(\omega_1^2 - \omega^2) + C_y C_x \omega^2)}\omega \end{cases} \tag{4-31}$$

Combining Eq.4-29, Eq.4-30 with Eq.4-31 or Eq.4-28, Eq.4-30 with Eq.4-31, the parameters of Eq.4-23 can be obtained.

$$\begin{cases} A_1 = \begin{cases} \dfrac{\dfrac{S_1((\omega_1^2 - \omega^2) + C_y\omega)\omega}{((\omega_2^2 - \omega^2)(\omega_1^2 - \omega^2) - C_x C_y \omega^2)} - \dfrac{C_y\omega_\phi^2}{(\omega_\theta^2 - \omega_2^2)} \dfrac{S_1(C_x\omega + (\omega_2^2 - \omega^2))}{((\omega_2^2 - \omega^2)(\omega_1^2 - \omega^2) - C_x C_y \omega^2)})}{(\dfrac{C_y\omega_\theta^2}{(\omega_\theta^2 - \omega_2^2)} - \dfrac{C_y\omega_\phi^2}{(\omega_\phi^2 - \omega_2^2)})} \dfrac{C_y\omega_\theta}{(\omega_\theta^2 - \omega_2^2)} \\ + \dfrac{S_1(C_x\omega + (\omega_2^2 - \omega^2))}{((\omega_2^2 - \omega^2)(\omega_1^2 - \omega^2) - C_x C_y \omega^2)} \dfrac{C_y\omega_\theta}{(\omega_\theta^2 - \omega_2^2)} \end{cases} \\ A_2 = \begin{cases} -\dfrac{\dfrac{C_y\omega_\theta}{(\omega_\theta^2 - \omega_2^2)} \dfrac{S_2(C_x\omega + (\omega_2^2 - \omega^2))\omega}{\omega_\theta((\omega_2^2 - \omega^2)(\omega_1^2 - \omega^2) + C_y C_x \omega^2)} - \dfrac{S_0}{\omega_2^2} - \dfrac{S_2((\omega_1^2 - \omega^2) - C_y\omega)}{((\omega_2^2 - \omega^2)(\omega_1^2 - \omega^2) + C_y C_x \omega^2)}}{(\dfrac{C_y\omega_\phi}{(\omega_\phi^2 - \omega_2^2)} - \dfrac{C_y\omega_\phi}{(\omega_\theta^2 - \omega_2^2)})} \dfrac{\omega_\phi}{\omega_\theta} \dfrac{C_y\omega_\theta}{(\omega_\theta^2 - \omega_2^2)} \\ - \dfrac{S_2(C_x\omega + (\omega_2^2 - \omega^2))}{\omega_\theta((\omega_2^2 - \omega^2)(\omega_1^2 - \omega^2) + C_y C_x \omega^2)} \dfrac{C_y\omega_\theta}{(\omega_\theta^2 - \omega_2^2)} \end{cases} \\ A_3 = -\dfrac{C_y\omega_\phi}{(\omega_\phi^2 - \omega_2^2)} \dfrac{\dfrac{S_1((\omega_1^2 - \omega^2) + C_y\omega)\omega}{((\omega_2^2 - \omega^2)(\omega_1^2 - \omega^2) - C_x C_y \omega^2)} - \dfrac{C_y\omega_\phi^2}{(\omega_\theta^2 - \omega_2^2)} \dfrac{S_1(C_x\omega + (\omega_2^2 - \omega^2))}{((\omega_2^2 - \omega^2)(\omega_1^2 - \omega^2) - C_x C_y \omega^2)})}{(\dfrac{C_y\omega_\theta^2}{(\omega_\theta^2 - \omega_2^2)} - \dfrac{C_y\omega_\phi^2}{(\omega_\phi^2 - \omega_2^2)})} \\ A_4 = \dfrac{C_y\omega_\phi}{(\omega_\phi^2 - \omega_2^2)} \dfrac{\dfrac{C_y\omega_\theta}{(\omega_\theta^2 - \omega_2^2)} \dfrac{S_2(C_x\omega + (\omega_2^2 - \omega^2))\omega}{\omega_\theta((\omega_2^2 - \omega^2)(\omega_1^2 - \omega^2) + C_y C_x \omega^2)} - \dfrac{S_0}{\omega_2^2} - \dfrac{S_2((\omega_1^2 - \omega^2) - C_y\omega)}{((\omega_2^2 - \omega^2)(\omega_1^2 - \omega^2) + C_y C_x \omega^2)}}{(\dfrac{C_y\omega_\phi}{(\omega_\phi^2 - \omega_2^2)} - \dfrac{C_y\omega_\phi}{(\omega_\theta^2 - \omega_2^2)})} \end{cases} \tag{4-32}$$

$$
\begin{cases}
B_1 = \begin{cases} -\dfrac{\dfrac{S_1((\omega_1^2-\omega^2)+C_y\omega)\omega}{((\omega_2^2-\omega^2)(\omega_1^2-\omega^2)-C_xC_y\omega^2)}-\dfrac{C_y\omega_\phi^2}{(\omega_\theta^2-\omega_2^2)}\dfrac{S_1(C_x\omega+(\omega_2^2-\omega^2))}{((\omega_2^2-\omega^2)(\omega_1^2-\omega^2)-C_xC_y\omega^2)})}{(\dfrac{C_y\omega_\theta^2}{(\omega_\theta^2-\omega_2^2)}-\dfrac{C_y\omega_\phi^2}{(\omega_\phi^2-\omega_2^2)})} \\ -\dfrac{S_1(C_x\omega+(\omega_2^2-\omega^2))}{((\omega_2^2-\omega^2)(\omega_1^2-\omega^2)-C_xC_y\omega^2)} \end{cases} \\
B_2 = \begin{cases} -\dfrac{\dfrac{C_y\omega_\theta}{(\omega_\theta^2-\omega_2^2)}\dfrac{S_2(C_x\omega+(\omega_2^2-\omega^2))\omega}{\omega_\theta((\omega_2^2-\omega^2)(\omega_1^2-\omega^2)+C_yC_x\omega^2)}-\dfrac{S_0}{\omega_2^2}-\dfrac{S_2((\omega_1^2-\omega^2)-C_y\omega)}{((\omega_2^2-\omega^2)(\omega_1^2-\omega^2)+C_yC_x\omega^2)}}{(\dfrac{C_y\omega_\phi}{(\omega_\phi^2-\omega_2^2)}-\dfrac{C_y\omega_\phi}{(\omega_\theta^2-\omega_2^2)})}\dfrac{\omega_\phi}{\omega_\theta} \\ -\dfrac{S_2(C_x\omega+(\omega_2^2-\omega^2))}{\omega_\theta((\omega_2^2-\omega^2)(\omega_1^2-\omega^2)+C_yC_x\omega^2)} \end{cases} \\
B_3 = \dfrac{\dfrac{S_1((\omega_1^2-\omega^2)+C_y\omega)\omega}{((\omega_2^2-\omega^2)(\omega_1^2-\omega^2)-C_xC_y\omega^2)}-\dfrac{C_y\omega_\phi^2}{(\omega_\theta^2-\omega_2^2)}\dfrac{S_1(C_x\omega+(\omega_2^2-\omega^2))}{((\omega_2^2-\omega^2)(\omega_1^2-\omega^2)-C_xC_y\omega^2)})}{(\dfrac{C_y\omega_\theta^2}{(\omega_\theta^2-\omega_2^2)}-\dfrac{C_y\omega_\phi^2}{(\omega_\phi^2-\omega_2^2)})} \\
B_4 = \dfrac{\dfrac{C_y\omega_\theta}{(\omega_\theta^2-\omega_2^2)}\dfrac{S_2(C_x\omega+(\omega_2^2-\omega^2))\omega}{\omega_\theta((\omega_2^2-\omega^2)(\omega_1^2-\omega^2)+C_yC_x\omega^2)}-\dfrac{S_0}{\omega_2^2}-\dfrac{S_2((\omega_1^2-\omega^2)-C_y\omega)}{((\omega_2^2-\omega^2)(\omega_1^2-\omega^2)+C_yC_x\omega^2)}}{(\dfrac{C_y\omega_\phi}{(\omega_\phi^2-\omega_2^2)}-\dfrac{C_y\omega_\phi}{(\omega_\theta^2-\omega_2^2)})}
\end{cases}
\tag{4-33}
$$

Therefore, the homogeneous solution for Eq.4-15 is expressed as:

$$
\begin{cases}
\phi_{\text{hom}}(t) = A_1\sin\omega_\theta t + A_2\cos\omega_\theta t + A_3\sin\omega_\phi t + A_4\cos\omega_\phi t \\
\theta_{\text{hom}}(t) = B_1\cos\omega_\theta t + B_2\sin\omega_\theta t + B_3\cos\omega_\phi t + B_4\sin\omega_\phi
\end{cases}
\tag{4-34}
$$

Then, the complete solutions for Eq.4-15 are the sum of the particular solution and the homogeneous solution, as shown in Eq.4-35. It shows that the spindle rotor vibrates for the tilting motions at three kinds of frequencies, involving one pair of reciprocally coupled natural frequencies (CTFs) and the spindle rotational frequency (SRF) corresponding to the spindle speed. It is deduced that the spiral, radial and two fold patterns will form at a machined surface. To identify the surface topography influenced by spindle vibration, the simulated and experimental surface generation is employed.

$$
\begin{aligned}
\theta(t) &= \begin{cases} \theta_1\cos\omega t - \theta_2\sin\omega t \\ +B_1\cos\omega_\theta t + B_2\sin\omega_\theta t + B_3\cos\omega_\phi t + B_4\sin\omega_\phi \end{cases} \\
\phi(t) &= \begin{cases} \phi_0 + \phi_1\sin\omega t + \phi_2\cos\omega t \\ +A_1\sin\omega_\theta t + A_2\cos\omega_\theta t + A_3\sin\omega_\phi t + A_4\cos\omega_\phi t \end{cases}
\end{aligned}
\tag{4-35}
$$

4.2.2 Dynamic Responses of the Spindle

Matlab Simulink is a powerful integral part of analytical methods of science and technology, being used to simulate, model and analyze the linear or non-linear system to obtain its numerical solutions or its numerical responses, known as the numerical simulation. In this study, Matlab Simulink is employed to simulate the dynamic responses of the spindle rotor motions, involving the translational motions and the tilting motions for its dynamic equations of Eq.3-17 and Eq.3-19 with its specification tabulated in Table 4.1, where the linear damping ratio is set at 0.025 and the angular damping ratio is set at zero, under different cutting conditions with the configuration parameters of Matlab Simulink with the ode45 (Dormand-Prince) method, as shown in Figure 4.1.

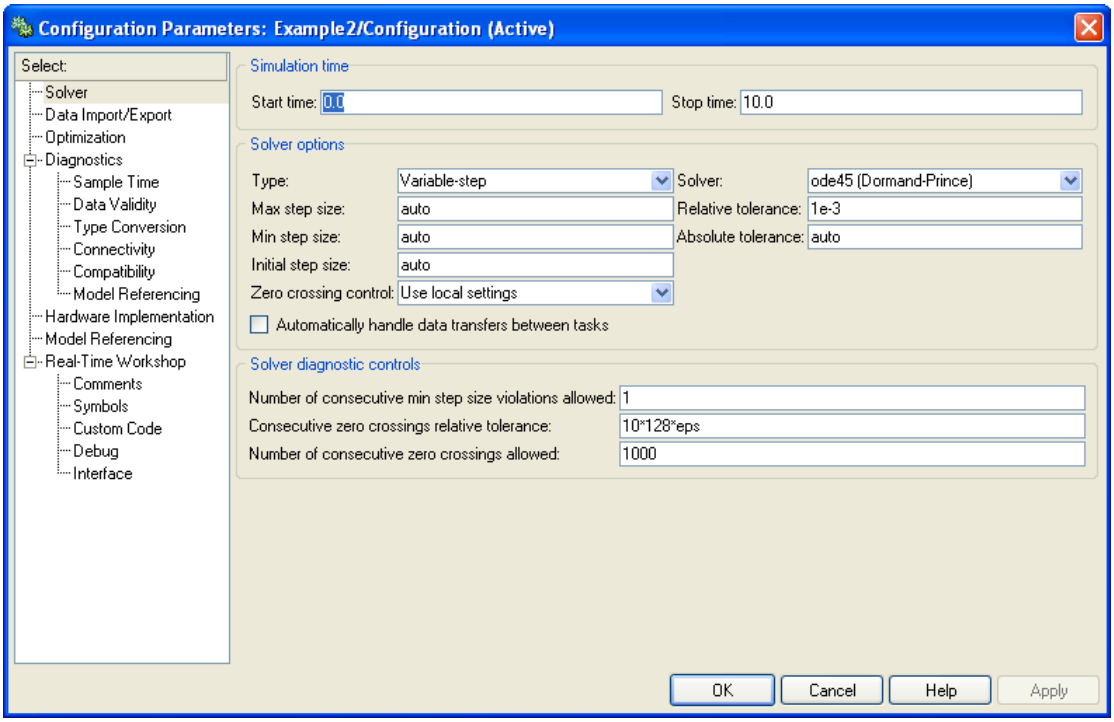

Figure 4.1 Configuration parameters of the Simulink model regarding the simulation

4.2.2.1 Spindle Responses under Air Cutting

Since under air cutting the cutting forces are zero, Eq.3-18 and Eq.3-20 describe free vibration of the spindle system. The titling motions, the radial motions and the axial motion are only caused by the inertia force and the inertia torque relative to quadratic spindle speed. Using Matlab Simulink with the Dormand-Prince (ode45) method to simulate the spindle vibration, the dynamic responses are obtained as shown in Figure 4.2 under the initial conditions of zero with their corresponding power spectral densities shown in Figure 4.3.

In Figure 4.2(a), the extremely tiny vibration amplitude for the axial motion of the spindle rotor along the *Z*-axis decreases sharply to one negligible constant value, which is noted as the steady state, and its power spectral density (PSD) (see Appendix VIII) plots the characteristic frequencies of 5000/60Hz corresponding to the spindle rotational frequency (SRF), about 1100Hz for the axial response and 2000Hz for the tilting response of the spindle rotor with a harmonic frequency of 4000Hz, as shown in Figure 4.3(a). Figure 4.2(b) and Figure 4.2(c) demonstrate the radial motions of the spindle rotor that it mainly vibrates at the frequencies of about 1000Hz and 5000/60Hz (spindle speed) as shown in Figure 4.3(b) and Figure 4.3(c). At the steady state, the vibration at the frequency of 5000/60Hz with the amplitude of several nanometers along the radial axis at a balance position away from the inertia center is induced by the centrifugal/inertial force, which plays an extremely important role, and the vibration at 1000Hz deeply attenuates to disappear due to damping. Figure 4.2(d) and Figure 4.2(e) depict the tilting motions of the spindle rotor that it periodically tilts by means of the product of two kinds of vibration at the CTFs of 2016Hz and 1934Hz in a certain range with a balance tilting angle as shown in Figure 4.3(d) and Figure 4.3(e), which is caused by the inertia moment. It is also inferred that the orbit of the spindle rotor center is regular and symmetric and that it could be at the steady state after several tens of milliseconds. According to Eq.4-4, Eq.4-12 and Eq.4-13, the natural angular frequencies ω_i of the spindle rotor in the system are calculated. The natural frequencies can be calculated by the following equations, respectively:

$$f_i = \frac{1}{2\pi}\omega_i \qquad (i{=}x, y, z) \tag{4-36}$$

$$f_i = \frac{1}{2\pi}\omega_i \qquad (i{=}\phi \text{ and } \theta) \tag{4-37}$$

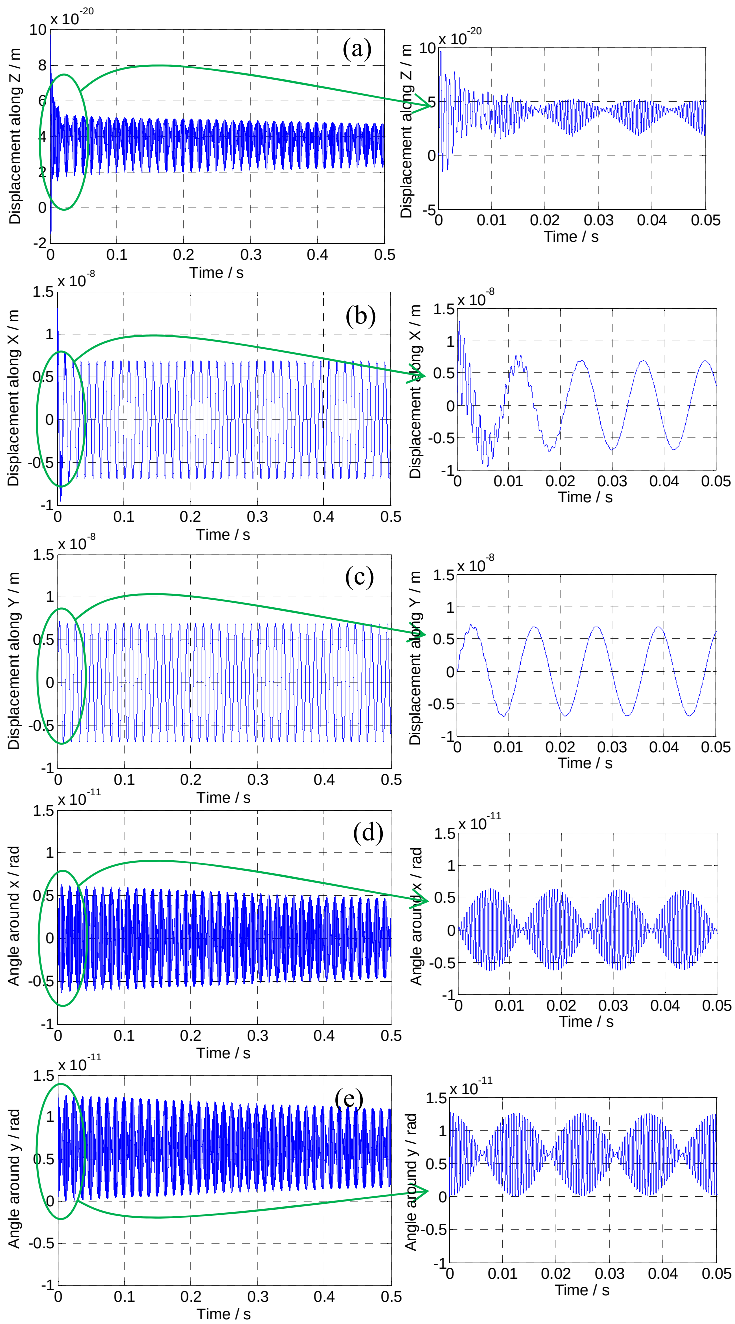

Figure 4.2 Dynamic responses of the spindle rotor under air cutting at the spindle speed of 5000rpm with the specifications of Table 4.1, involving: (a) the translational motion along the spin axis, (b) and (c) the translational motions along the radial axes, and (d) and (e) the tilting motions deviating away from the spin axis

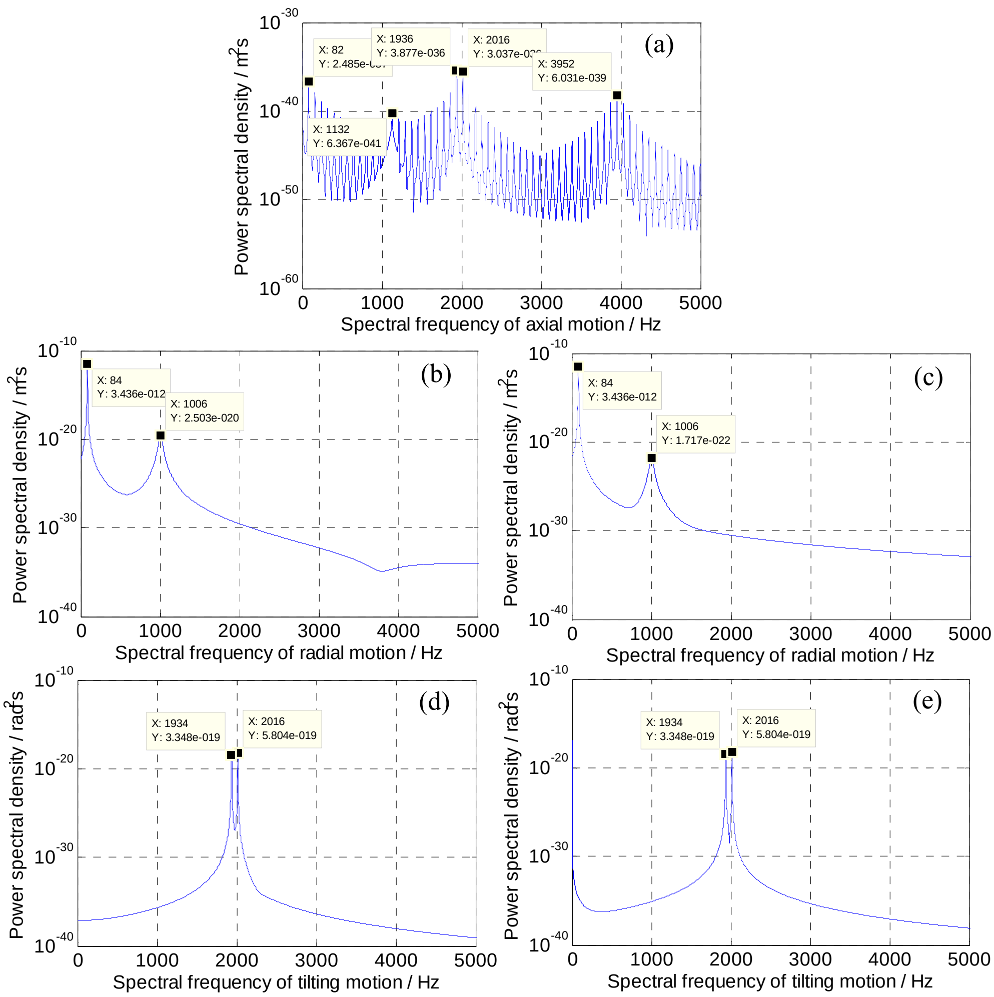

Figure 4.3 PSDs of dynamic responses of the spindle rotor for Figure 4.2: (a) the translational motion along the spin axis, (b) and (c) the translational motions along the radial axes, and (d) and (e) the tilting motions deviating away from the spin axis

One kind of frequency originates from the spindle speed, i.e. the SRF. Four kinds of frequencies as tabulated in Table 4.2 are corresponding to the PSD results. In summary, it is self-exited by the inertial force and moment at the frequency of about 5000/60Hz (spindle speed) and vibrates at the frequencies of about 1100Hz and 1000Hz for the translational motions and at the CTFs of about 2000Hz for the tilting motions. It is also interesting to note that the non-linear equations of Eq.3-17 and Eq.3-19 can be linearized into Eq.3-21 and Eq.3-22, respectively, because the variables have a minuscule influence on each other at the relatively low spindle speed. Hence, the simulation results identify why the non-linear equations can be linearized.

Table 4.2 Natural frequencies of the spindle rotor in the spindle system

Translational frequency in the axial direction (f_z) (Hz)	1125
CTFs around the radial direction (f_θ/f_ϕ) (Hz)	1975±41
Translational frequency in the radial direction (f_x/f_y) (Hz)	1006
SRF corresponding to spindle speed (f) (Hz)	5000/60

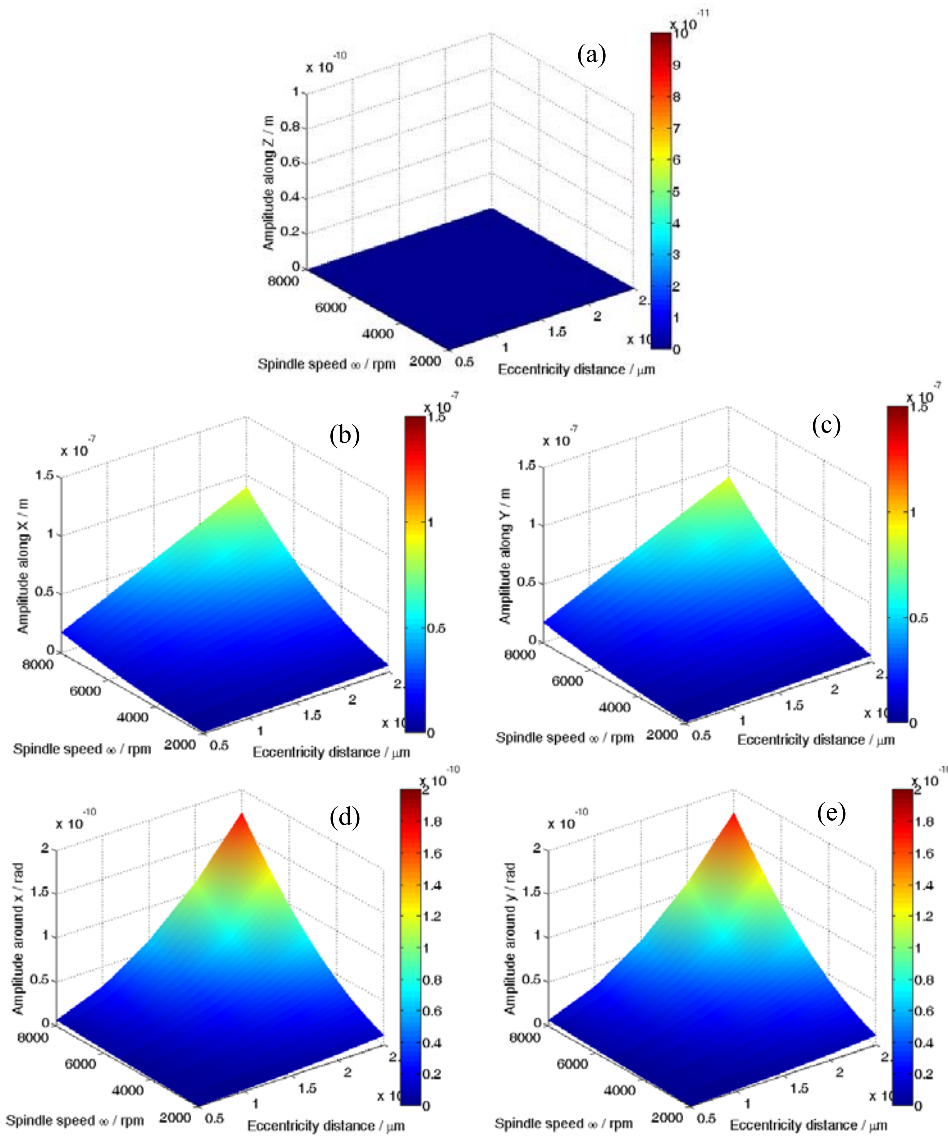

Figure 4.4 Effects of spindle speeds with eccentric distances on the vibration amplitude of (a) the translational motion along the spin axis, (b) and (c) the translation motions along the radial axes, and (d) and (e) the tilting motions deviating away from the spin axis under air cutting at the steady state

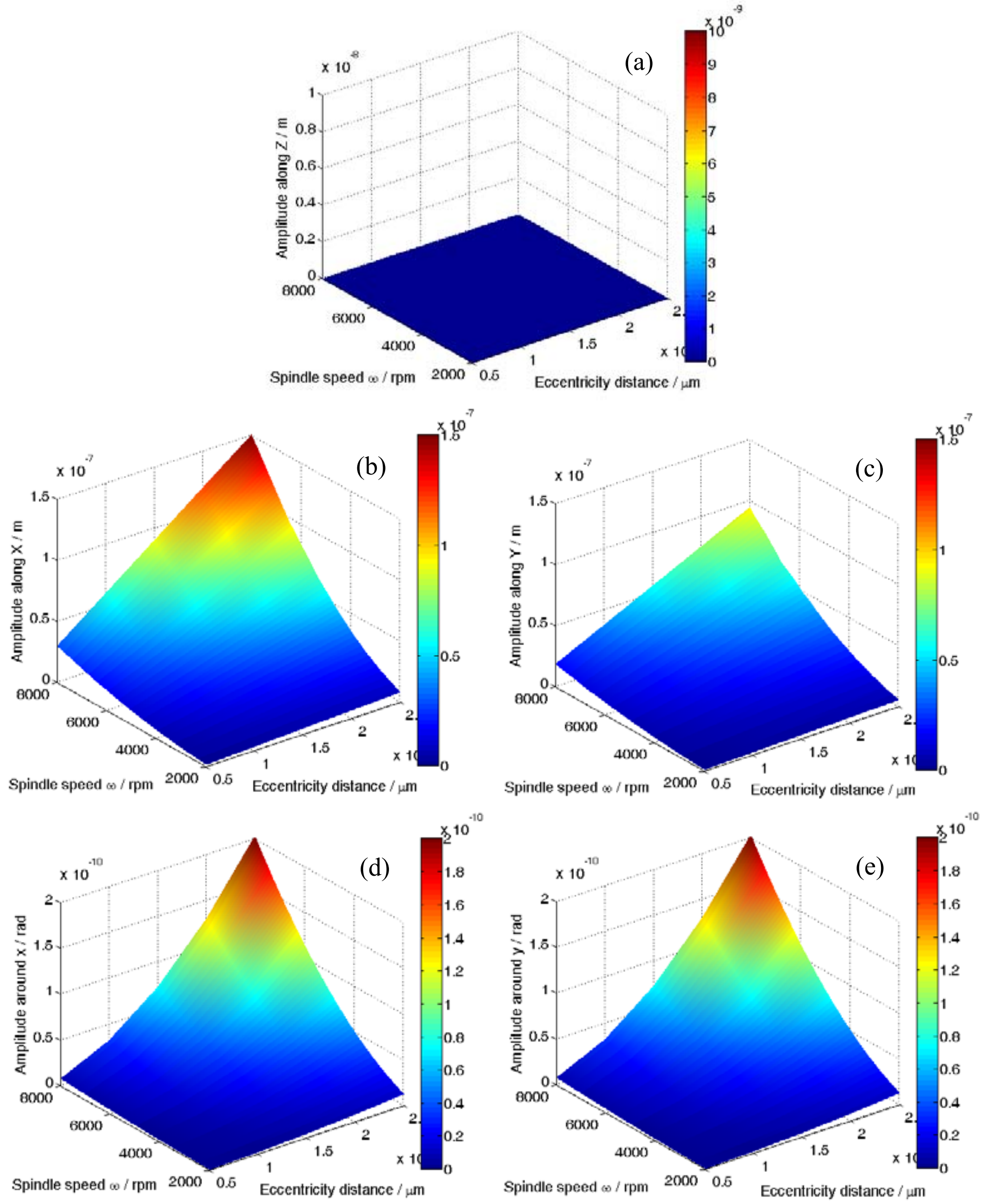

Figure 4.5 Effects of spindle speeds with eccentric distances on the vibration amplitude of (a) the translational motion along the spin axis, (b) and (c) the translation motions along the radial axes, and (d) and (e) the tilting motions deviating away from the spin axis under air cutting at the transient state

In air cutting, the spindle speed and the eccentric distance are only two factors influencing the vibration amplitudes of the spindle rotor, due to the inertial force and moment related to it. Figure 4.4 and Figure 4.5 display the amplitudes influenced by the spindle speed and the eccentric distance at the steady state and the transient state, respectively. In Figure 4.4(a) and Figure 4.5(a), the influence along the spin axis can be ignored as zero. As the spindle speed and the eccentric distance increase, in Figure 4.4(b) and Figure 4.4(c), the vibration amplitude of the radial translational motions quadratically and quasi-quadratically develops at the steady state, and Figure 4.5(b) and Figure 4.5(c) draw the same results at the transient state, but the difference is the influence of damping on the amplitude. In Figure 4.4(d) and Figure 4.4(e), the insignificant vibration amplitude of the tilting motions quadratically and quasi-quadratically rises at the steady state. Figure 4.5(d) and Figure 4.5(e) illustrate the same results at the transient state, since the angular damping ratio is very small. Therefore, the dynamic behaviors of the spindle are influenced by the two factors. This implies that as the eccentricity decreases, the amplitude efficiently dwindles.

4.2.2.2 Spindle Responses under Continuous Cutting

In the cutting process, cutting forces are indirectly applied to the spindle rotor through the workpiece. When the cutting speed ($2\pi d_1\omega$) is larger than the vibration speed, the cutting process is continuous, but as the d_1 is very small, i.e. the cutting speed is less than the vibration speed, the cutting process is intermittent. Its dynamic behavior is influenced by the cutting forces, according to Eq.4-17 and Eq.4-19, in which the cutting forces F_t, F_r and F_m are defined as 0.05N, 0.003N and 0.05N, respectively. The simulation is conducted using Matlab Simulink with the Dormand-Prince (ode45) method to obtain dynamic responses of the spindle rotor with the spindle specifications of Table 4.1 under constant cutting forces. The initial conditions are set as zero for the spindle rotor motions with the spindle speed of 5000rpm. The dynamic responses are plotted in Figure 4.6 and the corresponding power spectral densities (PSDs) are shown in Figure 4.7.

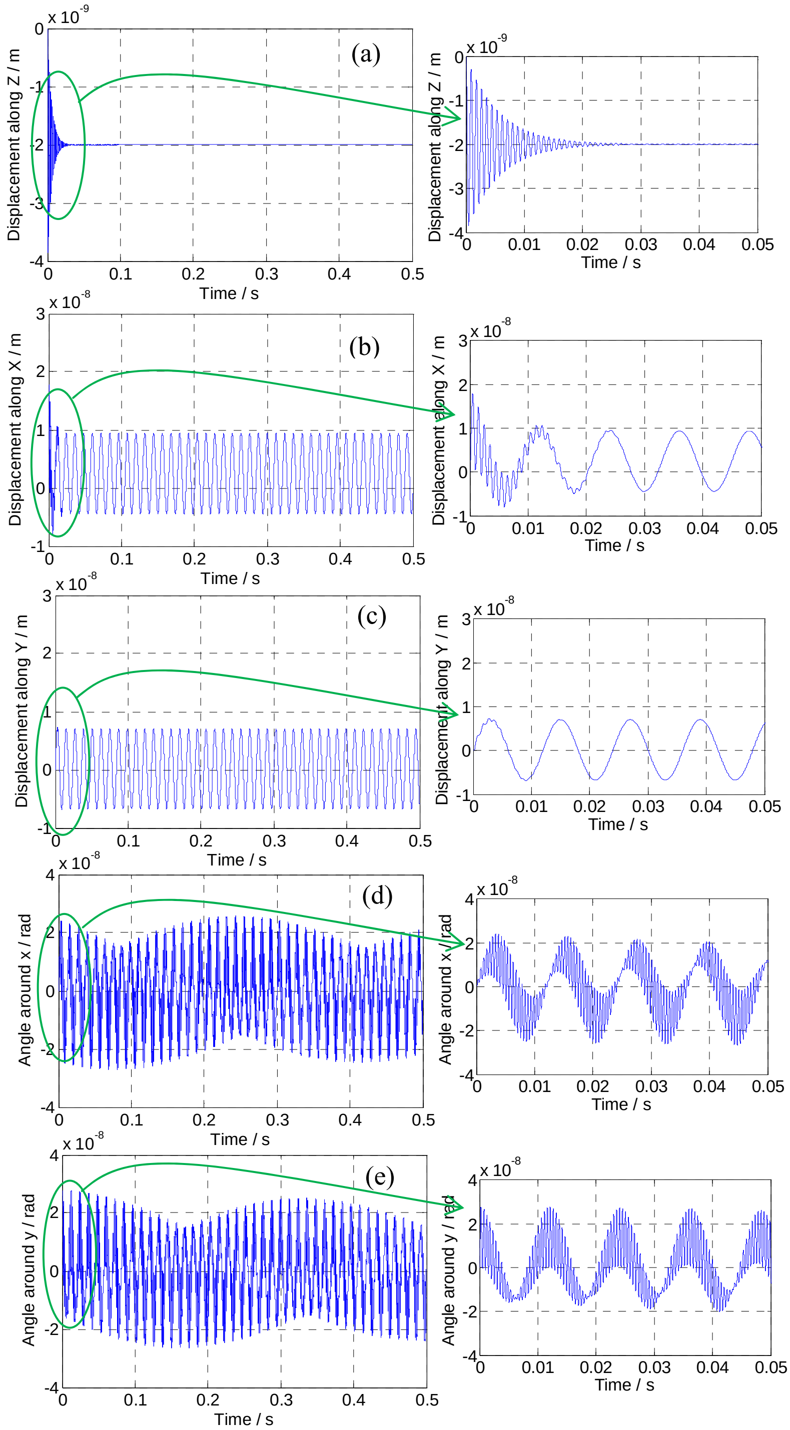

Figure 4.6 Dynamic responses of the spindle rotor with (a) the translational motion along the spin axis, (b) and (c) the translation motions along the radial axes, and (d) and (e) the tilting motions deviating away from the spin axis with the spindle speed of 5000rpm and constant cutting forces (0.05 N, 0.05 N, 0.003N) under the spindle specifications of Table 4.1

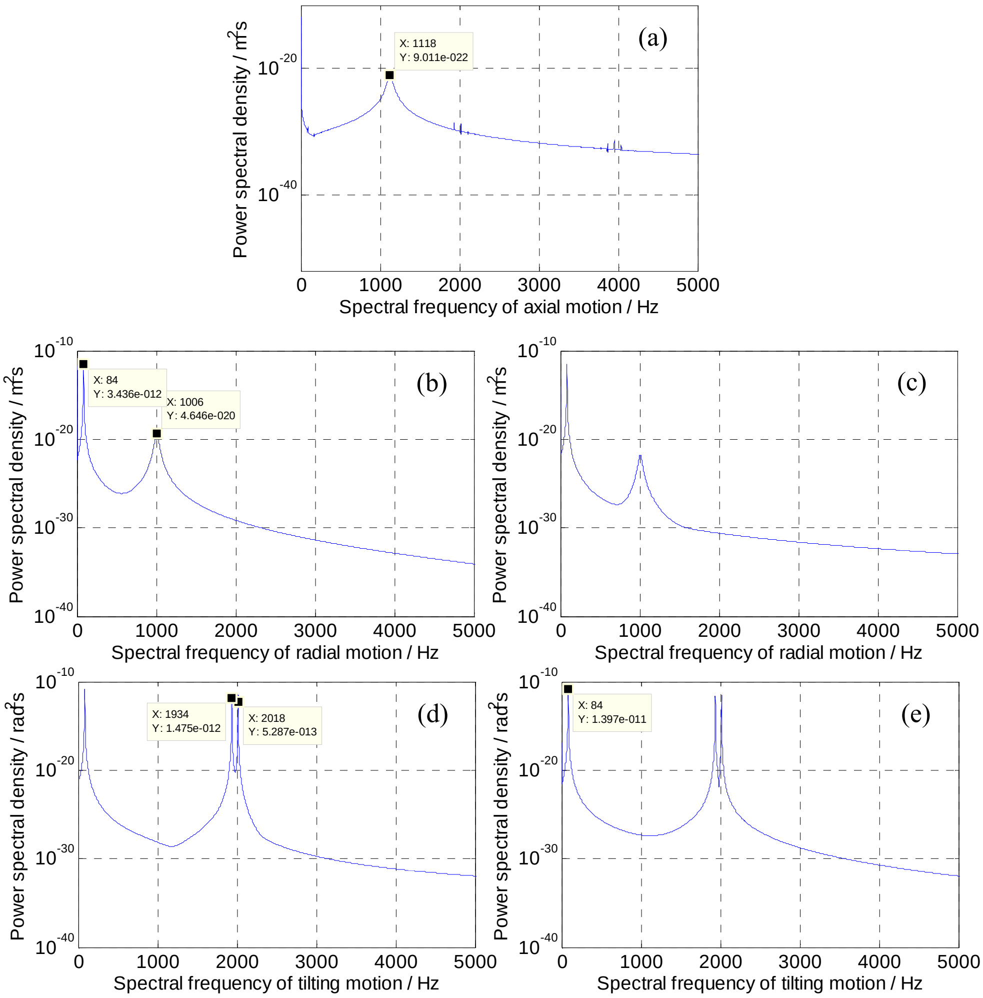

Figure 4.7 PSDs of dynamic responses of the spindle rotor in Figure 4.6 for (a) the translational motion along the spin axis, (b) and (c) the translation motions along the radial axes, and (d) and (e) the tilting motions around the radial axes

Figure 4.6(a), (b) and (c) show that the dynamic responses of the spindle rotor excited by the cutting forces F_t, F_r and F_m rapidly develop from the transient state into the steady state. The spindle rotor harmonically vibrates in the radial direction at the spindle rotational frequency (RSF) of 5000/60Hz (spindle speed) at the vibration amplitude determined by the centrifugal force and the balance position determined by the cutting forces. Figure 4.6(d) and (e) portray that the titling motions of the spindle rotor applied by the harmonic torques originating from the constant cutting forces extremely slowly develop from the transient state into the steady state, due to the tiny angular damping ratio. For the tilting motions, the spindle vibrates at three kinds of frequencies, involving one pair of close frequencies producing the "beating" phenomenon and the SRF generating harmonics (see Appendix VII). The relevant characteristic frequencies are obtained by the PSDs in Figure 4.7. The effects of the coupled variables in Eq.4-17 and Eq.4-19 on each other can be ignored, so that these equations can be simplified as Eq.3-21 and Eq.3-22, respectively.

Comparing Figure 4.6 with Figure 4.4, at the steady state, the spindle deviates at constant values due to the external forces, such as the cutting forces and the inertial force, and the external moments such as the inertial moment and the cutting torques, and vibrate at constant amplitudes which are directly influenced by the inertial force and the moments. This indicates that in the continuous cutting process, the dynamic responses of the spindle rotor are influenced by the cutting forces and the cutting torques, which can be explained by Eq.4-8 and Eq.4-9.

4.2.2.3 Spindle Responses under Intermittent Cutting

To observe the natural frequencies of the spindle system, the intermittent cutting forces at different frequencies are used to excite the spindle system. When the intermittent excitation at the frequency equivalent to the intermittent cutting forces synchronizes the spindle system, i.e. the excitation frequency equal to one of the natural frequencies of the spindle system, the resonance takes place. Therefore, the frequency responses of the spindle under the excitation at different frequencies are employed to observe the natural frequencies of the spindle system. In this section, the intermittent cutting forces at the half-periodical pulse wave in the form of 0.05 N, 0.05 N, and 0.003N at different frequencies are input into the dynamic model under the spindle specifications of Table 4.1 with a spindle speed of 5000rpm. The simulated results using Matlab Simulink with the Dormand-Prince (ode45) method present the effects of intermittent cutting forces at different frequencies on vibration amplitudes. Figure 4.8 shows the natural frequencies of the spindle system.

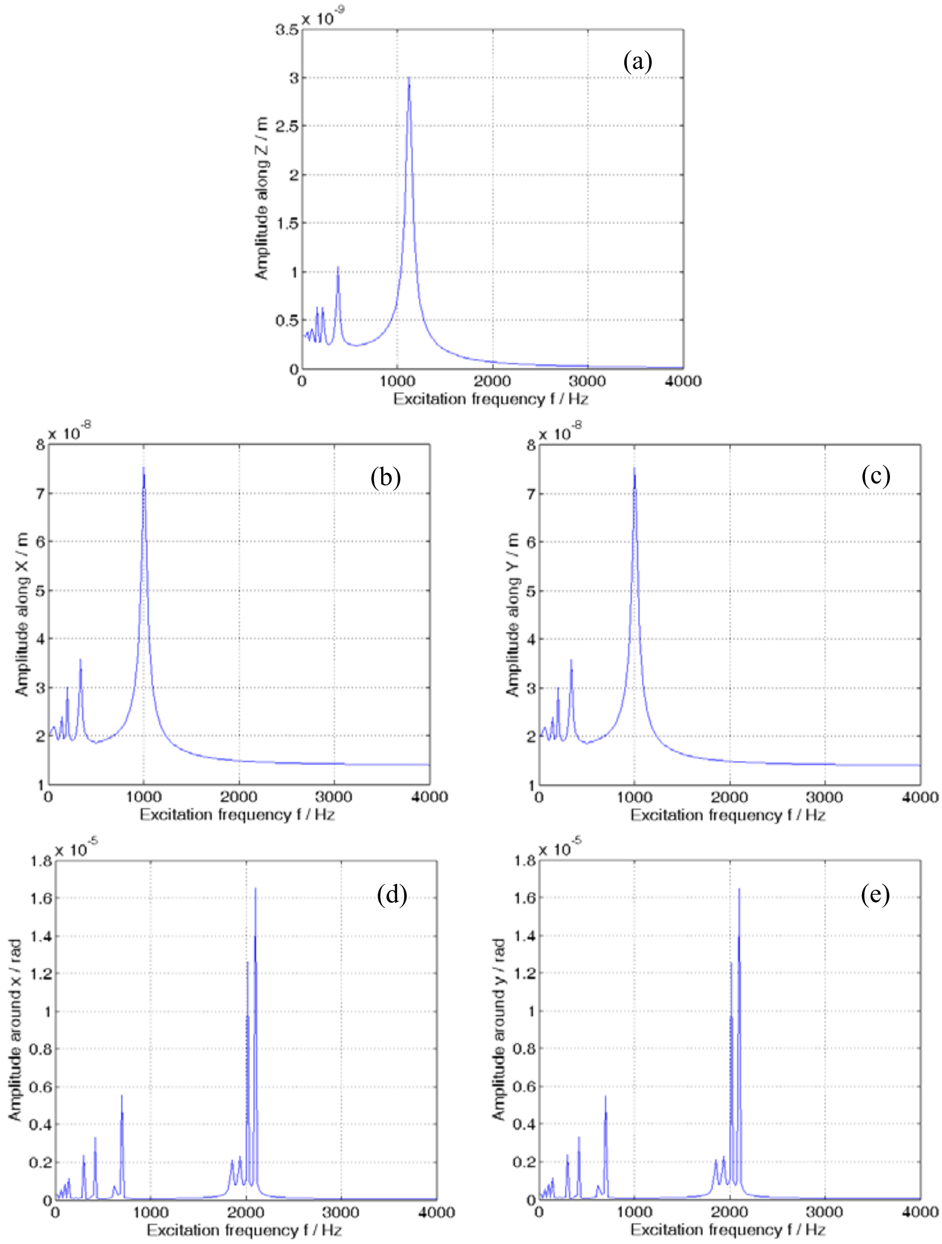

Figure 4.8 Effects of cutting force frequencies on the vibration amplitudes of (a) the translational motion along the spin axis, (b) and (c) the translation motions along the radial axes, and (d) and (e) the tilting motions deviating away from the spin axis acted by intermittent cutting forces (half-periodical pulse wave in the form of 0.05 N, 0.05 N, 0.003N) under the spindle specifications of Table 4.1 with the spindle speed of 5000rpm

Table 4.3 Spindle performance specifications with cutting forces for simulation

Spindle rotor mass (m) (kg)	0.5
Radial stiffness (k_2/ k_3) (N/μm)	20
Axial stiffness (k_1) (N/μm)	25
Eccentric position of the mass imbalance away from the rotor axis (e) (μm)	0.5~2.5
Position of the centre of mass center relative to its equilibrium along the z-axis (l_1/ l_2) (mm)	50+5e / 50-5e
Radius of spindle rotor (R) (mm)	25
Inertial tensor around y-axis (J_z) (gm^2)	0.05
Inertial tensor around z/x-axis (J_x/J_y) (gm^2)	1.4
The distance of tilting center of spindle rotor to the tool tip (d_2) (mm)	60
The distance of tool tip away from the spindle axis in cutting (d_1) (mm)	3
Damper ratio μ	0.025
Angular damper ratio ξ	0.5×10^{-4}
Main cutting force (Fm) (N)	0.05
Thrust cutting force (Ft) (N)	0.05
Feed cutting force (Fr) (N)	0.003

4.2.3 Influences of Eccentric Distances with Spindle Speeds on Vibration Amplitudes

In this section, the study focuses on the influences of eccentric distances of the spindle rotor under a certain range of spindle speeds with the excitation of the cutting forces on the vibration amplitudes in the constant cutting mode. The inputs for the simulation of Matlab Simulink with the Dormand-Prince (ode45) method are tabulated in Table.4.3. The variables are the spindle speed and the eccentric distance. Figure 4.9 and Figure 4.10 show the influences of the eccentric distances combining the spindle speeds.

In Figure 4.9, at the transient state, as the spindle speed increases, the axial amplitude along the *Z*-axis keeps constant and is only relative to the cutting forces and is not influenced by the eccentric distance. As shown in Figure 4.9(a), the radial amplitudes along the *X*-axis and the *Y*-axis quadratically increase and are almost linearly impacted by the eccentric distance, as shown in Figure 4.9(b) and (c). And the angular amplitudes around the *x*-axis and the *y*-axis gradually increase at a inertial-moment-induced deviation with a little fluctuation and are not affected by the eccentric distance, as shown in Figure 4.9(d) and (e).

At the steady state, as shown in Figure 4.10, since the damping dissipates the energy of the vibration, the spindle rotor goes into a steady state moving in equilibrium. Where the deviation along the *Z*-axis is zero, the deviation along the *X*/*Y*-axes is one circle whose radius is relevant to the inertial force and the tilting deviation around the *x*/*y*-axes is a spiral curve in a form related to the inertial moment. The above results can be calculated based on the transient solutions and the steady solutions of the spindle rotor motions, Eq.4-6, Eq.4-7, Eq.4-23 and Eq.4-34. This implies that Eq.4-8 and Eq.4-35 are reliable enough to describe the dynamic system of the spindle. It should be noted that as the eccentric distance decreases, the amplitude induced by the inertial force is directly reduced, which has a linear impact on surface topography.

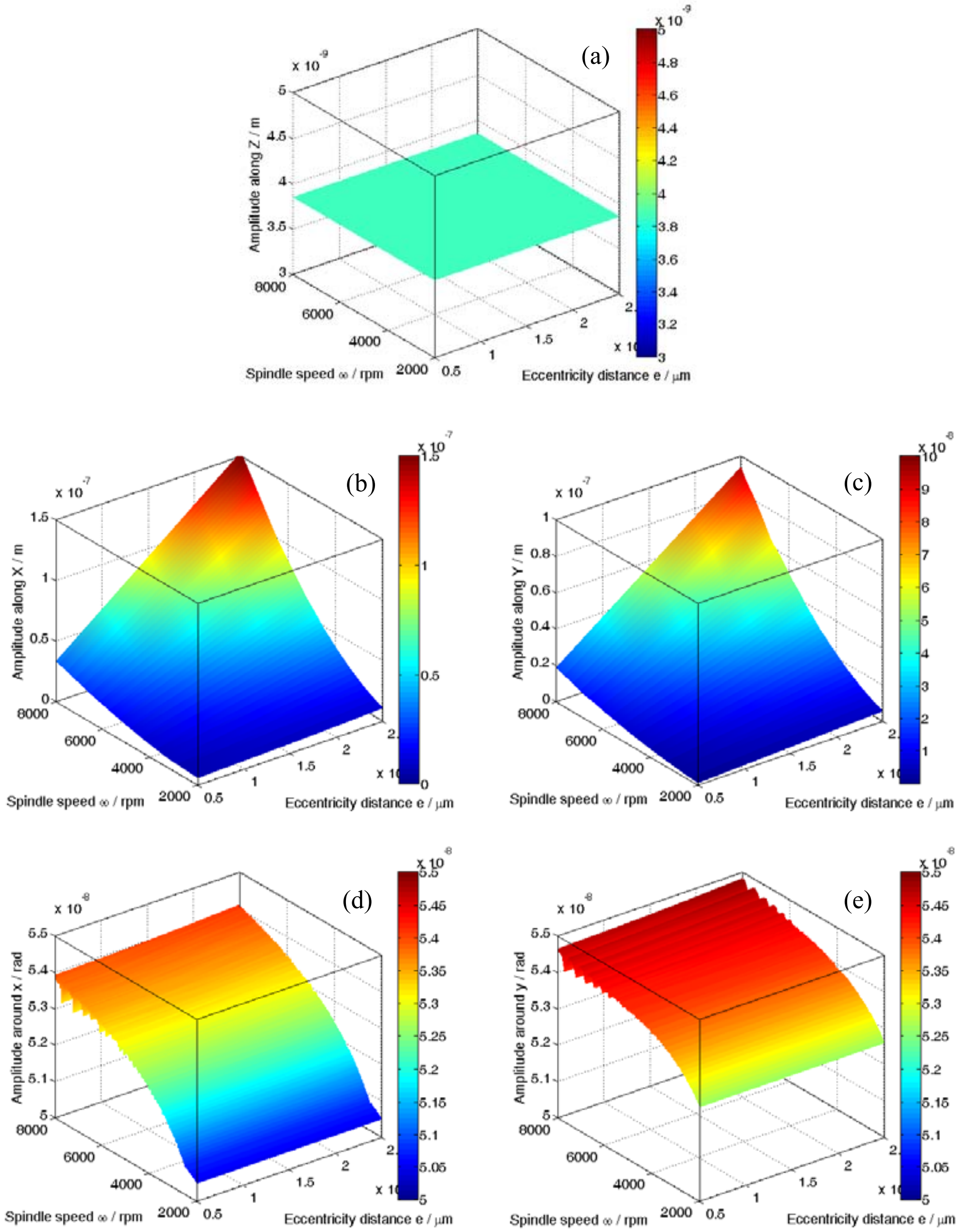

Figure 4.9 Effect of eccentric distances on amplitudes of spindle vibration combining the spindle speeds with the simulation parameters of Table 4.3 at the transient state for (a) the translational motion along the spin axis, (b) and (c) the translation motions along the radial axes, and (d) and (e) the tilting motions deviating away from the spin axis under air cutting

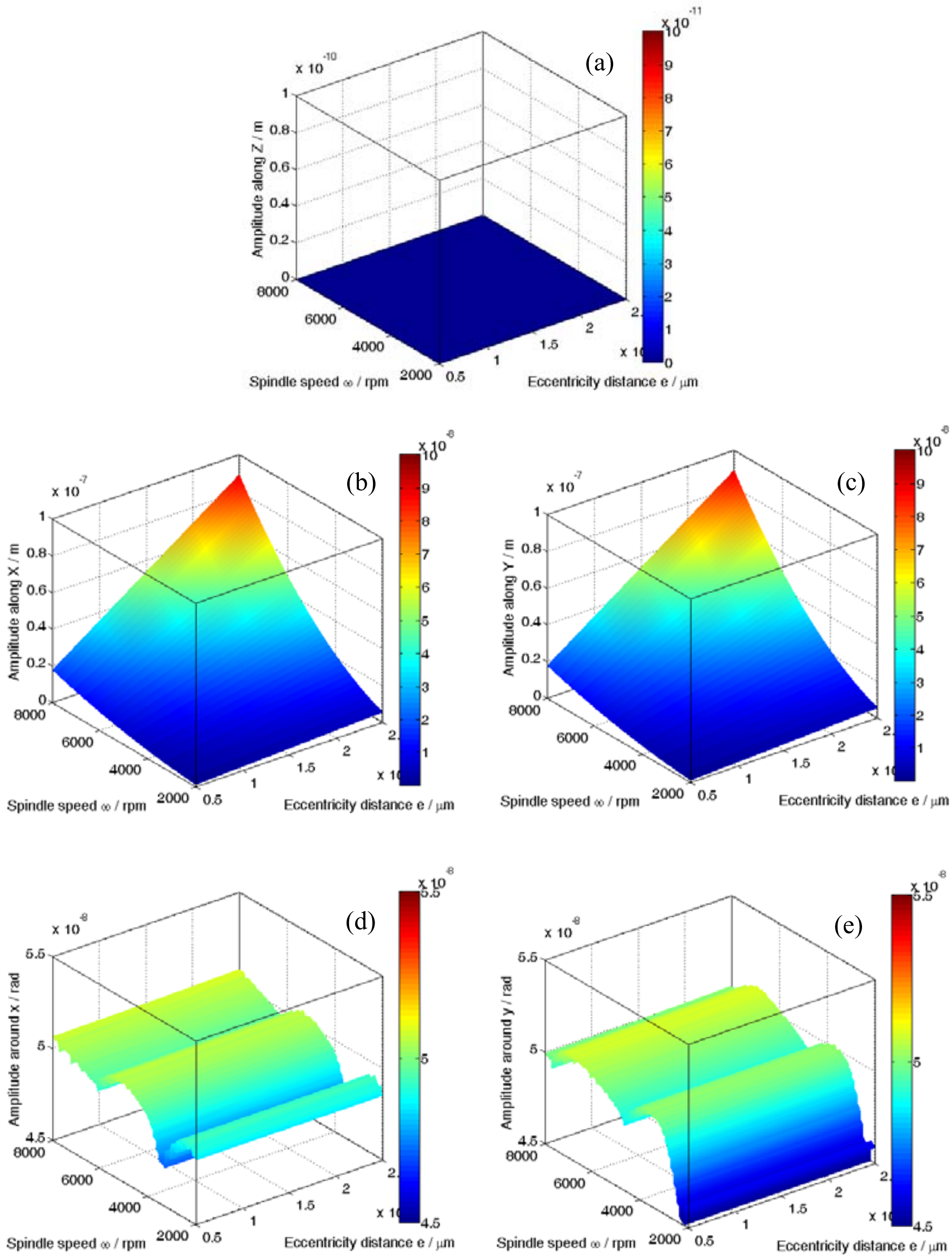

Figure 4.10 Effects of eccentric distances on amplitudes of spindle vibration combining the spindle speeds with the simulation parameters of Table 4.3 at the steady state for (a) the translational motion along the spin axis, (b) and (c) the translation motions along the radial axes, and (d) and (e) tilting motions deviating away from the spin axis

4.2.4 Influences of Cutting Forces with Spindle Speed on Vibration Amplitudes

This section discusses the influences of the cutting forces combined with the spindle speed on the amplitudes of spindle vibration. The spindle system is acted by a range of continuous cutting forces under variable spindle speeds. The parameters are inputted to the simulation of Matlab Simulink with the Dormand-Prince (ode45) method as tabulated in Table.4.4. The variables are the spindle speed and the cutting forces. The simulation results are shown in Figure 4.11 and Figure 4.12.

At the transient state, accompanying the increase of the cutting forces, the amplitude in the axial direction linearly rises but is not relevant to the spindle speed, as shown in Figure 4.11(a); the radial amplitudes slightly develop and are majorly influenced by the spindle speed, as shown in Figure 4.12(b) and (c), since the cutting forces are less than the inertial force, according to Eq.4-8; and the tilting amplitude linearly increases and is irrelevant to the spindle speed, as shown in Figure 4.11(d) and (e), which is explained by the Eq.4-35.

At the steady state, the spindle rotor moves in equilibrium due to damping and the equilibrium deviation is determined by the inertial force, the cutting forces and the moments. In Figure 4.12(a), the amplitude is close to zero and the deviation along the Z-axis can be computed by Eq.4-6; in Figure 4.12(b) and (c), the deviation is relative to the inertial forces determined by the spindle speed, whose profile per revolution is one circle in form; and in Figure 4.12(d) and (e), the tilting deviation around the x/y-axes is not influenced by the spindle speed, but with the increment of the cutting forces, it linearly rises. The results can be explained by Eq.4-8 and Eq.4-35. Therefore, Eq.4-8 and Eq.4-5 can be used to describe the spindle rotor motions of the system. It is inferred that surface roughness decreases with the reduction of the cutting forces. By decreasing the eccentric distance of the spindle (balancing the spindle), increasing the stiffness of the spindle or/and decreasing the cutting forces (depth of cut, feed rate etc.), it is beneficial for the effects of spindle vibration on surface topography.

Table 4.4 Spindle performance specifications with cutting forces in UPDT

Spindle rotor mass (m) (kg)	0.5
Radial stiffness (k_2/ k_3) (N/μm)	20
Axial stiffness (k_1) (N/μm)	25
Eccentric position of the mass imbalance away from the rotor axis (e) (μm)	1
Position of the centre of mass center relative to its equilibrium along the z-axis (l_1/ l_2) (mm)	50+5e / 50-5e
Radius of spindle rotor (R) (mm)	25
Inertial tensor around y-axis (J_z) (gm^2)	0.05
Inertial tensor around z/x-axis (J_x/J_y) (gm^2)	1.4
The distance of tilting center of spindle rotor to the tool tip (d_2) (mm)	60
The distance of tool tip away from the spindle axis in cutting (d_1) (mm)	3
Damper ratio μ	0.025
Angular damper ratio ξ	0.5×10^{-4}
Constant coefficient (k)	1, 2, 3, 4,5
Main cutting force (Fm) (k*N)	0.025
Thrust cutting force (Ft) (k*(N)	0.025
Feed cutting force (Fr) (k*N)	0.0015

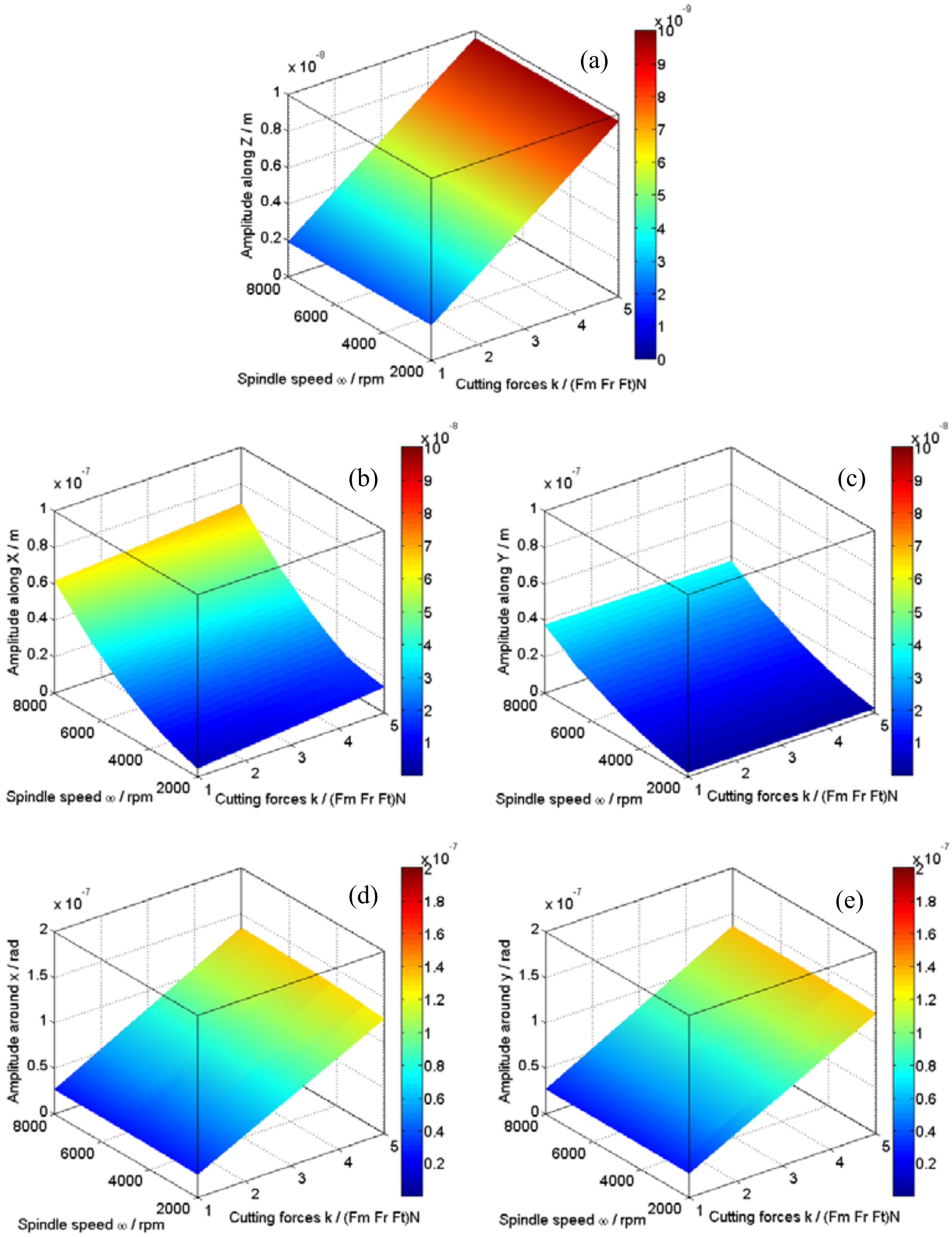

Figure 4.11 Effect of cutting forces (Fm=0.025 Fr=0.0015 Ft=0.025) on amplitude of spindle vibration combining the spindle speed with the simulation parameters of Table 4.4 at the transient state for (a) the translational motion along the spin axis, (b) and (c) the translation motions along the radial axes, and (d) and (e) the tilting motions deviating away from the spin axis

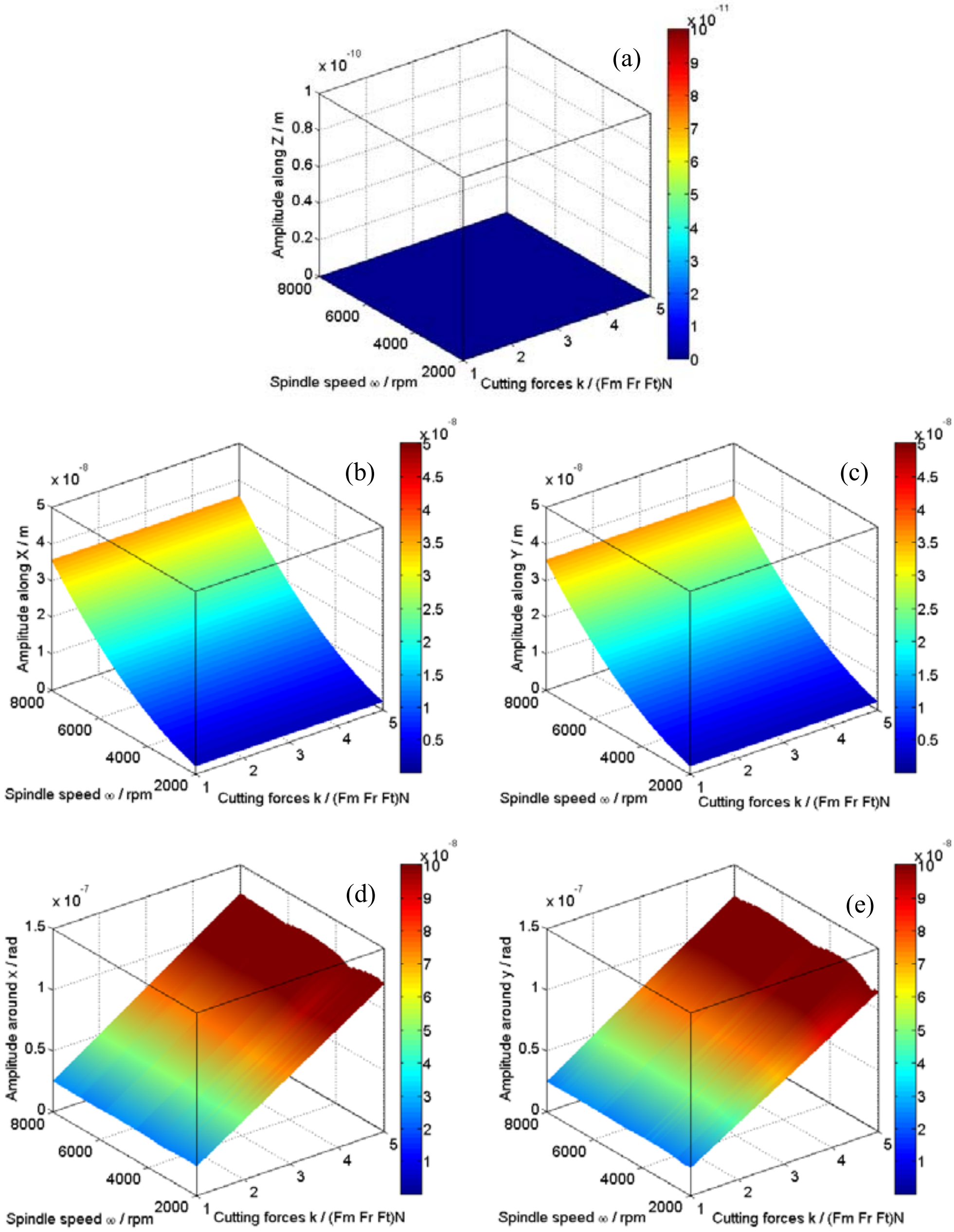

Figure 4.12 Effect of cutting forces (Fm=0.025 Fr=0.0015 Ft=0.025) on amplitude of spindle vibration combining the spindle speed with the simulation parameters of Table 4.4 at the steady state for (a) the translational motion along the spin axis, (b) and (c) the translation motions along the radial axes, and (d) and (e) the tilting motions deviating away from the spin axis

4.3 Dynamic Characteristics of Spindle Vibration in UPRM

4.3.1 Solutions of Spindle Motion Equations

Eq.3-26 presents the dynamic responses of the aerostatic bearing spindle system under a periodic pulse excitation of cutting forces of UPRM. It contains two parts: the translational motions and the tilting motions of the spindle rotor. Although the damping will dissipate the system energy, the sequent cutting forces in the form of a periodic pulse wave trigger the system. Therefore, the responses of the system are considered as the transient responses.

For the translational motions, according to Eq.3-26, the transient state equations are:

$$\begin{cases} m\ddot{y} + c_1\dot{y} + k_1 y = 0 \\ m\ddot{x} + c_2\dot{x} + k_2 x = 0 \\ m\ddot{z} + c_3\dot{z} + k_3 z = 0 \end{cases} \tag{4-38}$$

Since the contact time or duration of the intermittent cutting forces τ is very short, according to the momentum theorem, the initial velocity in the first period can be defined as Eq.4-39.

$$v = \frac{F\tau}{m} \tag{4-39}$$

Hence, the initial conditions for Eq.3-26 in the first period are:

$$\begin{cases} \dot{y}(0) = \dfrac{\{-F_r\}\tau}{m}, y(0) = 0 \\ \dot{x}(0) = \dfrac{\{-F_m\}\tau}{m}, x(0) = 0 \\ \dot{z}(0) = \dfrac{\{-F_t\}\tau}{m}, z(0) = 0 \end{cases} \tag{4-40}$$

Then, the transient solution in the first period for Eq.3-26 is:

$$\begin{cases} y(t)=\dfrac{\dfrac{\{-F_r\}\tau}{m}}{\omega_y\sqrt{1-\mu^2}}e^{-\mu\omega_y t}\sin(\omega_y\sqrt{1-\mu^2}t) \\ x(t)=\dfrac{\dfrac{\{-F_m\}\tau}{m}}{\omega_x\sqrt{1-\mu^2}}e^{-\mu\omega_x t}\sin(\omega_x\sqrt{1-\mu^2}t) \qquad t\in(0\quad T] \\ z(t)=\dfrac{\dfrac{\{-F_t\}\tau}{m}}{\omega_z\sqrt{1-\mu^2}}e^{-\mu\omega_z t}\sin(\omega_z\sqrt{1-\mu^2}t) \end{cases} \tag{4-41}$$

where $\begin{cases} \omega_y=\sqrt{\dfrac{k_1}{m}} \\ \omega_x=\sqrt{\dfrac{k_2}{m}} \\ \omega_z=\sqrt{\dfrac{k_3}{m}} \end{cases}$ and $\begin{cases} c_1=2\mu\sqrt{k_1 m} \\ c_2=2\mu\sqrt{k_2 m} \\ c_3=2\mu\sqrt{k_3 m} \end{cases}$.

Finally, the general solution can be defined as a sequential set of Eq.4-42.

$$\begin{cases} y(t)=e^{-\mu\omega_y(t-iT)}(y(iT)\cos(\omega_z\sqrt{1-\mu^2}(t-iT) \\ +\dfrac{\dot{y}(iT)+\dfrac{\{-F_r\}\tau}{m}+\mu\omega_y y(iT)}{\omega_y\sqrt{1-\mu^2}}\sin(\omega_y\sqrt{1-\mu^2}(t-iT))) \\ x(t)=e^{-\mu\omega_x(t-iT)}(x(iT)\cos(\omega_z\sqrt{1-\mu^2}(t-iT)) \\ +\dfrac{\dot{x}(iT)+\dfrac{\{-F_m\}\tau}{m}+\mu\omega_x x(iT)}{\omega_x\sqrt{1-\mu^2}}\sin(\omega_x\sqrt{1-\mu^2}(t-iT))) \qquad t\in(iT\quad (i+1)T] \\ z(t)=e^{-\mu\omega_z(t-iT)}(z(iT)\cos(\omega_z\sqrt{1-\mu^2}(t-iT)) \\ +\dfrac{\dot{z}(iT)+\dfrac{\{-F_t\}\tau}{m}+\mu\omega_z z(iT)}{\omega_z\sqrt{1-\mu^2}}\sin(\omega_z\sqrt{1-\mu^2}(t-iT))) \end{cases} \tag{4-42}$$

where i=0, 1,···, N.

For the tilting motions, according to Eq.3-26, the transient equations are:

$$\begin{cases} J_z\ddot{\theta}-(J_x-J_y)\omega\dot{\phi}+d_z\dot{\theta}+((k_2+k_3)(l_1^2+l_2^2)+k_1R^2)\theta=0 \\ J_x\ddot{\phi}+(J_z-J_y)\omega\dot{\theta}+d_x\dot{\phi}+((k_2+k_3)(l_1^2+l_2^2)+k_1R^2)\phi=0 \end{cases} \tag{4-43}$$

According to the angular momentum theorem, the initial angular velocities in the first period can be ideally defined as Eq.4-44, because of the short contact time of the cutting forces. And, the initial angular in the first period is Eq.4-45.

$$\begin{cases} \dot{\theta}(0) = \dfrac{F_m d_2}{J_z} \\ \dot{\phi}(0) = \dfrac{F_r d_1 - F_t d_2}{J_x} \end{cases} \tag{4-44}$$

$$\begin{cases} \theta(0) = 0 \\ \phi(0) = 0 \end{cases} \tag{4-45}$$

According to Eq.4-12 and Eq.4-13, the angular frequencies of the tilting motions of the spindle rotor are:

$$\omega_\phi = \sqrt{\frac{\omega_1^2 + \omega_2^2 + \dfrac{J_y - J_z}{J_x}\omega\dfrac{J_x - J_z}{J_y}\omega}{2} - \sqrt{\frac{(\omega_1^2 + \omega_2^2 + \dfrac{J_y - J_z}{J_x}\omega\dfrac{J_x - J_z}{J_y}\omega)^2 - (\omega_1\omega_2)^2}{2}}} \tag{4-46}$$

$$\omega_\theta = \sqrt{\frac{\omega_1^2 + \omega_2^2 + \dfrac{J_y - J_z}{J_x}\omega\dfrac{J_x - J_z}{J_y}\omega}{2} + \sqrt{\frac{(\omega_1^2 + \omega_2^2 + \dfrac{J_y - J_z}{J_x}\omega\dfrac{J_x - J_z}{J_y}\omega)^2 - (\omega_1\omega_2)^2}{2}}} \tag{4-47}$$

According to Section 4.2.1.2, the corresponding solution in the first period with its first order differential equation and its second order differential equation is expressed as:

$$\begin{cases} \phi = A_1 \sin\omega_\theta t + A_2 \cos\omega_\theta t + A_3 \sin\omega_\phi t + A_4 \cos\omega_\phi t + 0 \\ \theta = B_1 \cos\omega_\theta t + B_2 \sin\omega_\theta t + B_3 \cos\omega_\phi t + B_4 \sin\omega_\phi t + 0 \end{cases} \tag{4-48}$$

$$\begin{cases} \dot{\phi} = A_1\omega_\theta \cos\omega_\theta t - A_2\omega_\theta \sin\omega_\theta t + A_3\omega_\phi \cos\omega_\phi t - A_4\omega_\phi \sin\omega_\phi t \\ \dot{\theta} = -B_1\omega_\theta \sin\omega_\theta t + B_2\omega_\theta \cos\omega_\theta t - B_3\omega_\phi \sin\omega_\phi t + B_4\omega_\phi \cos\omega_\phi t \end{cases} \tag{4-49}$$

$$\begin{cases} \ddot{\phi} = -A_1\omega_\theta^2 \sin\omega_\theta t - A_2\omega_\theta^2 \cos\omega_\theta t - A_3\omega_\phi^2 \sin\omega_\phi t - A_4\omega_\phi^2 \cos\omega_\phi t \\ \ddot{\theta} = -B_1\omega_\theta^2 \cos\omega_\theta t - B_2\omega_\theta^2 \sin\omega_\theta t - B_3\omega_\phi^2 \cos\omega_\phi t - B_4\omega_\phi^2 \sin\omega_\phi t \end{cases} \tag{4-50}$$

Thus, the initial conditions in the first period are denoted as:

$$\begin{cases} \phi(t=0) = A_2 + A_4 = 0 \\ \theta(t=0) = B_1 + B_3 = 0 \end{cases} \tag{4-51}$$

$$\begin{cases} \dot{\phi}(t=0) = A_1\omega_\theta + A_3\omega_\phi = \dfrac{F_r d_1 - F_t d_2}{J_x} \\ \dot{\theta}(t=0) = B_2\omega_\theta + B_4\omega_\phi = \dfrac{F_m d_2}{J_z} \end{cases} \tag{4-52}$$

Substituting Eq.4-48, Eq.4-49 and Eq.4-50 into Eq.4-43, Eq.4-43 is expressed as:

$$\begin{cases} -B_1\omega_\theta^2\cos\omega_\theta t - B_2\omega_\theta^2\sin\omega_\theta t - B_3\omega_\phi^2\cos\omega_\phi t - B_4\omega_\phi^2\sin\omega_\phi t \\ -C_z(A_1\omega_\theta\cos\omega_\theta t - A_2\omega_\theta\sin\omega_\theta t + A_3\omega_\phi\cos\omega_\phi t - A_4\omega_\phi\sin\omega_\phi t) \\ +\omega_1^2(B_1\cos\omega_\theta t + B_2\sin\omega_\theta t + B_3\cos\omega_\phi t + B_4\sin\omega_\phi t) = 0 \\ -A_1\omega_\theta^2\sin\omega_\theta t - A_2\omega_\theta^2\cos\omega_\theta t - A_3\omega_\phi^2\sin\omega_\phi t - A_4\omega_\phi^2\cos\omega_\phi t \\ +C_x(-B_1\omega_\theta\sin\omega_\theta t + B_2\omega_\theta\cos\omega_\theta t - B_3\omega_\phi\sin\omega_\phi t + B_4\omega_\phi\cos\omega_\phi t) \\ +\omega_2^2(A_1\sin\omega_\theta t + A_2\cos\omega_\theta t + A_3\sin\omega_\phi t + A_4\cos\omega_\phi t) = 0 \end{cases} \tag{4-53}$$

$$\begin{cases} C_z = \dfrac{(J_x - J_y)\omega}{J_z} \\ D_z = \dfrac{d_z}{J_z} \\ \omega_1^2 = \dfrac{((k_2+k_3)(l_1{}^2 + l_2{}^2) + k_1R^2)}{J_z} \\ C_x = \dfrac{(J_z - J_y)\omega}{J_x} \\ D_x = \dfrac{d_x}{J_x} \\ \omega_2^2 = \dfrac{((k_2+k_3)(l_1{}^2 + l_2{}^2) + k_1R^2)}{J_x} \end{cases} \tag{4-54}$$

Eq.4-53 is a system of identity equations, not relevant to time t, so two linear systems of equations are obtained as Eq.4-55 and Eq.4-56. Since it is extremely tiny, the angular damper is ignored.

$$\begin{cases} -B_1\omega_\theta^2 - C_zA_1\omega_\theta + \omega_1^2B_1 = 0 \\ -B_2\omega_\theta^2 + C_zA_2\omega_\theta + \omega_1^2B_2 = 0 \\ -B_3\omega_\phi^2 - C_zA_3\omega_\phi + \omega_1^2B_3 = 0 \\ -B_4\omega_\phi^2 + C_zA_4\omega_\phi + \omega_1^2B_4 = 0 \end{cases} \tag{4-55}$$

$$\begin{cases} -A_1\omega_\theta^2 - C_x B_1 \omega_\theta + \omega_2^2 A_1 = 0 \\ -A_2\omega_\theta^2 + C_x B_2 \omega_\theta + \omega_2^2 A_2 = 0 \\ -A_3\omega_\phi^2 - C_x B_3 \omega_\phi + \omega_2^2 A = 0 \\ -A_4\omega_\phi^2 + C_x B_4 \omega_\phi + \omega_2^2 A_4 = 0 \end{cases} \tag{4-56}$$

Combining Eq.4-51, Eq.4-52 with Eq.4-55, the corresponding coefficients of Eq.4-48 are:

$$\begin{cases} A_1 = \dfrac{(F_r d_1 - F_t d_2)((\omega_\phi^2 - \omega_\theta^2)\omega_2^2 - (\omega_\theta^2 - \omega_2^2)\omega_\phi^2)}{J_x \omega_\theta (\omega_\phi^2 - \omega_\theta^2)\omega_2^2} \\ A_2 = -\dfrac{C_x F_m d_2}{J_z(\omega_\phi^2 - \omega_\theta^2)(\omega_\phi^2 - \omega_2^2)} \\ A_3 = \dfrac{(F_r d_1 - F_t d_2)(\omega_\theta^2 - \omega_2^2)\omega_\phi}{J_x(\omega_\phi^2 - \omega_\theta^2)\omega_2^2} \\ A_4 = \dfrac{C_x F_m d_2}{J_z(\omega_\phi^2 - \omega_\theta^2)(\omega_\phi^2 - \omega_2^2)} \\ B_1 = \dfrac{(F_r d_1 - F_t d_2)(\omega_\phi^2 - \omega_2^2)(\omega_\theta^2 - \omega_2^2)}{J_x C_x (\omega_\phi^2 - \omega_\theta^2)\omega_2^2} \\ B_3 = -\dfrac{(F_r d_1 - F_t d_2)(\omega_\phi^2 - \omega_2^2)(\omega_\theta^2 - \omega_2^2)}{J_x C_x (\omega_\phi^2 - \omega_\theta^2)\omega_2^2} \\ B_2 = \dfrac{F_m d_2}{J_z \omega_\theta (\omega_\phi^2 - \omega_\theta^2)}((\omega_\phi^2 - \omega_\theta^2) - 1) \\ B_4 = \dfrac{F_m d_2}{J_z \omega_\phi (\omega_\phi^2 - \omega_\theta^2)} \end{cases} \tag{4-57}$$

Finally, the general solutions are:

$$\begin{cases} \phi = A_1 \sin \omega_\theta (t - iT) + A_2 \cos \omega_\theta (t - iT) \\ + A_3 \sin \omega_\phi (t - iT) + A_4 \cos \omega_\phi (t - iT) \\ \theta = B_1 \cos \omega_\theta (t - iT) + B_2 \sin \omega_\theta (t - iT) \\ + B_3 \cos \omega_\phi (t - iT) + B_4 \sin \omega_\phi (t - iT) \end{cases} \tag{4-58}$$

where, $t \in (iT \quad (i+1)T]$ and

$$
\begin{cases}
A_1 = \dfrac{-\theta(iT)(\omega_\theta^2-\omega_1^2)(\omega_\phi^2-\omega_1^2)+C_z(\omega_1^2-\omega_\theta^2)(\dot{\phi}(iT)+\dfrac{F_r d_1 - F_t d_2}{J_x})}{C_z\omega_\theta(\omega_\phi^2-\omega_\theta^2)} \\
A_2 = \phi(iT) - \dfrac{\dot{\theta}(iT)(\omega_\phi^2-\omega_1^2)+\dfrac{F_m d_2 \omega_\theta}{J_z}(\omega_\theta^2-\omega_1^2)+C_z\omega_\theta^2\phi(iT)}{C_z(\omega_\theta^2-\omega_\phi^2)\omega_1^2}(\omega_\phi^2-\omega_1^2) \\
A_3 = \dfrac{\theta(iT)(\omega_\theta^2-\omega_1^2)(\omega_\phi^2-\omega_1^2)+C_z(\omega_\phi^2-\omega_1^2)(\dot{\phi}(iT)+\dfrac{F_r d_1 - F_t d_2}{J_x})}{C_z\omega_\phi(\omega_\phi^2-\omega_\theta^2)} \\
A_4 = \dfrac{\dot{\theta}(iT)(\omega_\phi^2-\omega_1^2)+\dfrac{F_m d_2 \omega_\theta}{J_z}(\omega_\theta^2-\omega_1^2)+C_z\omega_\theta^2\phi(iT)}{C_z(\omega_\theta^2-\omega_\phi^2)\omega_1^2}(\omega_\phi^2-\omega_1^2) \\
B_1 = \dfrac{\theta(iT)(\omega_\phi^2-\omega_1^2)+C_z(\dot{\phi}(iT)+\dfrac{F_r d_1 - F_t d_2}{J_x})}{(\omega_\phi^2-\omega_\theta^2)} \\
B_2 = \dfrac{\dot{\theta}(iT)(\omega_\theta^2\omega_1^2-\omega_\phi^2\omega_\phi^2)+\dfrac{F_m d_2 \omega_\theta}{J_z}\omega_\theta^2(\omega_1^2-\omega_\phi^2)-C_z\omega_\phi^2\omega_\theta^2\phi(iT)}{\omega_\theta(\omega_\theta^2-\omega_\phi^2)\omega_1^2} \\
B_3 = -\dfrac{\theta(iT)(\omega_\theta^2-\omega_1^2)+C_z(\dot{\phi}(iT)+\dfrac{F_r d_1 - F_t d_2}{J_x})}{(\omega_\phi^2-\omega_\theta^2)} \\
B_4 = \dfrac{\dot{\theta}(iT)(\omega_\phi^2-\omega_1^2)+\dfrac{F_m d_2 \omega_\theta}{J_z}(\omega_\theta^2-\omega_1^2)+C_z\omega_\theta^2\phi(iT)}{(\omega_\theta^2-\omega_\phi^2)\omega_1^2}\omega_\phi
\end{cases}
\tag{4-59}
$$

with the corresponding initial conditions as:

$$
\begin{cases}
\phi(t=iT) = A_2 + A_4 = \phi(iT) \\
\theta(t=iT) = B_1 + B_3 = \theta(iT)
\end{cases}
\quad t \in (iT \quad (i+1)T]
\tag{4-60}
$$

$$
\begin{cases}
\dot{\phi}(t=iT) = A_1\omega_\theta + A_3\omega_\phi = \dot{\phi}(iT) + \dfrac{F_r d_1 - F_t d_2}{J_x} \\
\dot{\theta}(t=iT) = B_2\omega_\theta + B_4\omega_\phi = \dot{\theta}(iT) + \dfrac{F_m d_2}{J_z}
\end{cases}
\quad t \in (iT \quad (i+1)T]
\tag{4-61}
$$

The above equations present the dynamic responses of the spindle under the intermittent excitation of the cutting forces, using the mathematical formulas. It implies that the spindle vibration will play a significant role in influencing surface topography, since one tiny part of the profile of the spindle vibration will be formed at the milled surface. The mathematical equations can be developed to predict the effects of the spindle vibration on surface topography and optimize the cutting conditions to improve surface quality in UPRM.

Table 4.5 Spindle performance specifications with cutting forces in UPRM

Spindle rotor mass (m) (kg)	2.5
Radial stiffness (k_2/ k_3) (N/µm)	22
Axial stiffness (k_1) (N/µm)	31
Eccentric position of the mass imbalance away from the rotor axis (e) (µm)	0
Position of the centre of mass center relative to its equilibrium along the z-axis (l_1/ l_2) (mm)	100
Radius of spindle rotor (R) (mm)	25
Inertial tensor around y-axis (J_y) (gm^2)	0.25
Inertial tensor around z/x-axis (J_x/J_z) (gm^2)	15.03
The distance of tilting center of spindle rotor to the tool tip (d_2) (mm)	180
The distance of tool tip away from the spindle axis (Swing distance) (d_1) (mm)	23
Damper ratio μ	0.025
Angular damper ratio ξ	0.5×10^{-4}
Main cutting force (Fm) (N)	0.05
Thrust cutting force (Ft) (N)	0.05
Feed cutting force (Fr) (N)	0.003

Table 4.6 Cutting conditions of UPRM

Spindle speed (ω) (rpm)	4000
Feed rate (f_r) (mm/min)	60
Depth of cut (d_o) (µm)	3
Swing distance (d_1) (mm)	23
Step distance (s_r) (µm)	10
Tool nose radius (R_r) (mm)	0.78
Tool rake angle (^{o})	0
Front clearance angle (^{o})	15
Cutting strategy	Horizontal cutting / Vertical cutting

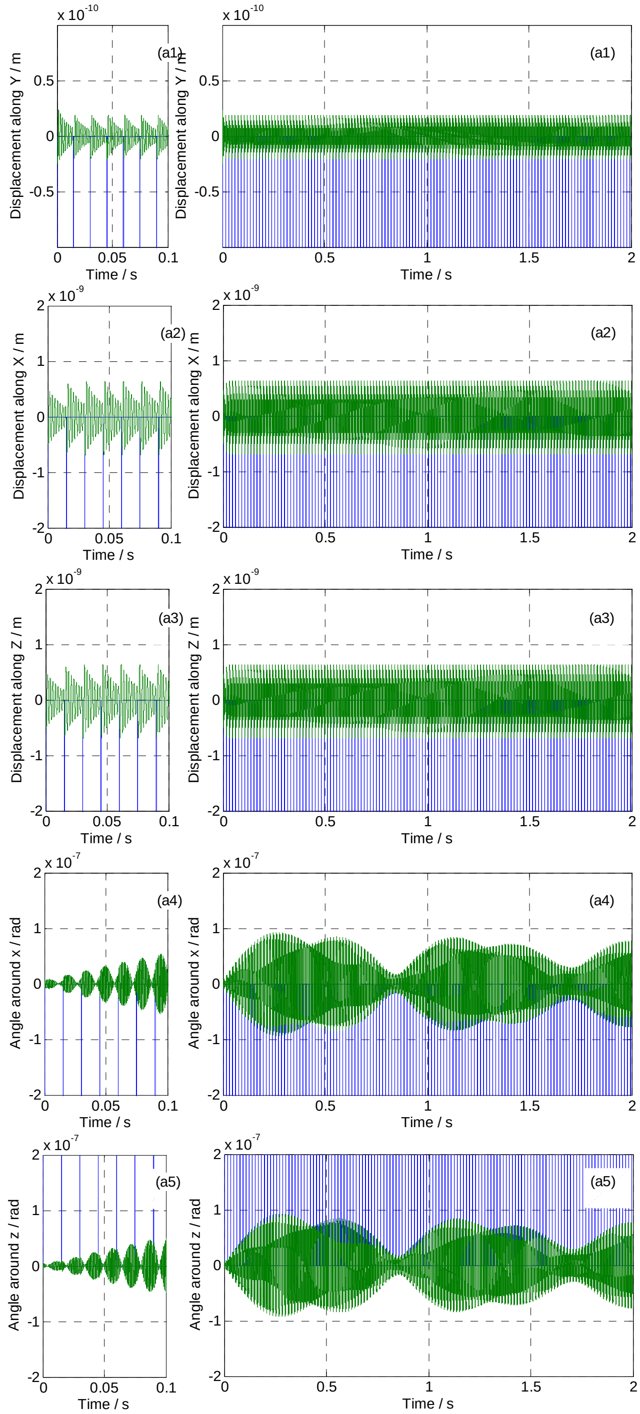

Figure 4.13 Dynamic responses of the spindle applied by intermittent cutting forces of Table 4.5 under the spindle specifications of Table 4.5 and the cutting conditions of Table 4.6: (a1) the axial motion along the *Y*-axis, (a2) the radial motion along the *X*-axis, (a3) the radial motion along the *Z*-axis, (a4) the tilting motion around the *x*-axis and (a5) the tilting motion around the *z*-axis

4.3.2 Dynamic Responses of the Spindle under Intermittent Cutting Forces

The numerical simulation is carried out to obtain numerical responses of spindle vibration. For this study, the spindle of the UPRM machine Precitech Freeform 705G is employed with the performance specifications provided by the machine tool manufactures, as listed in Table 4.5. Matlab Simulink of the Dormand-Prince method is used for its dynamic equations of Eq.3-26 before being linearized. The cutting conditions are listed in Table 4.6. The results are plotted in Figure 4.13.

Figure 4.13(a1) demonstrates that the axial motion of the spindle along the *Y*-axial direction is almost zero. Figure 4.13(a2) and Figure 4.13(a3) plot the radial motions of the spindle along the *X*-axial direction and the *Z*-axial direction, respectively. Figure 4.13(a4) and Figure 4.13(a5) present the tilting motions around the *x*-axial direction and the *z*-axial direction, respectively. They show that the spindle rotor is excited by the intermittent cutting forces at an extremely short contact time without the centrifugal force and then freely vibrates with damping. The contact time is less than one quarter of one period of the spindle vibration.

4.3.3 Influences of Intermittent Cutting Forces with Spindle Speed

In the cutting process, dynamic responses of the spindle are mainly influenced by cutting forces, spindle speed and depth of cut. The contact time in milling is relative to spindle speed, swing distance and depth of cut, computed by $60 \times \arccos((d_1 - d_0)/d_1)/\pi/\omega$. The spindle speed influences the tilting frequencies of the spindle. More importantly, if the cutting forces at the short contact time synchronously excited the system, the excitation would promote the vibration. In this section, the effects of the intermittent cutting forces and the spindle speeds on the vibration amplitudes of the spindle are majorly discussed, employing Matlab Simulink with the Dormand-Prince method. The spindle performance specifications are listed in

Table 4.5 and the cutting conditions are tabulated in Table 4.6.

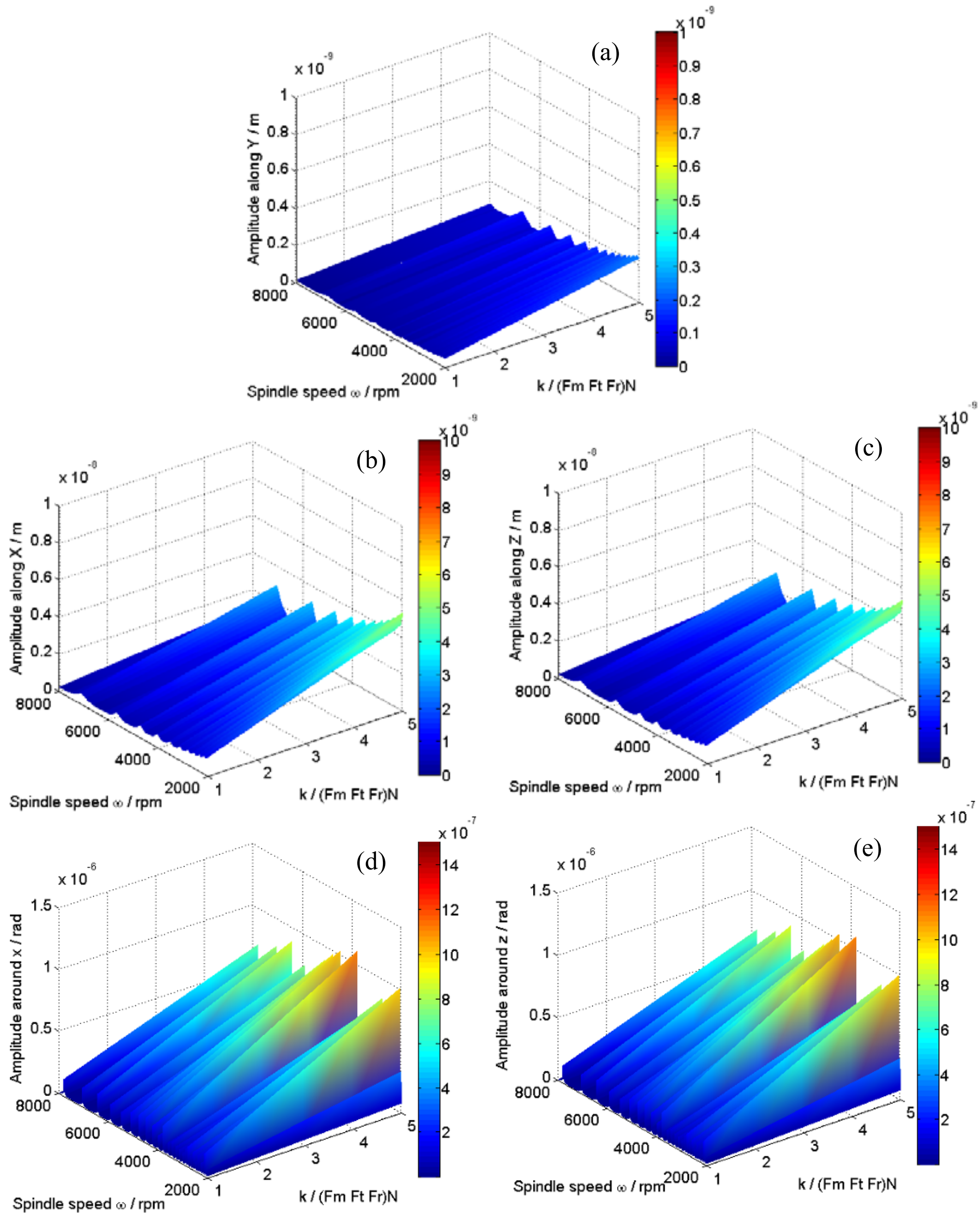

Figure 4.14 Vibration amplitudes of the spindle at different spindle speeds with different cutting forces k (Fm=0.025, Ft=0.025 and Fr=0.0015) with damping (a) along the *Y*-axis, (b) along the *X*-axis, (c) along the *Z*-axis, (d) around the *x*-axis and (e) around the *z*-axis

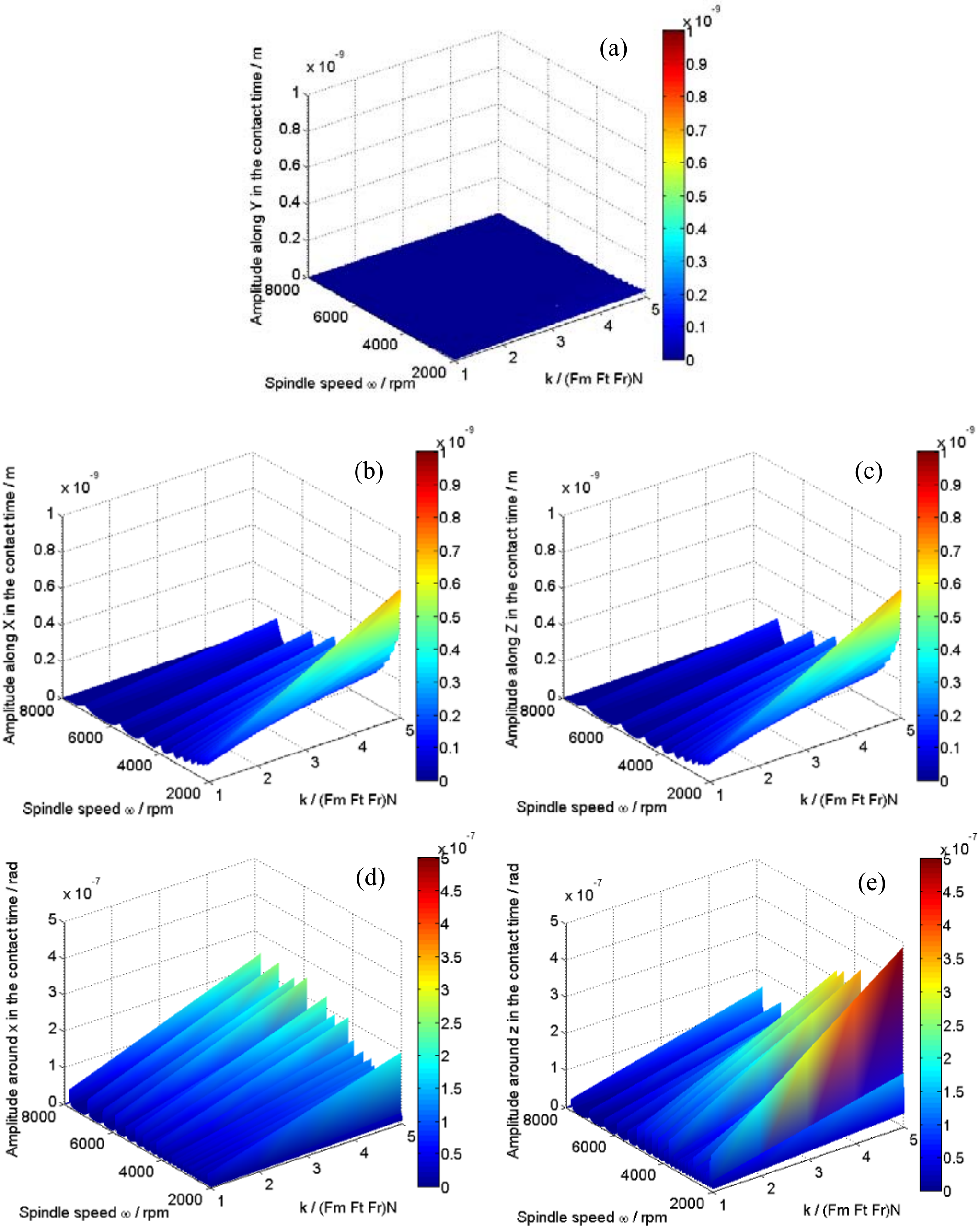

Figure 4.15 Vibration amplitudes in contact time at different spindle speeds with different cutting forces k (Fm=0.025, Ft=0.025 and Fr=0.0015) with damping (a) along the *Y*-axis, (b) along the *X*-axis, (c) along the *Z*-axis, (d) around the *x*-axis and (e) around the *z*-axis

The simulation results are shown in Figure 4.14 and Figure 4.15. Figure 4.14 maps the vibration amplitudes of spindle along the *Y*-axis, the *X*-axis and the *Z*-axis, and around the *x*-axis and around the *z*-axis under the different spindle speed and the cutting forces. Figure 4.15 shows the vibration amplitudes of the spindle along the *Y*-axis, the *X*-axis and the *Z*-axis, and around the *x*-axis and around the *z*-axis under the different spindle speed and cutting forces in the contact time. They show that the cutting forces linearly increase the vibration amplitudes and the spindle speed increases the vibration amplitudes. Furthermore, the minimal vibration amplitudes can be obtained at certain higher spindle speeds. The vibration trajectory in each contact time in milling is directly positioned into surface generation through tool loci generating inhomogeneous scallops. This infers that the cutting conditions corresponding to the minimal vibration amplitudes can be helpful to improve surface quality.

4.3.4 Influences of Depths of Cut with Spindle Speed

In this section, the contact time in milling with different spindle speeds influencing the vibration amplitudes of the spindle is studied. According to the previous section, the contact time is only influenced by the spindle speed and the depths of cut as shown in Table 4.5 and Table 4.6. The effects of depths of cut on the cutting forces are not considered in this simulation. The contact time is calculated by $60 \times \arccos((d_1 - d_0)/d_1)/\pi/\omega$. The simulated results are plotted in Figure 4.16 and Figure 4.17. Figure 4.16 demonstrates the vibration amplitudes of the spindle along the *Y*-axis, the *X*-axis and the *Z*-axis, and around the *x*-axis and around the *z*-axis under the different spindle speeds and depths of cut in the contact time. As the depth of cut increases, the vibration amplitudes quasi-linearly increase, and the spindle speed makes the vibration amplitudes fluctuate. It is interesting to note that by choosing a certain high spindle speed the vibration is minimal to achieve.

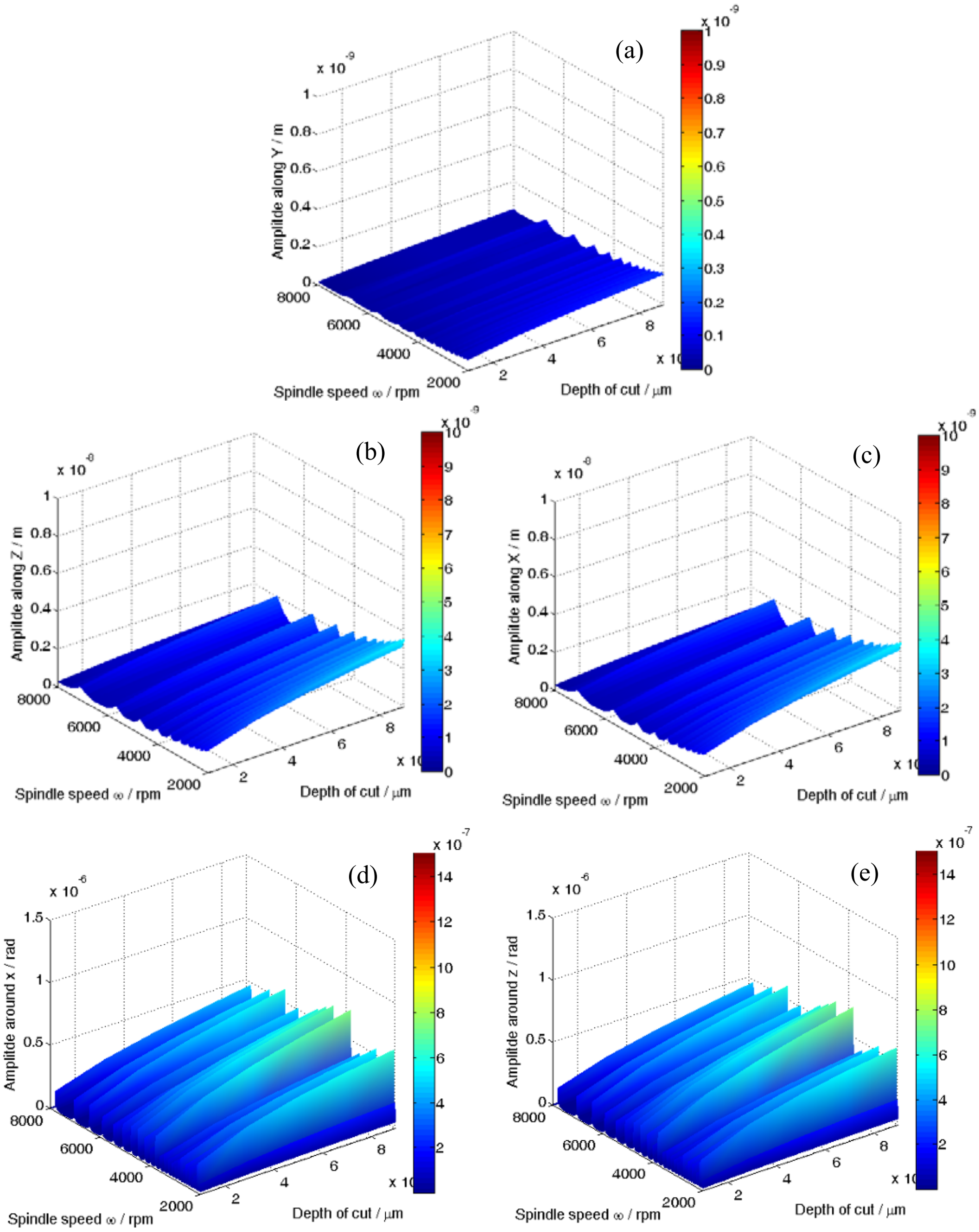

Figure 4.16 Vibration amplitudes of spindle at different spindle speeds with different depths of cut (a) along the *Y*-axis, (b) along the *X*-axis, (c) along the *Z*-axis, (d) around the *x*-axis and (e) around the *z*-axis

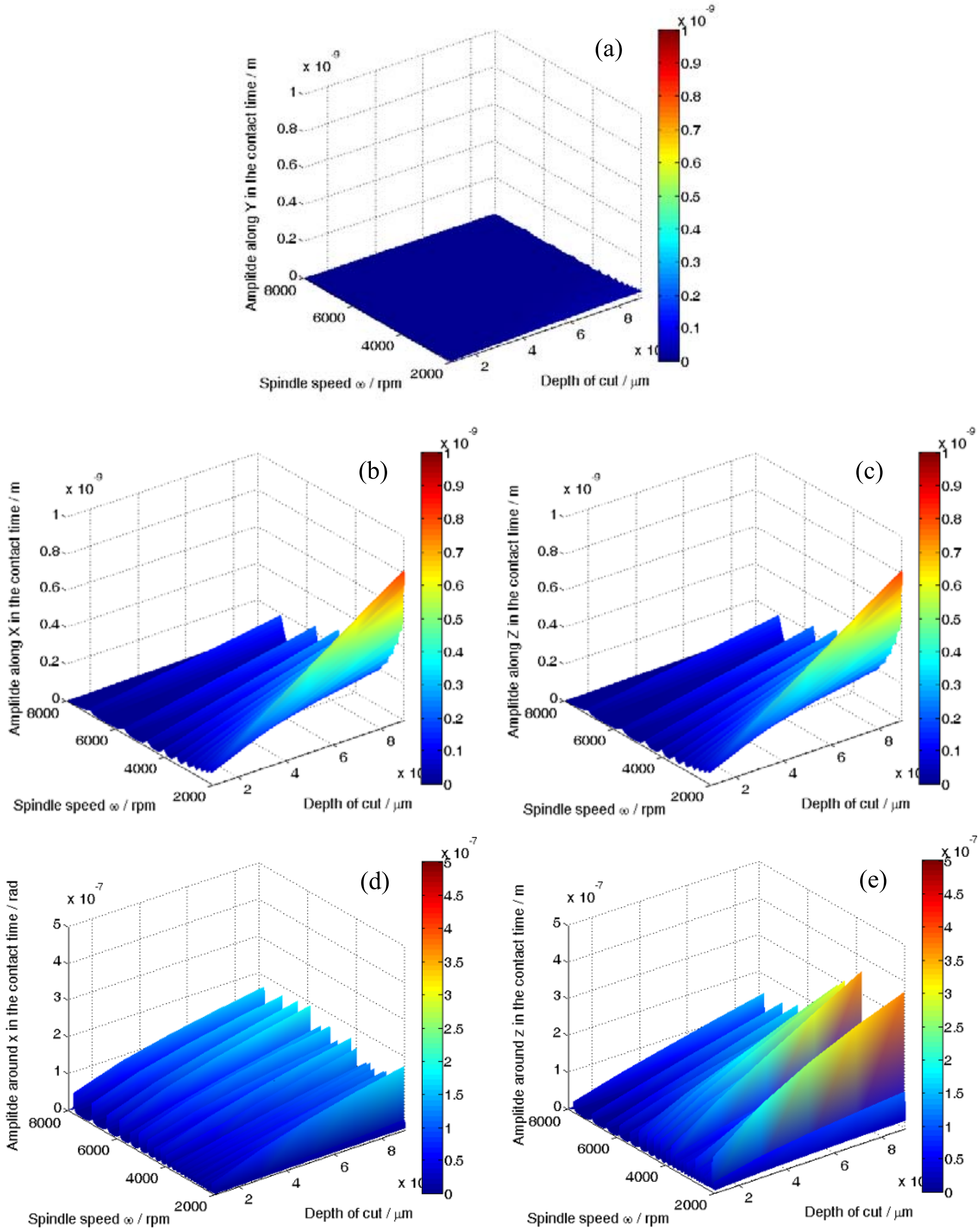

Figure 4.17 Vibration amplitudes in contact time at different spindle speeds with different depths of cut (a) along the *Y*-axis, (b) along the *X*-axis, (c) along the *Z*-axis, (d) around the *x*-axis and (e) around the *z*-axis

4.4 Summary

This chapter discusses the dynamic characteristics of the aerostatic bearing spindle in UPM and successfully provides the analytic solutions for its dynamic responses under different cutting parameters in UPM. The solutions can provide an effective means for predicting and optimizing surface generation in UPM. Furthermore, the effects of external conditions such as spindle speed, eccentric distance, cutting forces, and depths of cut, on the dynamic responses of spindle vibration in UPDT and UPRM have been discussed. A better understanding of dynamic characteristics of an aerostatic bearing spindle in UPM is provided. The content comprises the analytic solutions for the linearized dynamic equations for the aerostatic bearing spindle of UPM excited by the cutting force, the formulas on the frequency characteristics of the aerostatic bearing spindle and the numerical simulation for the dynamic model of the spindle with Matlab Simulink. The major findings are summarized as below:

(i) Since the linearized dynamic equations of the aerostatic bearing spindle in UPM in Chapter 3 represent the developed five-degree-of-freedom dynamic model, the corresponding solutions are derived to present the dynamic responses of the aerostatic bearing spindle.

(ii) The analytic solutions and the numerical simulations provide the multiple frequency characteristics, involving the axial natural frequency for the translational motion in the axial direction, the radial natural frequencies for the translational motions along the radial directions and the coupled tilting natural frequencies (CTFs) for the tilting motions around the radial directions producing the dynamic responses of the "beating" phenomena as observed in the waveform. The frequencies will be influenced by variable damping.

(iii) In UPDT, the cutting forces and the eccentric distances linearly impact on the translational motions of the spindle, the spindle speed leads a quadratic influence on the translational motions, and the cutting forces linearly affect the tilting motions, whereas the effects of the eccentric distance and the spindle speed on the tilting motions are negligible.

(iv) In UPRM, the cutting forces and the depths of cut have linear effects upon the dynamic responses of the spindle, and the spindle speed contributes to the quasi-periodic fluctuation in the vibration amplitudes of the dynamic responses of the spindle. In addition, the optimal selection of the spindle speed can effectively reduce the vibration amplitudes to a minimum.

(v) The excitation frequency of the intermittent cutting forces of UPRM, i.e. the spindle rotational frequency (SRF), plays a deterministic role in the effects influencing the dynamic responses of the spindle vibration of UPRM.

Chapter 5 Prediction and Optimization of Surface Generation in UPM

5.1 Introduction

The surface generation technique is a powerful tool to analyze surface topography in machining. The basic surface formation mechanism is the geometric intersection between the trace of the tool cutting edge with the workpiece through the material removal mechanics, i.e. the tool loci at the machined surface. Many scholars (C. F. Cheung, S. To, M. N. Cheng, M. C. Kong, L. B. Kong, S. J. Wang, etc.) have developed and made use of the method to produce surface topography, predict surface roughness and optimize surface generation in ultra-precision machining (UPM).

In this chapter, a surface generation model is firstly proposed to generate surface topographies, integrated with the spindle vibration in UPM. Secondly, the effects of the spindle vibration on surface topographical generation are discussed. Thirdly, the prediction model for the effects of spindle vibration on surface topography in UPM is provided and the corresponding optimization strategies on surface topographical generation are given.

5.2 Surface Generation in UPDT

In this section, an ideal surface topography model is presented to simulate surface generation under various cutting conditions in ultra-precision diamond turning (UPDT) (as shown in Figure 3.1), not taking into consideration other factors influencing surface topography, such as material pile-up, material swelling and recovery, tool-tip vibration, except spindle vibration. The successful development of the surface generation model allows explanation for the surface topography generation in the UPDT cutting process and is essential for the better understanding of cutting mechanisms.

5.2.1 Modeling of Surface Generation

In the model developed for this research, it is assumed that the cutting process is orthogonal, the workpiece materials are homogeneous and isotropic, and the material is geometrically removed. In the cutting process of face turning, surface topography can be separated into two parts: one is a spiral path of a tool arc center rotating along the spindle axis Z-axis and the other is a surface profile influenced by a tool arc in the radial direction ρ-axis, as shown in Figure 5.1. In Figure 5.1(a), the spiral trajectory $A(\varphi(t), \rho(t), Z(t))$ of the tool arc center can be described in the φ-ρ-Z coordinates as:

$$A(\varphi(t), \rho(t), Z(t)) = A(2\pi \cdot \omega \cdot t, \omega \cdot f_r \cdot t, Z(t)) \tag{5-1}$$

where ω is the spindle speed, f_r is the feed rate of the tool, t is the time, and $Z(t)$ is the relative distance between the tool and the workpiece, which is expressed by:

$$\begin{aligned} &Z(t) = a_z \cdot \sin(2\pi \cdot f_z \cdot t + \alpha_z) \\ &+ d_1 \cdot \sin(a_\theta \cdot \sin(2\pi \cdot f_\theta \cdot t + \alpha_\theta) + a_\phi \cdot \sin(2\pi \cdot f_\phi \cdot t + \alpha_\phi) + a_f \cdot \sin(2\pi \cdot f \cdot t + \alpha_f)) \end{aligned} \tag{5-2}$$

where d_1 represents the distance between the tool tip and the Z-axis, f_z, f_θ and f_ϕ are the axial and coupled tilting frequencies (CTFs) of the spindle rotor influencing the relative distance, f is the spindle rotational frequency (SRF) corresponding to ω, a_z, a_ϕ, a_θ and a_f are the corresponding amplitudes of these frequencies, and α_z, α_ϕ, α_θ and α_f are the corresponding phase of the vibration, respectively. The effect of the frequencies f_x and f_y in the radial directions on surface topography is extremely tiny so that it is ignored. In Figure 5.1(b), the surface profile between two adjacent points A_1 and A_2 of the spiral trajectory in the radial direction can be expressed as:

$$Z_1(t_1) + (1 - R_r \cdot \cos(\alpha)) \text{ and } Z_2(t_2) + (1 - R_r \cdot \cos(\beta)) \text{ , } t_2 = t_1 + \frac{1}{\omega} \tag{5-3}$$

$$\alpha = 0 \sim \frac{\pi}{2} + \arctan(\frac{Z_2 - Z_1}{f_r}) - \arccos\frac{\sqrt{f_r^2 + (Z_2 - Z_1)^2}}{2R_r} \tag{5-4}$$

$$\beta = 0 \sim \frac{\pi}{2} - \arctan(\frac{Z_2 - Z_1}{f_r}) - \arccos\frac{\sqrt{f_r^2 + (Z_2 - Z_1)^2}}{2R_r} \tag{5-5}$$

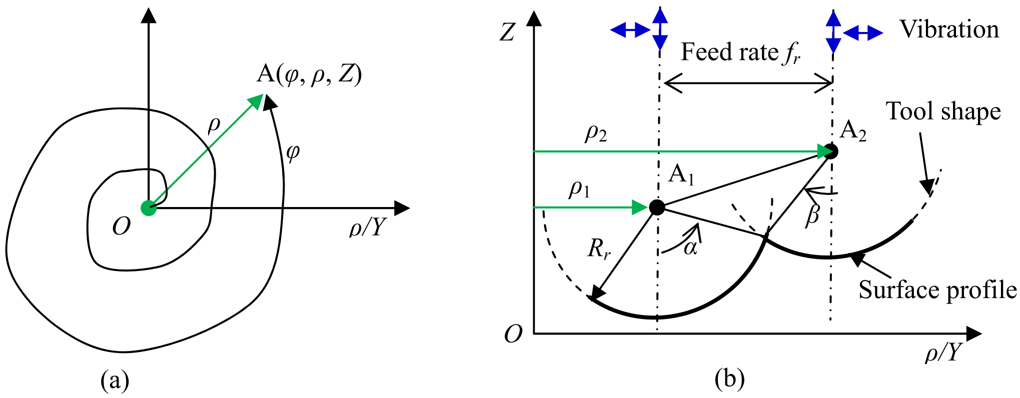

Figure 5.1 Schematic diagram of surface generation (a) a tool spiral trajectory and (b) a surface profile in the radial direction

5.2.2 Results of Surface Generation

Under the ideal cutting conditions of Table 5.1, the surface topography is formed by the spiral trajectory of the tool tip profile at intervals of feed per revolution, combining the spindle-induced vibration affecting the spiral trajectory, which is considered as the distance between the workpiece fixed on the spindle rotor and the tool.

Table 5.1 Cutting conditions in UPDT

Spindle speed (ω) (rpm) / the SRF (f) (Hz)	3000 / 50
Feed rate (f_r) (mm/rev)	0.005
Depth of cut (Doc) (µm)	5
Tool nose radius (R_r) (mm)	0.762
Tool rake angle (^{o})	0
Front clearance angle (^{o})	15

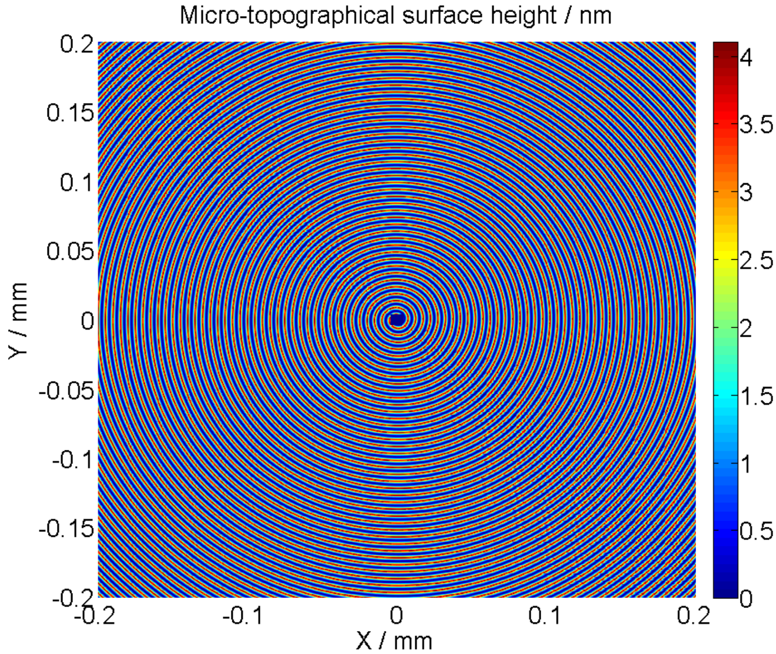

Figure 5.2 Simulated surface topography at the sample center without vibration under the cutting conditions of Table 5.1

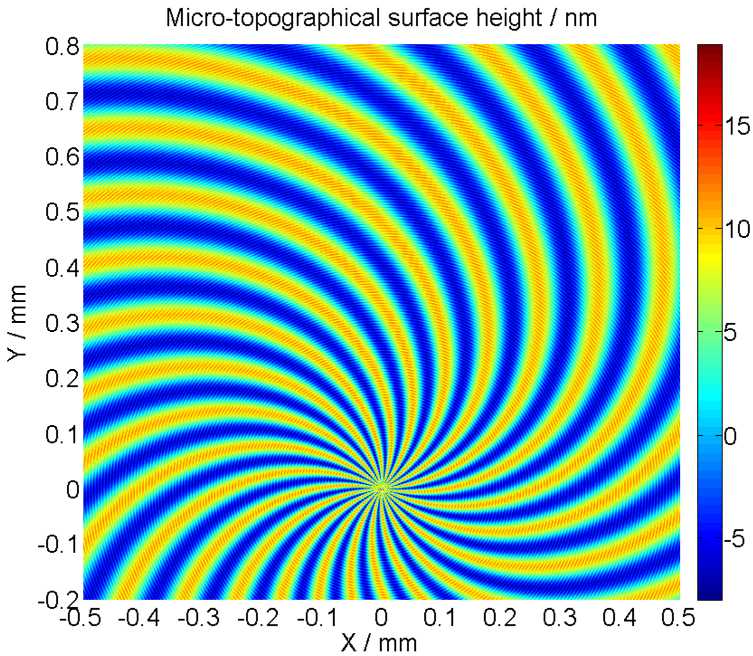

Figure 5.3 Simulated surface topography at the sample center under the cutting conditions of Table 5.1 with the vibration at the frequency of 1098.3 and the amplitude of 8nm

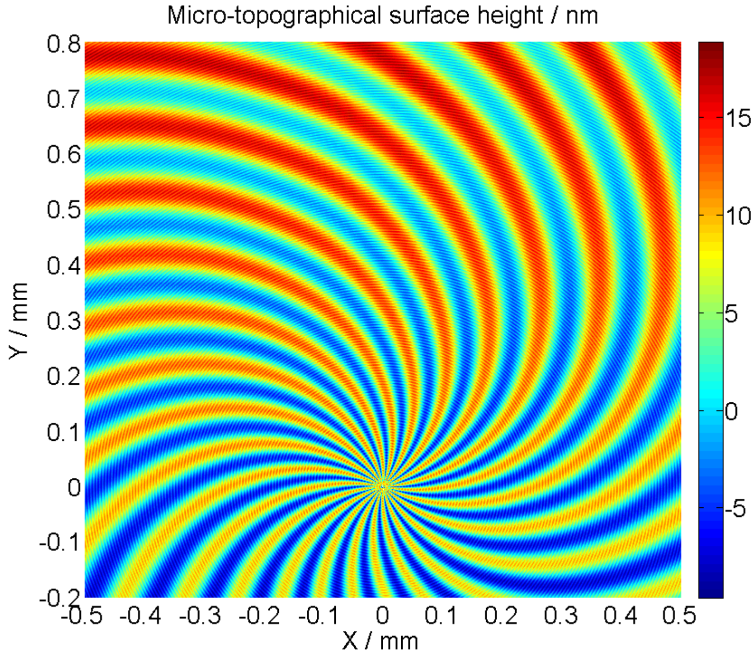

Figure 5.4 Simulated surface topography at the sample center under the cutting conditions of Table 5.1 with the vibration at the frequency of 1098.3Hz and the amplitude of 8nm and at the SRF of 50Hz and the amplitude of 8nm

5.2.2.1 Surface Topography

According to the above surface generation model, surface topographies are formed under the cutting conditions tabulated in Table 5.1. Based on the previous theoretical results of the spindle vibration in Chapter 4, when surface topography is generated at the center of a surface, the axial vibration of the spindle without the tilting vibration induced by the harmonic torques is only considered. And when the surface topography is formed away from the center of a surface, the tilting vibration induced by the harmonic moments of cutting forces is considered. Figure 5.2 shows that a surface topography at the center is generated by the spiral tool mark under the cutting conditions without vibration. In Figure 5.2, a surface topography at the center is generated by combining the axial vibration with the surface topography shown in Figure 5.3. Spiral and radial patterns are formed at the surface topography. Figure 5.4

presents a surface topography in the center formed by adding the axial vibration and the harmonic tilting induced by the moment of the cutting forces acting the spindle rotor. The harmonic frequency is the SRF. It shows spiral, radial and two-fold patterns at the surface.

Moreover, a series of simulated surface generations are conducted at a distance of 3mm away from the surface center under the cutting conditions of Table 5.1 with/without the vibration at the tilting frequencies of 2001Hz, 1953Hz and 50Hz corresponding to the amplitudes of 8nm. Figure 5.5 shows a surface formed by the tool mark without the vibration. Figure 5.6 exhibits periodic concentric, spiral and radial patterns (PCSRPs) generated at the surface under the cutting conditions of Table 5.1 with the vibration at the coupled tilting frequencies (CTFs) of 2001Hz and 1953Hz and the amplitudes of 8nm. Figure 5.7 displays the patterns formed at the surface under the cutting conditions of Table 5.1 with the vibration at the CTFs of 2001Hz and 1953Hz and the SRF of 50Hz and the amplitudes of 8nm. But the tilted surface in Figure 5.7 induced by the SRF is not observed, since the simulated area is away from the surface center. The PCSRPs are also formed in Figure 5.6. The results reveal that the spindle vibration produces different kinds of surface topographical patterns at the machined surface.

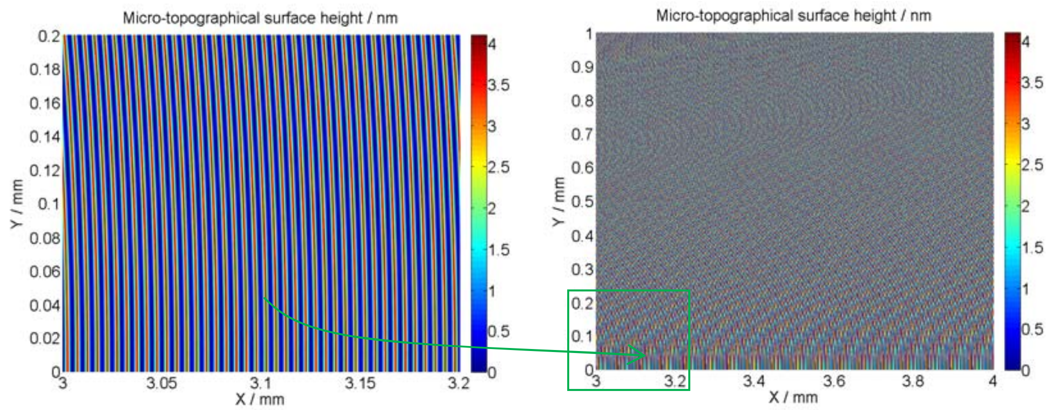

Figure 5.5 Simulated surface topography away from the surface center under the cutting conditions of Table 5.1 without vibration

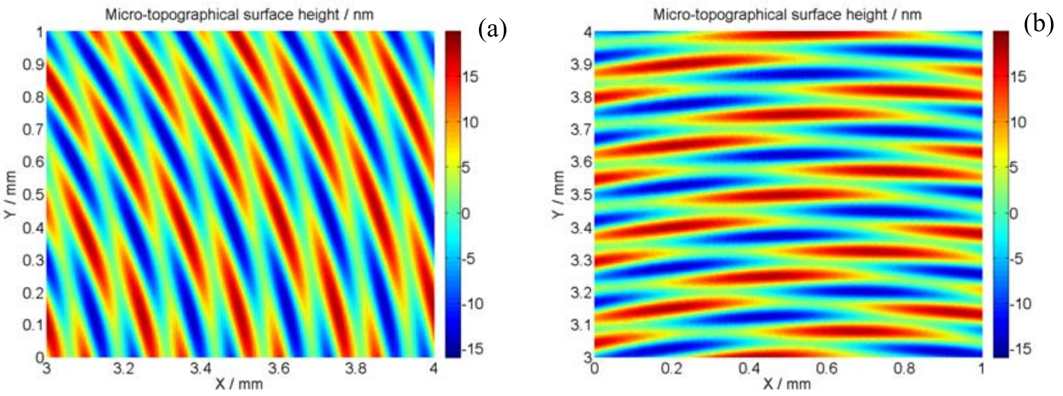

Figure 5.6 Simulated surface topographies at 3mm away from the sample center under the cutting conditions of Table 5.1 at the CTFs of 2001Hz and 1953Hz and the amplitudes of 8nm (a) in the feed direction and (b) in the cutting direction

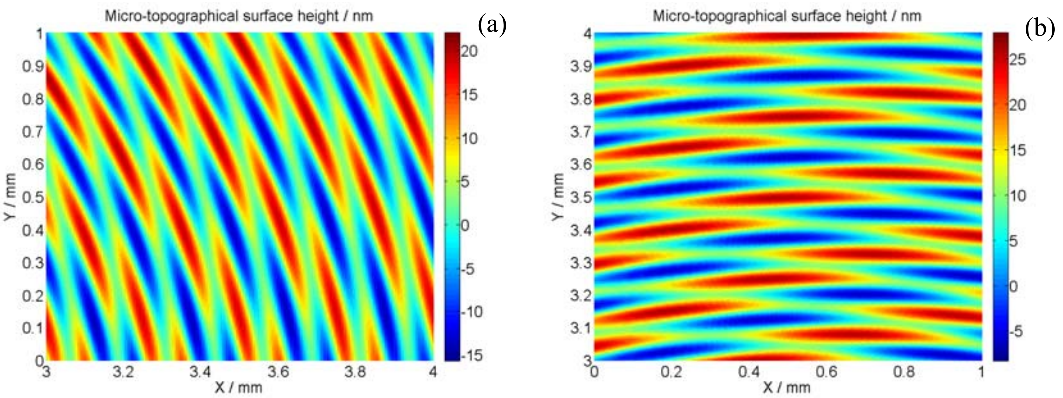

Figure 5.7 Simulated surface topographies away from the sample center under the cutting conditions of Table 5.1 with the vibration at the frequencies of 2001Hz, 1953Hz and 50Hz corresponding to the amplitudes of 8nm (a) in the feed direction and (b) in the cutting direction

5.2.2.2 Influences of Damping Ratios

Damping not only makes a system dissipate, but it also influences the natural frequencies of the system. Eq.4-4 supports that variable dampers cause the damped natural frequency shift. In this section, the simulation of surface topography generation under the cutting conditions of Table 5.1 with the spindle vibration is conducted. The simulated surface topographies are shown in Figure 5.8 and Figure 5.9. Figure 5.8 illustrates that periodic concentric, spiral and radial patterns are generated with the vibration at the axial frequency (PCF) of 1098.3Hz and its derivative frequency (DCF) of 1096.6Hz with the same amplitudes of 8nm. And Figure 5.9 demonstrates that periodic concentric, spiral, radial and two-fold patterns (PCSRPs) are formed with the vibration at the axial frequency (PCF) of 1098.3Hz, its derivative frequency (DCF) of 1096.6Hz and the SRF of 50Hz with the amplitudes of 8nm, respectively.

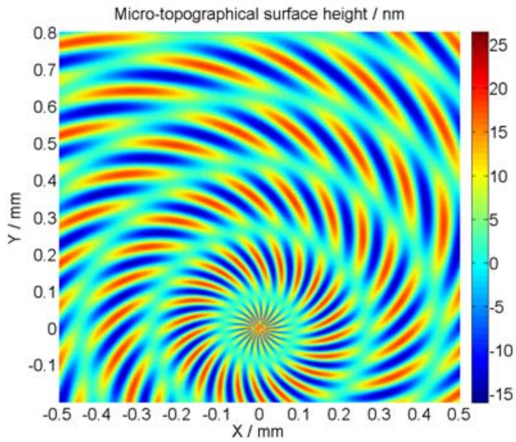

Figure 5.8 Simulated surface topography at the sample center under the cutting conditions of Table 5.1 with the vibration at the axial frequency of 1098.3Hz and its derivative frequency of 1096.9Hz with the same amplitudes of 8nm

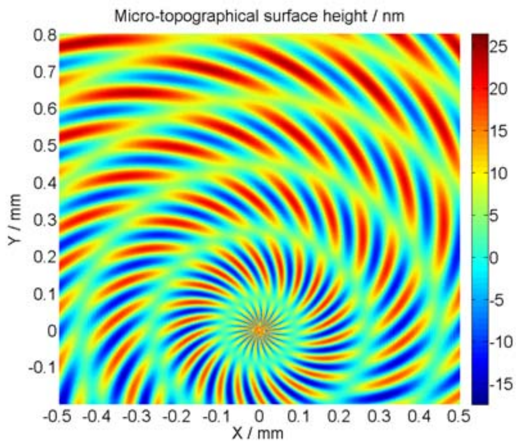

Figure 5.9 Simulated surface topography at the surface center under the cutting conditions of Table 5.1 at the axial frequency of 1098.3Hz, its derivative frequency of 1096.9Hz and the SRF of 50Hz with the amplitudes of 8nm

5.2.2.3 Effects of Phase Shift of Vibration

In the cutting process, the natural frequencies of the spindle are inherent, but the spindle speed can be changed. For the surface topography generation, the phase shift is related to the ratio between the frequency of the vibration and the SRF (the spindle speed), and is expressed as:

$$\alpha + \varepsilon = \frac{f_i}{f} \tag{5-6}$$

where α is an integer, which means the number of the surface patterns along the radial direction per revolution, and ε is a decimal fraction in the range $0<\varepsilon<1$ indicating the shift level of the surface patterns around the rotational direction of the machined surface, i.e. the axial direction, and causing the spiral patterns generated at a surface.

Figure 5.10 shows the graphical illustration of the ideal cutting profiles with the vibration in the feed direction at the phase shift of zero and the phase shift of 0.5. This indicates that when the phase shift is 0.5, the surface height Rt from the valley to the peak is minimal, and when it is 0, the surface height Rt is maximal.

A series of simulation of surface generation under the cutting conditions of Table 5.2 and Table 5.3 with the tilting vibration of the spindle at the corresponding frequencies as tabulated in Table 5.4 with the same amplitudes of 8nm. The simulated surface topographies are shown in Figure 5.11 and Figure 5.12. As increasing of the spindle speeds, surface patterns spread and expand. More importantly, Rts of surface topographies fluctuate, which is explained by the phase shift of the vibration influencing surface heights, and the Rts of the surface topographies in Figure 5.11(f) and Figure 5.12(f) are minimal in all, which principally supports that choosing the optimal spindle speed to change the phase shift is one selective in order to improve the surface quality, but in practice it is difficult due to the existences of various errors such as spindle speed error and the cutting force variation. In Table 5.4, the differences between the CTFs are close to the SRFs.

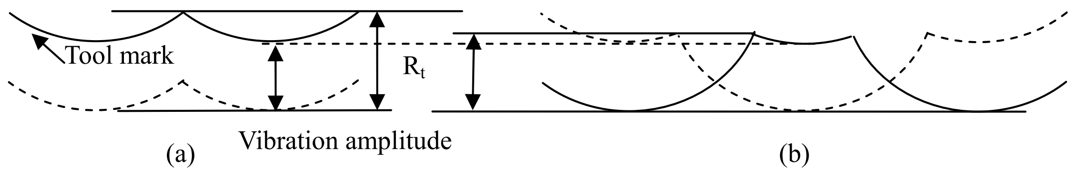

Figure 5.10 Graphical illustrations of ideal cutting profiles with vibration in the feed direction (a) without the phase shift (b) with the half phase shift

Table 5.2 Cutting conditions with the tool radius of 0.762mm in UPDT

Spindle speed (ω) (rpm)	2000, 3000, 4000, 5000, 6000
Feed rate (f_r) (mm/rev)	0.005
Depth of cut (Doc) (µm)	5
Tool nose radius (R_r) (mm)	0.762
Tool rake angle (^{o})	0
Front clearance angle (^{o})	15

Table 5.3 Cutting conditions with the tool radius of 0.128mm in UPDT

Spindle speed (ω) (rpm)	2000, 3000, 4000, 5000, 6000
Feed rate (fr) (mm/rev)	0.005
Depth of cut (Doc) (µm)	5
Tool nose radius (R_r) (mm)	0.128
Tool rake angle (^{o})	0
Front clearance angle (^{o})	15

Table 5.4 Spindle speeds with its corresponding CTFs for the tilting motions of the spindle rotor under the spindle specifications tabulated in Table 4.1

Spindle speed ω / rpm	SRF f ±0.05 / Hz	Frequency f_θ ±1 / Hz	Frequency f_ϕ ±1 / Hz	Difference between f_θ and f_ϕ ±1Hz
2000	33.3	1961	1993	32
3000	50	1953	2001	48
4000	66.7	1945	2009	64
5000	83.3	1937	2017	82
6000	100	1929	2025	96
7000	116.7	1921	2033	112
8000	133.3	1913	2041	128

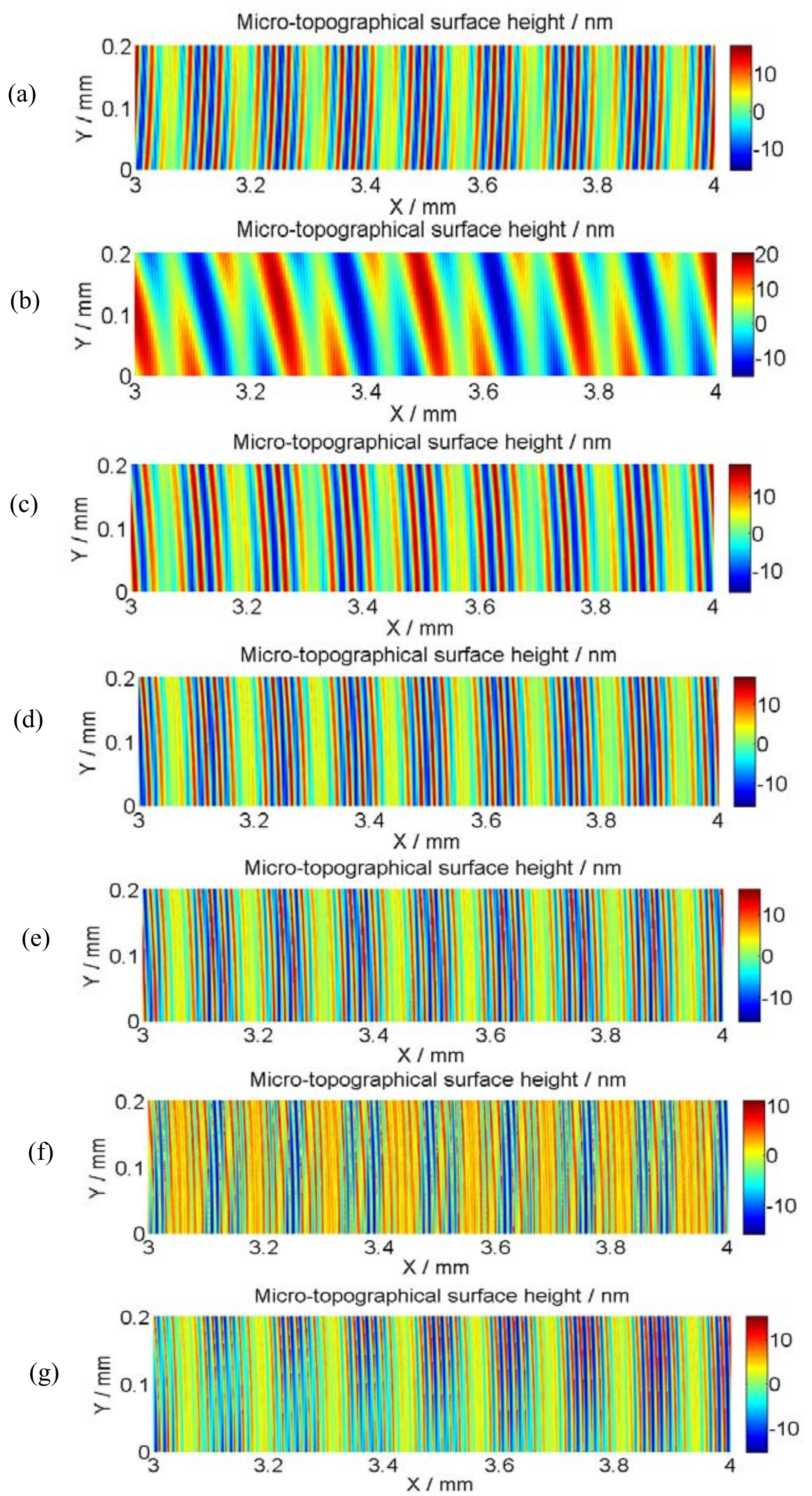

Figure 5.11 Simulated surface topographies generated at the place of 3mm away from the surface center under the cutting conditions of Table 5.2 with the tilting vibration at the frequencies of Table 5.4 with the same amplitudes of 8nm under the spindle speeds of (a) 2000, (b) 3000, (c) 4000, (d) 5000, (e) 6000, (f) 7000 and (g) 8000rpm

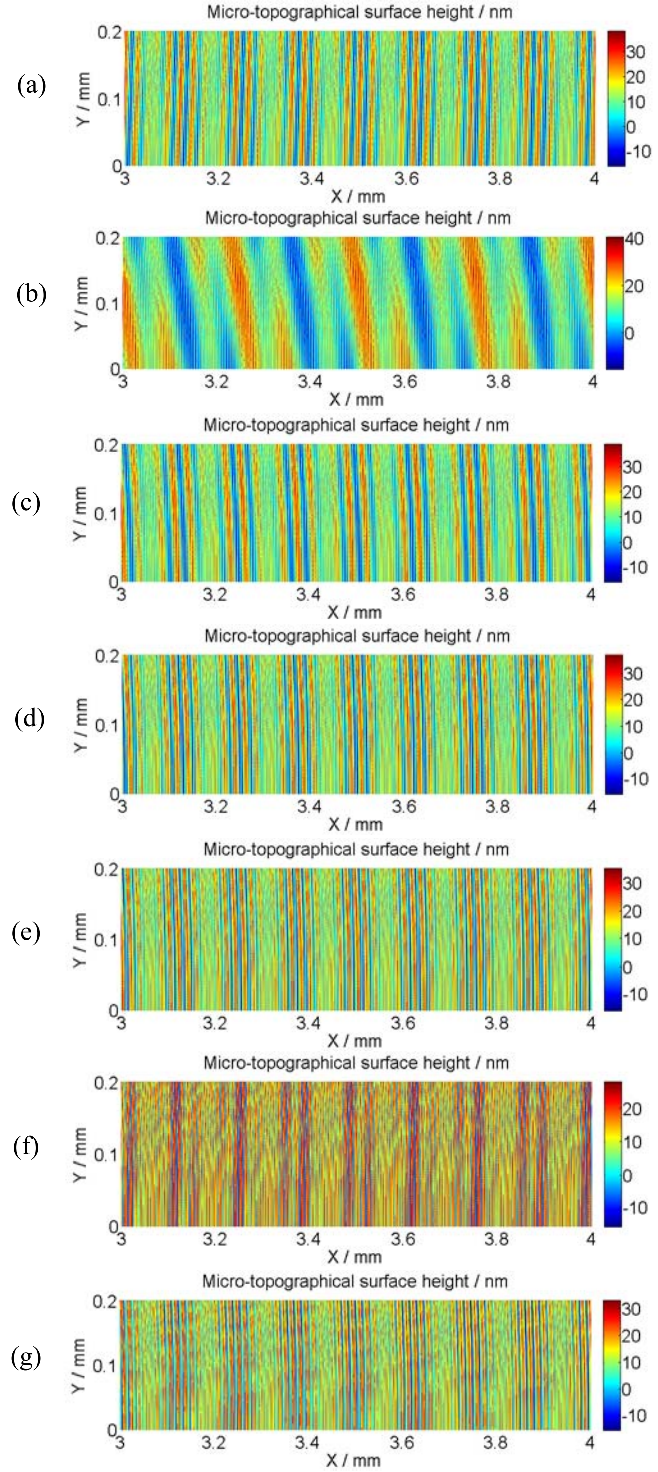

Figure 5.12 Simulated surface topographies generated at the place of 3mm away from the surface center under the cutting conditions of Table 5.3 with the tilting vibration at the frequencies of Table 5.4 with the same amplitudes of 8nm under the spindle speeds of (a) 2000, (b) 3000, (c) 4000, (d) 5000, (e) 6000, (f) 7000 and (g) 8000rpm

5.2.2.4 Prediction of Vibration Effects on Surface Topography

In the cutting process, the relative vibration distance between a workpiece and a tool is determined by the spindle vibration along the axial direction and around the radial direction. Eq.4-8 expresses the dynamic response of the axial vibration of the spindle in the inertial system $O(XYZ)$ and Eq.4-35 describes the dynamic responses of the rotational vibration of the spindle in the reference system $o(xyz)$, but considering that the cutting process takes place in the inertial system, the angular velocity of the spindle's tilting motions in the inertial system $O(XYZ)$ is:

$$\begin{bmatrix} \omega_X \\ \omega_Y \\ \omega_Z \end{bmatrix} = C_{OO_2} \begin{bmatrix} 0 \\ \dot{\phi} \\ \omega \end{bmatrix} + \begin{bmatrix} \dot{\theta} \\ 0 \\ 0 \end{bmatrix} = \begin{bmatrix} \phi\omega\cos\omega t + (\dot{\phi} + \theta\omega)\sin\omega t + \dot{\theta} \\ -\phi\omega\sin\omega t + (\dot{\phi} + \theta\omega)\cos\omega t \\ \omega \end{bmatrix} \tag{5-7}$$

Then, the relative vibration distance along the direction of depth of cut between a workpiece and a tool moving along the feed direction in the inertial system is written as:

$$Z(t) = \begin{cases} z(t) + d_1 \sin\left(\int_0^t \left(\phi\omega\cos\omega t + (\dot{\phi} + \theta\omega)\sin\omega t + \dot{\theta}\right)dt\right) \\ + d_2\left[1 - \cos\left(\int_0^t \left(\phi\omega\cos\omega t + (\dot{\phi} + \theta\omega)\sin\omega t + \dot{\theta}\right)dt\right)\right] \end{cases}$$

$$= \begin{cases} \dfrac{F_t}{k_1} - \dfrac{F_t}{k_1}\dfrac{e^{-\mu\sqrt{\frac{k_1}{m}}t}}{\sqrt{1-\mu^2}}\sqrt{1-\mu^2}\cos\left(\sqrt{\dfrac{k_1}{m}}\sqrt{1-\mu^2}\,t\right) \\ + \dfrac{F_t}{k_1}\dfrac{e^{-\mu\sqrt{\frac{k_1}{m}}t}}{\sqrt{1-\mu^2}}\mu\sin\left(\sqrt{\dfrac{k_1}{m}}\sqrt{1-\mu^2}\,t\right) \\ \quad + d_1\left(\theta + \phi\sin\omega t + \int_0^t (\theta\omega\sin\omega t)dt\right) \end{cases} \tag{5-8}$$

Since the spindle is excited by the cutting forces in the whole cutting process, the damping is not considered. Therefore, Eq.5-8 is rewritten as:

$$Z(t) = \frac{F_t}{k_1} - \frac{F_t}{k_1}\cos\left(\sqrt{\frac{k_1}{m}}t\right) + d_1\left(\theta(t) + \phi(t)\sin\omega t + \int_0^t \left(\theta(t)\omega\sin\omega t\right)dt\right) \tag{5-9}$$

In this equation, it proposes multiple frequencies, i.e. the axial frequency of the spindle $\frac{1}{2\pi}\sqrt{\frac{k_1}{m}}$, the SRF $\frac{1}{2\pi}\omega$, the coupled frequency $2\frac{1}{2\pi}\omega$ of the SRF, other four frequencies determined by the CTFs with the SRF, which are calculated by the below equations according to Eq.VII-2 in Appendix VII.

$$\begin{cases} f_{\theta 1} = \dfrac{1}{2\pi}\omega_{\theta 1} = \dfrac{1}{2\pi}(\omega_\theta - \omega) \\ f_{\theta 2} = \dfrac{1}{2\pi}\omega_{\theta 2} = \dfrac{1}{2\pi}(\omega_\theta + \omega) \\ f_{\phi 1} = \dfrac{1}{2\pi}\omega_{\phi 1} = \dfrac{1}{2\pi}(\omega_\phi - \omega) \\ f_{\phi 2} = \dfrac{1}{2\pi}\omega_{\phi 1} = \dfrac{1}{2\pi}(\omega_\phi + \omega) \end{cases} \tag{5-10}$$

The four kinds of frequencies, named the double-coupled tilting frequencies (DCTFs) at the approximate interval of the SRF, produce the "beating" phenomenon. It is deduced that these frequencies are exhibited by the PCSRPs at the generated surface, which is certified by the simulated surface topography such as Figure 5.6 and Figure 5.7, and observed through the frequency characteristics of cutting forces at the approximate interval of the SRF. Eq.5-9 is named the prediction model of the spindle vibration for surface generation of UPDT.

5.2.2.5 Optimization of Vibration Effects on Surface Topography

Optimization of surface topography is conducted to obtain a better surface in cutting process. In the literature, researchers have optimized the cutting parameters to improve the surface integrity and to decrease the machining time. In this study, the effects of the spindle vibration on surface generation are only considered. In Section 5.2.2.3, when the phase shift is set as 0.5, the best surface can be principally generated, but due to the spindle speed error and the influence of damping on the vibration frequency, the way is difficult to increase surface quality. Apart from this, one approach to optimization of surface generation is controlling the vibration amplitude. According to Eq.4-8, Eq.4-39 and Eq.5-9, the strategies for optimization are as follows:

(1) Increasing the system stiffness;

(2) Decreasing the cutting forces, e.g. the cutting conditions being carried out at the low feed rate, the small depth of cut and the relatively high spindle speed;

(3) Balancing the spindle system, i.e. decreasing the eccentric distance of the spindle; and

(4) Reducing the inertial moment of the spindle.

5.3 Surface Generation in UPRM

The surface generation technique describes how surface topography is formed and characterizes surfaces in the cutting process. Ultra-precision raster milling (UPRM) is a newly developed technique for fabricating ultra-precision freeform surfaces with nanometric surface roughness and sub-micrometric form accuracy without any subsequent polishing, that has been shown to be a comprehensive solution for producing optics, photonics and telecommunication products. Surface topography or surface roughness is one of crucial parameters in estimating a component's surface quality. The factors influencing surface roughness or surface topography in UPRM, including cutting conditions, tool geometry, cutting strategies, material properties, tool wear, tool path generation, and kinematic errors of sliders, have received the attention from many researchers. In this study, the spindle vibration of UPRM is considered under various cutting conditions without other factors influencing surface topography.

5.3.1 Modeling of Surface Generation

In the face raster milling process, surface topography in vertical cutting, as shown in Figure 3.4(a), can be separated into two parts. One part is the profile of a tool tip rotating around the spindle axis at the swing distance d_1 in the X-axial direction (in the raster direction), and the other is the surface profile determined by the tool tip shape in the axial direction Y-axis (in the feed direction). In Figure 5.13(a), the surface profile of the tool shape per one feed rate at the milled surface along the feed direction is schematically shown in vertical cutting of the raster milling system. In Figure 5.13(b), the surface profile of the tool swing path in the raster direction is schematically plotted in vertical cutting of the raster milling system, where A_1, A_2, A_3

and A_4 are the relative distances between a workpiece and a tool at each corresponding contact time, whereas generating tool loci / scallops at the milled surface. Then, the surface profiles are described as:

$$Z_1 + (1 - R_r \cdot \cos(\alpha_1)) \quad \text{and} \quad Z_2 + (1 - R_r \cdot \cos(\beta_1)) \tag{5-11}$$

$$Z_3 + (1 - d_1 \cdot \cos(\alpha_2)) \quad \text{and} \quad Z_4 + (1 - d_1 \cdot \cos(\beta_2)) \tag{5-12}$$

where, $\alpha_1 = 0 \sim \frac{\pi}{2} + \arctan(\frac{Z_2 - Z_1}{f_r + Y_2 - Y_1}) - \arccos\frac{\sqrt{f_r^2 + (Z_2 - Z_1)^2}}{2R_r}$,

$\beta_1 = 0 \sim \frac{\pi}{2} - \arctan(\frac{Z_2 - Z_1}{f_r + Y_2 - Y_1}) - \arccos\frac{\sqrt{f_r^2 + (Z_2 - Z_1)^2}}{2R_r}$,

$\alpha_2 = 0 \sim \frac{\pi}{2} + \arctan(\frac{Z_4 - Z_3}{s_r + X_4 - X_3}) - \arccos\frac{\sqrt{s_r^2 + (Z_4 - Z_3)^2}}{2d_1}$,

$\beta_2 = 0 \sim \frac{\pi}{2} - \arctan(\frac{Z_4 - Z_3}{s_r + X_4 - X_3}) - \arccos\frac{\sqrt{s_r^2 + (Z_4 - Z_3)^2}}{2d_1}$.

Similarly, in horizontal cutting, as shown in Figure 3.4(b), surface topography can also be separated into two parts. One part is the profile that a tool arc center rotates around the spindle axis at the swing distance d_1 in the feed direction (in the X-axial direction) and the other is the tool shape in the Y-axial direction (in the raster direction).

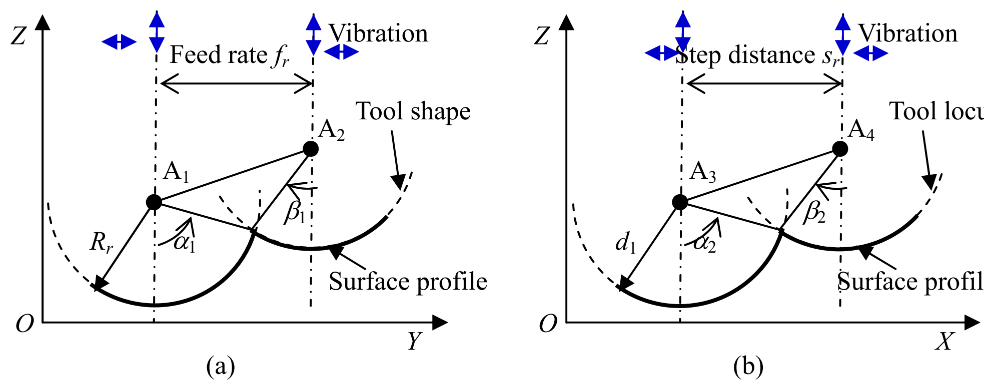

Figure 5.13 Schematic diagram of surface generation in vertical cutting (a) a vertical surface profile and (b) a horizontal surface profile

The relative distances $a_{\theta x}$ /$a_{\phi z}$ between a tool tip and a workpiece in the *X*/*Z*-axis only induced by the tilting motion around the *z*/*x*-axis at each contact time are calculated with Eq.5-13 and Eq.5-14.

$$a_{\theta x} = d_2 \sin\theta(iT) + d_1 \cos\theta(iT) - d_1 \tag{5-13}$$

$$a_{\phi z} = d_2 \sin\phi(iT) + d_1 \cos\phi(iT) - d_1 \tag{5-14}$$

And the relative distances $a_{\theta y}$ /$a_{\phi y}$ between a tool tip and a workpiece in the *Y*-axis only induced by the tilting motion around the *z*/*x*-axis at each contact time are calculated with Eq.5-15 and Eq.5-16.

$$a_{\theta y} = d_2 - d_2 \cos\phi(iT) + d_1 \sin\phi(iT) \tag{5-15}$$

$$a_{\phi y} = d_2 - d_2 \cos\theta(iT) + d_1 \sin\theta(iT) \tag{5-16}$$

Overall, the corresponding spindle vibration wave generated at the milled surface is named the spindle-vibration-induced profile (SVIP). All relative distances along the different directions between a tool and a milled workpiece are obtained from the spindle vibration model and then directly output into the surface generation model to produce surface topography. The whole simulation system is shown in Figure 5.14.

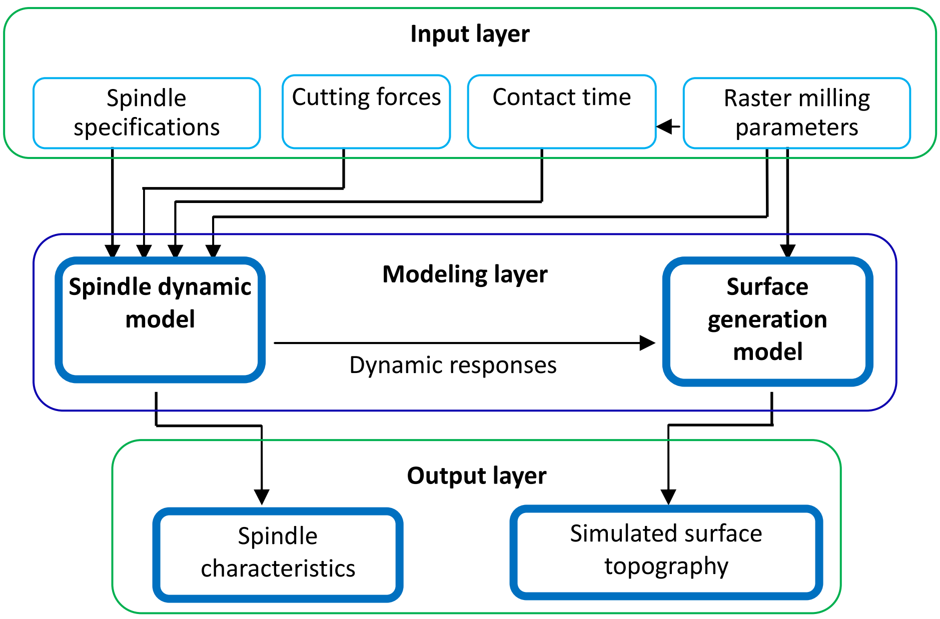

Figure 5.14 A framework for the whole simulation system

Table 5.5 Cutting conditions for surface generation in UPRM

Spindle speed (ω) (rpm)	4000	
Feed rate (f_r) (mm/min)	60	40
Depth of cut (d_o) (μm)	3	
Swing distance (d_1) (mm)	23	
Step distance (s_r) (μm)	10	15
Tool nose radius (R_r) (mm)	0.78	
Tool rake angle (^{o})	0	
Front clearance angle (^{o})	15	
Cutting strategy	Horizontal cutting	Vertical cutting
Cutting mode	Up-cutting	

Table 5.6 Spindle performance specifications with the cutting forces of UPRM

Spindle rotor mass (m) (kg)	2.5
Radial stiffness (k_2/ k_3) (N/μm)	22
Axial stiffness (k_1) (N/μm)	31
Eccentric position of the mass imbalance away from the rotor axis (e) (μm)	0
Position of the centre of mass center relative to its equilibrium along the z-axis (l_1/ l_2) (mm)	100
Radius of spindle rotor (R) (mm)	25
Inertial tensor around y-axis (J_y) (gm^2)	0.25
Inertial tensor around z/x-axis (J_x/J_z) (gm^2)	15.03
The distance of tilting center of spin rotor to the tool tip (d_2) (mm)	180
The distance of tool tip away from the spindle axis (Swing distance) (d_1) (mm)	23
Damper ratio μ	0.025
Angular damper ratio ξ	0.5×10^{-4}
Main cutting force (Fm) (N)	0.05
Thrust cutting force (Ft) (N)	0.05
Feed cutting force (Fr) (N)	0.003

5.3.2 Results of Surface Generation

5.3.2.1 Surface Topography

According to the previous surface generation model integrated with the proposed dynamic model of spindle vibration, surface topographies are formed under the cutting conditions listed in Table 5.5 and the performance specifications of the employed spindle tabulated in Table 5.6. The results are shown in Figure 5.15 and Figure 5.16. Figure 5.15 shows the surface topographies are generated under horizontal cutting and Figure 5.16 shows surface topographies are formed under vertical cutting.

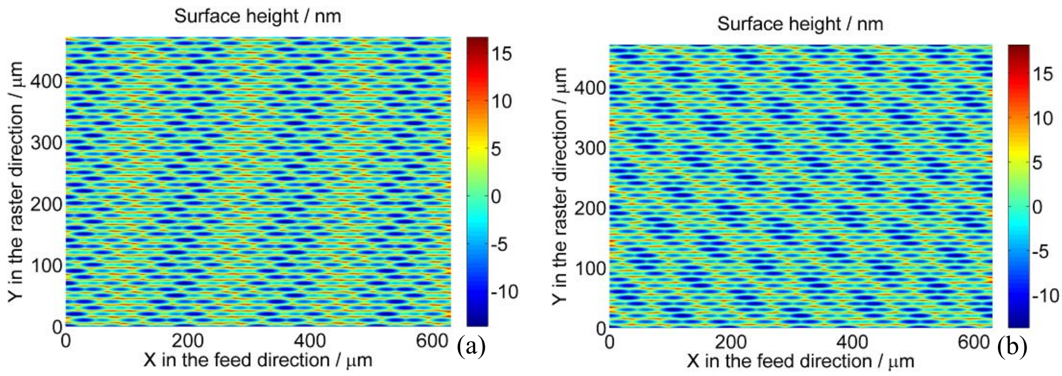

Figure 5.15 Simulated surface topographies under horizontal cutting (a) with the uniform phase shift of zero and (b) with the phase shift of 0.5

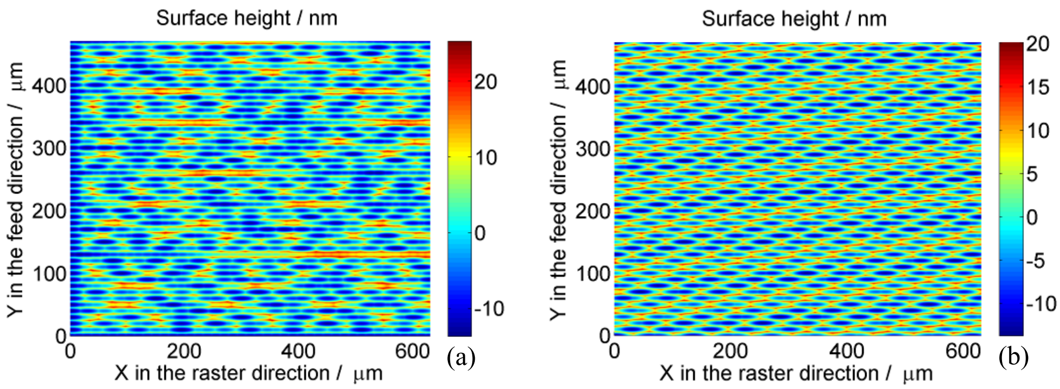

Figure 5.16 Simulated surface topographies under vertical cutting (a) with the random phase shift and (b) with the phase shift of 0.5

Figure 5.15 and Figure 5.16 show that various patterns are generated by the repetition of the profiles at intervals of tool paths (step distances) in the raster direction and by the repetition of the tool rotation at intervals of feed rate as a combination of vibration waves (named SVIPs) at the simulated surface in UPRM. In Figure 5.15(a), the ribbon-stripe patterns in the raster direction periodically occur when the phase shift of the SVIPs along the feed direction is approximately 0 in the raster direction, and in Figure 5.16(a), some ribbon-stripe patterns with the more aliased tool loci (named the aliased patterns or run-out) formed by the inhomogeneous scallops occur at the random phase shift. In Figure 5.15(b) and Figure 5.16(b), the ribbon-stripe or aliased patterns disappear and the lattice-like patterns appear, because the phase shift of the vibration wave along the feed direction is 0.5 in the raster direction. Therefore, the same phase shift for each profile produces the uniform patterns, and the random phase shift for each profile makes the surface patterns be uncertain, but not eliminate or obviously reduce the effects of the vibration on surface profiles.

In practice, these aliased patterns induced by the vibration in milling cannot be man-made, but they are randomly generated, since the phase shift is not precisely enough to control. Because the vibration curve of the spindle in each contact time forming the SVIP is intermittently and geometrically positioned into the milled surface, it discretely generates the inhomogeneous scallops to form the aliased patterns or the ribbon-stripe patterns through the tool loci. The dynamic responses of the spindle under the excitation of the intermittent cutting forces in each contact time produce the SVIPs along the feed direction. Therefore, the SVIPs are not smooth but discrete to generate the aliased tool loci as shown in Figure 15 and Figure 16, whose aliased tool locus is named the run-out (Cheng, 2006).

Overall, the solutions or the simulation for the dynamic responses of the spindle vibration theoretically support that the spindle vibration under the intermittent cutting forces produces the inhomogeneous scallops some ribbon-stripe and aliased patterns at the generated surfaces and explains the run-out phenomenon taking place at the milled surfaces through the aliased tool loci induced by the spindle vibration.

5.3.2.2 Shift Length of Tool Loci and Phase Shift of Vibration Influencing Surface Topography

In UPRM, the tool is rotating with the spindle to intermittently mill the surface material to produce tool loci/scallops (Figure 3.4(c), which generate surface topography. Under horizontal cutting or vertical cutting, due to the non-synthesis of the tool loci in cutting, a tool locus of a succeeding tool path will shift relative to the previous one of a previous tool path, where the relative displacement among the adjacent loci is named the shift length. Surface topography is influenced by the shift length (Wang, 2010). Figure 3.4(a2) and Figure 3.4(b2) illustrate the tool loci with a shift length, and Figure 5.17 shows the surface profiles with/without a shift length. When the shift length is zero, the surface height Rt is maximum, being calculated in Eq.5-17, and when the shift length is half, the surface height Rt is minimal (Wang, 2010), being calculated in Eq.5-18.

$$R_t = d_1 - \sqrt{d_1^2 - (\frac{f_r}{2\omega})^2} + R_r - \sqrt{R_r^2 - (\frac{s_r}{2})^2} = R_{t1} + R_{t2} \tag{5-17}$$

$$R_t = R_{t1} + R_r - \sqrt{R_r^2 - (s_r - \sqrt{R_r^2 - (R_r - R_{t1})^2})^2} \tag{5-18}$$

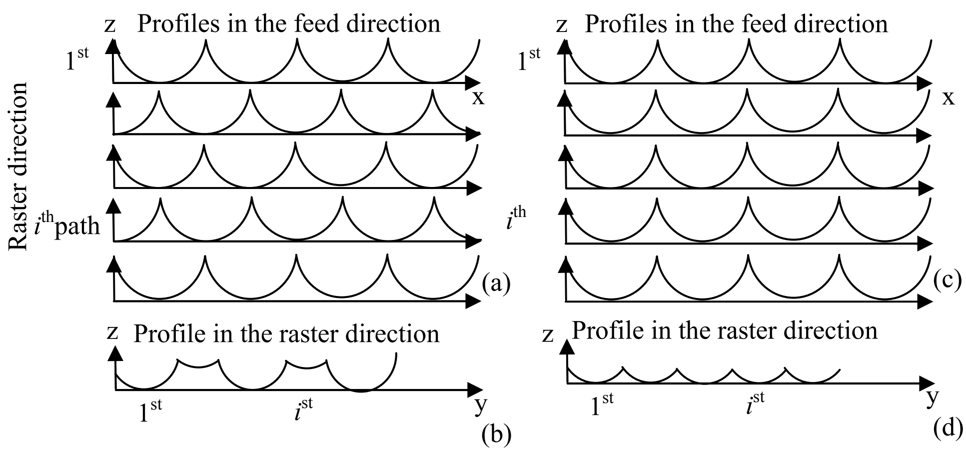

Figure 5.17 Schematic milled profiles (a) in the feed direction with a shift length, (b) in the raster direction with a shift length, (c) in the feed direction without a shift length and (d) in the raster direction without a shift length

In the section 5.2.2.3, the vibration-induced phase shift can be used to improve surface quality. In UPRM, the vibration trajectory of a tool tip is projected into the being-milled surface to form the vibration wave. Similarly, if the phase shift between the vibration waves is 0.5, the surface height is minimal. As shown in Figure 5.16, the surface height with the phase shift of 0.5 (Figure 5.16(b)) is less than that with the random phase shift (Figure 5.16(a)), but it is difficult to control the phase shift in the practical cutting process because it is random. Consequently, in principle, to control the phase shift and the shift length is a potential approach to improving surface quality.

5.3.2.3 Prediction of Vibration Effects on Surface Topography

According to the previous results, the relative distances between a workpiece and a tool in the different directions in UPRM are determined by the radial vibration, the axial vibration and the tilting vibration of the spindle, which are presented by Eq.4-42, Eq.4-58, Eq.5-11, Eq.5-12, Eq.5-13 and Eq.5-14, respectively. Not considering the effect of damping ratios on the dynamic responses of the spindle, Eq.4-42 and Eq.4-58 in each contact time are rewritten as:

$$\begin{cases} y((i+1)T) = y(iT)\cos(\omega_z T) + \dfrac{\dot{y}(iT) + \dfrac{\{-F_r\}\tau}{m}}{\omega_y}\sin(\omega_y T) \\ x((i+1)T) = x(iT)\cos(\omega_z T) + \dfrac{\dot{x}(iT) + \dfrac{\{-F_m\}\tau}{m}}{\omega_x}\sin(\omega_x T) \\ z((i+1)T) = z(iT)\cos(\omega_z T) + \dfrac{\dot{z}(iT) + \dfrac{\{-F_t\}\tau}{m}}{\omega_z}\sin(\omega_z T) \end{cases} \tag{5-19}$$

$$\begin{cases} \phi((i+1)T) = A_1 \sin\omega_\theta(T) + A_2\cos\omega_\theta(T) + A_3\sin\omega_\phi(T) + A_4\cos\omega_\phi(T) \\ \theta((i+1)T) = B_1\cos\omega_\theta(T) + B_2\sin\omega_\theta(T) + B_3\cos\omega_\phi(T) + B_4\sin\omega_\phi(T) \end{cases} \tag{5-20}$$

where, $\begin{cases} \dot{y}((i+1)T) = -\omega_z y(iT)\sin(\omega_z T) + (\dot{y}(iT) + \dfrac{\{-F_r\}\tau}{m})\cos(\omega_y T) \\ \dot{x}((i+1)T) = -\omega_z x(iT)\sin(\omega_z T) + (\dot{x}(iT) + \dfrac{\{-F_m\}\tau}{m})\cos(\omega_x T) \\ \dot{z}((i+1)T) = -\omega_z z(iT)\cos(\omega_z T) + (\dot{z}(iT) + \dfrac{\{-F_t\}\tau}{m})\sin(\omega_z T) \end{cases}$ and

$$\begin{cases}\dot{\phi}((i+1)T) = \omega_\theta A_1 \cos\omega_\theta(T) - \omega_\theta A_2 \sin\omega_\theta(T) + \omega_\phi A_3 \cos\omega_\phi(T) - \omega_\phi A_4 \sin\omega_\phi(T) \\ \dot{\theta}((i+1)T) = -\omega_\theta B_1 \sin\omega_\theta(T) + \omega_\theta B_2 \cos\omega_\theta(T) - \omega_\phi B_3 \sin\omega_\phi(T) + \omega_\phi B_4 \cos\omega_\phi(T)\end{cases}.$$

Combining Eq.5-19 and Eq.5-20 with Eq.5-11, Eq.5-12, Eq.5-13 and Eq.5-14, the relative distances along the different directions in $O(xyz)$ in each contact time are:

$$y((i+1)T) = \begin{cases} y(iT)\cos(\omega_z T) + \dfrac{\dot{y}(iT) + \dfrac{\{-F_r\}\tau}{m}}{\omega_y}\sin(\omega_y T) \\ + d_2 - d_2\cos\phi((i+1)T) + d_1 \sin\phi((i+1)T) \\ + d_2 - d_2\cos\theta((i+1)T) + d_1 \sin\theta((i+1)T) \end{cases} \tag{5-21}$$

$$x((i+1)T) = \begin{cases} x(iT)\cos(\omega_z T) + \dfrac{\dot{x}(iT) + \dfrac{\{-F_m\}\tau}{m}}{\omega_x}\sin(\omega_x T) \\ + d_2 \sin\theta((i+1)T) + d_1\cos\theta((i+1)T) - d_1 \end{cases} \tag{5-22}$$

$$z((i+1)T) = \begin{cases} z(iT)\cos(\omega_z T) + \dfrac{\dot{z}(iT) + \dfrac{\{-F_t\}\tau}{m}}{\omega_z}\sin(\omega_z T) \\ + d_2 \sin\phi((i+1)T) + d_1\cos\phi((i+1)T) - d_1 \end{cases} \tag{5-23}$$

The above equations present the effects of spindle vibration on surface topography. These can be used to predict the effects of spindle vibration under the intermittent cutting forces on surface topography or surface roughness in UPRM.

5.3.2.4 Optimization of Vibration Effects on Surface Topography

Generally, if the cutting forces synchronously excite the spindle system, the vibration amplitudes of the spindle gradually increase and the "resonance" takes place, i.e. the direction of the cutting forces is the same as the velocity direction of the spindle vibration, otherwise, reversely. Figure 4.14, Figure 4.15, Figure 4.16 and Figure 4.17 show the effects of the spindle speed, i.e. the excitation frequency of the cutting forces, on the amplitudes of spindle vibration. The amplitudes are mainly determined by the natural frequencies of the spindle and the spindle speed. If the ratio between the rotation period of the spindle and the period of the spindle vibration is 0.5, the minimal amplitudes of the spindle vibration are obtained as:

$$\begin{cases} n_y T_y + 0.5T_y = T \\ n_x T_x + 0.5T_x = T \\ n_z T_z + 0.5T_z = T \\ n_{tilting} T_{tilting} + 0.5T_{tilting} = T \end{cases} \tag{5-24}$$

where n_y, n_x and n_z are integers, $\begin{cases} T_y = \dfrac{2\pi}{\omega_y} \\ T_x = \dfrac{2\pi}{\omega_x} \\ T_z = \dfrac{2\pi}{\omega_z} \end{cases}$, $T_{tilting} = \dfrac{4\pi}{\omega_\theta + \omega_\phi}$ and $T = \dfrac{60}{\omega}$.

Apart from that, the strategies for optimization are added as follows:

(1) Increasing the system stiffness;

(2) Decreasing the cutting forces, e.g. selecting the low feed rate, the low depth of cut and the relative high certain spindle speed;

(3) Balancing the spindle system, i.e. decreasing the eccentric distance of the spindle; and

(4) Reducing the contact time.

5.4 Summary

In this chapter, surface generation models with the combination of the spindle vibration in UPDT and UPRM are proposed. The effects of the damping ratio and the phase shift of the vibration on the surface topography generation are discussed. And a prediction model and an optimization model for the effects of the spindle vibration on surface topography are developed, based on the dynamic simulation or the solutions describing the dynamic responses of the spindle vibration of UPM in Chapter 4. The major findings are summarized as below:

(i) In UPDT, a new surface generation model integrated with the spindle vibration is developed to simulate surface topographies. It explains that the periodic concentric, spiral, radial and two-fold patterns (PCSRPs) are produced by the spindle vibration with its derivative vibration induced by damping, the phase shift of the vibration.

(ii) In UPRM, a novel surface generation model is developed considering the dynamic responses of the spindle vibration. It shows that the aliased tool loci and the aliased patterns and the ribbon-stripe patterns are induced by the SVIPs generated at the surface along the feed direction which are discrete and determined by the dynamic responses of the spindle excited by the intermittent cutting forces. It also explains why the run-out phenomenon takes place in milling.

(iii) The simulation results show that the phase shift of vibration and the shift length of the tool locus influence surface profiles. The half phase shift and the half shift length can be selected though these factors are not readily controllable to improve surface quality because the phase shift and the shift length produce the uncertainty for surface roughness in UPM. However, the phase shift and the shift length of 0.5 are optimal to achieve the best surface quality in UPM.

(iv) The effects of the spindle vibration on surface topography are predicted using a prediction model, and the corresponding optimization strategies on surface topographical generation are provided with an optimization model, based on the solutions for the dynamic model solved in Chapter 4. The optimization and prediction models are created to make ultra-precision machining more predictive and effective and to make a potential contribution to improving surface quality in an efficient way for UPM. The selection of the cutting conditions is crucial to improve surface quality.

Chapter 6 Experimental Investigation and Analysis

6.1 Introduction

This chapter proposes the cutting experiments conducted as part of this research to study the effects of the aerostatic bearing spindle on surface topographies under different cutting conditions in ultra-precision machining (UPM). It comprises two parts.

In part one, a series of face-cutting tests were carried out on a two-axis CNC ultra-precision diamond turning (UPDT) (Optoform 30 from Taylor Hobson Pneumo Co., UK) (see Appendix I), cutting forces were measured by a force sensor (see Appendix IX) and processed by the power spectral density (PSD) technique (see Appendix VIII) based on fast Fourier transform (FFT) (see Appendix IV), and the machined surfaces under various cutting conditions were measured by the Optical Profiling System (WYKO NT8000) (see Appendix X) and analyzed by the PSD technique.

In part two, a series of flat-cutting tests were performed on a five-axis CNC ultra-precision raster milling (UPRM) machine (Precitech Freeform 705G, Precision Inc., USA) (see Appendix II), intermittent cutting forces were measured by a force transducer, and the machined surfaces under various cutting conditions were measured by the Optical Profiling System (WYKO NT8000).

6.2 Experimental Setup in UPDT

6.2.1 Cutting Conditions

All face-cutting tests with flat surfaces were performed on a two-axis CNC ultra-precision lathe (Optoform 30 from Taylor Hobson Pneumo Co., UK) under the cutting conditions listed in Table 6.1. In the two-axis CNC ultra-precision lathe, X represents the main cutting force direction, Y is the feed direction and Z is the thrust cutting force direction corresponding to the spindle axis Z. l denotes the position of the mass center relative to the spindle bearing on two sides along the Z-axis. d_1 means the distance between the tool tip and the spindle axis along the Y-axis when cutting and d_2 is the distance from the workpiece surface to the equilibrium center of the spindle rotor along the Z-axis, as shown in Figure 3.1 and Figure 3.9 in Chapter 3. F_r is the feed cutting force in the Y-axial direction, F_t is the thrust cutting force in the Z-axial direction and F_m is the main cutting force in the X-axial direction. The spindle rotor turning around the spin axis, i.e. the depth of cut direction (namely the axial direction), is flowed and supported by a constant pressurized air film. In the cutting process, the cutting forces are indirectly applied to the spindle rotor with its self-eccentricity through the specimens. The spindle performance specifications are shown in Table 4.1 in Chapter 4.

Table 6.1 Cutting conditions of diamond turning

Spindle speed (ω) (rpm)	3000, 4000, 5000, 6000
Feed rate (f_r) (mm/rev.)	0.005
Depth of cut (Doc) (μm)	1, 5, 25
Tool nose radius (R_r) (mm)	0.762, 0.128
Tool rake angle (^{o})	0
Front clearance angle (^{o})	15

6.2.2 Measurement of Cutting Forces

In general, a cutting force measurement system contains three major parts, a force sensor, charge amplifiers, and a data acquisition system. The Kistler 9252A force transducer that was used, as shown in Figure 6.1, is a 3-component force sensor for measuring the three orthogonal components, such as F_x, F_y and F_z, of a dynamic or quasi-static force acting in an arbitrary direction, possessing a very extended measuring range, high stiffness and low cross talk. Its uncertainty provided by the instrument manufacturers is 0.002N after it is calibrated. More details are provided in Appendix IX.

Figure 6.1 A Kistler 9252A 3-component force sensor

The Kistler 5011B amplifiers are employed for the three-component force sensor measuring system requiring charge amplifiers for each channel to amplify the electrical charge signals of the sensor and convert the signals into voltages exactly proportional to the acting force. A data acquisition system records, digitizes and saves the signals for post processing.

To measure the UPDT cutting forces, the Kistler 9252A force transducer was mounted between the tool shank and the tool holder with a pre-loaded force. The signals of the cutting forces were recorded and digitized by the 10-bit Tektronix TDS 774A digitizing oscilloscope with the uncertainty of 0.002N after being pre-amplified by the Kistler 5011B charge amplifiers. The experiment set up is shown in Figure 6.2. The experiment aimed to indirectly achieve the frequency characteristics of the aerostatic bearing spindle through measuring the cutting forces under various cutting conditions. The sampling frequency was set at 1MHz. Thus, the frequencies below 0.5MHz can be accurately calculated in the power spectral density (PSD) analysis with regard to the Nyquist limit. The signals obtained in the time domain were transformed to that in the frequency domain by the fast Fourier transform (FFT) (Appendix IV). The PSD analysis (Appendix VIII) was performed based on the output of FFT. In this study, the 32-bit computer was employed for the data processing. The uncertainty is further less than 0.1nm.

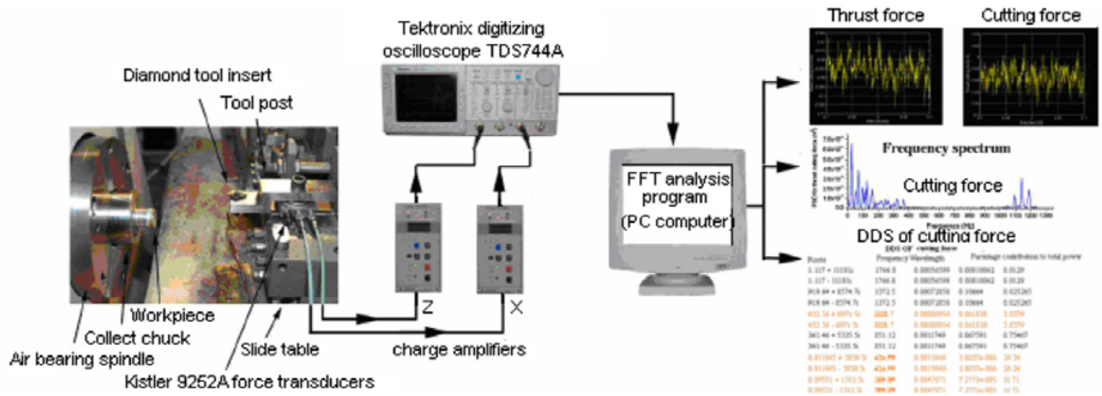

Figure 6.2 Configuration of the cutting force measurement system in UPDT

In addition, the cutting forces were measured in $O(XYZ)$. When the tool was cutting a specimen and moving from the outside to the center along the feed direction, a series of the cutting forces were acquired in order, as shown in Figure 6.3.

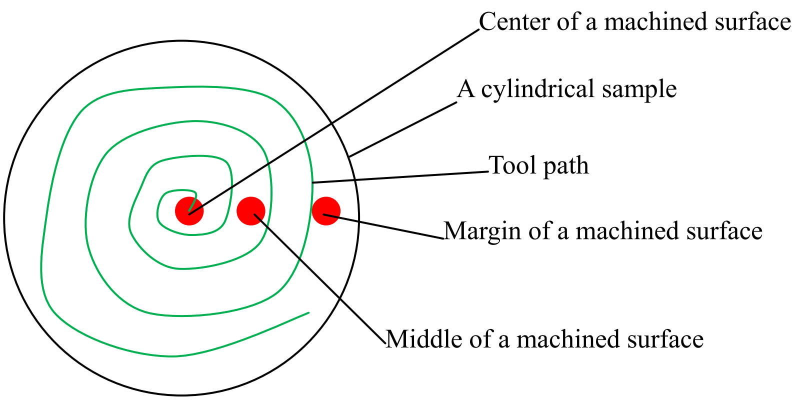

Figure 6.3 Schematic diagram of the cutting force measurement in the cutting process

6.2.3 Measurement of Surface Topographies

The Optical Profiling System (WYKO NT8000) (Figure 6.4) is Veeco's eighth generation optical profiler which is the most capable optical profiler available, for the rapid measurement of step heights, surface roughness and surface topography with non-contact 3D measurement from 0.1 nm to 8 millimeters, with a sub-nanometer resolution and a lateral resolution up to 1μm. Its uncertainty for the roughness measurement of a flat surface is 2nm. A unique, internal reference signal enables a self-calibrating accuracy over the entire scan range. Combined with 100μm/sec scan speed and full automation, the NT8000 is the tool of choice for demanding research and production applications in materials, metals, MEMS, semiconductors, optics and more. More details are presented in Appendix X.

In this study, the NT8000 was employed to measure surface topographies of the machined specimens with an effective magnification within an effective view field per measurement at one place, where the measurement instrument captured surface topographies of samples under the PSI mode. The surface profile data were analyzed using the power spectral density (PSD) technique based on the fast Fourier transform (FFT) (see Appendix IV and Appendix VIII).

Overall, the uncertainty is relatively little, as compared with others like spindle vibration, material swelling and recovery, material pile-up. Therefore, it is not considered in this study.

Figure 6.4 Wyko NT8000 Optical Profiling System

6.3 Experimental Results and Analysis in UPDT

6.3.1 Variation of Cutting Forces

In the cutting process, cutting force variation directly reflects the system vibration, such as the spindle vibration. To achieve the characteristics of the thrust cutting forces, the PSD technique was utilized to transform the thrust cutting force signals in the time domain to those in the frequency domain by FFT. When the tool was cutting a specimen and moving from the outside to the center along the feed rate direction, i.e. the distance d_1 reducing, a series of thrust cutting forces under the cutting conditions of Table 6.1 (the tool radius of 0.762mm, the spindle speed of 3000rpm and the depth of cut of 5μm) were acquired in order. According to Eq.4-3, Eq.4-12, Eq.4-13, Eq.4-36, Eq.4-37 and Eq.5-10, the frequencies of the spindle system, observed along the depth of cut direction in $O(XYZ)$ at the spindle speed of 3000rpm, are computed and tabulated in Table 6.2.

The thrust cutting forces and the corresponding PSDs are plotted in Figure 6.5(a)-(l). The PSD results show: two principle characteristic peaks at 1100Hz and 1150Hz with some little peaks, corresponding to the axial and radial frequencies (PCFs) with their derivative frequencies (DCFs), respectively; four principle characteristic peaks for 2000Hz at the interval of 50Hz with multiple little peaks, which are the double-coupled tilting frequencies (DCTFs) with the multiple derivative frequencies (MCDCFs); the peaks at 4000Hz, which is the harmonic frequency of 2000Hz; and the mini peak at 50Hz which is the spindle rotational frequency (SRF) corresponding to the spindle speed of 3000rpm. The frequencies in the PSD results are in agreement with the theoretical results shown in Table 6.2. The characteristic peaks of 2000Hz dramatically decrease, since the distance d_1 decrease, but the characteristic peaks for 1100Hz and 1150Hz are almost constant. This supports the prediction model for surface generation in Eq.5-9.

Accordingly, the PSDs of the thrust cutting forces identify the natural frequencies (PCFs) of the spindle rotor with their derivative frequencies (DCFs) and the harmonic frequencies. And the coupled tilting frequencies (CTFs) of the spindle rotor in the body-fixed system $o(xyz)$ produce the double-coupled tilting frequencies (DCTFs) at the interval of the SRF in the cutting process of the inertial system $O(XYZ)$.

Table 6.2 Natural frequencies of the spindle rotor with the spindle speed of 3000rpm under the spindle specifications tabulated in Table 4.1

SRF / Hz	Coupled SRF / Hz	Radial frequency (RF) / Hz	Axial frequency (AF) / Hz	Fundamental tilting frequency (FTF) / Hz	CTFs / Hz	DCTFs / Hz
50	100	1000	1100	1975	1950	1900
						2000
					2000	1950
						2050

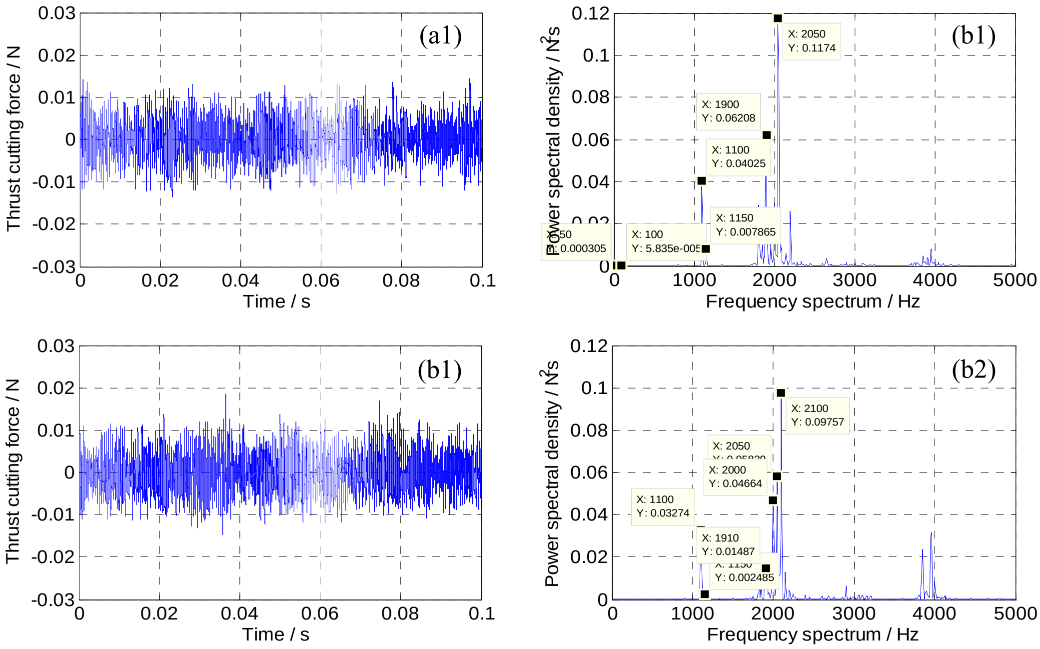

Figure 6.5 A series of the thrust cutting forces measured in order (a1)-(l1) and their corresponding PSDs (a2)-(l2) as the tool was moving from the outside to the machined surface center under the cutting conditions of Table 6.2 (the tool radius of 0.762mm, the spindle speed of 3000rpm and the depth of cut of 5μm)

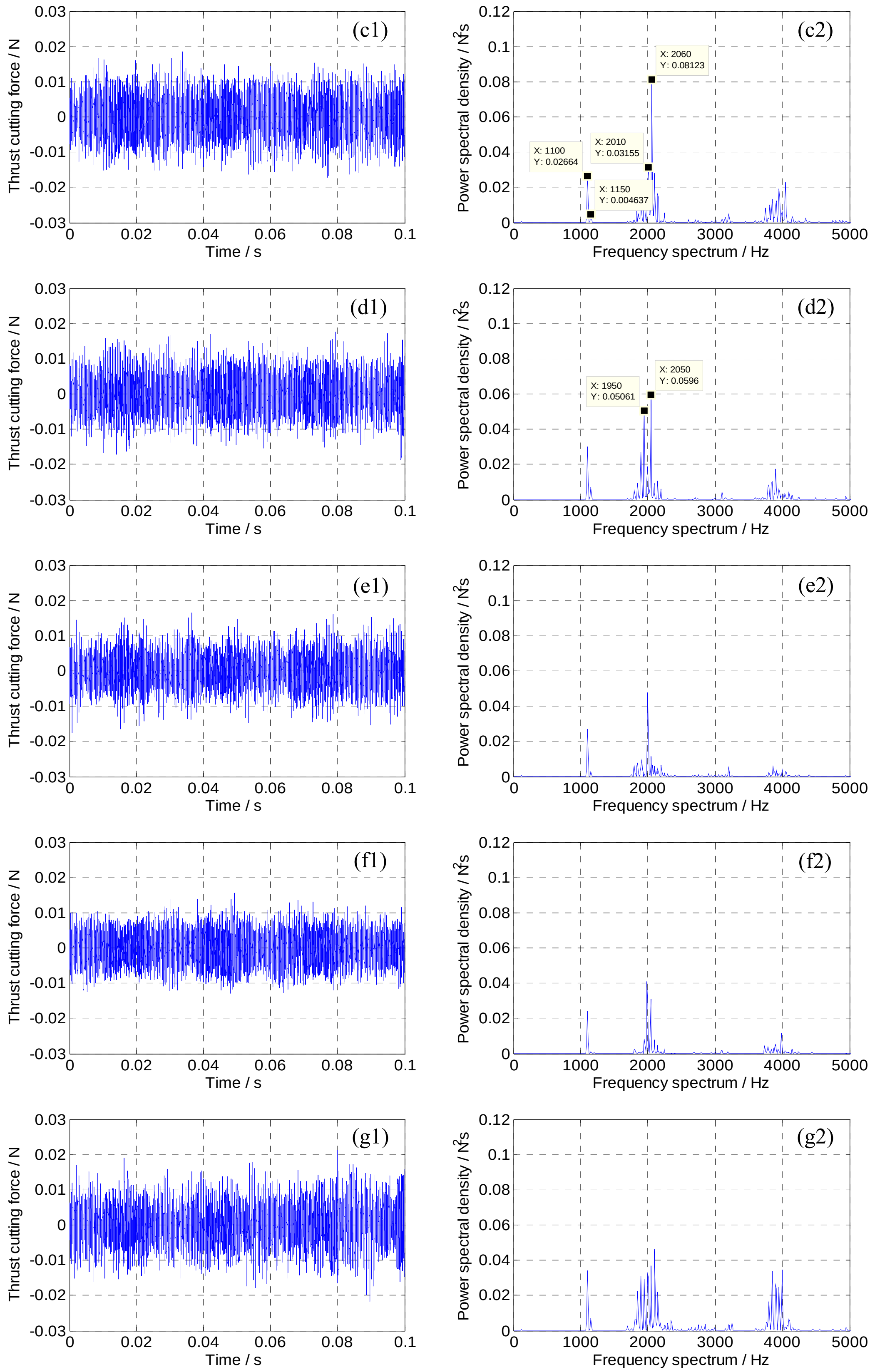

Figure 6.5 Continued

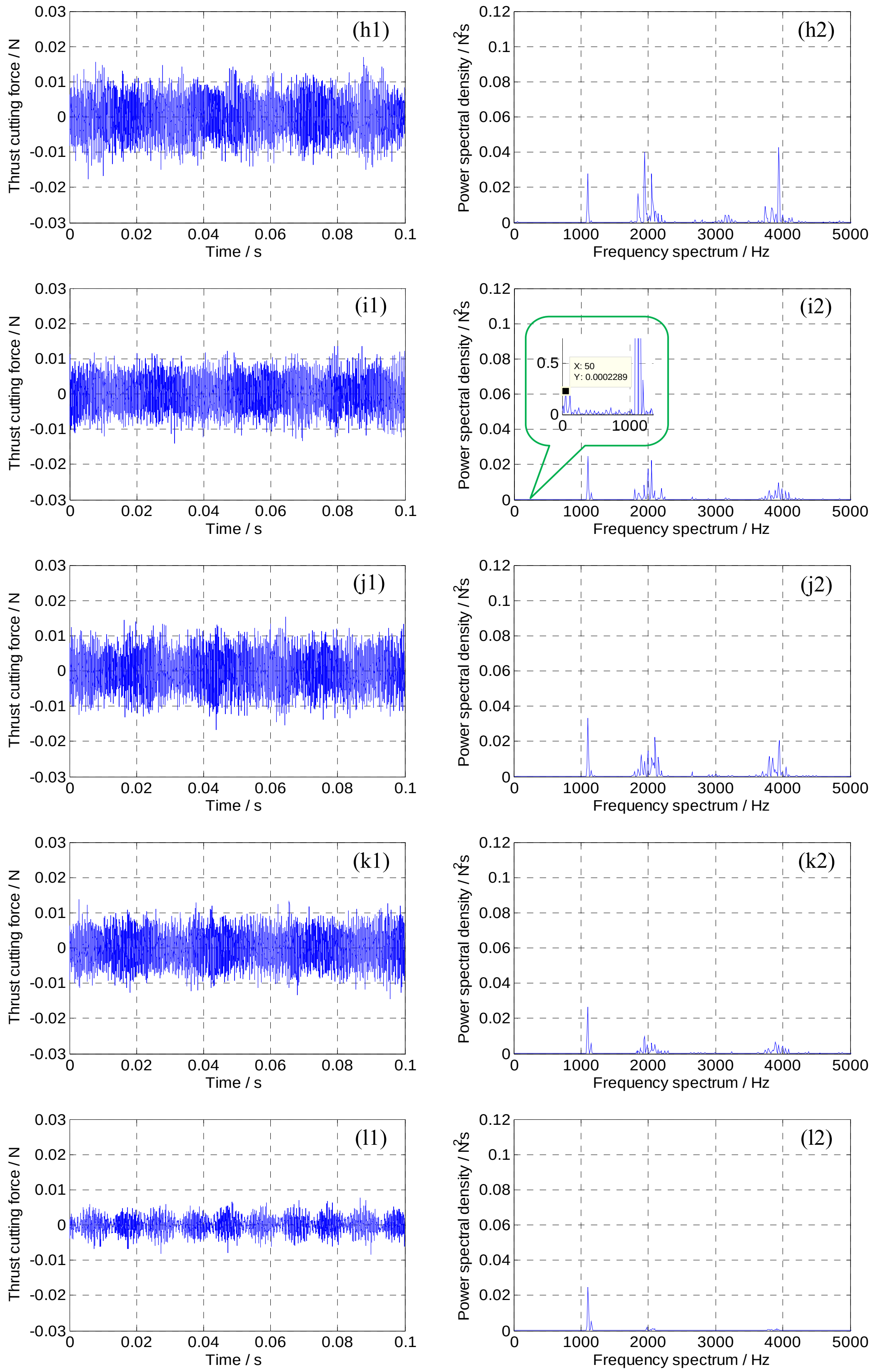

Figure 6.5 Continued

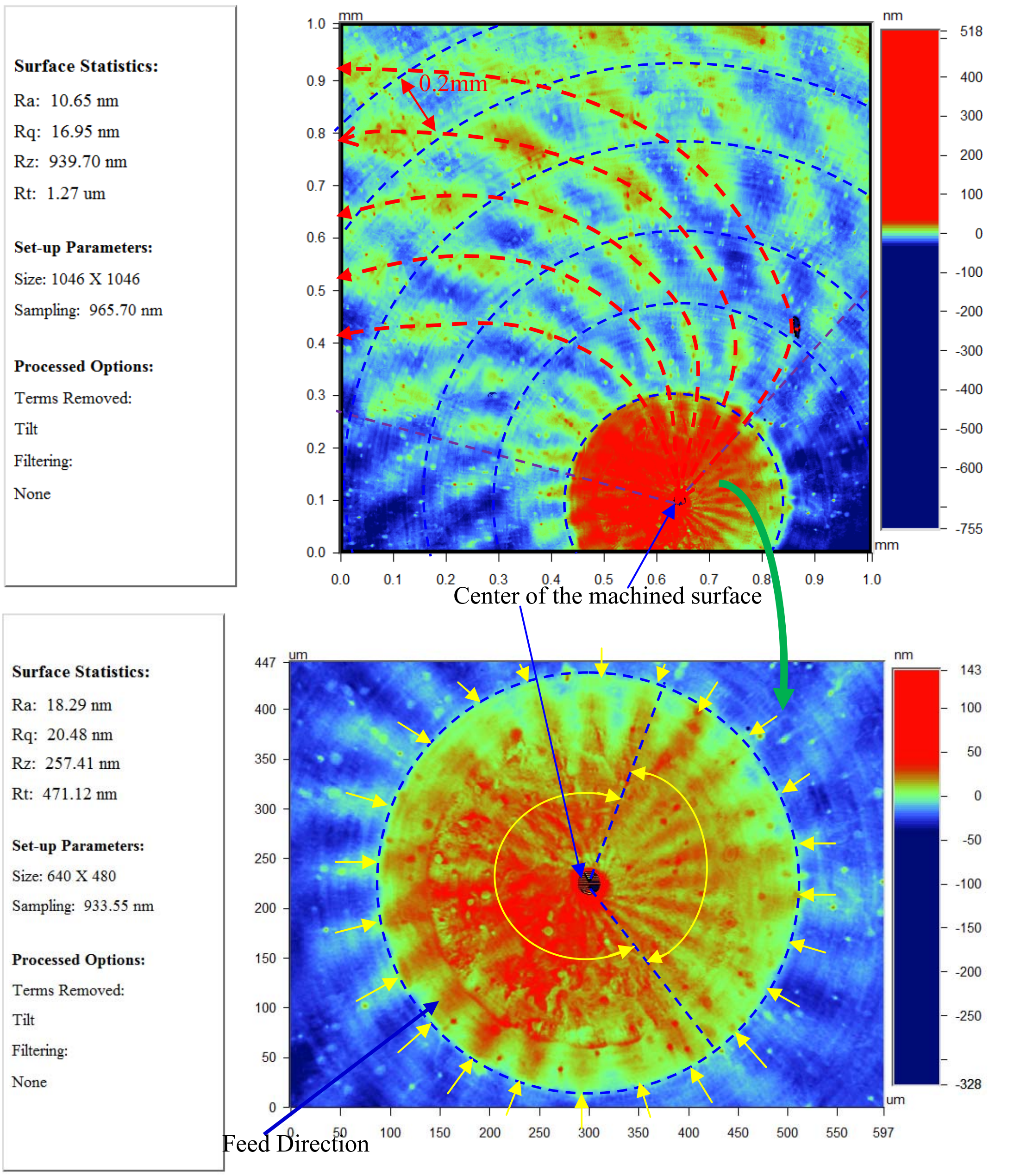

Figure 6.6 Measured surface topography of the sample center generated under the cutting conditions (the tool radius of 0.762mm, the spindle speed of 3000rpm, the feed rate of 0.005mm/rev., the depth of cut of 5μm) in Table 6.1

6.3.2 Characteristics of Surface Topographies

The spindle vibration at the frequencies of Table.5.2 has been confirmed by the PSDs of the cutting forces. Further, the spindle vibration directly produces an impact upon surface generation in the cutting process. To observe the effects of the spindle vibration on the surface topography generation, the Optical Profiling System (WYKO NT8000) was used to measure surface topographies of the machined specimens under the cutting conditions of Table 6.1 (the tool radius of 0.762mm, the spindle speed of 3000rpm, the feed rate of 0.005mm/rev., the depth of cut of 5μm).

In Figure 6.6, it indicates that as measured in the surface center of the machined sample, about 23 pairs of radial patterns, indicated by arrows forming a circle, occur. Its corresponding vibration frequency was calculated at about 1150Hz ($23\times\omega=23\times3000/60$), which is close to the natural frequency of the spindle in the axial direction. A two-fold pattern, shown by a dash line, is observed. The corresponding vibration frequency is equal to the SRF of 50Hz (3000rpm/60), according to Eq.5-9, but the effects of the DCTFs' vibration on the surface topography through the interval of them close to SRF exhibits a two-fold pattern at the machined surface. In the center of the machined surface, a concave occurs, because the material in the center was removed and over cut due to vibration along the radial and axial directions. In addition, Figure 6.6 also displays periodic concentric, spiral, radial, and two-fold patterns (PCSRPs), which identify the simulation result of Figure 5.8 and Figure 5.9. This is because the overlap vibration of two close frequencies produces the 'beating' phenomenon that generates the periodic concentric patterns at the machined surface, the phase shift of the vibration induces the phenomenon of the spiral and radial patterns, whereas the two-fold patterns are formed by the SRF vibration. The phenomena are explained by the simulated surface topography under the same cutting conditions, as shown in Fig 5.9. There is the inference that damping induces a shift of the axial frequency. Furthermore, for the DTFs, since the distance d_1 between the place where the machined surface is formed and the surface center gradually decreases as the tool moves to the center, their influence on surface topography with their corresponding patterns is also eliminated simultaneously.

In Figure 6.7, the surface topography measured at the distance of 3mm away from the center of the machined specimen shows the millimetric-scale spiral patterns at a frequency of about 2100Hz ($3\text{mm}\times2\times\pi\times3000\text{rpm}/0.45\text{mm}$) close to the DTF of the spindle vibration, and the periodic concentric, spiral and radial patterns (PCSRPs) at the machined surface are obviously observed, since the DTFs' vibration produces the 'beating' phenomenon, but the two-fold patterns cannot be examined due to the extremely small scale with regard to the whole machined surface. The PCSRPs are also explained by the simulation results of Figure 5.6 and Figure 5.7 in Chapter 5.

Overall, the experimental findings have been supported by the simulation results to further explain the effects of the spindle vibration on surface topographies.

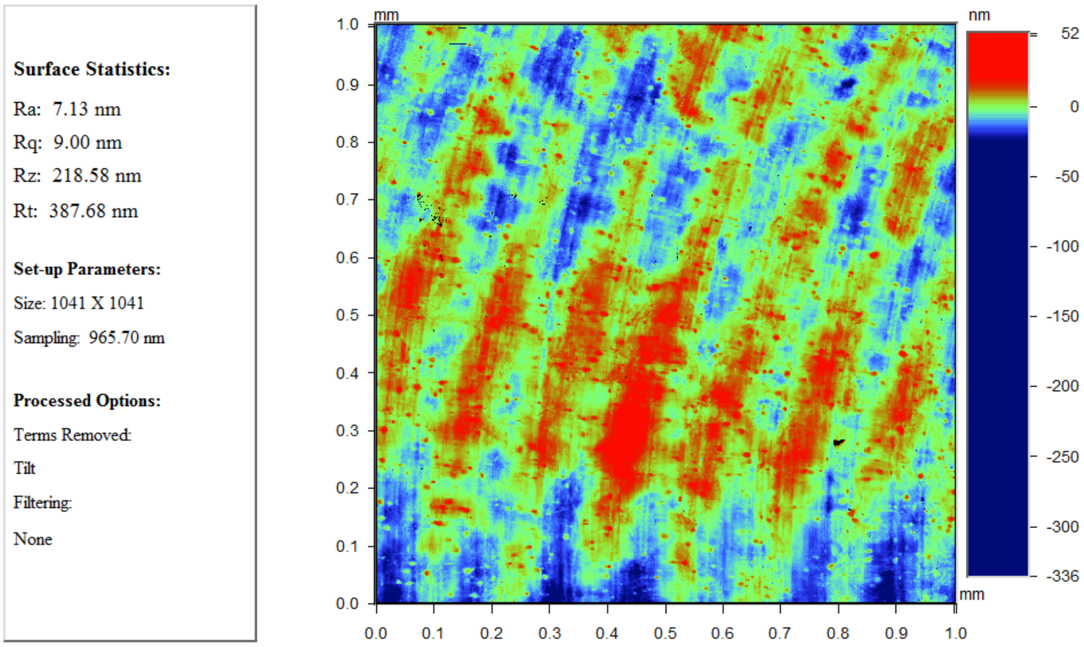

Figure 6.7 Measured surface topography at the place of 3mm away from the center generated under the cutting conditions (the tool radius of 0.762mm, the spindle speed of 3000rpm, the feed rate of 0.005mm/rev., the depth of cut of 5μm)

6.3.3 Effects of Depths of Cut on Surface Topographies

Depth of cut is one of the most important parameters in the cutting process for removing material to create a new surface. As the depth of cut increases, the cutting forces increases, which results in the increase of the amplitudes of the spindle vibration according to Eq.5-9 in Section 5.2.2.4 of Chapter 5. Figure 6.8 plots the surface topographies created under the following cutting conditions: Tool radius of 0.762mm, Spindle speed of 3000rpm, Feed rate of 0.005mm/rev., Depths of cut of 1, 5, 25μm, measured at the place 3mm away from the sample center within an effective view field of 1mm×0.12mm. Their corresponding PSDs are presented in Figure 6.9. The result indicates that the dynamic patterns were generated from the vibration. With increasing the depth of cut, surface topographies were enhanced and the PSDs of the characteristic spatial frequency (CSF) obviously increase. This result confirms the previous theoretical results of Chapter 5.

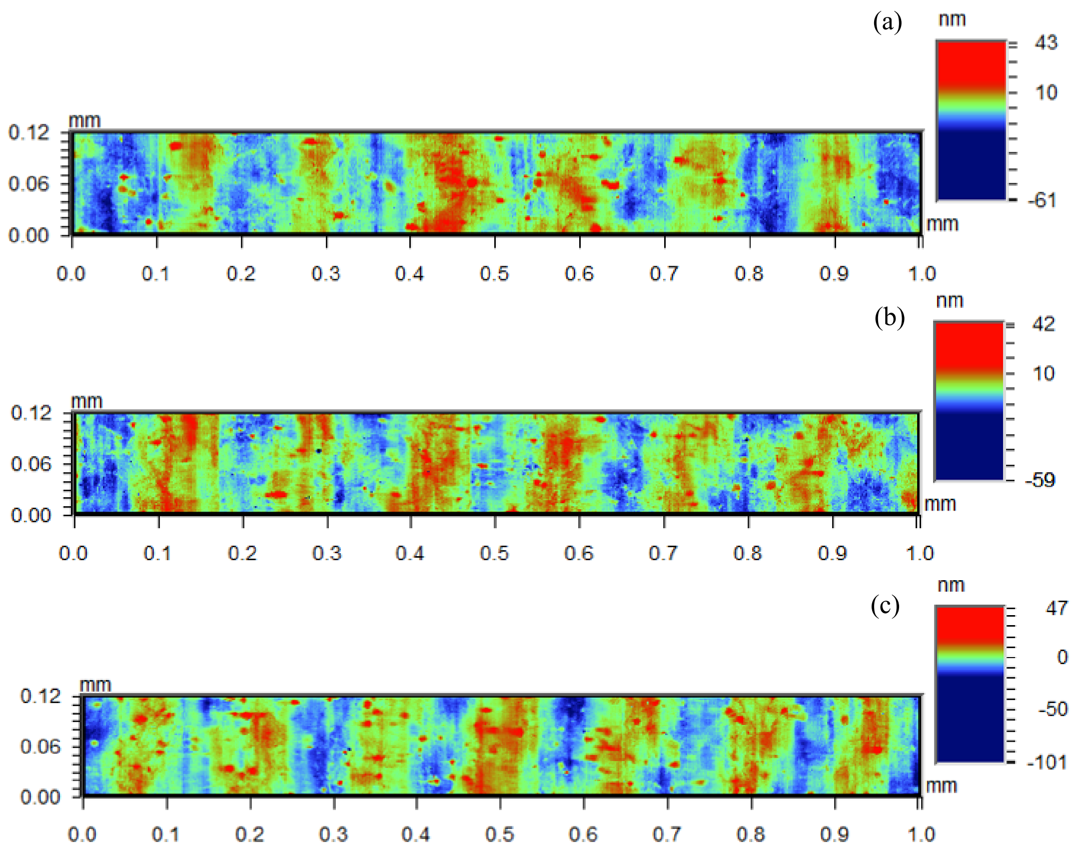

Figure 6.8 Measured surface topographies at the place of 3mm away from the center generated under the cutting conditions: Tool radius of 0.762mm, spindle speed of 3000rpm, feed rate of 0.005mm/rev., depths of cut of (a) 1, (b) 5 and (c) 25μm

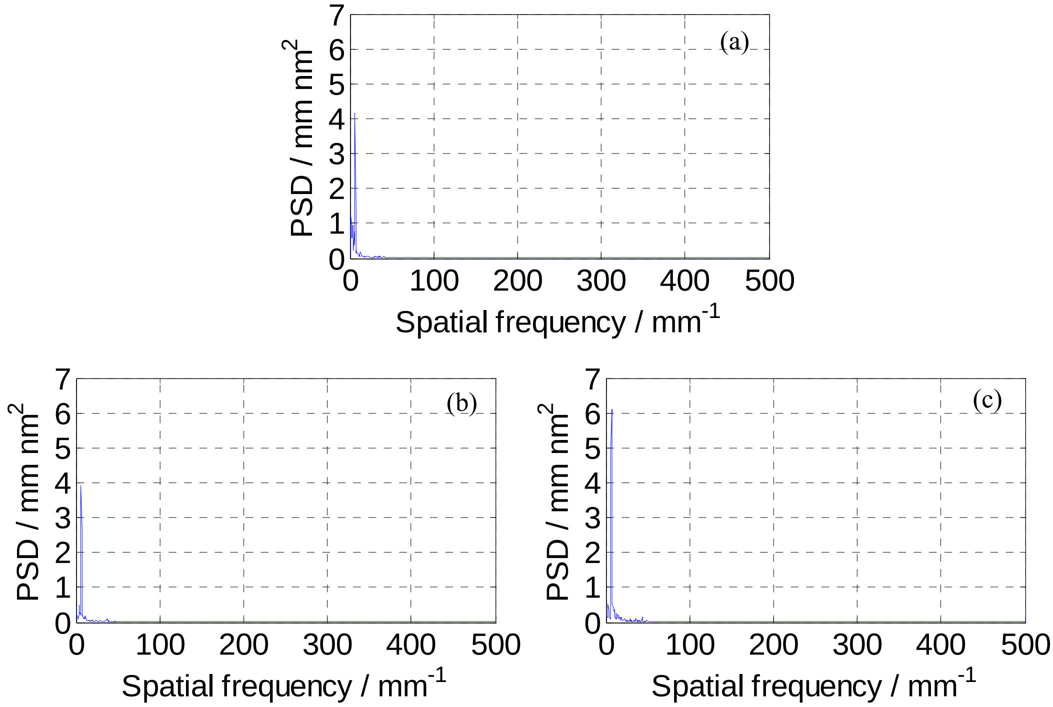

Figure 6.9 Corresponding PSDs of the measured surface topographies in Figure 6.8(a)-(b)

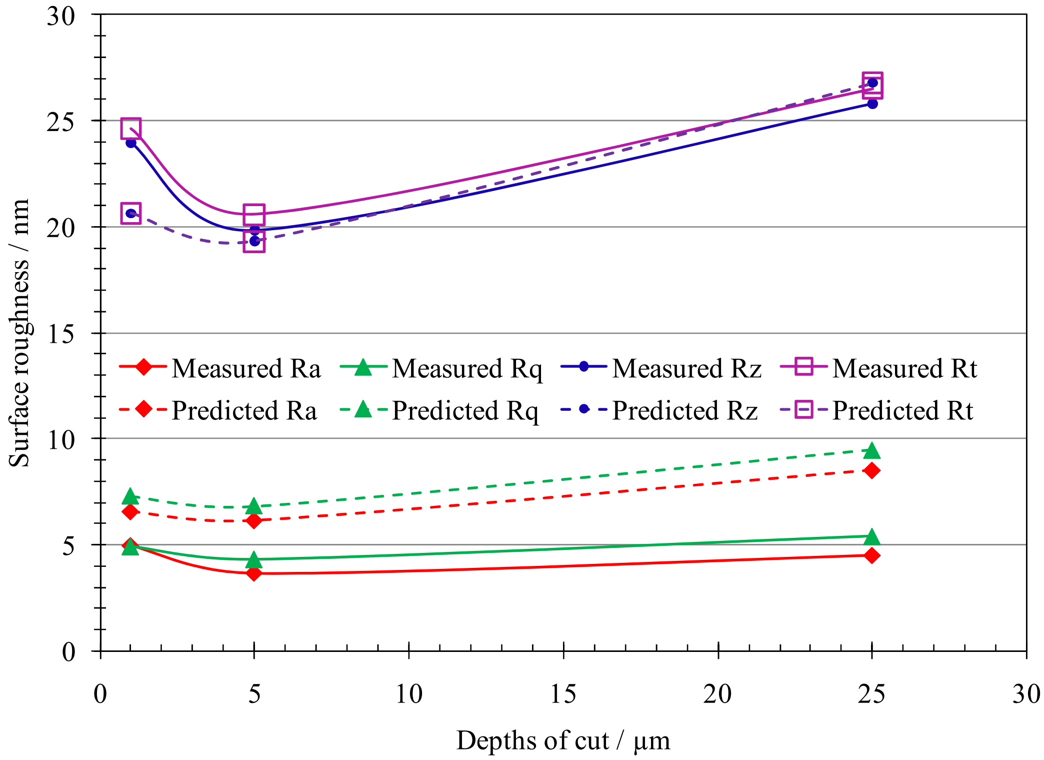

Figure 6.10 Measurend and predicted surface roughness only considering the spindle vibration under various depths of cut

Further, only considering the effects of the spindle vibration on surface topographies, the surface topographies in Figure 6.8 were processed using Fourier Filtering (Low Pass) of the software of the Wyko NT8000 system. The filtering method is efficient to filter the random sharp peaks at the machined surface. Then, the left surface topographies can be considered as that induced by the spindle vibration without the material flow because the material pile-up can be negligible according to the PSD results presented in Figure 6.9. The cutting forces were measured and substituted into the prediction model of the spindle vibration influencing surface generation, i.e. Eq.5-9, to calculate the surface roughness.

In addition, the eccentric distance is ideally set at zero, since the eccentric distance cannot be obtained and the effects relating to the SRF on surface topography cannot be totally measured due to the measured region further less than its effective influencing region. The results are depicted in Figure 6.10. It shows that the predicted surface roughness is close to the measured surface roughness, only considering the effects of the spindle vibration in UPDT. The predicted Ra and Rq are more than the measured Ra and Rq because of the material swelling and recovery not being filtered. This indicates that decreasing the cutting forces is one of efficient ways to improve surface quality. It is interesting to note that when the depth of cut decreases less than 1μm, the cutting forces reversely increase. That can be explained by the fact that when the depth of cut is reduced, ploughing takes a more great contribution than cutting in the material removal process of UPM so that the cutting forces increase.

6.3.4 Effects of Spindle Speeds on Surface Topographies

Cutting speed is another important parameter in the cutting process for increasing the efficiency of removing material. The cutting speed is directly related to the spindle speed and the distance between the tool tip and the surface center. It influences material pile-up. In the previous theoretical results, as the cutting speed increases, the tilting amplitudes do not obviously change. To clearly observe the influence of the cutting speed on surface topography, the machined surfaces were generated under the following cutting conditions: tool radius of 0.128mm, feed rate of 0.005mm/rev., depth of cut of 5μm, spindle speeds of 2000rpm, 3000rpm, 4000rpm, 5000rpm and 6000rpm. These were measured within an effective view field of 1mm×0.12mm at the place 3mm away from the surface center. The measured surface topographies are shown in Figure 6.11 and their corresponding PSDs are plotted in Figure 6.12. Two kinds of characteristic spatial frequencies (CSFs) are shown. As the spindle speeds increase, the PSDs of $200mm^{-1}$ corresponding to the feed rate induced by the tool mark decrease. This shows that the higher the cutting speed is, the smaller the material pile-up. But the PSDs of the other low frequencies at first do not obviously change and then its peak decreases suddenly or disappears sharply. This is because when cutting at the higher cutting speeds, the cutting forces decrease (Zhang, 1991), which results in reducing the amplitudes of the vibration, and because the patterns induced by the phase shift of vibration expand and spread, as shown in Figure 6.11. That supports the theoretical result in Section 5.2.2.3 of Chapter 5. Therefore, the higher the spindle speed is, i.e. the cutting velocity, the better the surface quality is.

To easily observe and estimate the effects of the spindle vibration on surface topographies under different spindle speeds, the surface topography data in Figure 6.8 were dealt with through Fourier Filtering (Low Pass). Then, the left surface topographies were influenced by the spindle vibration and the material flow. According to the PSD results of Figure 6.12, the material pile-up plays a crucial role in surface profiles, since the tool radius is small enough to make the material easily flow. Figure 6.13 shows one profile of the surface topography in Figure 6.11(b) after being filtered by Fourier Filtering. The material pile-up height is about 10nm. It also demonstrates plough ditching, which influences the machined surface height. The plough ditches are induced by the Built-up edge (BUE) formed in the cutting process. Therefore, the three factors make majorly impacts upon the generated surface generation.

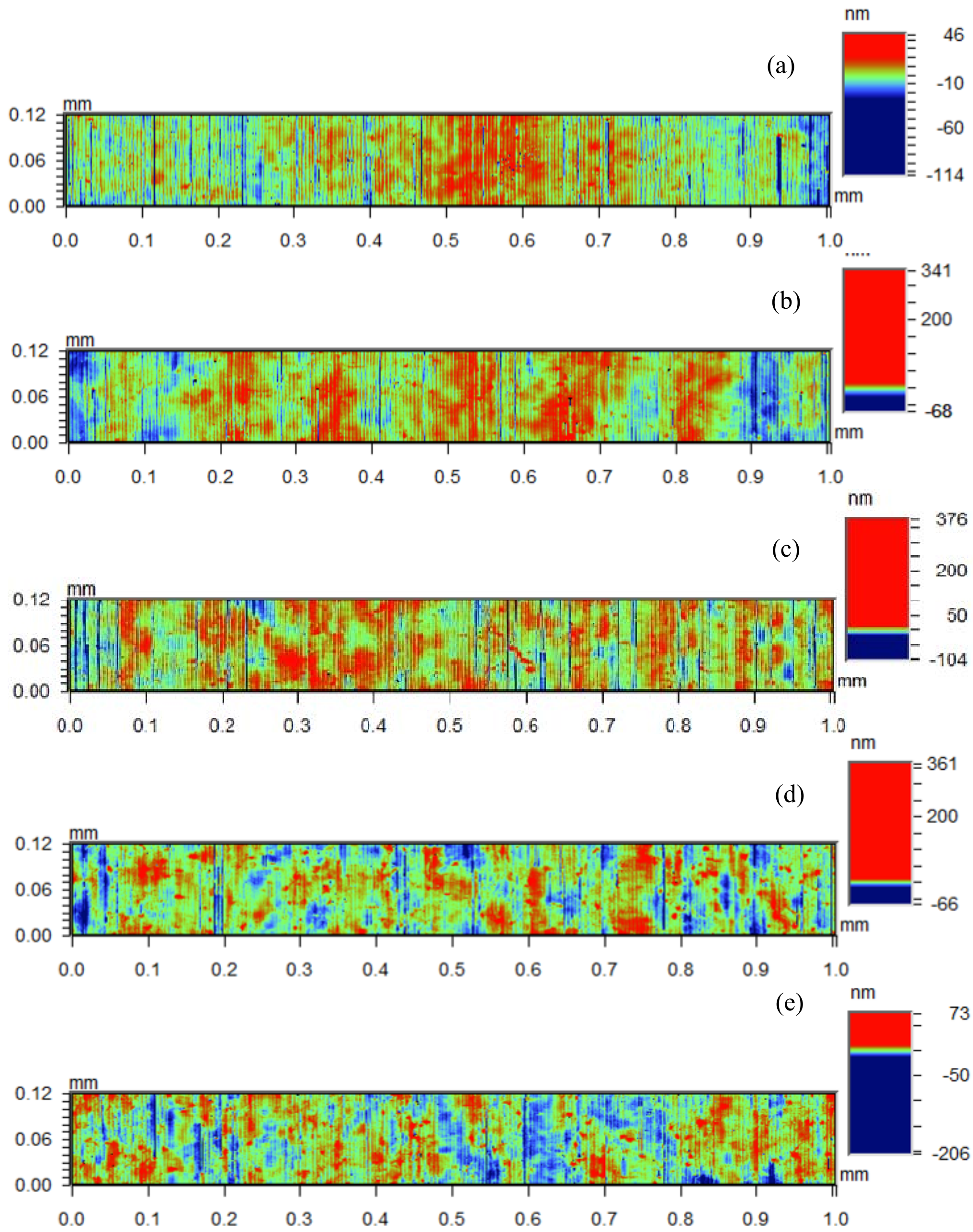

Figure 6.11 Measured surface topographies at the place of 3mm away from the center generated under the cutting conditions: the tool radius of 0.128mm, the feed rate of 0.005mm/rev., the depth of cut of 5μm, the spindle speeds of (a) 2000rpm, (b) 3000rpm, (c) 4000rpm, (d) 5000rpm and (e) 6000rpm

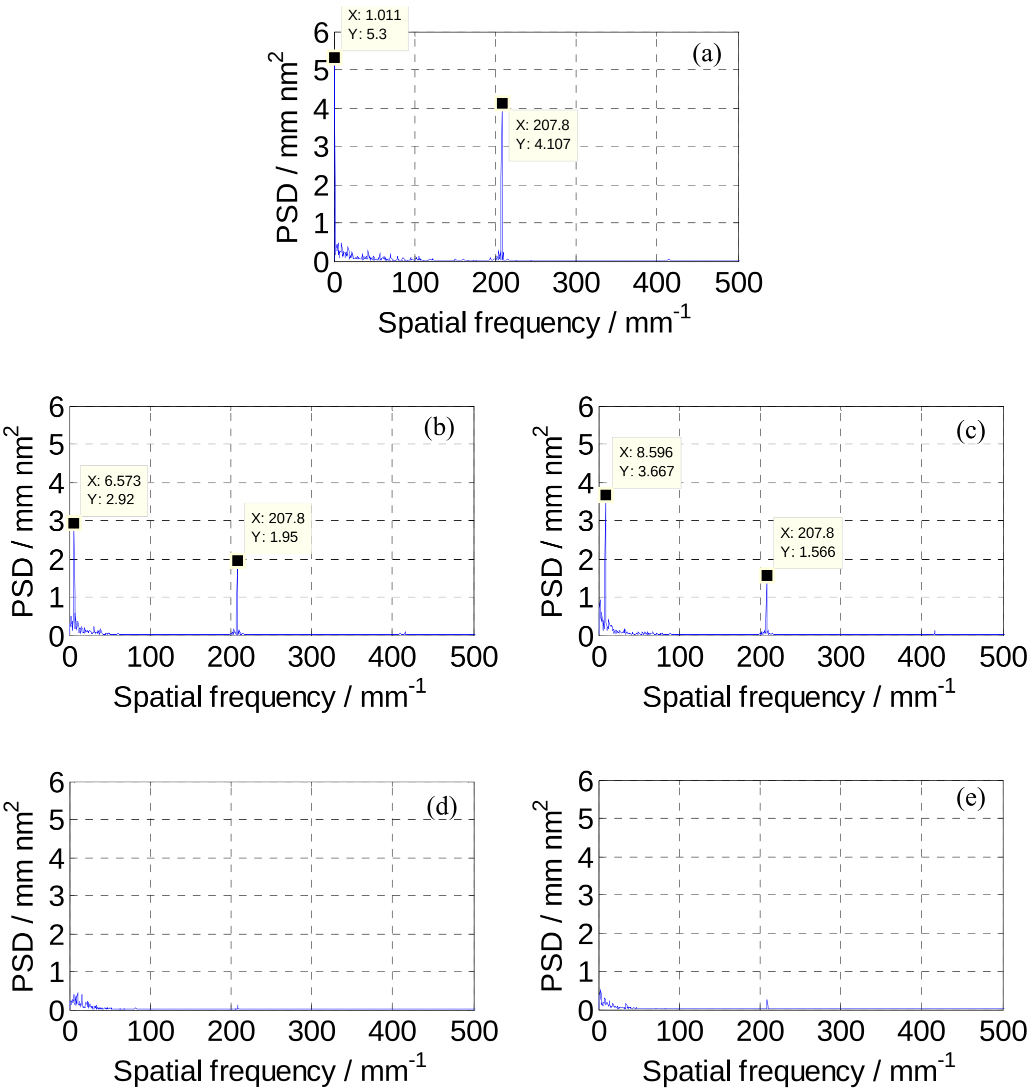

Figure 6.12 PSD plots of the measured surface topographies in Figure 6.11(a)-(e)

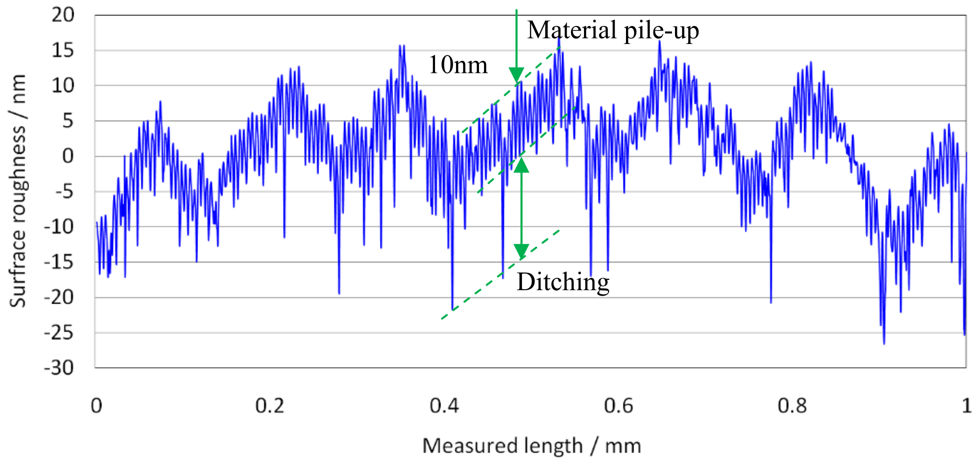

Figure 6.13 A surface profile of Figure 6.11(b)

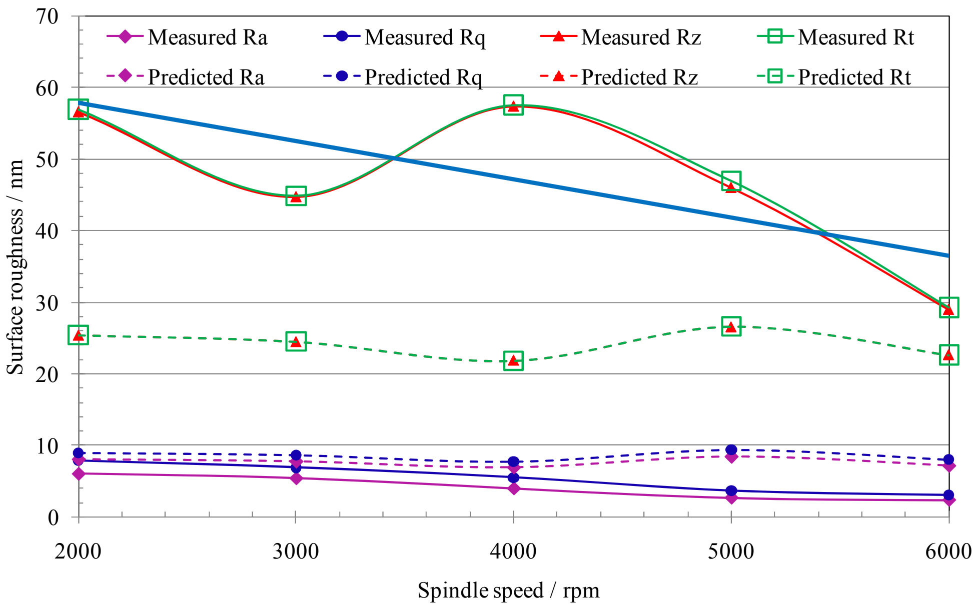

Figure 6.14 Measurend and predicted surface roughness under different spindle speeds

In addition, the cutting forces were measured and substituted into the prediction model of the spindle vibration influencing surface generation, i.e. Eq.5-9, to calculate the surface roughness. The eccentric distance is not considered due to the reasons presented above in Section 6.3.3. The predicted and measured results are pictured in Figure 6.14, which shows that the predicted surface roughness Ra and Rq is higher than the measured surface roughness, since the machined surface material swelled and recovered. This is because the predicted surface roughness Ra and Rq is calculated as only considering the effects of the spindle vibration in UPDT, whereas the measured surface roughness Ra and Rq is related to the vibration effects, the material pile-up, the plough ditches, and the material swelling and recovery. It also explains why the measured surface roughness Rz and Rt is larger than the predicted surface roughness. As the spindle speed increases, the gap between the predicted surface roughness Rz and Rt and the measured surface roughness Rz and Rt decreases, but the gap exists due to the ditches and the material swelling and recovery. Figure 6.14 also indicates that the predicted surface roughness Rz and Rt is almost constant, because the measured cutting forces are not obviously different. Apart from that, as compared with the results of the above section, it can be inferred that the material pile-up and the BUE are easily produced by the relatively small tool radius in the ultra-precision cutting process.

6.4 Experimental Setup in UPRM

6.4.1 Cutting Conditions

All flat-cutting tests were performed on an UPRM machine (Precitech Freeform 705G, Precision Inc., USA) (Appendix II) as shown in Figure 3.3. The UPRM machine system possesses three linear axes (X, Y and Z) and two rotational axes (B and C). A diamond tool is rotated with the spindle being set up on the C axis to intermittently cut a work-piece, and the work-piece is installed on the B axis rotation table. The profile for the machined surface is formed by the repetition of the tool tip profile at intervals of the tool feed rate along the feed direction and intervals of a step distance along the raster direction under cutting conditions by two cutting strategies and two cutting directions.

Table 6.3 Cutting conditions of raster milling

Spindle speed (ω) (rpm) at intervals of 20 rpm	4000~4900
Feed rate (f_r) (µm/rev.)	20
Depth of cut (d_o) (µm)	5, 10, 20
Swing distance (d_1) (mm)	28.48
Step distance (s_r) (µm)	10
Tool nose radius (R_r) (mm)	0.619
Tool rake angle (^{o})	0
Front clearance angle (^{o})	15
Cutting strategy	Horizontal cutting
Cutting mode	Up-cutting

The spindle rotor rotating around the spin axis is flowed and supported by a constant pressure air film, so the intermittent cutting forces and its self-eccentric mass will induce the spindle vibration. The spindle performance specifications of the employed UPRM machine are tabulated in Table 4.5. The experimental tests were carried out on the UPRM machine to flat-mill copper alloys under the cutting conditions of Table 4.6 to observe the impact of spindle vibration on surface topography, and under the cutting conditions of Table 6.3 to discuss the effects of the spindle vibration influenced by spindle speeds and depths of cut on surface topography.

6.4.2 Measurement of Cutting Forces

The cutting force measurement system presented in Section 6.2.2 was directly implanted into the UPRM machine. The Kistler 9252A force transducer was mounted between a work-piece and a fixture positioned on the B-axis with a pre-loading force to sense the cutting forces. The signals of the cutting forces in the three directions were recorded by a NI PCI-6132 14-bit multifunction DAQ card at the sampling frequency 1MHz after being pre-amplified by the Kistler 5011B charge amplifiers. The whole system for the measurement of the cutting forces is shown in Figure 6.15. The uncertainty is less than 0.002N. Since the uncertainty for the predicted surface roughness induced by the uncertainty of measured cutting forces is further less than that induced by other factors, it is not considered in this study.

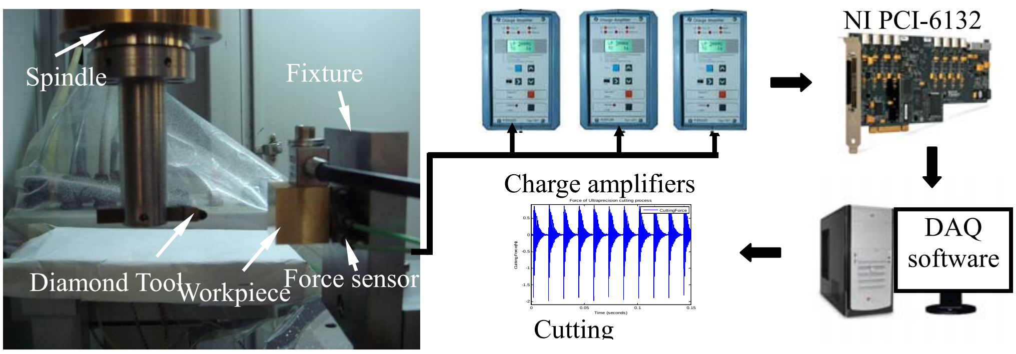

Figure 6.15 Configuration of the cutting force measurement system in UPRM

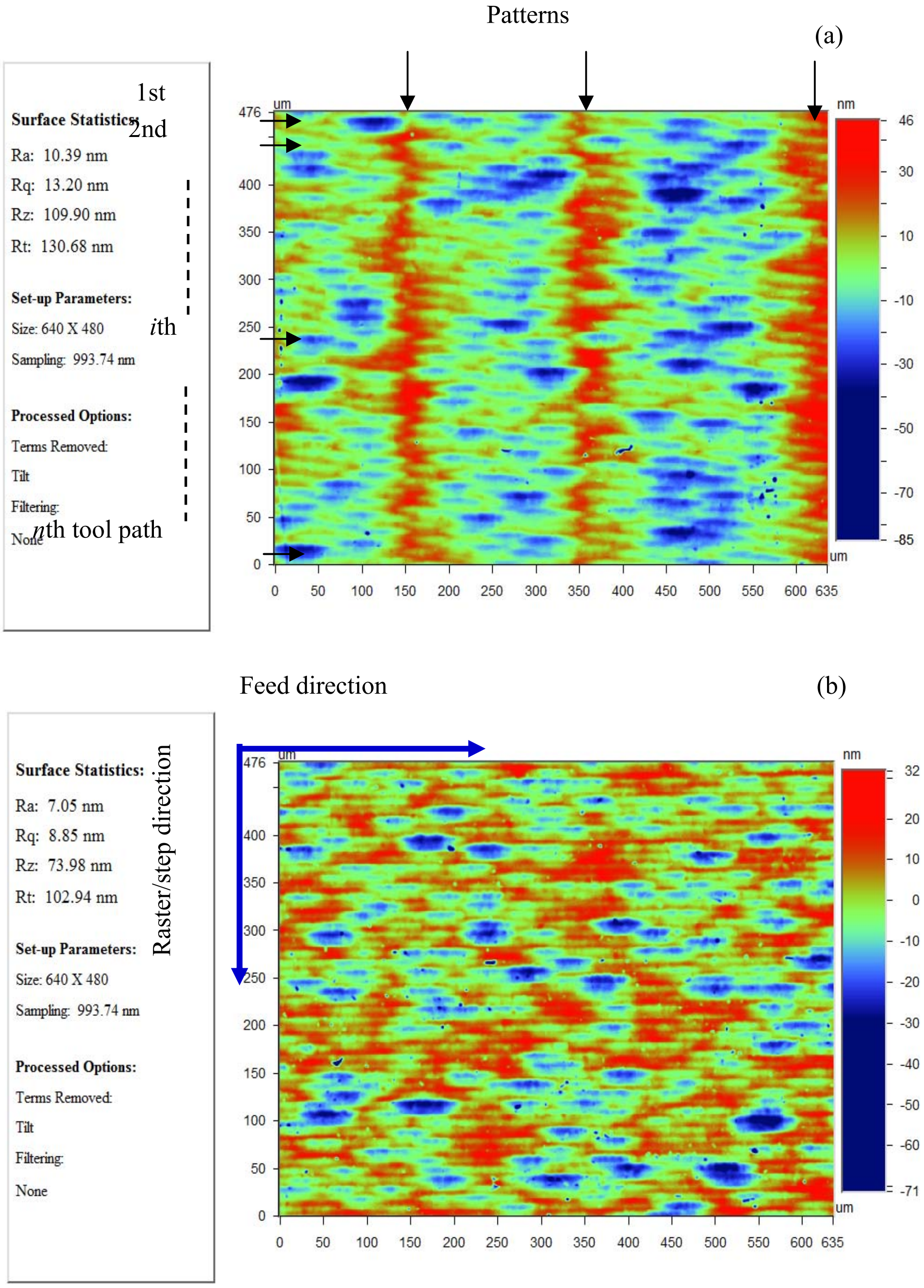

Figure 6.16 Measured surface topographies under horizontal cutting (a) with uniform patterns and (b) with random patterns

6.4.3 Measurement of Surface Topography

In this study, the Optical Profiling System presented in Section 6.2.3 was utilized to measure surface topographies of machined specimens in order to estimate the effects of the aerostatic bearing spindle vibration of UPRM on surface topography. Surface topographies were acquired under an effective magnification within an effective field.

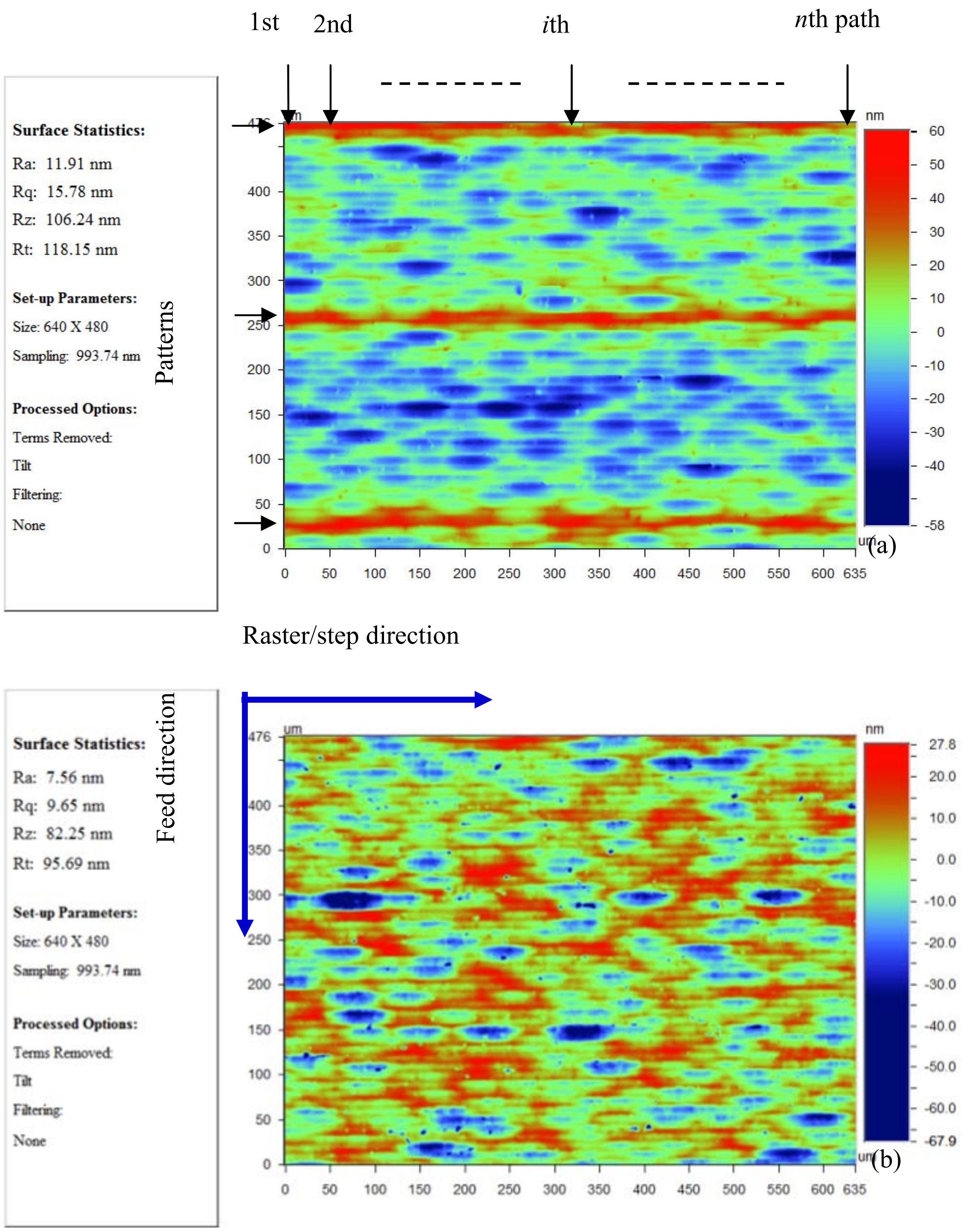

Figure 6.17 Measured surface topographies under vertical cutting (a) with uniform patterns and (b) with random patterns

6.5 Experimental Results and Analysis in UPRM

6.5.1 Surface Characteristics

In UPRM, spindle vibration in each contact time geometrically influences a milled surface through tool loci with inhomogeneous scallops to generate various patterns. Surface topographies milled under the cutting conditions of Table 4.5 by horizontal cutting and vertical cutting in up-cutting were measured by the Optical Profiling System NT8000. Surface topographies were acquired, as shown in Figure 6.16 and Figure 6.17.

In Figure 6.16(a) and Figure 6.17(a), the ribbon-stripe patterns indicated by arrows formed in the raster direction. These patterns were generated by the repetition of the profiles at intervals of a step distance in the raster direction, and the profiles were produced by the repetition of the tool rotation at intervals of feed rate with the spindle-vibration-induced profiles (SVIPs). In raster milling, the dynamic responses of the spindle under the excitation of intermittent cutting forces are the relative distances between the tool and the workpiece, and the relative distances in each contact time form the SVIPs in the feed direction. Hence, the SVIPs produce the patterns through the tool loci or the scallops generated at the milled surface. If the phase shift of each profile for each tool path is uniform, the ribbon-strips patterns are generated as shown in Figure 6.16(a) and Figure 6.17(a) matching the simulation results of Figure 5.15(a). The aliased tool loci are obviously observed, since the SVIPs are not smooth but discrete. The aliased tool locus is known as the run-out.

In Figure 6.16(b) and Figure 6.17(b), the ribbon-stripe patterns disappear and the aliased or lattice-like patterns appear, because the phase shift of each profile is random in the raster/step direction, but the aliased tool loci called the run-out are obviously observed. This is explained by the previous simulation of surface generation as shown in Figure 5.15 and Figure 5.16.

On the whole, the various patterns of surface topographies are produced by the phase shift of the spindle vibration. The ribbon-stripe patterns, the aliased patterns and the run-out phenomenon at the milled surface are explained well by the simulation results of Section 5.3.1.

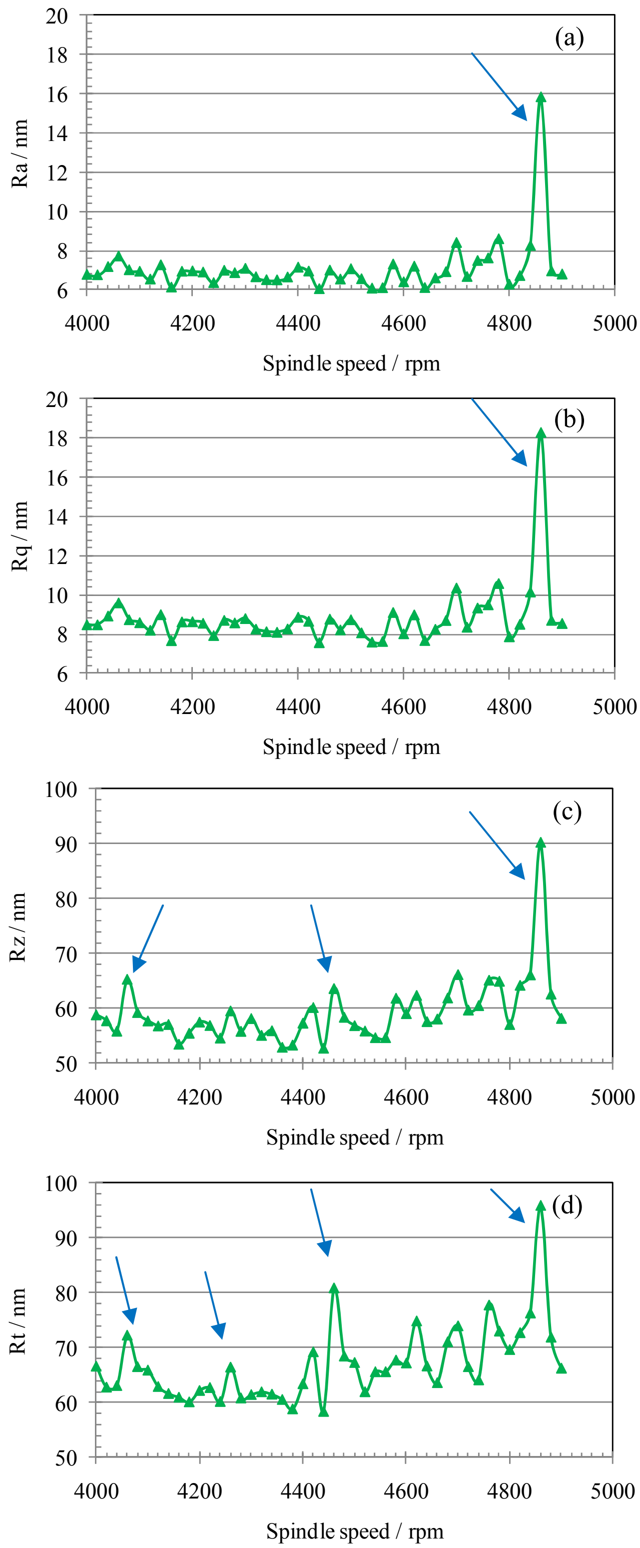

Figure 6.18 Measured surface roughness (a) Ra, (b) Rq, (c) Rz and (d) Rt of Table 6.4

6.5.2 Effects of Spindle Speeds on Surface Topographies

In this section, the effects of spindle speed on surface material pile-up influencing surface topography in UPRM are not majorly discussed, but the effects of spindle speed on the spindle vibration are studied and the vibration will be exhibited at the milled surface topographies. In the experiments, the cutting conditions are: spindle speeds of 4000-4900rpm at the interval of 20rpm, depth of cut of 5μm and others tabulated in Table 6.3. Milled surfaces were acquired by the Optical Profiling System NT8000. The measured surface topographies are shown in Table 6.4. The aliased patterns, the ribbon-stripe patterns and the aliased tool loci (run-out) are clearly observed, which are explained by the simulated surface topographies in Section 5.3.2. The corresponding surface roughness Ra, Rq, Rz and Rt are plotted in Figure 6.18. It demonstrates that, as the spindle speed increases, the surface roughness fluctuates quasi-periodically, and the surface roughness at some spindle speeds is much higher than others, as indicated by the arrows. It can be deduced that if the selection of the spindle speed is not optimal, the surface quality is worse. However, at certain spindle speeds the surface finish is good. The quasi-periodical fluctuation can be explained by the theoretical results of Section 4.3.3.

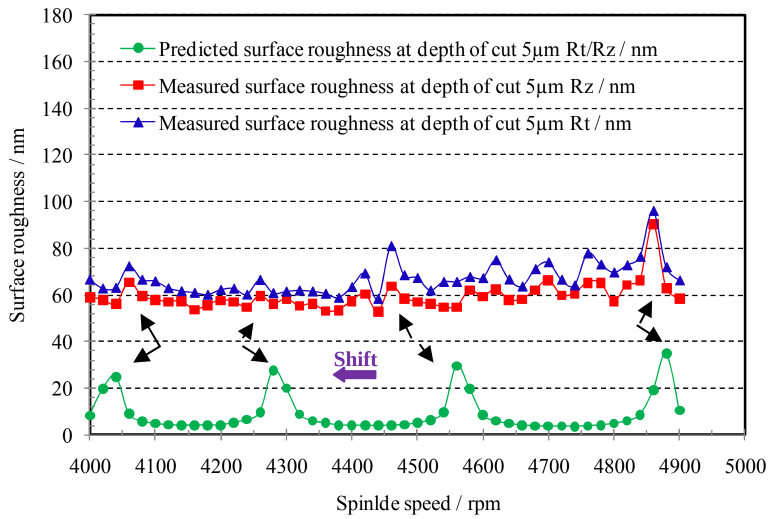

Figure 6.19 Measured and predicted surface roughness Rt under the cutting conditions: the spindle speeds of 4000rpm-4900rpm at the interval of 20rpm, the depth of cut of 5μm and others tabulated in Table 6.3

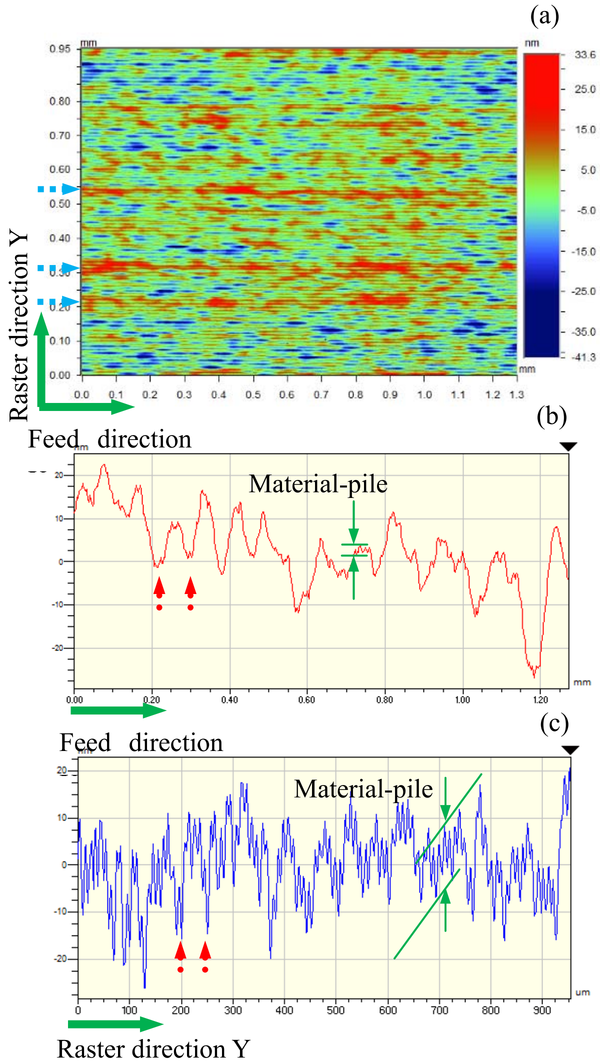

Figure 6.20 Measured surface topography and its profiles milled under the cutting conditions: the spindle speeds of 4900rpm, the depth of cut of 5μm and others tabulated in Table 6.3

Table 6.4 Measured surface topographies being milled under the cutting conditions: the spindle speeds of 4000rpm-4900rpm at the interval of 20rpm, the depth of cut of 5μm and others tabulated in Table 6.3

Spindle speed / rpm	Measured surface topographies	Spindle speed / rpm	Measured surface topographies
4000	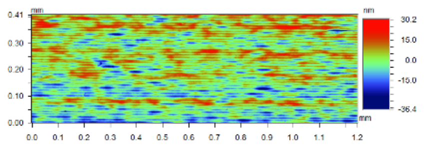	4460	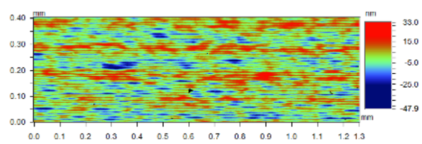

4020	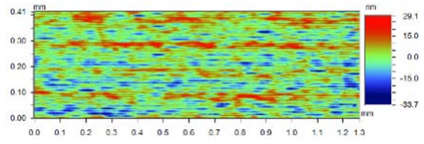	4480	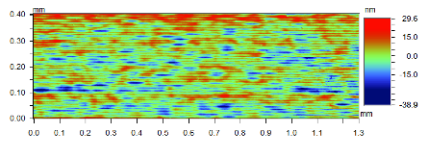
4040	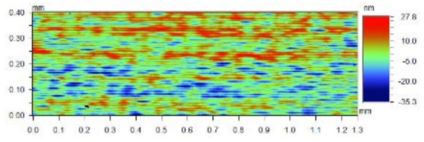	4500	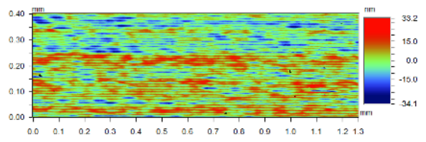
4060	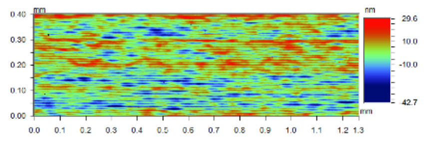	4520	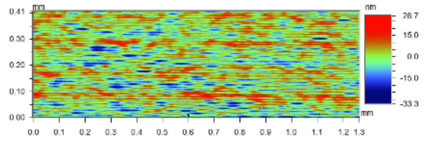
4080	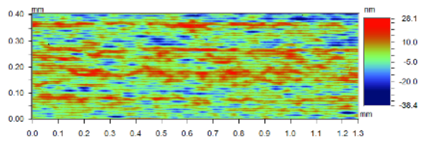	4540	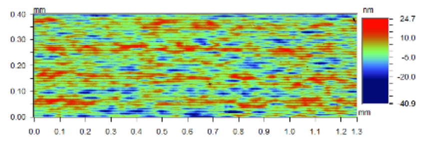
4100	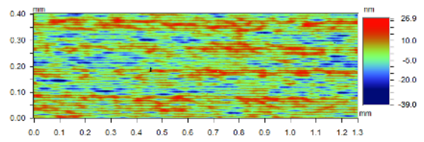	4560	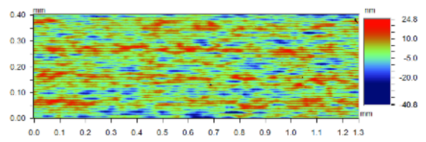
4120	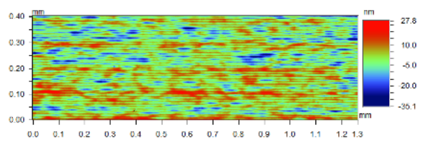	4580	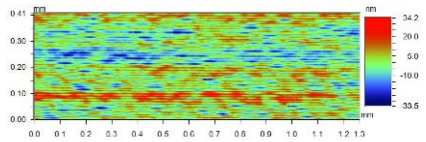
4140	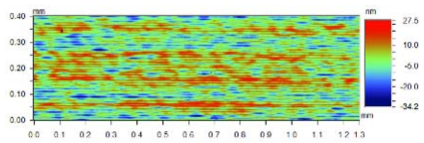	4600	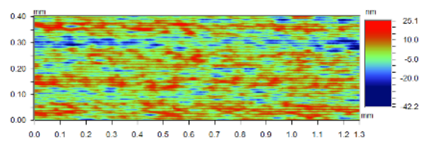
4160	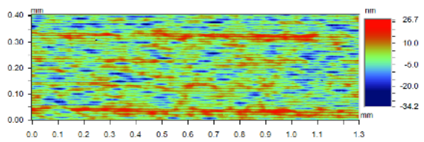	4620	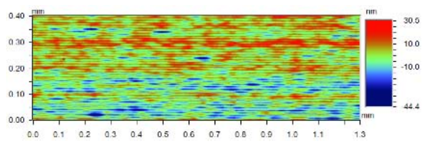
4180	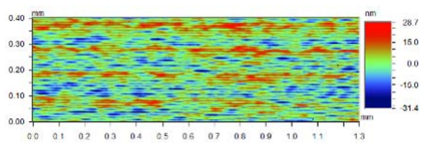	4640	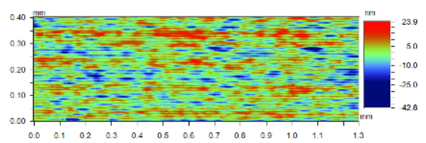
4200	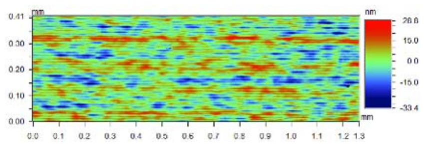	4660	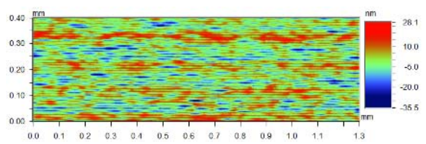
4220	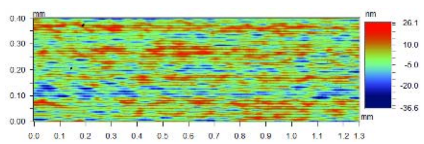	4680	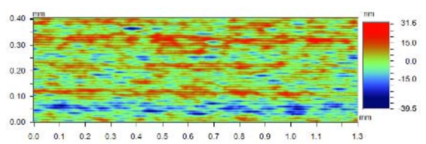

4240	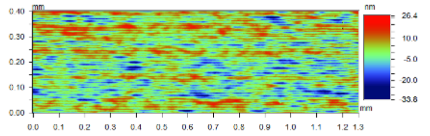	4700	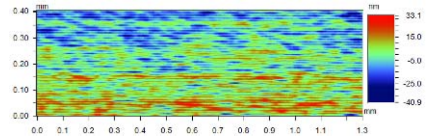
4260	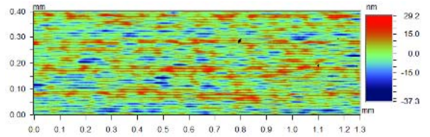	4720	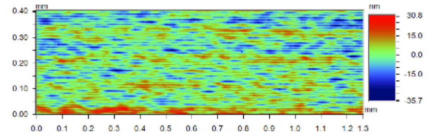
4280	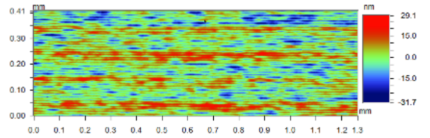	4740	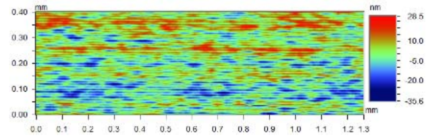
4300	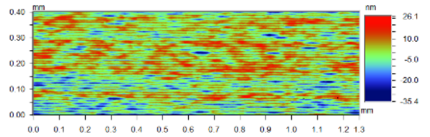	4760	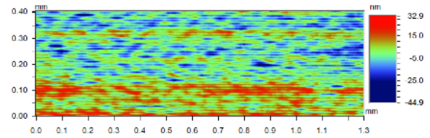
4320	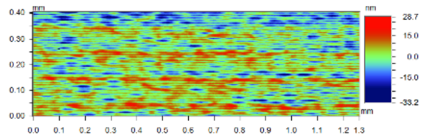	4780	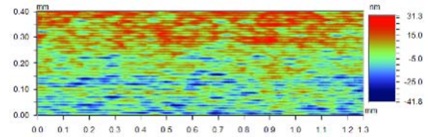
4340	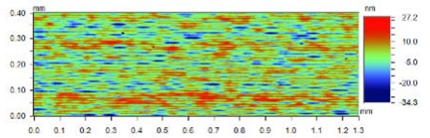	4800	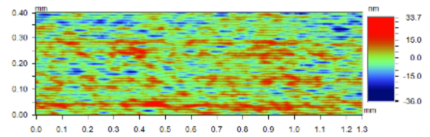
4360	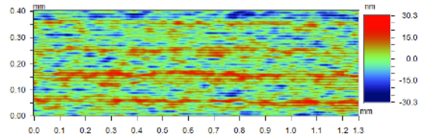	4820	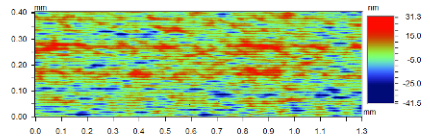
4380	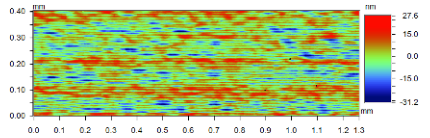	4840	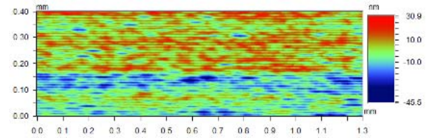
4400	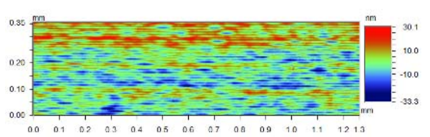	4860	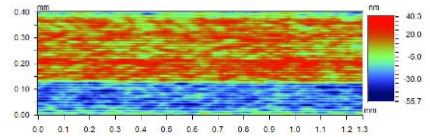
4420	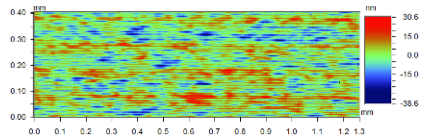	4880	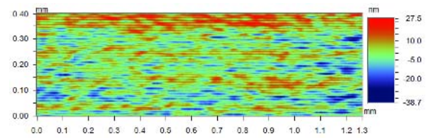
4440	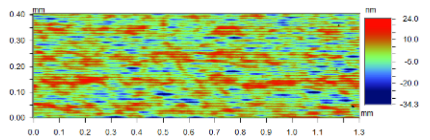	4900	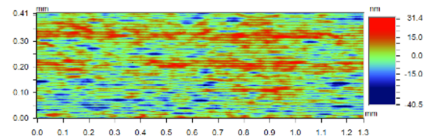

Apart from that above, the cutting forces were measured and substituted into the prediction model of the spindle vibration influencing surface generation for UPRM, i.e. Eq.5-21, Eq.5-22 and Eq.5-23, to compute the surface roughness. Since the prediction model presents the spindle-vibration-induced relative distance between the tool and the workpiece, the surface roughness Rz/Rt is employed to estimate. The predicted and measured surface roughness Rz/Rt is depicted in Figure 6.19. It demonstrates that the variation tendency of the predicted surface roughness Rz/Rt with the increase of spindle speed is consistent with that of the measured surface roughness, but there is a considerable gap between them. Some reasons should be considered: (1) the surface is influenced by the effects of material flow in the cutting process, the material pile-up height in the feed direction measured at 1-2nm, and the material pile-up height in the raster direction is 12-15nm, as shown in Figure 6.20, whose surface was generated under the cutting conditions (spindle speeds of 4900rpm, depth of cut of 5μm and others tabulated in Table 6.3); (2) surface material swelling and recovery increases surface height at about 20nm, as reported by Wang (2010); (3) and due to such things as material swelling and recovery, and spindle speed error, contact time will be increased so that the predicted surface roughness is enlarged (the effect is not discussed in this study). Therefore, the predicted surface roughness Rz/Rt is modified as Figure 6.21. It shows that the predicted results are close to the measured results. Due to the errors of spindle performance specifications and the spindle speed error, the variation tendency will shift as shown in Figure 6.21.

In Figure 6.20, it is interesting to note that the aliased patterns (the lattice-like patterns), the ribbon-stripe patterns and the aliased tool loci (the run-out) were generated through the inhomogeneous scallops, as shown in Figure 6.20(a), the SVIPs change sharply but not smoothly, as indicated by the round-dot arrows in Figure 6.20(b) that plots one profile along the feed direction and in Figure 6.20(c) that depicts one profile along the raster direction. This supports that the various patterns generated through the inhomogeneous scallops are determined and influenced by the phase shift of the SVIPs and the dynamic responses of the spindle vibration under the intermittent cutting forces of UPRM. All in all, the experimental results verify the previous theoretical results with regard to the prediction model in Section 5.3.2.3 and the optimization model in Section 5.3.2.4 of Chapter 5.

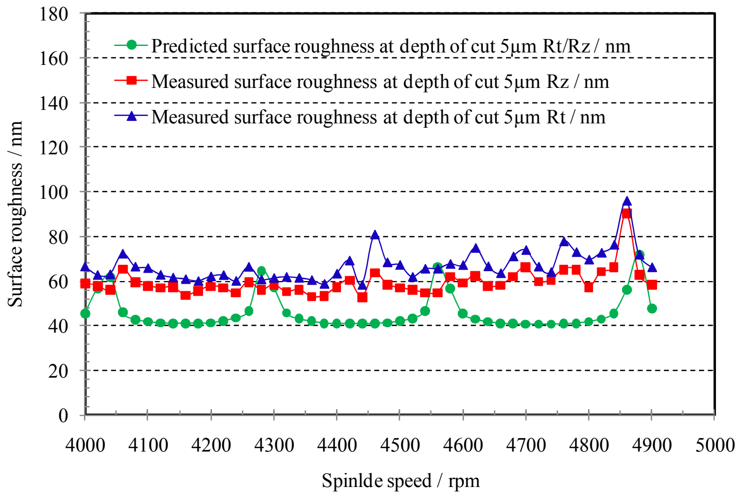

Figure 6.21 Measured and predicted surface roughness Rt/ Rz under the cutting conditions: the spindle speeds of 4000rpm-4900rpm at the interval of 20rpm, the depth of cut of 5μm and others tabulated in Table 6.3

6.5.3 Effects of Depths of Cut on Surface Topographies

In this section, the effects of depth of cut on the spindle vibration are discussed by measuring the milled surface topographies. A series of cutting experiments were conducted in UPRM under the cutting conditions of Table 6.3. The milled surfaces were acquired by the Optical Profiling System NT8000, and the cutting forces were measured by the cutting force measurement system (as shown in Figure 6.15) simultaneously. The measured surface roughness Ra, Rq, Rz and Rt is depicted in Figure 6.22. Along with the increase of spindle speed, the surface roughness fluctuates quasi-periodically, and the surface roughness at some spindle speeds is heavily higher than others, as indicated by the arrows. This indicates that the selection of spindle speed is extremely important. Apart from that, with an increasing depth of cut, the surface roughness evidently increases. The experimental results identify the theoretical results in Section 4.3.3 and Section 4.3.3 of Chapter 4.

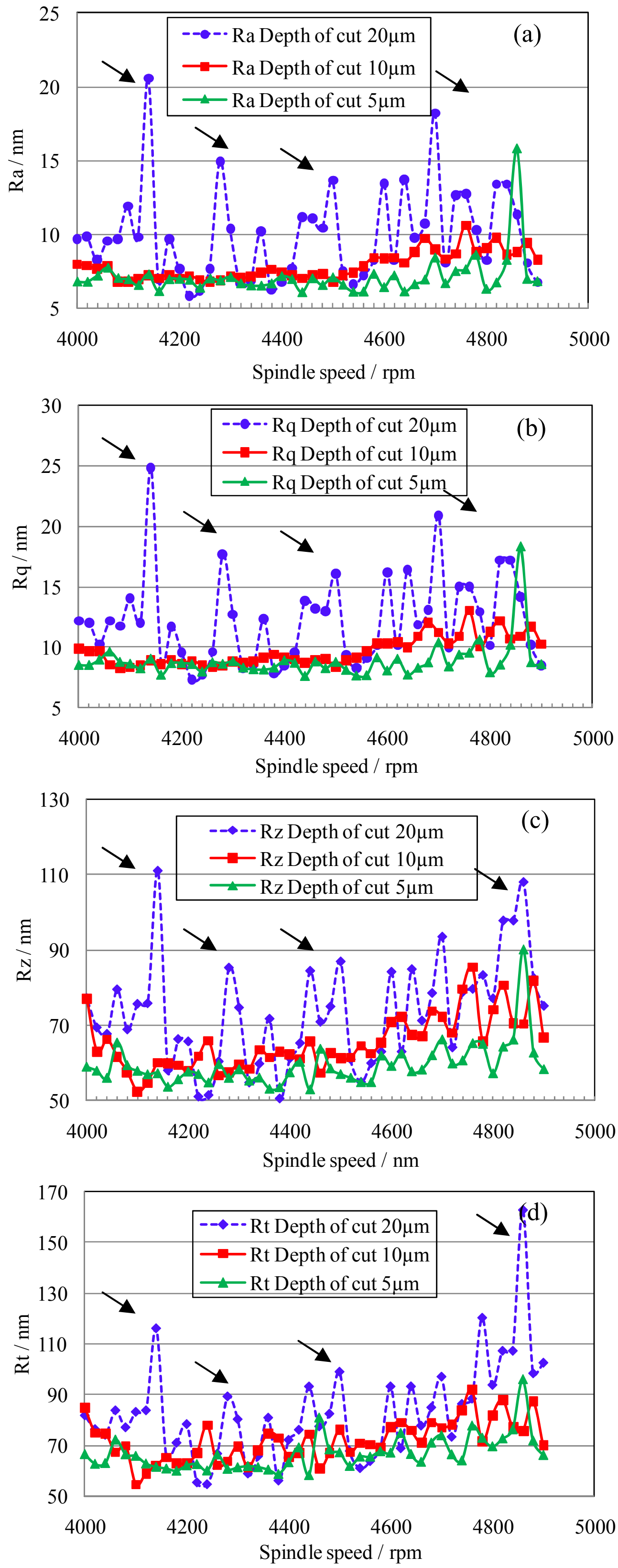

Figure 6.22 Measured surface roughness (a) Ra, (b) Rq, (c) Rz and (d) Rt generated under the cutting conditions of Table 6.3

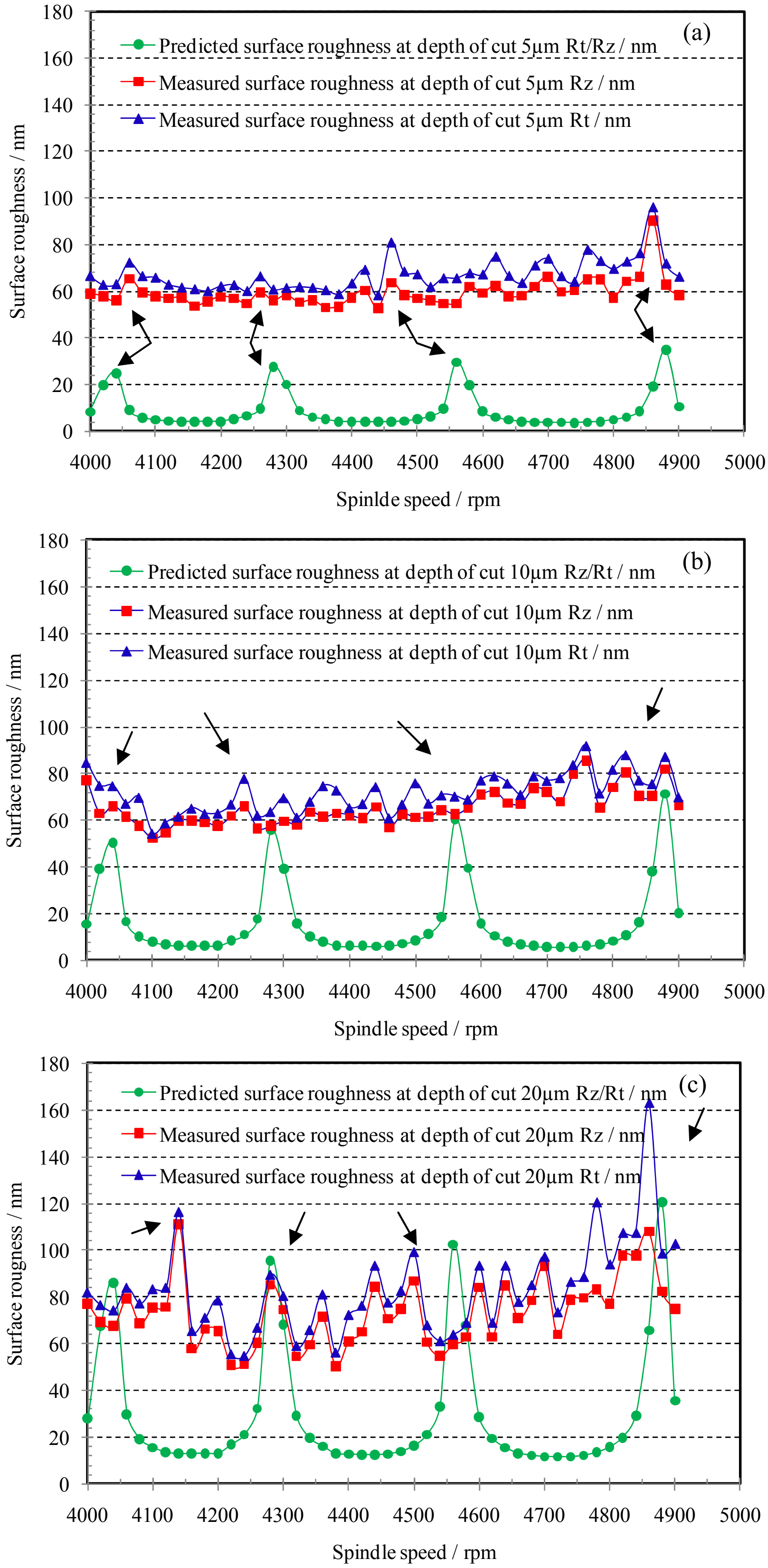

Figure 6.23 Measured and predicted surface roughness Rz and Rt under the cutting conditions of Table 6.3 with the depths of cut of (a) 5μm, (b) 10μm and (c) 20μm

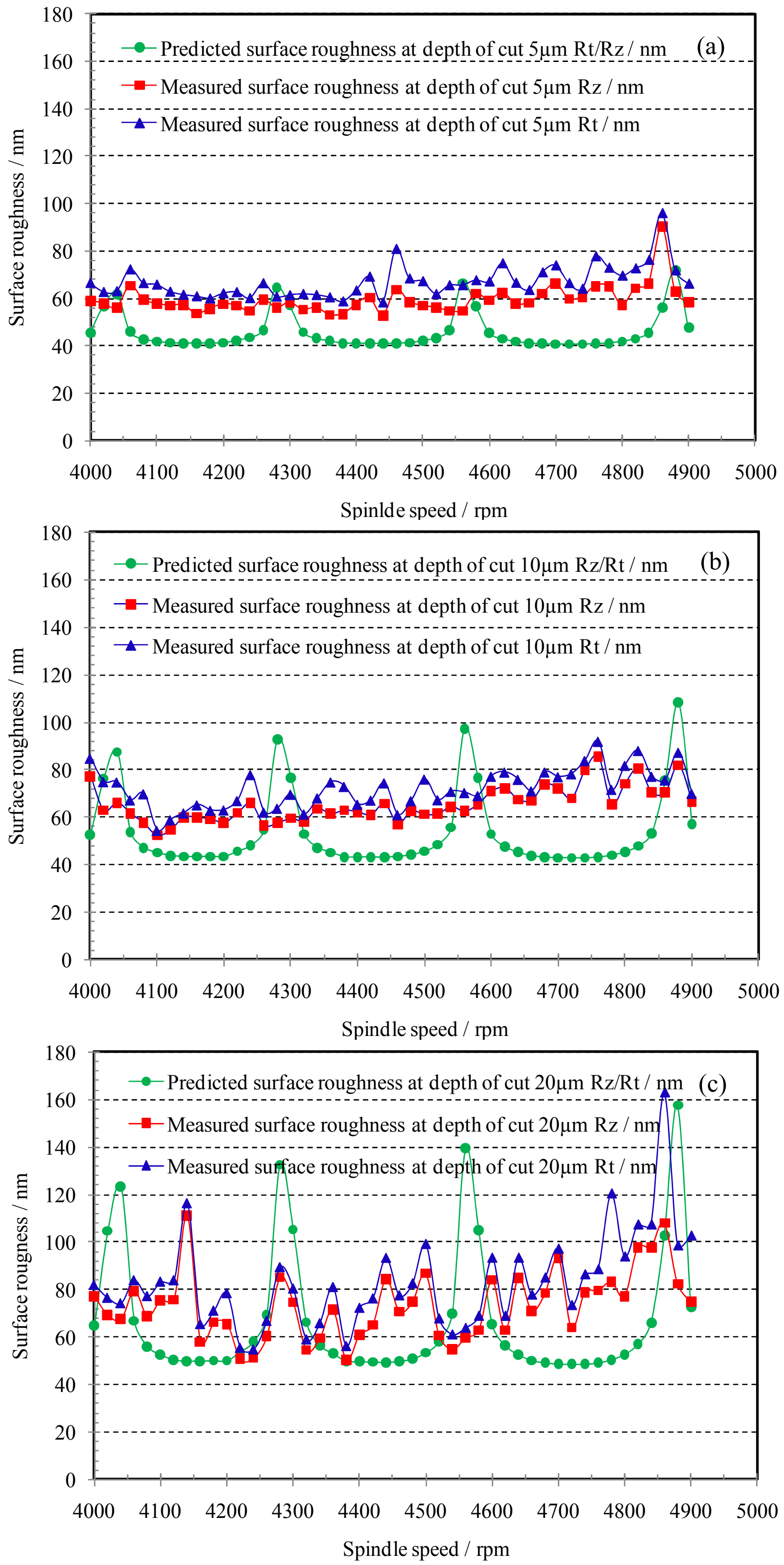

Figure 6.24 Measured and modified-predicted surface roughness Rz and Rt under the cutting conditions of Table 6.3 with the depths of cut of (a) 5µm, (b) 10µm and (c) 20µm

According to Eq.5-21, Eq.5-22 and Eq.5-23, the predicted surface roughness Rz/Rt under the cutting condition of Table 6.3 is depicted in Figure 6.23 with the measured surface roughness. Adding the effects of material flow (the material pile-up height in the feed direction is measured at 1-2nm and the material pile-up height in the raster direction is 12-15nm, as shown in Figure 6.20) and surface material swelling and recovery (surface height at about 20nm), the predicted surface roughness Rz/Rt is modified, as shown in Figure 6.24 with the measured surface roughness. The variation tendency of the predicted surface roughness is consistent with that of the predicted surface roughness at a certain shift, and the optimization can be conducted to achieve the best surface quality at some certain spindle speed. This confirms that the predicted model can be used to predict surface roughness in UPRM.

6.6 Summary

In this chapter, to verify the dynamic characteristics of spindle vibration and its effects on surface topography in UPDT and UPRM, a series of cutting experiments were executed. The major findings are summarized as below:

(i) In UPDT, the dynamic characteristics of a series of measured cutting forces identify the multi-frequency characteristics of the employed aerostatic bearing spindle, including the spindle rotational frequency (SRF), the radial frequencies, the axial frequency and the coupled tilting frequencies (CTFs), which are obtained according to the results of Chapter 4 based on the five-degree-of-freedom dynamic model of the spindle developed in Chapter 3, using the power spectral density (PSD) technique.

(ii) The machined surfaces clearly present the surface topographies with the periodic concentric, spiral, radial, and two-fold patterns (PCSRPs) as proposed in the simulation of surface generation, and the surface patterns reveal that the vibration originates from the spindle of UPDT.

(iii) The experimental results in UPDT indicate that the effects of the depth of cut boost the spindle vibration that influences the surface topographies, and the spindle speed without the eccentric distance does not clearly increase the spindle vibration.

(iv) The developed prediction model based on the dynamic model of the spindle can be used to predict and optimize the surface generation in UPDT, which is identified by the machined surface topographies under various cutting conditions. The results demonstrate that the spindle vibration, material swelling and recovery and material pile-up mainly influence the surface profiles, and the material pile-up can be reduced by increasing the spindle speed and the tool radius.

(v) In UPRM, the milled surfaces under various cutting conditions identify that the generated aliased patterns, ribbon-stripe patterns and aliased tool loci are induced by spindle vibration, as supported by the simulation of surface generation of Section 5.3.2.1. The run-out phenomenon at the ultra-precision raster milled surface is induced by the spindle vibration under the intermittent cutting forces of UPRM.

(vi) The developed prediction model in UPRM based on the dynamic model of the spindle can be employed to precisely predict surface roughness. The experimental results present that the spindle vibration, the material swelling and recovery and the material pile-up contribute to surface profiles in UPRM and the shift length produces an uncertainty for surface roughness.

(vii) The selection of spindle speed in UPRM to minimize surface roughness based on the dynamic simulation of Chapter 4 or the optimization model developed in Chapter 5 is confirmed by a series of cutting experiments.

(viii) It is interesting to note that the frequency of the intermittent cutting forces in UPRM, i.e. the SRF, influences the dynamic responses of the spindle. It is therefore extremely important to find the best surface quality that can be achieved under certain cutting conditions for a specific machine, which will contribute significantly to the further improvement of ultra-precision raster milling for the optimization and prediction of surface topography.

Chapter 7 Conclusions and Suggestions for Future Studies

7.1 Overall Conclusions

In ultra-precision machining (UPM), surface integrity is influenced by many factors, such as (i) cutting conditions and machining parameters of tool tip radius, spindle speed, depth of cut, and feed rate; (ii) material properties of crystallographic orientation and anisotropy as well as micro-structural changes, and the elastic and plastic properties in relation to the phenomena of material pile-up, material swelling and recovery; (iii) the dynamic characteristics of machine tools such as tool vibration, spindle vibration and slide vibration etc.; and (iv) tool wear and its indirect adverse effects. Surface roughness or surface topography is a deterministic means for evaluating the quality and integrity of the component surface produced by UPM, which directly determines the performance, functional life and stability of the component. Since UPM provides an enhanced machining accuracy for the machined components with sub-micrometric form accuracy and nanometric surface roughness, it is widely employed in the production of components of symmetric, asymmetric and freeform surfaces for optics, photonics, and telecommunication applications that are in great demand across all sectors of society. Therefore, a better understanding of the surface generation mechanism in UPM is vital for further development and improving designs of ultra-precision machine tools to meet the need for higher achievable precision in the future.

Since many factors affect the machined surface topography including surface profiles, waviness, form error, etc. in UPM, substantial research interest has been attracted to studying the principle of surface generation, the modeling and prediction for surface roughness and the optimization for surface generation, with particular emphasis on ultra-precision raster milling (UPRM) where, due to its operating complexity, the surface quality depends largely on the selection of cutting conditions and cutting strategies. Traditionally, it mainly relies on the technician's experience and skills to maintain high-quality surface finish through an expensive trial-and-error approach. Although some significant research has been conducted to develop the practical models for surface generation, prediction and optimization, the effects of the aerostatic bearing spindle vibration of UPM on surface topography of a machined surface have not attracted sufficient attentions and been taken into consideration. Therefore, the dynamics of aerostatic bearing spindle vibration and its effects on surface generation in UPM are addressed in this thesis.

The answers to the critical problems mentioned above have been sought with the following steps: (i) building up a five-degree-of-freedom dynamic model for the vibration of aerostatic bearing spindle in UPM under the external excitations imposed by cutting forces; (ii) discussing the dynamic characteristics of spindle vibration and deriving the analytic solutions for the dynamic responses of the spindle under external excitations; (iii) modeling of surface generation and explaining the forming principle of surface topography in the ultra-precision cutting process based on the mechanism of micro-cutting and material removal; (iv) developing the prediction and optimization models based on the analytic solutions for the dynamic model of the spindle vibration; and (v) carrying out a series of cutting experiments to verify the simulation results by the proposed theoretical models. A summary of the major findings and their significance in the theoretical and experimental study of spindle vibration and its influence on surface generation in UPM are given as below:

(1) Based on the linear momentum principle of Newton and the angular momentum principle of Euler, a five-degree-of-freedom dynamic model for aerostatic bearing spindle vibration under the excitation of cutting forces of UPM is developed to explore the dynamic characteristics of spindle vibration with the linearization of Newton-Euler equations of motion.

(2) The dynamic responses of spindle vibration are expressed by the analytic solutions to the linearized Newton-Euler equations, which are confirmed by the numerical simulation of the proposed dynamic model. The dynamic responses of spindle vibration under the excitation of its inertial, external

forces and the resultant moments of the external forces are periodic, sub-harmonic, quasi-periodic and coupled-periodic in the radial, axial, tilting and directions, respectively. Spindle speed, cutting forces and contact time make a quasi-quadratic, quasi-linear and linear impact upon the dynamic responses of the spindle vibration, respectively

(3) According to the proposed dynamic model of spindle vibration, the frequency characteristics of spindle vibration consist of the axial frequency, the radial frequencies and the coupled tilting frequencies (CTF) influenced by the spindle rotational frequency (SRF). They are identified by the characteristics of cutting forces in UPDT using the technique of power spectral density (PSD) analysis based on fast Fourier transform (FFT).

(4) In ultra-precision diamond turning (UPDT), a surface generation model integrated with the dynamic model is built up. It reveals that the spindle vibration produces the periodic concentric, spiral, radial, and two-fold patterns (PCSRPs) on the simulated surface, which are in agreement with the measured surface topographies in the cutting experiments.

(5) In ultra-precision raster milling (UPRM), the aliased or lattice-like patterns, the ribbon-stripe patterns and the aliased tool loci (run-out) are observed in the experimental results. It is explained by a developed surface generation integrated with the proposed dynamic model in UPRM that these patterns result from the spindle-vibration-induced profiles (SVIPs) along the feed direction which are discrete and determined by the dynamic responses of the spindle excited by the intermittent cutting forces.

(6) Prediction and optimization models for surface generation of UPM are proposed. The experimental results have verified that these models are applicable for the prediction of surface roughness under various cutting conditions and the selection of optimal machining parameters. Particularly in UPRM, the optimal selection of spindle speed has been identified as pivotal task to minimize surface roughness and improve surface quality.

On the whole, the theoretical and experimental study of the thesis contributes to a deeper insight into the dynamic characteristics of aerostatic bearing spindle vibration and its effects on surface generation in UPM. The proposed dynamic model provides a better understanding of the dynamic characteristics of spindle vibration in UPM and assistance of the outcome of machine tool design. The newly developed prediction models are applicable to predict surface roughness in UPM, and the established optimization models are significant for the selection of optimal machining parameters in UPM to improve surface quality. Further, this study makes a contribution to the advancement of the state-of-the-art in UPM, involving the enabling technology of the spindle design and analysis and the mechanism of material removal in UPM and surface generation.

7.2 Suggestions for Future Work

Ultra-precision machining (UPM) is widely employed to directly produce high quality surfaces without any need of subsequent post-polishing. The achievable surface finish is determined by the process factors, the material factors and the dynamic factors in machining. The spindle system of UPM is the sole power source to remove surface material. Its complex dynamic behaviors as well as the complex UPM system are not perfectly understood. The following are some suggestions for the related topics in further studies.

(1) In-situ measurement of diamond tool wear and its effects on surface integrity in UPRM

Ultra-precision raster milling (UPRM) with a single crystal diamond tool is an advanced manufacturing process for machining freeform surfaces with nano-metric surface roughness and sub-micrometric form error. In relation to long-time milling processes, diamond tool wear plays an extremely important role because a slight degradation of a diamond tool will lead to poor surface integrity in UPRM. In UPRM, the time required for setting up is much longer than that in conventional machining.

More importantly, the machining time is generally several weeks for the manufacture of freeform products. If tool failure takes place, the previous setup time and the previous machining time will be wasted, which reduces productivity and induces considerable economic loss. In order to improve both the quality of the fabricated components and productivity, the critical issues of monitoring and predicting tool wear must be soundly solved. Various studies on tool wear in single point diamond turning or conventional machining have been conducted by researchers, but little attention has been paid to monitoring and predicting diamond tool wear in UPRM and few researchers have focused on studying the effects of tool wear on surface material properties in UPRM, where ensuing changes will significantly influence the fatigue life of components.

In the author's preliminary work, a novel auto-regressive 3D tool wear measurement algorithm was firstly identified, where 3D topographies of diamond tool wear lands were reconstructed based on an auto-regressive method with the digital signal processing technique to in-situ monitor diamond tool wear using a CCD camera with 100X microscopy lens to extract diamond tool wear features. Furthermore, a self-adaptive predictive model was developed to control the machining time and to predict tool wear stages by using linear and non-linear least square methods to avoid tool failure and control the quality of components. Finally, the effects of tool wear on machining of the heat-treatable Zn-Al alloys under different tool wear stages were discussed using different methodologies. The surface structural changes were studied by X-ray Diffraction (XRD) and Back-scattered Electron Mode (BSEM), and the hardness of the machined surface was measured with a nano-indentation test statistically based on a multi-measured method.

In the following work with a series of cutting experiments, an in-situ 3D measurement system of tool wear will be firstly implemented on an ultra-precision raster milling machine Precitech Freeform 705G to in-situ detect diamond tool wear. Secondly, based on experimental results, the measurement and prediction methods of tool wear will be developed. Finally, the effects of tool wear on machining of aluminum and copper single crystals will be discussed in depth based on the previously established methods, where power spectral density (PSD) analysis and a data dependent system (DDS) will be utilized to evaluate the topographies of the machined surfaces measured by an optical profiling system.

The proposed novel 3D in-situ measurement system can be directly mounted on the Precitech Freeform 705G machine which greatly facilitates the in-situ monitoring of diamond tool wear to control the surface quality of components. The developed self-adaptive prediction model is applied to significantly improve productivity by reducing unnecessary economic loss.

(2) Robust stability of spindle system and the spindle vibration measurement in UPM

According to the five-degree-of-freedom dynamic model developed in Chapter 3, the stability of spindle system should be further discussed based on the Nyquist stability criterion because the performance specifications of the system determine the system's reliability, performance and effects on surface quality in UPM. With an in-depth understanding of the spindle features, this research will help further development and better designs of ultra-precision machine tools. In addition, the measurement of spindle vibration can be applied to calibrate the spindle performance specifications for more accurate prediction and optimization of surface generation so as to improve surface quality. Furthermore, the phase shift and the shift length influence surface profiles, and due to various errors they are not precisely enough controlled in the practical system mentioned in Chapter 5. If the spindle performance specifications can be calibrated with elevated accuracy, the surface quality can be improved even more significantly. Thus, it is necessary to conduct more quantitative research in this respect.

(3) Investigation into the relationship between the material pile-up and the cutting conditions in UPM

In the metal cutting process, the material flow has an important influence on surface quality, which is experimentally observed in Chapter 6. The preliminary experimental results show that the larger the tool radius is, the lower the material pile-up is, while the higher the spindle speed is, the smaller the material pile-up is. However, no theoretical model has been proposed to consider spindle speed and other factors in the study of such relationship between different factors in relation to the machining process. In the future work, systematic experimental work is needed to establish a theoretical model and the finite element (FE) modeling technique is required to describe the effect of material pile-up on the accurate prediction of the surface roughness in UPM.

References

Abouelatta, O.B. and Mádl, J., "Surface roughness prediction based on cutting parameters and tool vibrations in turning operations", *J. Mater. Process. Technol.*, Vol.118, pp.269-277 (2001).

Adiletta, G., Guido, A.R. and Roosi, C., "Nonlinear dynamics of a rigid unbalanced rotor in short bearings. Part I: Theoretical analysis", *Nonlinear Dynam.*, Vol.14, pp.57-87 (1997a).

Adiletta, G., Guido, A.R. and Roosi, C., "Nonlinear dynamics of a rigid unbalanced rotor in short bearings. Part II: Experimental analysis", *Nonlinear Dynam.*, Vol.14, pp.157-189 (1997b).

Aggarwal, A. and Singh, H., "Optimiztion of machining techniques-A retrospective and literature review", Sādhanā, Vol.30, Part 6, pp.699-711 (2005).

Agilent Technologies, http://www.home.agilent.com, 2012.

Ahuja, B.B., Computer aided study and analysis of a dynamic characteristics of a CNC machining system, Ph.D. thesis, University of Pune (1996).

Alauddin, M., EI-Baradie, M.A. and Hashmi, M.S.J., "Prediction of tool life in end milling by response surface methodology", *Journal of Materials Processing Technology*, Vol.71, pp.456-465 (1997).

Alberti, M., Ciurana, J., and Rodriguez, C.A., "Experimental analysis of dimensional error vs. cycle time in high-speed milling of aluminium alloy", *International Journal of Machine Tools and Manufacture*, Vol.47, pp.236-243 (2007).

Altintas, Y. and Chan, P.K., "In-process detection and suppression of chatter in milling", *International Journal of Machine Tools and Manufacture*, Vol.32, No.3, pp.329-347 (1992).

An, C.H., Zhang, Y., Xu, Q., Zhang, F.H., Zhang, J.F., Zhang, L.J. and Wang, J.H., "Modeling of dynamic characteristic of the aerostatic bearing spindle in an ultra-precision fly cutting machine", *International Journal of Machine Tools and Manufacture*, Vol.50, pp.374-385 (2010).

Angstrom Advanced Inc., http://www.angstrom-advanced.com, 2012.

ANSI/ASME Standard B5.54, Method for performance evaluation of CNC machining center, 1992.

ANSI/ASME B5.57, Method for performance evaluation of CNC turning center, 1998.

ANSI/ASME B89.3.4, Axes of rotation, methods for specifying and testing, 2010.

Ausman, J. S., "Linearized ph Stability Theory for Translatory Half- Speed Whirl of Long Self-Acting Gas-Lubricated Journal Bearings", *ASME J. Basic Eng.*, Vol.83, pp. 611–619 (1963).

Baek, D.K., Ko, T.J. and Kim, H.S., "Optimization of feedrate in a face milling operation using a surface roughness model", *International Journal of Machine Tools and Manufacture*, Vol.41, No.3, pp.451-462 (2001).

Bang, Kyung-Geun and Lee, Dai-Gil, "Design of carbon fiber composite shafts for high speed air spindles", *J. Comp. Struct.*, Vol.55, pp.247–259 (2002a).

Bang, Kyung-Geun and Lee, Dai-Gil, "Thrust bearing design for high-speed composite air spindles", *Composite Structures*, Vol.57, pp.149-160 (2002b).

Basuray, P. K., Misra, B. K., and Lal, G. K., "Transition from ploughing to cutting during machining with blunt tool", *Wear*, Vol.43, pp.341-349 (1977).

Belforte, Guido, Raparelli, Terenziano, Viktorov, Vladimir, Trivella, Andrea and Colombo, Federico, "An experimental study of high-speed rotor supported by air bearings: test RIG and first experimental results", *Tribology International*, Vol.39, pp.839-845 (2006).

Benaroya, Haym and Nagurka, Mark L., Mechanical Vibration-Analysis, Uncertainties and Control, 3ird ed., CRC Press, 2010.

Binnig, G., Quate, C.E and Gerber, C., "Atomic force microscopy", *Physical Review Letters*, Vol.56, pp.930-933 (1986).

Boothroyd, G. and Knight, W.A., Fundamentals of Machining and Machine Tools, Marcel Dekker, New York (1989).

Botman, M., "Experiments on oil film dampers for turbomachinery", *ASME J. Eng. Power*, Vol.98, pp.393–400 (1976).

Boujelbene, M., Moisan, A., Tounsi, N. and Brenier, B., "Productivity enhancement in dies and molds manufacturing by the use of C1 continuous tool path", *International Journal of Machine Tools & Manufacture*, Vol.44, pp.101-107 (2004).

Brown, R.D., Addision, P. and Chan, A.H.C., "Chaos in the unbalance response of journal bearings", *Nonlinear Dynamics*, Vol.5, pp.421-432 (1994).

Bryan J., Clouser, R. and Holland, E., "Spindle accuracy", *American Machinist*, Vol.111, pp.149-164 (1967).

Bryan, J.B., "Design and Construction of an Ultra-precision 84 inch Diamond Turning Machine", *Precision Engineering*, Vol.1, No.1, pp.13-17 (1979).

Brzeski, L. and Kazimierski, Z., "High Stiffness Bearing", *Journal of Lubrication Technology*, Vol.110, No.5, pp.520-525 (1979).

Brzeske, L. and Kazimierski, Z., "Infinite Stiffness Gas Bearings for Precision Spindles", *Precision Eng.*, Vol.14, No.2, pp.105-109 (1992).

Burdekin, C. Goddard, "A measuring system for the evolution of spindle rotation accuracy", *Proceedings of the 13th MTDR-Conference*, Birmingham, 1972.

Chang, C.F. and Chen, J.J., "Vibration monitoring of motorized spindles using spectral analysis techniques", *Mechatronics*, Vol.19, pp.726-734 (2009).

Castelli, V., and Elrod, H. G., "Solution of the Stability Problem for 360 Degree

Self-Acting, Gas-Lubricated Bearing", *ASME J. Basic Eng.*, Vol.87, pp. 199–212 (1965).

Chen, J.S., Huang, Y.K. and Chen, M.S., "Feedrate optimization and tool profile modification for the high-efficiency ball-end milling process", *International Journal of Machine Tools & Manufacture*, Vol.45, pp.1070-1076 (2005).

Chen, M., Sun, F., Wang, H., Yuan, R., Qu, Z. and Zhang, S., "Experimental research on the dynamic characteristics of the cutting temperature in the process of high-speed milling", *Journal of Materials Processing Technology*, Vol.138, pp.468-471 (2003).

Chen, M.J., Pang, Q.L., Wang, J.H. and Cheng, K., "Analysis of 3D microtopography in machined KDP crystal surface based on fractal and wavelet methods", *International Journal of Machine Tools & Manufacture*, Vol.48, pp.905-913 (2008).

Cheng M.N., Optimization of surface generation in ultra-precision multi-axis raster milling, MPhil thesis, The Hong Kong Polytechnic University, October 2006.

Cheng, M.N., Cheung, C.F., Lee, W.B. and To, S., "Optimization of surface finish in ultra-precision raster milling", Proceedings of Internatinal conference on Leading Edge Manufacturing in 21st century: LEM21 2005(3), pp.1019-1024 (2005).

Cheng, M.N., Cheung, C.F., Lee, W.B. and To, S., "A study of factors affecting surface quality in ultra-precision raster milling", *Key Engineering Materials*, Vol.339, pp.400-406 (2007).

Cheng, M.N., Cheung, C.F., Lee, W.B., To, S. and Kong, L.B., "Theoretical and experimental analysis of nano-surface generation in ultra-precision raster milling", *International Journal of Machine Tools and Manufacture*, Vol.48, pp.1090-1102 (2008).

Cheung, C.F., Modelling and simulation of nano-surface generation in ultra-precision machining, Ph.D. thesis, The Hong Kong Polytechnic University, April 2000.

Cheung, C.F., "Influence of cutting friction on anisotropy of surface properties in ultra-precision machining of brittle single crystals", *Scripta Materialia*, Vol.48, pp.1213-1218 (2003).

Cheung, C.F., Kong, L.B., Lee, W.B. and To, S., "Modelling and simulation of freeform surface generation in ultra-precision raster milling", *Proc. IMechE Part B: J. Engineering Manufacture*, Vol.220, pp.1787-1801 (2006).

Cheung, C.F. and Lee, W.B., "Study of factors affecting the surface quality in ultra-precision diamond turning", *Mater. Manuf. Process*, Vol.15, No.4, pp. 481-502 (2000).

Cheung, C.F., and Lee, W.B., "An Investigation of Cutting Dynamics in Single Point Diamond Turning", *JSME International Journal Series C: Mechanical Systems Machine Elements and Manufacturin*g, Vol.43, No.1, pp.116-126 (2000).

Cheung, C.F. and Lee, W.B., "A multi-spectrum analysis of surface roughness formation in ultra-precision machining", *Precision Engineering*, Vol.24, No.1, pp.77-87 (2000a).

Cheung, C.F. and Lee, W.B., "Modelling and Simulation of Surface Topography in Ultra-precision Diamond Turning", *Proceedings of The Institute of Mechanical Engineers, Part B, Journal of Engineering Manufacture*, Vol.214, No.B6, pp.463-480 (2000b).

Cheung, C.F. and Lee, W.B., "A Theoretical and Experimental Investigation of Surface Roughness Formation in Ultra-precision Diamond Turning", *International Journal of Machine Tools and Manufacture*, Vol.40, No.7, pp.979-1002 (2000b).

Cheung, C.F., and Lee, W.B., "Characterization of Nanosurface Generation in Single-Point Diamond Turning", *International Journal of Machine Tools and Manufacture*, Vol.41, No.6, pp.851-875 (2001).

Cheung, C.F. and Lee, W.B., "Predication of the effect of tool interference on surface generation in single-point diamond turning", *International Journal of Advanced*

Manufacturing Technology, Vol.19, No.4, pp.245-252 (2002).

Cheung, C.F. and Lee, W.B., Surface generation in ultra-precision diamond turning: modelling and practices, Professional Engineering, London (2003).

Cheung, C.F., Lee, W.B. and To, S., "A framework of a model-based simulation system for predicting surface generation in ultra-precision raster milling of freeform surfaces", *Annual of American Society for Precision Engineering Proceedings*, Orlando, Florida, Oct.24-19, 2004.

Cheung, C.F., To, S. and Lee, W.B., "Anisotropy of surface roughness in diamond turning of brittle single crystals", *Materials and Manufacturing Processes*, Vol.17, No. 2, pp.251-267 (2002).

Cho, Durk-Hyun, Lee, D.G. and Choi, Jin-Ho, "Manufacture of one pieceauto drive shafts with aluminum and composite materials", *J. Comp. Struct.*, Vol.38, pp.309-319 (1997).

Choi, J.K. and Lee, D.G., "Manufacture of a carbon fiber-epoxy composite spindle-bearing system for a machine tool", *Comput. Struct.*, Vol.37, pp.241-251 (1997).

Choi, In-Hyu and Kim, Jeong-Du, "Development of monitoring system on the diamond tool Wear", *International Journal of Machine Tools & Manufacture*, Vol.39, pp.505–515 (1999).

Cooley, J. W., Lewis, P. and Welch, P., "The Fast Fourier Transform and its Applications", *IEEE Trans on Education*, Vol.12, No.1, pp.28-34 (1969).

Cooley, James W., and Tukey John W., "An algorithm for the machine calculation of complex Fourier series", *Math. Comput.*, Vol.19, pp.297–301 (1965). doi:10.2307/2003354.

Corbett, J., McKeown, P. A., Peggs, G. N. and Whatmore, R., "Nanotechnology: International Developments and Emerging Products", *Annals of the CIRP*, Vol.49, No.2, pp.523-544 (2000).

Cranfield Precision, http://www.cranfieldprecision.com/, 2011.

Dexter, Johnson, Gerald, V. Brown and Daniel J., Inman, "Adaptive variable bias magnetic bearing control", *Proceedings of the American Control Conference*, Philadelphia, Pennsylvania, pp.2217-2223 (1998).

Dhar, N. R., Paul, S. and Chattopadhyay, A. B., "Machining of AISI 4140 steel under cryogenic cooling—tool wear, surface roughness and dimensional deviation", *Journal of Materials Processing Technology*, Vol.123, No.3, pp.483-489 (2002).

Donaldson, R.R., "A sample method for separating spindle error from test ball roundness error", *CIRP Annals*, Vol.21, No.1, pp.125–126 (1972).

Draghici, G., and Paltinea, C., "Calculation by convex mathematical programming of the optimum cutting condition when cylindrical milling", *International Journal of Machine Tool Designing Research*, Vol.14, pp.143-160 (1974).

Ehrich, F.F., "Subharmonic vibration of rotors in bearing clearance", *ASME*, Paper No.66-MD-1 (1966).

Eskicioglu, A. M. and Eskicioglu, H., "Application of three nonlinear programming techniques in optimizing machining conditions" , *Proceedings of the Institution of Mechanical Engineers Part B*, Vol.206, pp.183-188 (1992).

FANUC Ltd., ROBONANO, http://www.fanuc.jp/en/product/robonano/index.html, 2011.

Frew, D.A. and Scheffer, C., "Numerical modelling of a high-speed rigid rotor in a single-aerostatic bearing using modified Euler equations of motion", *Mechanical Systems and Signal Processing*, Vol.22, pp.133-154 (2008).

Frigo, M. and Johnson, S. G., "The Design and Implementation of FFTW3", *Proceedings of the IEEE*, Vol.93, pp.216–231 (2005).

Fuller D.D., "A review of the state-of-the-art for the design of self-acting gas lubricated bearings", *J. Lub. Technol.*, Vol.91, pp.1-16 (1969).

Gao, W., Kiyono, S., and Nomura, T., "A new multiprobe method of roundness measurements", *Precision Engineering*, Vol.19, pp.37-45 (1996).

Gao, W., Kiyono, S., and Sugawara, T., "High-accuracy roundness measurement by a new error separation method", *Precision Engineering*, Vol.21, pp.123-133 (1997).

Gao, W., Kiyono, S., and Sato, E., "Precision measurement of multi-degree-of-freedom spindle errors using two-dimensional slope sensors", *CIRP Annals-Manufacturing Technology*, Vol.51, pp.447-450 (2002).

Gao, W., Sato, E, Onuma, T, and Kiyono,, S., "Roundness and spindle error measurement by angular three-probe method", *Journal of the Japan Society for Precision Engineering*, Vol.68, pp.1195-1199 (2002a).

Gao, W., Tano, M., Araki, T. Kiyono, S., and Park, C.H., "Measurement and compensation of error motions of a diamond turning machine", *Precision Engineering*, Vol.31, pp.310-316 (2007).

Gasvik, K.J., Optical Metrology, Wiley, New York, 1995.

Ge, Yingfei, Xu, Jiuhua and Yang, Hui, "Diamond tools wear and their applicability when ultra-precision turning of SiCp/2009Al matrix composite", *Wear*, doi:10.1016/j.wear.2009.09.002 (2009).

Ginsberg, Jerry, Engineering Dynamics, Cambridge University Press, Cambridge, 2008.

Grabchenko, Anatoliy I., Mamalis, Athanasios G. and Lavrynenko, "Sergiy N., Microwear of cutting tool in ultraprecision single-point diamond machining of polymers for optical and bioengineering application", Int. J. Nanomanufacturing, Vol. 1, No.2, p.181-188 (2006).

Grassam, N.S. and Powell, J.W., Gas lubricated bearings, London, Butterworths, 1964.

Grejda, Robert, Marsh, Eric and Vallance, Ryan, "Techniques for calibrating spindles with nanometer error motion", *Precision Engineering*, Vol.29, pp.113-123 (2005).

Gross, W.A., "Investigation of whirl in externally pressurised air-lubricated journal bearings", *Transaction of A.S.M.E., Journal of Basic Engineering*, Vol.84, pp.132-139 (1962).

Gross, W. A., and Zachmanaglou, E. C., "Perturbation Solutions for Gas-Lubricating Films", *ASME J. Basic Eng.*, 83, pp. 139–144 (1961).

Hekman, K.A. and Liang, S.Y., "In-process monitoring of end milling cutter runout", *Mechatronics*, Vol.7, No.1, pp.1-10 (1997).

Heo, E.Y., Kim, B.H. and Kim, D.W., "Estimation of sculptured surface NC machining time", *Trans. Korean Soc. CAD/CAM Eng.*, Vol.8, No.4, pp.254-261 (2003)

Heo, E.Y., Kim, D.W., Kim, B.H. and Chen, F.F., "Estimation of NC machining time using NC block distribution for sculptured surface machining", *Robotics and Computer-Integrated Manufacturing*, Vol.22, pp.427-446 (2006).

Hirn, G.A., "Study of the principle phenomena shown by friction of various methods of determining the viscosity of lubricants", *Bull. Soc. Industr. Mulhous*, Vol.26, No.129, pp.188-277 (1854).

Holmes, A. G., Ettles, C. M., and Mayes, I. W., "Aperiodic Behavior of a Rigid Shaft in Short Journal Bearings", *Int. J. Numer. Methods Eng.*, Vol.12, pp.695–702 (1978).

Horikawa, O. and Shimokobe, A., "An active air bearing", *JSME Int. J.*, Vol.33, pp.55-60 (1990).

Horiuchi, Teruyoshi, Aono, Kazuyuki and Hiyoshi, Hiroaki, "Development of aerostatic bearing spindle for precision machine tools", *NTN Technical review*, No.74, pp.34-37 (2006).

Hough, C.L. and Goforth, R.E., "Optimization of the second order logarithmic machining economics problem by extended geometric programming Part II, Posynomial constraints", *AIIE Transactions*, Vol.13, No.3, pp.234-242 (1981).

Hu, S., Hoa, S.V. and Ganesan, R., "A new evaluation method for surface finish of composite automotive panels using waveform analysis", *Journal of Composite Materials*, Vol.43, No.8, pp.843-876 (2009).

Ikawa, N., Shimada, S. and Morooka, H., "Technology of Diamond Tool for Ultraprecision Metal Cutting", *Bulletin of JSPE*, Vol.21, No.4, pp.233-238 (1987).

Ikawa, N., Shimada, S., and Tsuwa, H., "Non-destructive strength evaluation of diamond for ultra-precision cutting tool", *Annals of the CIRP*, Vol.34, No.1, p.117 -120 (1985).

Ikawa, N., Donaldson, R. R., Komanduri, R., König, W., Aachen, T. H., McKeown, P.A., Moriwaki, T., and Stowers, I. F., "Ultra-precision metal cutting - the past, the present and the future", *Annals of the CIRP*, Vol. 40, No.1, pp.587-594 (1991).

ISO 230 Part3, Test conditions for metal cutting machine tools, Evaluation of thermal effects, 2001.

ISO 3685, Tool-life testing with single-point turning tools, 1993.

ISO 4287, Geometrical product specification-surface texture: Profile method-terms, definitions and surface texture parameters, 1997.

ISO 25178, Geometrical product specification-surface texture: Areal method-terms, definitions and surface texture parameters, 2009.

Jang, G.H. and Kim, Y.J., "Calculation of dynamic coefficients in a hydrodynamic bearing considering five degrees of freedom for a general rotor-bearing system", *ASME J. Tribology*, Vol.121, pp.499-505 (1999).

Kakino, Y., Yamamoto, Y. and Ishii, N., "New measuring method of rotation accuracy of spindle", *Ann. CIRP*, Vol.26, pp.241-244 (1977).

Kazimierski, Zbyszko, Brzeski, Lech and Horodko, Longin, "Gas Bearing of Infinite

Stiffness”, *J. Trib. Trans. ASME.*, Vol.114, No.4, pp.270-273 (1992).

Kim, Bo, Byound, H. and Choi, K., “Machining efficiency comparison direction-parallel tool path with contour-parallel tool path”, *Computer-Aided Design*, Vol.34, pp.89-95 (2002).

Kim, Dong-Sik, Chang, In-Cheol, Kim, Seung-Woo, “Microscopic topographical analysis of tool vibration effects on diamond turned optical surfaces”, *Precis. Eng.*, Vol.26, pp.168-174 (2002).

Kim, Jinbo, Shim, Dongik, Yun, Deokwon and Han, Changsoo, “The analysis of radial/axial error motion on a precision rotation stage”, *World Academy of Science, Engineering and Technology*, Vol.29, pp.173-177 (2007).

Kim, K.W., Kim, K.M., Park, J.P. and Lim, J.R., “A study on the improvement of the stability of a rigid rotor supported by hybrid gas bearing”, *Int. Conference on Hydrodynamic Bearing-Rotor System Dynamics*, Xi'an Jiaotong University, China (1990).

Kingsburry, A., “Experiments with an air lubricated bearing”, *JASNE*, Vol.9, pp.267-292 (1897).

Klaus, S., Luis, H.A. and Castellari, P.S., “The influence of the manufacturing strategy on the production of molds and dies”, *Journal of Materials Processing Technology*, Vol.179, pp.172-177 (2006).

Kline, W.A., and DeVor, R.E., “The effect of runout on cutting geometry and forces in end milling”, *International Journal of Machine Tool Design and Research*, Vol.23, No.2-3, pp.123-140 (1983).

Ko, J. H., Yun, W. S., Cho, D. W. and Ehmann, K. F., “Development of a virtual machining system, Part 1: approximation of the size effect for cutting force prediction”, *International Journal of Machine Tools and Manufacture*, Vol.42, No.15, pp.1595-1605 (2002).

Kong, L.B., Modeling of ultra-precision raster milling and characterization of optical freeform surface, PhD thesis, The Hong Kong Polytechnic University, August 2009.

Kong, L.B., Cheung, C.F., To, S. and Lee, W.B., "Development of a dynamic model for ultra-precision raster milling", *Key Engineering Materials*, Vol.364-366, pp.58-63 (2008).

Kong, L.B., Cheung, C.F., To, S. and Lee, W.B., "An investigation into surface generation in ultra-precision raster milling", *Journal of Materials Processing Technology*, Vol.209, pp.4178-4185 (2009).

Kong, M.C., A study of materials swelling and its characterization on nano-surface generation in ultra-precision machining, Mphil thesis, The Hong Kong Polytechnic University, October 2006.

Kong, M.C., Lee, W.B., Cheung, C.F. and To, S., "A study of materials swelling and recovery in single point diamond turning of ductile materials", *Journal of Materials Processing Technology*, Vol.180, pp.210-215 (2006).

Kong, M.C., Lee, W.B., Cheung, C.F. and To, S., "The Effect of Up-cutting and Down-cutting Directions Materials Swelling in Ultra-precision Raster Milling", *Materials Science Forum*, Vol.532-533, pp. 697-700 (2006a).

Kruglov, E.I. and Darymov, O.I., "Optimization of face milling", *Machines and Tooling*, Vol.49, No.3, pp.35-37 (1978).

Ku, S.S., Larsen, G. and Cetinkunt, S., "Fast tool servo control for ultra-precision machining at extremely low feed rates", *Mechatronics*, Vol.8, No.4, pp.381-393 (1998).

Kugler, Standard Machines, http://www.kugler-precision.com/machines.html. 2011.

Kurgano, J., Suzuki, H. and Kimura, F., "Generation of NC Tool Path for Subdivision Surface", *CAD/Graphics' 2002*, Kumming, *International Academic Publisher*, Vol. 22-24, p.1-7 (2002).

Larson, R.H. and Richardson, H.H., "A preliminary study of whirl instability for pressurized gas bearings", *J. Basic Eng. Trans. ASME*, Vol.84, pp.511-531 (1962).

Lee, Dai-Gil and Choi, Jim-Kyung, "Design and manufacture of an aerostatic spindle bearing system with carbon fiber–epoxy composites", J. Comp. Mater., Vol.34, No.14, pp.1150-1175 (2000).

Lee, D.G., Sin, H.C. and Suh, N.P., "Manufacturing of a graphite epoxy composite spindle for a machine tool", *Ann. CIRP*, Vol.34, pp.365-369 (1985).

Lee, W.B. and Cheung, C.F., "A dynamic surface topography model for the prediction of nano-surface generation in ultra-precision machining", *International Journal of Mechanical Sciences*, Vol.43, No.4, pp.961-991 (2001).

Lee, W.B., Cheung, C.F. and To, S., "Materials induced vibration in ultra-precision machining", *Journal of Materials Processing Technology*, Vol.89-90, pp.318-325 (1999).

Lee, W.B., Cheung, C.F. and To, S. "Characteristics of micro-cutting force variation in ultra-precision machining", *Materials and Manufacturing Processes*, Vol.16, No.2, p.177-193 (2001).

Lee, W.B., Cheung, C.F. and To, S. "A microplasticity analysis of micro-cutting force variation in ultra-precision diamond turning", *Trans. of ASME, Journal of Manufacturing Science and Engineering*, Vol.124, No.2, pp.170-177 (2002).

Lee, W.B., Cheung, C.F. and To, S., "Multi-scale modeling of surface topography in single-point diamond turning", *Journal of Achievements in Materials and Manufacturing Engineering*, Vol.24, No.1, pp.260-266 (2007).

Lee, W.B., To, S. and Cheung, C.F., Design and advanced manufacturing technology for freeform optics, The Hong Kong Polytechnic University, Hong Kong, 2005.

Li, L., Shinshi, T., Iijima, C., Zhang, X. and Shimokohbe, "Compensation of rotor imbalance for precision rotation of a planar magnetic bearing rotor", *Precision Engineering*, Vol.27, No,2, pp.140-150 (2002).

Li, X.H. and Taylor, D.L., “Nonsynchronous motion of squeeze-film damper systems”, *ASME J. Tribol.*, Vol.109, pp.169-176 (1987).

Liang, S. Y. and Wang, J. J., “Milling force convolution modeling for identification of cutter axis offset”, *International Journal of Machine Tools and Manufacture*, Vol.34, No.8, pp.1177-1190 (1994).

Lin, S.C. and Chang, M.F., “A study on the effects of vibrations on the surface finish using a surface topography simulation model for turning”, *International Journal of Machine Tools & Manufacture*, Vol.38, pp.763-782 (1998).

Liu, Kai and Melkote, Shreyes N., “Effect of plastic side flow on surface roughness in micro-turning process”, *International Journal of Machine Tools & Manufacture*, Vol. 46, pp.1778-1785 (2006).

LLNL, “The world's most accurate lathe, Science & Technology Review”, pp.12-14 (2001).

Lucca, D. A., and Seo, Y. W., “Effect of tool edge geometry on energy dissipation in ultraprecision machining”, *Annals of the CIRP*, Vol. 42, No.1, pp.83-86 (1993).

Lund, J.W., “A theoretical analysis of whirl instability and pneumatic hammer for a rigid rotor in pressurized gas journal bearings”, *ASME Transactions Journal of Lubrication Technology*, Vol.89, pp.154-166 (1967).

Ma, Yan, Xu, Jiankang and Zhang, Huarong, “System model and dynamic analysis of high speed magnetic suspension spindle”, *Journal of Xi'an University of Technology*, Vol.11, No.3, pp.161-167 (1995).

Marsh, E.R. and Grejda, R.D., “Experiences with the master axis method for measuring spindle error motion”, *Precision Engineering*, Vol.24, pp.50-57 (2000).

Marsh, E.R., Arneson, D.A., Van Doren, M.J. and Blystone, S.A., “The effects of spindle dynamics on precision flycutting”, *Proceedings of the American society for precision engineering 2005 annual meeting* (2005).

Marsh, E.R., Couey, J.A. and Vallance, R.R., “Roundness measurement of spherical artifacts at arbitrary latitude”, *Precision Engineering*, Vol.30, pp.353-356 (2006).

Marsh, H., “The stability of self-acting gas journal bearings with non-circular members and additional elements of flexibility”, *ASME J. of Lubric. Technol.*, pp. 113–119 (1969).

Martin, D.L., Tabenkin, A.N. and Parsons, F.G., “Precision spindle and bearing error analysis”, *Int. J. Mach. Tools Manufact.*, Vol.35, pp.187-193 (1995).

Matech Industrial Co. Ltd., Ultra-precision, http://www.matech-tw.com/, 2011.

Mehta, M. and Mital (ed.), A., “Recent Developments in Production Research”, *Elsevier, Amsterdam*, pp. 52-58 (1988).

Meirovitch, L., Methods of analytical dynamics, McGraw-Hill, 1970.

Mckeown, P.A., “The role of precision engineering in manufacturing of the future”, *Annals of the CIRP*, Vol.36, No.2, p.495 (1987)

Mitsui, K., “Development of a new measuring method for spindle rotation accuracy by three-points method”, *Proceedings of the 23rd International MTDR*, pp.115-121 (1982).

Mizumoto, H., Arii, S., Kami, Y., Goto, K., Yamamoto, T and Kawamoto, M., “Active inherent restrictor for air-bearing spindles”, *Precision Eng.*, Vol.19, pp.141-147 (1996).

Mizumoto, Hiroshi, Matsubara, Tomio, Hata, Naohide and Usuki Masao, “An aerostatically controlled restrictor for obtaining an infinite stiffness aerostatic thrust bearing”, *International Journal of JSPE*,Vol.55, No.1, pp.135-140 (1989) (Released in 2009).

Mizumoto, H., Matsubara, T., Hata, N. and Usuki M., “Zero-Compliance Aerostatic Bearing for an Ultra- precision Machine”, *Preci. Engineering*, Vol.12, No.2, pp.75-80 (1990).

Mizumoto, H., Tanaka, Y., Yabuta, Y., Arii, S., Tazoe, Y. and Yakouchi, S., "A high-speed air spindle employing active aerodynamic bearing system", *Proc. of the 10th Anniversary International Conference of the Euspen*, Vol.1, pp.394-397 (2008).

Mizumoto, H., Yabuta, Y., Arii, S., Tazoe, Y. and Yakouchi, S., "An active aerodynamic bearing for ultraprecision machining", *Proc. of the 10th International Conference of the Euspen*, Vol.1, pp.300-303 (2010).

Mizumoto, H., Yabuta, Y., Arii, S., Tazoe, Y., Atoji, K. and Hirose, T., "Active control of high-speed precision air-bearing spindle", *Proc. of the 11th Anniversary International Conference of the Euspen*, Vol.1, pp.394-397 (2011).

Moore Nanotech, Machines, http://test.nanotechsys.com/machines/, 2011.

Monreal, M. and Rodriguez, C.A., "Influence of tool path strategy on the cycle time of high-speed milling", *Computer-Aided Design*, Vol.35, pp.395-401 (1991).

Nachi-Fujikoshi Corp., Precision Machinery, http://www.nachi-fujikoshi.co.jp/eng/sei/kakouki/index.html, 2011.

Nader, Jalili and Karthik, Laxminarayana, "A review of atomic force microscopy imaging systems: application to molecular metrology and biological sciences", *Mechatronics*, Vol.14, pp.907-945 (2004).

Nakasuji, T., Kodera, S., Hara, S. and Matsunaga, H., "Diamond turning of brittle materials for optical components", *Annals of the CIRP*, Vol.39, No.1, p.89 (1990).

NanoScience Instruments, http://www.nanoscience.com, 2012.

Ni, J.M., "Dynamic stability and debugging of aerostatic-pressurized bearings in magnetic disk comprehensive instrumentation", *Journal of Huazhong University of Science and Technology*, Vol.13, pp.69-74 (1985).

Nikolajsen, J.I. and Holmes, R., "Investigation of squeeze-film isolators for the vibration control of a flexible rotor", *ASME J. Mech. Sci.*, Vol.21, pp.247-252

(1979).

Öktem, H., Erzurumlu, T. and Kurtaran, H., "Application of response surface methodology in the optimization of cutting conditions for surface roughness", *Journal of Materials Processing Technology*, Vol.170, pp.11-16 (2005).

Okuyama, Eiki, Nosaka, Nayu and Aoki, Jun, "Radial motion measurement of a high-revolution spindle motor", *Measurement*, Vol.40, pp.64-74 (2007).

Ostafiev, V. A., Globa, A.V. and Globa, L., "Integrated end milling optimization development", *Annals of CIRP*, Vol.33, No.1, pp.29-32 (1984).

Ostasevicius, V., Gaidys, R., Rimkeviciene, J. and Dauksevicius, R., "An approach based on tool mode control for surface roughness reduction in high-frequency vibration cutting", *Journal of Sound and Vibration*, Vol.329, pp.4866-4879 (2010).

Palanikumar, K., Mata, F. and Davim, J. Paulo, "Analysis of surface roughness parameters in turning of FRP tubes by PCD tool", *Journal of Materials Processing Technology*, Vol.204, pp.469-474 (2008).

Panasonic Corp., Ultra Accuracy 3-D Profilometer, UA3P, http://industrial.panasonic.com/ww/products_e/product_cat2/ADAH000_e/ua3p_siyou_e.html, 2011.

Park Systems, http://www.parkafm.com/, 2012.

Peigne, G., Paris, H., Brissaud, D. and Gouskov, A., "Impact of the cutting dynamics of small radial immersion milling operations on machined surface roughness", *International Journal of Machine Tools and Manufacture*, Vol.44, pp.1133-1142 (2004).

Precitech Inc., http://www.precitech.com/, 2011.

Puttick, K.E., Rudman, M.R., Smith, K.J., Franks, A. and Lindsey, K., "Single-point diamond machining of glasses", *Proceedings of the royal society of London*, *Series A*, *Mathematical and Physical Sciences*, Vol.426, No.1870, pp.19-30 (1989).

Qiu Li and Zou Kemin, Introduction to feedback control, Upper Saddle River, N.J.: Pearson Prentice Hall, 2010

Ruckman, J., Pollicove, H. and Golini, D., “Advanced Manufacturing Generates Conformal Optics”, *Optoelectronics World*, Vol.35, No.7, p.S13-S15 (1999).

Rützel, S., Lee, S.I. and Raman, A., “Nonlinear dynamics of atomic-force-microscope probes driven in Lennard-Jones potentials”, *Proc. R. Soc. Lond. A*, Vol.459, pp.1925-1948 (2003).

Salgado, D.R., Alonso, F.J., Cambero, I. and Marcedo, A., “In-process surface roughness prediction system using cutting vibrations in turning”, *Int. J. Adv. Manuf. Technol.*, Vol.43, pp.40-51 (2009).

Sata, T., “Surface finish in metal cutting”, *Ann. CIRP*, Vol.12, pp.190 (1964).

Schmalz, G., Technische Oberflaechenkunde, Springer, Berlin (1936).

Schmalz, G., “Uber Glatte und Ebenheit als Physikalisches und Physiologishes Problem”, *Verein Deatscher Ingenieure*, Vol.73, p.1441(1929).

Schmitza, T. L., Coueyb, J., Marshb, E., Mauntlera, N. and Hughesa, D., “Runout effects in milling: Surface finish, surface location error, and stability”, *International Journal of Machine Tools and Manufacture*, Vol.47, pp.841-851 (2007).

Sherwood, K.F., and Crookall, J.R., “Surface Finish Assessment by an Electrical Capacitance Technique”, *Proceedings of the Institution of Mechanical Engineers*, Vol.182, pp.344–349 (1968).

Simoneau A., Ng, E. and Elbestawi, M.A., “Surface defects during microcutting”, *International Journal of Machine Tools and Manufacture*, Vol.46, No.12-13, pp.1378-1387 (2006).

Son, S. M., Lim, H. S., and Ahn, J. H., “Effects of the friction coefficient on the minimum cutting thickness in micro cutting”, *International Journal of Machine Tools and Manufacture*, Vol.45, pp.529-535 (2005).

Son, S. M., Lim, H. S., and Ahn, J. H., "The effect of vibration cutting on minimum cutting thickness", *International Journal of Machine Tools and Manufacture*, Vol.46, No.15, pp.2066-2072 (2006).

Srinivasa, N., Ziegert, J.C. and Mize, C.D., "Spindle thermal drift measurement using the laser ball bar", *Precision Engineering*, Vol.18, pp.118-128 (1996).

Stedman, M., "Basis for comparing the performance of surface-measuring machine", *Precision Engineering*, Vol.9, pp.149-152 (1987).

Stevens, A. J. and Liang, S. Y., "Runout rejection in end milling through two-dimensional repetitive force control", *Mechatronics*, Vol.5, No.1, pp.1-13 (1995).

Stout, K.J. and Sweeney, F., "Design of aerostatic flat pad bearings using pocked orifice restrictors", *Tribology International*, Vol.17, No.4, pp.191-198 (1984).

Su, Y.S., "A new instrument for axis rotation metrology", *Ann. CIRP*, Vol.34, pp.439-444 (1985).

Sykes, J. E. H., and Holmes, R., "The effect of bearing misalignment on the non-Linear vibration of aero-engine rotor-damper assemblies", *Proceeding Institution of Mechanical Engineers*, Vol.204, pp. 83–99 (1990).

Syn, C.K., Taylor, J.S., and Donaldson, R.R., "Diamond tool wear vs. cutting distance on electroless nickel mirrors", *Proc. SPIE*, Vol.676, pp.128–140 (1986).

Tandon, V., El-Mounayri, H. and Kishawy, H., "NC end milling optimization using evolutionary computation", *International Journal of Machine and Tools Manufacture*, Vol.42, pp.595-605 (2002).

Taniguchi, N., "Current status in, and future trends of, ultra-precision machining and ultrafine materials processing", *Annals of the CIRP*, Vol.32, No.2, pp.573-582 (1983).

Taniguchi, N., Nanotechnology: integrated processing systems for ultra-precision and ultrafine products, Oxford University Press, UK, 1996.

Taniguchi, O., “Experimental study on instability of externally pressurized air journal bearing”, *Int. J. JSME*, Vol.33, pp.997-1004 (1967).

Taylor Hobson, Surface Profilers, Form Talysurf PGI, http://www.taylor-hobson.com/en/surface-profilers/, 2011.

Taylor, F.W., “On the art of cutting metals”, *Transaction of ASME*, Vol.28, pp.31-35 (1907).

To, S, Effect of crystallographic orientation on material behaviour in ultra-precision diamond turning of single crystals, PhD. thesis, The Hong Kong Polytechnic University, Hong Kong (2000).

To, S., Chan C.Y., Zhang S.J., Cheung C.F., Zhu Y.H. and Lee W.B., “Microstructural characterization of an ultra-precision-machined surface of a Zn-Al alloy”, *Journal of Micromechanics and Microengineering*, Vol.19, pp.054005-054011 (2009).

To, S., Cheung, C.F. and Lee, W.B. “Influence of material swelling upon surface roughness in diamond turning of single crystals”, *Materials Science and Technology*, Vol.17, No.1, pp.102-108 (2001).

To, S., Kwok, T.C., Cheung, C.F. and Lee, W.B., “Study of ultra-precision diamond turning of a microlens array with a fast tool servo system”, *Proceedings of the SPIE*, Vol.6149, p.61490S (2006).

To, S., Lee, W.B. and Chan, C.Y., “Ultraprecision diamond turning of aluminium single crystals”, *Journal of Materials Processing Technology*, Vol.63, pp.157-162 (1997).

To, S., Lee, W.B. and Chan, C.Y., “Effect of machining velocity on the crystallographic textures in a diamond turned single crystal”, *Texture and Microstructures*, Vol.31, pp.249-261 (1999).

To, S., Lee, W.B. and Cheung, C.F., “Orientation changes of substrate materials of aluminium single crystal in ultra-precision diamond turning”, *Journal of Materials Processing Technology*, Vol.140, No.1-3, pp.346-351 (2003).

To, S., Lee, W.B. and Zhu, Y.H., “Ultra-precision machining induced surface structural changes of Zn-Al alloy”, *Materials Science and Engineering A*, Vol.325, pp. 497-502 (2002).

To, S., Lee, W.B. and Zhu, Y.H., “Ultra-precision machining induced micro-plastic deformation in an Zn-Al based alloy”, *Journal of Materials Processing Technology*, Vol.167, No.2-3, pp.536-541 (2005).

To, S., Zhang, S.J., Cheung, C.F. and Lee, W.B., “Effect of cutting strategy on surface microstructural changes in ultraprecision raster milling”, *In conference: Asian Symposium for Precision Engineering and Nanotechnology (ASPEN2009)*, Kokura, Japan (2009a).

To, S., Zhu, Y.H., and Lee, W.B., “Ultra-precision machining induced phase decomposition at surface of Zn–Al based alloy”, *Appl. Surf. Sci.*, Vol.253, pp.2165-2170 (2006a).

To, S., Zhu, Y.H. and Lee, W.B., “Effects of cutting depth on the surface microstructure of a Zn–Al alloy during ultra-precision machining”, *Appl. Surf. Sci.*, Vol.254, pp.1559-1564 (2008).

Tse, Francis S., Morse, Ivan E. and Hinkle, Rolland T., Mechanical vibrations--Theory and Applications, 2nd ed., Allyn and Bacon, Inc., Boston, 1963.

Tu, Jay F., Bossmanns, Bernd and Hung, Spring C.C., “Modeling and error analysis for assessing spindle radial error motions”, *Precision Engineering*, Vol.21, pp.90-101 (1997).

Uddin, M. Sharif, Seah, K.H.W., Li, X.P., Rahman, M. and Liu, K., “Effect of crystallographic orientation on wear of diamond tools for nano-scale ductile cutting of silicon”, *Wear*, Vol. 257, pp.751–759 (2004).

Veeco, Metrology & Instrumentation: Optical Interferometric Profilers--Systems, http://www.veeco.com/Products/metrology_and_instrumentation/Optical_Profilers/index.aspx, 2011

Wada, R., Kodama, H., Nakamura, K., Mizutani, Y., Shimura,Y. and Takenaka, N., "Wear characteristics of single crystal diamond tool", *Ann. CIRP*, Vol.29, No.1, p. 47–52 (1980).

Wang, Sujuan, Modelling and optimization of cutting strategy and surface generation in ultra-precision raster milling, Ph.D. thesis, The Hong Kong Polytechnic University, Hong Kong (2010).

Wang, H., To, S., Chan, C.Y., Cheung, C.F. and Lee, W.B., "A theoretical and experimental investigation of the tool-tip vibration and its influence upon surface generation in single-point diamond turning", *International Journal of Machine Tools and Manufacturing*, Vol.50, pp.241-252 (2010).

Wang, S.J., To, S., Chan, C.Y., Cheung, C.F. and Lee, W.B., "A study of the cutting-induced hearting effect on the machined surface in ultra-precision raster milling of 6061 Al alloy", *International Journal of Advanced Manufacturing Technology*, Vol.51, pp.69-78 (2010).

Wang, C.C. and Chen, C.K., "Bifurcation analysis of self-acting gas journal bearings", *ASME Journal of Tribology*, Vol.123, pp.755-767 (2001).

Wang, C.C., Jang, M.J. and Chen, C.K., "Non-linear dynamic analysis of a flexible rotor supported by self-acting gas journal bearing", *IMech E*, Vol.218, pp.1527-1538 (2004).

Wang, C.C., "Nonlinear dynamic behavior and bifurcation analysis of a rigid rotor supported by a relatively short externally pressurized porous gas journal bearing system", *Acta Mechanic*a, Vol.183, pp.41-60 (2006).

Wang, C.C., Yau, H.T., Jang, M.J. and Yeh, Y.L., "Theoretical analysis of the non-linear behavior of a flexible rotor supported by herringbone grooved gas journal bearings", *Tribology International*, Vol.40, pp.533-541 (2007).

Wang, C.C., "Theoretical and nonlinear behavior analysis of a flexible rotor supported by a relative short herringbone-grooved gas journal-bearing system", *Physica D*, Vol.237, pp.2282-2295 (2008)

Wang, C.C. and Yau, H.T., "Theoretical analysis of high speed spindle air bearings by a hybrid numerical method", *Applied Mathematics and Computation*, Vol.217, pp.2084-2096 (2010).

Wang, J. J. and Zheng, C.M., "Identification of cutter offset in end milling without a prior knowledge of cutting coefficients", *International Journal of Machine Tools and Manufacture*, Vol.43, No.7, pp.687-697 (2003).

Whitehouse, D.J., Handbook of surface metrology, Institute of Physics Publication, Bristol, Philadephia (1994).

Whitten, L.G., and Lewis, T.G., "Machining and Measurement to Submicron Tolerances," *Proc. of the 7th International Machine Tool Design and Research Conference*, Birmingham, England, Pergamon Press, UK, 1966.

Willis, Rev. R., "On the pressure produced on a flat surface when opposed to a stream of air issuing from an orifice in a plane surface", *Trans. Cambridge Phil. Soc.*, Vol.3, No.1, pp.121-140 (1828).

Yan, D., El-Wardany, T. I. and Elbestawi, M. A., "A multi-sensor strategy for tool failure detection in milling", *International Journal of Machine Tools and Manufacture*, Vol.35, No.3, p. 383-398 (1995).

Yan, X., Evaluation and improvement of productivity for machining centers, Ph.D. thesis, Kanazawa University, 1998.

Yan, X., Shirase, K. and Kawabata, H., "Improving productivity of machining centers based on NC program diagnostic system", *Journal of the Japan Society for Precision Engineering*, Vol.63, No.7, pp.1044-1048 (1997).

Yan, X, Shirase, K., Hirao, M. and Yasui, T., "NC program evaluator for higher machining productivity", *International Journal of Machine Tools & Manufacture*, Vol.39, pp.1563-1573 (1999)

Yang, Seung-Han, Kim, Ki-Hoon and Yong, Kuk Park, "Measurement of spindle thermal errors in machine tool using hemispherical ball bar test", *International Journal of Machine Tools & Manufacture*, Vol. 44, pp.333–340 (2004).

Yokota, H., Aoyama, T. and Inasaki, I., "Development of high stiffness externally pressurized journal air bearings with an automatically controlled restrictor", *International Journal of JSPE*, Vol.26, No.4, pp.338-339 (1992).

Yuan, Z.J., Lee, W.B., Yao, Y.X. and Zhou, M., "Effect of crystallographic orientation on cutting forces and surface quality in Diamond cutting of single crystal", *CIRP Annals- Manufacturing Technology*, Vol.43, No.1, pp.39-42 (1994).

Yuan, Z.J., Zhou, M., and Dong, S., "Effect of diamond tool sharpness on minimum cutting thickness and cutting surface integrity in ultraprecision machining", *Journal of Materials Processing Technology*, Vol.62, p. 327-330 (1996).

Yun, W. S., and Cho, D. W., "Accurate 3-D cutting force prediction using cutting condition independent coefficients in end milling", *International Journal of Machine Tools and Manufacture*, Vol.41, No.4, pp.463-478 (2001).

Yurkevich, V.V., "Measurement of cutting tool vibrations during turning", Measurement Techniques, Vol. 49, No. 7, p. 660-663 (2006).

Zain, A.M., Haron, H. and Sharif, S., "Application of GA to optimize cutting conditions for minimizing surface roughness in end milling machining process", *Expert Systems with Applications*, Vol.37, No.6, pp.4650-4659 (2010).

Zhang, G.X., Zhang, Y.H., Yang, S.M. and Li, Z., "A multipoint method for spindle error motion measurement", *Annals of the CIRP*, Vol.46, pp.441-445 (1997).

Zhang Jin-hua, Theory and Technique of Precision Cutting, 1st ed., Pergamon Press, Oxford, 1991.

Zhang, S.J., To, S., Chan, C.Y. and Cheung, C.F., "A study of cutting force variation influencing surface topography in ultra-precision machining", *The 2nd International Conference on Nanomanufacturing (nanoMan2010)*, 24-26 Sep., 2010, Tianjin, China.

Zhang, X.D., Fang, F.Z., Wang, H.B., Wei, G.S. and Hu, X.T., "Ultra-precision machining of sinusoidal surfaces using the cylindrical coordinate method", *Journal of Micromechanics and Microengineering*, Vol.19, pp.054004-054010 (2009).

Zhao, J.Y., Linnett, I.W. and Mclean, L.J., "Subharmonic and quasi-periodic motion of an eccentric squeeze film damper-mounted rigid rotor", *ASME J. Vibration Acoustics*, Vol.116, pp.357-363 (1994).

Zhao, Q.L., Wang, Y.L., Yu, G., Dong, S. and Zhang, X.Z., "Investigation of anisotropic mechanisms in ultra-precision diamond machining of KDP crystal", *Journal of Materials Processing Technology*, Vol.209, pp.4169-4177 (2009).

Zhou, L. and Cheng, K., "Dynamic cutting process modeling and its impact on the generation of surface topography and texture in nano/micro cutting", *Proc. IMechE, Part B: J. Engineering Manufacture*, Vol.223, No.3, pp.247-266 (2009).

Zhu, L. and Cheng, K., "Dynamic cutting process modeling and its impact on the generation of surface topography and texture in nano/micro cutting", *Proc. IMechE, Part B: J. Engineering Manufacture*, Vol.223, pp.247-266 (2009).

Zhu, Y.H., To, S., Lee, W.B., Zhang, S.J. and Cheung, C.F., "Ultra-precision raster milling-induced phase decomposition and plastic deformation at the surface of a Zn–Al-based alloy", *Scr. Mater.*, Vol.62, No.2, pp.101-104 (2010).

Zygo, Products, http://zygo.com/?/met/products/, 2011.

Appendices

Appendix I SPDT Optoform 30

The **OPTOFORM® 30** (Taylor Hobson Pneumo Co., UK) is a precision, two axis, continuous path CNC contouring lathe for directly fabricating rotationally symmetrical components, such as spherical, multi-curve, and aspheric contact lenses of a typical 12.7mm diameter, within nanometric surface roughness and sub-micrometric form error, as shown in Figure I-1. The machine employs an aerostatic bearing spindle and precision dovetail slides. The slides are mounted on a natural granite base and are positioned in a "T" configuration, moving via continuous path linear interpolation of the Y and Z axes. The Y-axis slide represents the cross arm of the "T" and carries the dual tool holder assembly, as well as the optional front surface probe. The Z-axis slide represents the stem of the T, and carries the aerostatic bearing spindle. The workpiece is mounted in an air actuated collet mechanism within the aerostatic bearing spindle rotor, drived by continuous torque DC servo motors. Any axis symmetrical contour mathematically defined as a surface of revolution can be generated by the system.

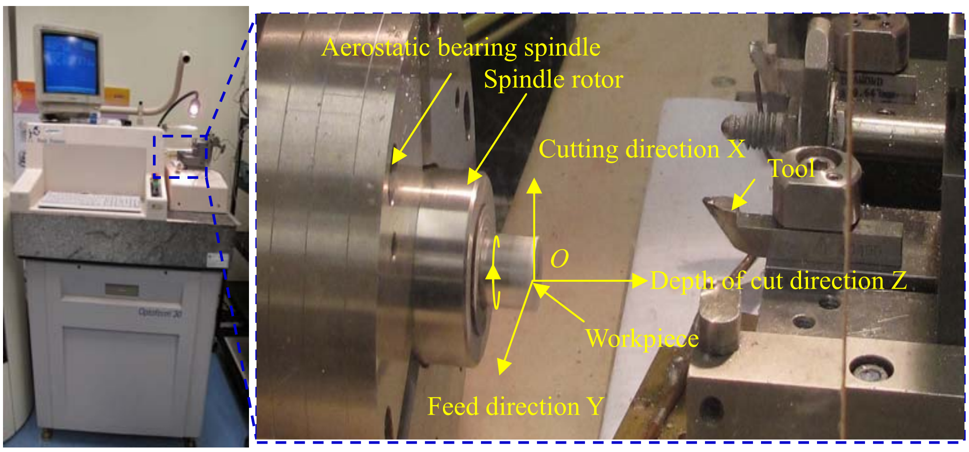

Figure I-1 Configuration of the Optoform 30 lathe

Machine Base

(1) Slide Travel: 150mm on the Y-axis and 100mm on the Z-axis;

(2) The maximum Feedrate: up to 1500mm/min;

(3) Spindle Rotation: up to 10,000 RPM with acceleration and deceleration times of less than 5 seconds;

(4) Control System: a PC based computer system, providing a powerful processing capability through the use of a Pentium 233MHz CPU with 32MB RAM, 1GB (or larger) hard drive, 3.5" floppy drive, and a high resolution VGA monitor, and a precise and reliable motion controller;

(5) Electrical Power: 230 Volts, 50/60 Hertz, Single Phase and 3.0 KVA;

(6) Compressed Air: 6 bar, 3 liters/sec., filtered to 0.3 micron solid particle size and Dry to 50° F pressure dew point;

(7) Approximate Floor Space: 1000mm x 906mm;

(8) Approximate Weight: 815Kg.

Spindle Specification

1. Spindle rotor mass (m), 0.5kg;
2. Radial stiffness (k_2/ k_3), 20N/μm;
3. Axial stiffness (k_1), 25N/μm;
4. Eccentric position of the mass imbalance away from the rotor axis after biasing (e), 1μm;
5. Position of the centre of mass center relative to its equilibrium along the z-axis (l_1/ l_2), 50mm±5e;
6. Radius of spindle rotor (R), 25mm;
7. Inertial tensor around y-axis (J_y), 0.05gm^2;
8. Inertial tensor around z/x-axis (J_x/J_z), 1.4gm^2;
9. The distance of tilting center of spin rotor to the tool tip (d_2), 60mm;
10. The distance of tool tip away from the spindle axis (Swing distance) (d_1), 3mm;
11. Linear damping ratio μ, 0.025;
12. Angular damping ratio ξ, 0.5×10^{-4}.

Appendix II UPRM Precitech Freeform 705G

Introducing the **Freeform® 705G** (Precision Inc., USA), a versatile, multi-axis machine platform specifically designed for the grinding/milling of three dimensional or freeform optics, optical molds, and mechanical components.

Key Features

• Slide Travel: X-350mm (14") Y-150mm (6") Z-250mm (10");

• Maximum Feedrate: 1500mm/min. (59"/min.);

• Process Capability:

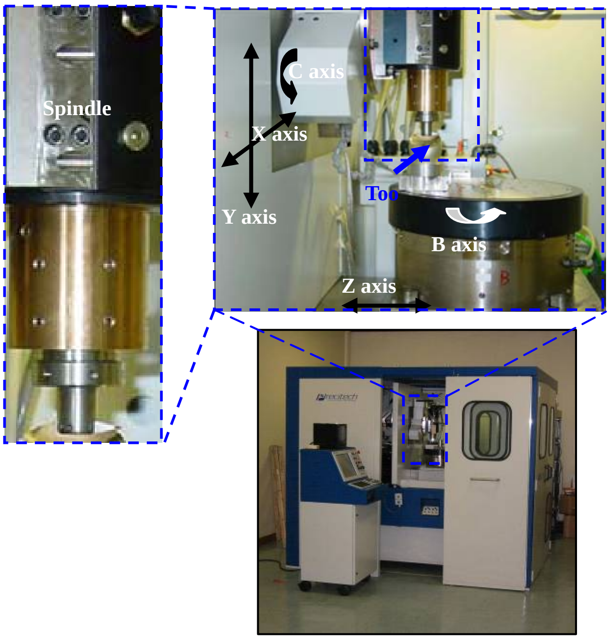

- Water Tight Machine Grinding X, Z;

- Water Tight Machine SPDT X, Z;

- Raster Milling X, Y, Z, B;

- Linear Grooving X, Y, Z;

- Diamond Ruling X, Y, Z.

Spindle performance specifications

1. Spindle rotor mass (m), 2.5kg;
2. Radial stiffness (k_2/ k_3), 22N/µm;
3. Axial stiffness (k_1), 31N/µm;
4. Eccentric position of the mass imbalance away from the rotor axis after biasing (e) 0µm;
5. Position of the centre of mass center relative to its equilibrium along the z-axis (l_1/ l_2), 100mm;
6. Radius of spindle rotor (R), 25mm;
7. Inertial tensor around y-axis (J_y), 0.25gm^2;
8. Inertial tensor around z/x-axis (J_x/J_z), 15.03gm^2;
9. The distance of tilting center of spin rotor to the tool tip (d_2), 180mm;
10. The distance of tool tip away from the spindle axis (Swing distance) (d_1), 23mm;
11. Linear damping ratio μ, 0.025;

12. Angular damping ratio ξ, 0.5×10^{-4}.

Product Features

(1) Sealed natural granite base eliminating machine contamination;

(2) Self leveling dual chamber isolation system minimizing vibration influences during machine operation;

(3) Linear motor driven, hydrostatic oil bearing slideways with advanced stiffness characteristics for the ultimate in performance;

(4) 8.6 or 1.4nm feedback resolution for improved velocity control. Slot-type thrust bearing spindle design available up to 5,000 RPM;

(5) Qnx® real time OS for advanced programming capacity;

(6) 1.0nm programming resolution for increased throughput;

(7) Optional rotational axes and grinding spindles available for advanced capabilities.

Product Options

(a) Adjustable & Flycutting Toolholders Milling Attachments;

(b) Aspheric grinding systems 50,000/15,000 RPM On-Machine Gage & Amplifier;

(c) Aspheric Programming Software Optical and LVDT Tool Setting Systems;

(d) FTS Fast Tool Servo Slow Tool Servo Positioning C-Axis;

(e) HydroRound Rotary B-Axis UltraComp™ On-Machine Metrology.

Appendix III State Space Equations

A state space equation (Qiu and Zou, 2010), also named a state space representation, is a mathematical model of a physical system to reorganize the relationship among a set of input, output and state variables for linear ordinary differential equations of a system. In the state space model, the inputs, outputs and states are abstracted, i.e.: the inputs and outputs are expressed as vectors, and the states are rewritten in matrix form (time invariant). The state space equation, known as the "time-domain method", gives a convenient and efficient approach to analyzing systems with multiple inputs and outputs, which state matrix describes intrinsic characteristics of the system. For a linear time-invariant system, the general form of a state space model is written as:

$$\begin{cases} \dot{x}(t) = Ax(t) + bu(t) \\ y(t) = cx(t) + du(t) \end{cases} \tag{III-1}$$

where:

A is called the "state matrix", $\in \mathrm{R}^{n\times n}$;

b is the "input matrix", $\in \mathrm{R}^{n\times 1}$;

c is the "output matrix",$\in \mathrm{R}^{1\times n}$;

d is the "feedforward matrix",$\in$R, which all are constant matrices,

$x(t)$ is called the "state vector", $\in \mathrm{R}^{n\times 1}$;

$y(t)$ is called the "output vector", $\in \mathrm{R}^{n\times 1}$;

$u(t)$ is called the "input vector", $\in \mathrm{R}^{n\times 1}$;

and $\dot{x}(t) = \dfrac{d}{dt}x(t)$.

By solving the characteristic equations of the above state matrix A, Eq.III-2, the eigenvalues λs of the state matrix A, Eq.III-3, are the complex conjugate roots, which represents the intrinsic characteristics of the system.

$$Ax = \lambda x \tag{III-2}$$

$$\det(A - \lambda I) = 0 \tag{III-3}$$

Appendix IV Fast Fourier Transform

A **fast Fourier transform** (FFT) is an efficient algorithm to fast calculate the discrete Fourier transform (DFT) (Cooley et al., 1965, 1969). There exist many distinct FFT algorithms involving a wide range of mathematics, from simple complex-number arithmetic to group theory and number theory. A DFT decomposes a sequence of values into components of different frequencies, which is useful in many data analysis fields. In mathematics, the DFT is a specific kind of discrete transform originating from the Fourier transform, used in the frequency-domain analysis for the sequence of values in a two-dimensional form, such as cutting forces to time and surface profile heights to the measured length in this research work, which is defined as the following formula:

$$X_k = \sum_{n=0}^{N-1} x_n e^{(-\frac{2\pi i}{N}kn)} \qquad k = 0,\cdots,N-1 \tag{IV-1}$$

where, the sequence of N real numbers, x_0, ..., x_{N-1} is transformed into the sequence of N complex numbers, X_0, ..., X_{N-1}, i is the imaginary unit and $e^{(-\frac{2\pi i}{N})}$ is a primitive N^{th} root of unity, and the $\frac{k}{N}$ is the angular frequency with the corresponding amplitude A_k / N and phase φ_k from the complex modulus and argument of X_k, respectively:

$$A_k = |X_k| = \sqrt{\mathrm{Re}(X_k)^2 + \mathrm{Im}(X_k)^2} \tag{IV-2}$$

$$\varphi_k = \arg(X_k) = \arctan\frac{\mathrm{Im}(X_k)}{\mathrm{Re}(X_k)} \tag{IV-3}$$

In particular, the DFT is widely employed in signal processing and related fields to analyze the frequencies contained in a sampled signal. A key enabling factor for these applications is the fact that the DFT can be computed efficiently in practice using a fast Fourier transform (FFT) algorithm, predating the term "fast Fourier transform" (Cooley et al., 1969). In this study, the Cooley–Tukey algorithm is employed as the FFT algorithm (Cooley and Tukey, 1965; Frigo and Johnson, 2005).

Appendix V Impedance Method

Impedance method (Tse, et al., 1963) is a harmonic analysis method to completely eliminate the differential equation approach for the determination of the steady-state response of a dynamic system, which is widely and efficiently employed for the steady-state response of a linear second order ordinary differential equation system in mechanical and electrical engineering. For Eq.3-21, the steady-state response (particular response) is:

$$\begin{cases} z_{steady-state} = \dfrac{F_t}{m} \\ y_{steady-state} = \dfrac{F_r}{m} + A_y \sin(\omega t - \beta_y) \\ x_{steady-state} = \dfrac{F_m}{m} + A_x \sin(\omega t + \pi/2 - \beta_x) \end{cases} \tag{V-1}$$

Deleting the step response (constant excitation), the steady-state response applied by harmonic excitation is:

$$\begin{cases} z_{steady-state} = 0 \\ y_{steady-state} = A_y \sin(\omega t - \beta_y) \\ x_{steady-state} = A_x \sin(\omega t + \pi/2 - \beta_x) \end{cases} \tag{V-2}$$

Using the vectorial representation of harmonic motions, the corresponding equations for Eq.3-21 and V-2 are expressed as:

$$\begin{cases} m\ddot{z} + c_z\dot{z} + k_1 z = 0 \\ m\ddot{y} + c_y\dot{y} + k_3 y = me\omega^2 e^{j\omega t} \\ m\ddot{x} + c_x\dot{x} + k_2 x = me\omega^2 e^{j(\omega t + \pi/2)} \end{cases} \tag{V-3}$$

$$\begin{cases} z_{steady-state} = 0 \\ y_{steady-state} = \overline{A}_y e^{j\omega t} \\ x_{steady-state} = \overline{A}_x e^{j(\omega t + \pi/2)} \end{cases} \tag{V-4}$$

By substituting Eq.V-4 into Eq.V-3 and factoring out the $e^{j\omega t}$ term, we can obtain:

$$\begin{cases} 0 = 0 \\ (m(j\omega)^2 + c_y(j\omega) + k_3)\overline{A}_y = me\omega^2 \\ (m(j\omega)^2 + c_x(j\omega) + k_2)\overline{A}_x = me\omega^2 \end{cases} \tag{V-4}$$

i.e.:

$$\begin{cases} 0 = 0 \\ \overline{A}_y = \dfrac{me\omega^2}{(m(j\omega)^2 + c_y(j\omega) + k_3)} = A_y e^{-j\beta_y} \\ \overline{A}_x = \dfrac{me\omega^2}{(m(j\omega)^2 + c_x(j\omega) + k_2)} = A_x e^{-j\beta_x} \end{cases} \tag{V-5}$$

where,

$$\begin{cases} 0 = 0 \\ A_y = \dfrac{me\omega^2}{\sqrt{(k_3 - m\omega^2)^2 + (\omega c_y)^2}} \\ A_x = \dfrac{me\omega^2}{\sqrt{(k_2 - m\omega^2)^2 + (\omega c_x)^2}} \end{cases} \tag{V-6}$$

$$\begin{cases} 0 = 0 \\ \beta_y = \arctan\dfrac{\omega c_y}{k_3 - m\omega^2} \\ \beta_x = \arctan\dfrac{\omega c_x}{k_2 - m\omega^2} \end{cases} \tag{V-7}$$

$$c_i = 2\mu_i\sqrt{k_j m} \qquad (i{=}x,\ y,\ z \text{ and } j{=}2,\ 3,\ 1) \tag{V-8}$$

Then, the complete steady-state solution (particular solution) under the step excitation and harmonic excitation is expressed as:

$$\begin{cases} z(t) = \dfrac{F_t}{k_1} \\ y(t) = \dfrac{F_r}{k_3} + \dfrac{e\omega^2}{(\frac{k_3}{m} - \omega^2)^2 + 4\mu^2\omega^2\frac{k_3}{m}}((\frac{k_3}{m} - \omega^2)\sin\omega t - 2\mu\omega\sqrt{\frac{k_3}{m}}\cos\omega t) \\ x(t) = \dfrac{F_m}{k_2} + \dfrac{e\omega^2}{(\frac{k_2}{m} - \omega^2)^2 + 4\mu^2\omega^2\frac{k_2}{m}}((\frac{k_2}{m} - \omega^2)\cos\omega t + 2\mu\omega\sqrt{\frac{k_2}{m}}\sin\omega t) \end{cases} \tag{V-9}$$

Appendix VI Transient State Solutions

The equations of Eq.3-21 in Chapter 3 describe the translational responses of the aerostatic bearing spindle rotor, which system is applied by external cutting forces, regarded as step excitation, and centrifugal force, named harmonic excitation. The complete response for Eq.3-21 contains two parts, such as the particular response, named the steady-state response, and the homogeneous response, named the transient-state response. The steady-state solution under harmonic excitation corresponding to the steady-state response and the steady-state solution under constant excitation corresponding to the steady-state response have been discussed in Appendix V. Then, to analyze the transient-state solution, Eq.3-21 is separated into two parts, step response and harmonic response. Firstly, deleting the part of the harmonic excitation of Eq.3-21, it is rewritten as Eq.VI-1.

$$\begin{cases} \ddot{z} + \dfrac{c_z}{m}\dot{z} + \dfrac{k_1}{m}z = \dfrac{F_t}{m} \\ \ddot{y} + \dfrac{c_y}{m}\dot{y} + \dfrac{k_3}{m}y = \dfrac{F_r}{m} \\ \ddot{x} + \dfrac{c_x}{m}\dot{x} + \dfrac{k_2}{m}x = \dfrac{F_m}{m} \end{cases} \tag{VI-1}$$

which output is called as step response. Using the Laplace transform and taking the inverse Laplace transform (Qiu and Zou, 2010, Benaroya and Nagurka, 2010), the complete solution combining the homogeneous solution with the particular solution can be gotten as:

$$\begin{cases} z(t) = \dfrac{F_t}{k_1}(1 - \dfrac{e^{-\mu\sqrt{\frac{k_1}{m}}t}}{\sqrt{1-\mu^2}}(\sqrt{1-\mu^2}\cos(\sqrt{\dfrac{k_1}{m}}\sqrt{1-\mu^2}\,t) + \mu\sin(\sqrt{\dfrac{k_1}{m}}\sqrt{1-\mu^2}\,t))) \\ y(t) = \dfrac{F_r}{k_3}(1 - \dfrac{e^{-\mu\sqrt{\frac{k_3}{m}}t}}{\sqrt{1-\mu^2}}(\sqrt{1-\mu^2}\cos(\sqrt{\dfrac{k_3}{m}}\sqrt{1-\mu^2}\,t) + \mu\sin(\sqrt{\dfrac{k_3}{m}}\sqrt{1-\mu^2}\,t))) \\ x(t) = \dfrac{F_m}{k_2}(1 - \dfrac{e^{-\mu\sqrt{\frac{k_2}{m}}t}}{\sqrt{1-\mu^2}}(\sqrt{1-\mu^2}\cos(\sqrt{\dfrac{k_2}{m}}\sqrt{1-\mu^2}\,t) + \mu\sin(\sqrt{\dfrac{k_2}{m}}\sqrt{1-\mu^2}\,t))) \end{cases} \tag{VI-2}$$

where, the initial conditions are zeros.

Then, deleting the part of the step excitation of Eq.3-21, it is rewritten as Eq.VI-3.

$$\begin{cases} \ddot{z} + \dfrac{c_z}{m}\dot{z} + \dfrac{k_1}{m}z = 0 \\ \ddot{y} + \dfrac{c_y}{m}\dot{y} + \dfrac{k_3}{m}y = e\omega^2 \sin\omega t \\ \ddot{x} + \dfrac{c_x}{m}\dot{x} + \dfrac{k_2}{m}x = e\omega^2 \cos\omega t \end{cases} \tag{VI-3}$$

Employing the Laplace transform and taking the inverse Laplace transform (Qiu and Zou, 2010; Benaroya and Nagurka, 2010), the complete solution combining the homogenous solution with the particular solution under the initial conditions of zeros can be gotten as:

$$\begin{cases} y(t) = A_y e^{-\mu\sqrt{\frac{k_3}{m}}t} \sin(\sqrt{1-\mu^2}\sqrt{\dfrac{k_3}{m}}t + \alpha_y) + \dfrac{e\omega^2}{(\frac{k_3}{m} - \omega^2)^2 + 4\mu^2\omega^2\frac{k_3}{m}}((\dfrac{k_3}{m} - \omega^2)\sin\omega t - 2\mu\omega\sqrt{\dfrac{k_3}{m}}\cos\omega t) \\ x(t) = A_x e^{-\mu\sqrt{\frac{k_2}{m}}t} \sin(\sqrt{1-\mu^2}\sqrt{\dfrac{k_2}{m}}t + \alpha_x) + \dfrac{e\omega^2}{(\frac{k_2}{m} - \omega^2)^2 + 4\mu^2\omega^2\frac{k_2}{m}}((\dfrac{k_2}{m} - \omega^2)\cos\omega t + 2\mu\omega\sqrt{\dfrac{k_2}{m}}\sin\omega t) \end{cases} \tag{VI-4}$$

$$\begin{cases} A_y = \dfrac{1}{\sqrt{4\mu^2\dfrac{k_3}{m}\omega^2 + \left(\dfrac{k_3}{m} - \omega^2\right)^2}} \dfrac{e\omega^3}{\sqrt{\dfrac{k_3}{m}(1-\mu^2)}} \\ A_x = \dfrac{1}{\sqrt{\dfrac{k_2}{m}(1-\mu^2)}} \dfrac{e\omega^2\sqrt{\dfrac{k_2}{m}}}{\sqrt{4\mu^2\dfrac{k_2}{m}\omega^2 + \left(\dfrac{k_2}{m} - \omega^2\right)^2}} \end{cases} \tag{VI-5}$$

$$\begin{cases} \alpha_y = \arctan\dfrac{-2\mu\dfrac{k_3}{m}\sqrt{(1-\mu^2)}}{\dfrac{k_3}{m} - \omega^2} \\ \alpha_x = -\arctan\dfrac{\sqrt{(1-\mu^2)}}{\mu} - \arctan\dfrac{2\mu\sqrt{(1-\mu^2)}\dfrac{k_2}{m}}{\dfrac{k_2}{m} - \omega^2} \end{cases} \tag{VI-6}$$

Finally, the general solution for Eq.3-21 is the sum of Eq.VI-2 and Eq.VI-4, as below:

$$
\begin{cases}
z(t)=\begin{cases}
\dfrac{F_t}{k_1}\\
-\dfrac{F_t}{k_1}\dfrac{e^{-\mu\sqrt{\frac{k_1}{m}}t}}{\sqrt{1-\mu^2}}\sqrt{1-\mu^2}\cos\left(\sqrt{\dfrac{k_1}{m}}\sqrt{1-\mu^2}t\right)\\
+\dfrac{F_t}{k_1}\dfrac{e^{-\mu\sqrt{\frac{k_1}{m}}t}}{\sqrt{1-\mu^2}}\mu\sin\left(\sqrt{\dfrac{k_1}{m}}\sqrt{1-\mu^2}t\right)
\end{cases}\\
y(t)=\begin{cases}
\dfrac{F_r}{k_3}\left(1-\dfrac{e^{-\mu\sqrt{\frac{k_3}{m}}t}}{\sqrt{1-\mu^2}}\left(\sqrt{1-\mu^2}\cos\left(\sqrt{\dfrac{k_3}{m}}\sqrt{1-\mu^2}t\right)+\mu\sin\left(\sqrt{\dfrac{k_3}{m}}\sqrt{1-\mu^2}t\right)\right)\right)\\
+A_y e^{-\mu\sqrt{\frac{k_3}{m}}t}\sin\left(\sqrt{1-\mu^2}\sqrt{\dfrac{k_3}{m}}t+\alpha_y\right)\\
+\dfrac{e\omega^2}{\left(\dfrac{k_3}{m}-\omega^2\right)^2+4\mu^2\omega^2\dfrac{k_3}{m}}\left(\left(\sqrt{\dfrac{k_3}{m}}-\omega^2\right)\sin\omega t-2\mu\omega\sqrt{\dfrac{k_3}{m}}\cos\omega t\right)
\end{cases}\\
x(t)=\begin{cases}
\dfrac{F_m}{k_2}\left(1-\dfrac{e^{-\mu\sqrt{\frac{k_2}{m}}t}}{\sqrt{1-\mu^2}}\left(\sqrt{1-\mu^2}\cos\left(\sqrt{\dfrac{k_2}{m}}\sqrt{1-\mu^2}t\right)+\mu\sin\left(\sqrt{\dfrac{k_2}{m}}\sqrt{1-\mu^2}t\right)\right)\right)\\
+A_x e^{-\mu\sqrt{\frac{k_2}{m}}t}\sin\left(\sqrt{1-\mu^2}\sqrt{\dfrac{k_2}{m}}t+\alpha_x\right)\\
+\dfrac{e\omega^2}{\left(\dfrac{k_2}{m}-\omega^2\right)^2+4\mu^2\omega^2\dfrac{k_2}{m}}\left(\left(\dfrac{k_2}{m}-\omega^2\right)\cos\omega t+2\mu\omega\sqrt{\dfrac{k_2}{m}}\sin\omega t\right)
\end{cases}
\end{cases}
\tag{VI-7}
$$

$$
\begin{cases}
A_y=\dfrac{1}{\sqrt{4\mu^2\dfrac{k_3}{m}\omega^2+\left(\dfrac{k_3}{m}-\omega^2\right)^2}}\dfrac{e\omega^3}{\sqrt{\dfrac{k_3}{m}(1-\mu^2)}}\\
A_x=\dfrac{1}{\sqrt{\dfrac{k_2}{m}(1-\mu^2)}}\dfrac{e\omega^2\sqrt{\dfrac{k_2}{m}}}{\sqrt{4\mu^2\dfrac{k_2}{m}\omega^2+\left(\dfrac{k_2}{m}-\omega^2\right)^2}}
\end{cases}
\tag{VI-8}
$$

$$
\begin{cases}
\alpha_y=\arctan\dfrac{-2\mu\dfrac{k_3}{m}\sqrt{(1-\mu^2)}}{\dfrac{k_3}{m}-\omega^2}\\
\alpha_x=-\arctan\dfrac{\sqrt{(1-\mu^2)}}{\mu}-\arctan\dfrac{2\mu\sqrt{(1-\mu^2)}\dfrac{k_2}{m}}{\dfrac{k_2}{m}-\omega^2}
\end{cases}
\tag{VI-9}
$$

Appendix VII Beating Phenomenon

Beating phenomenon represents that the dynamic system responses in the waveform at two slightly different harmonic frequencies, which can be described by the following mathematical formula.

$$x(t) = X[\cos \omega t + \cos(\omega t + \varepsilon)] = 2X \cos\frac{\varepsilon}{2}t \cos(\omega + \frac{\varepsilon}{2})t \qquad \text{(VII-1)}$$

where, $\varepsilon << \omega$. The resultant response $x(t)$ in the waveform may be considered as a cosine wave with the circular frequency $\omega + \frac{\varepsilon}{2}$, and with a varying amplitude $2X \cos\frac{\varepsilon}{2}t$, named the enveloping curve in a profile of a cosine wave at the amplitude of $2X$ with the circular frequency $\frac{\varepsilon}{2}$, which is a small quantity. The resultant response is illustrated in Figure VII-1.

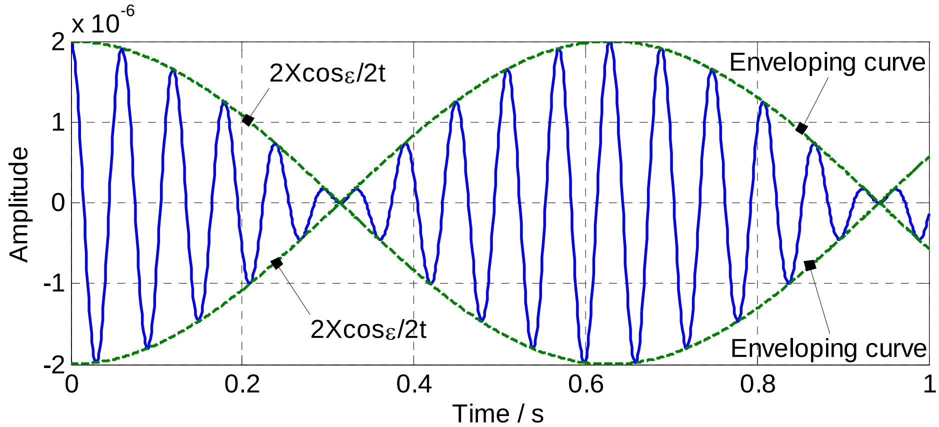

Figure VII-1 Graphical representation of beats (X=1×10^{-6}nm, $\varepsilon = 5$ and $\omega = 100$ rad/s)

When the above system is applied by harmonic excitation, the function can be rewritten as:

$$\begin{aligned} x(t) &= X_1[\cos \omega_1 t + \cos(\omega_1 t + \varepsilon)] + X_2 \cos \omega_2 t \\ &= 2X_1 \cos\frac{\varepsilon}{2}t \cos(\omega_1 + \frac{\varepsilon}{2})t + 2X_2 \cos \omega_2 t \end{aligned} \qquad \text{(VII-2)}$$

The above equation includes two parts, the beating response and harmonic response. The last one is a datum curve in the cosine waveform. The resultant response is illustrated in Figure VII-2. This kind of response is called the harmonic beating phenomenon.

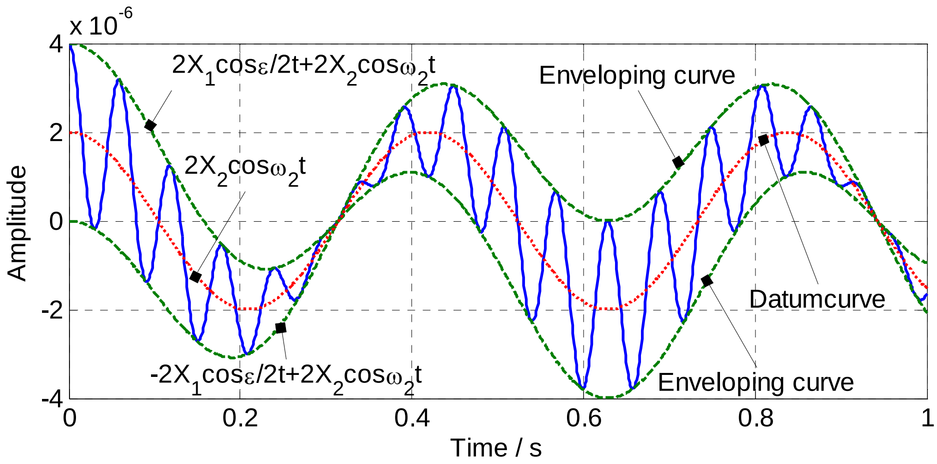

Figure VII-2 Graphical representation of beats (X_1=1×10^{-6} nm, X_2=1×10^{-6} nm, $\varepsilon = 5$, $\omega_1 = 100$ rad/s and $\omega_2 = 15$ rad/s)

Appendix VIII Power Spectral Density

A surface profile is analyzed by power spectrum analysis. The power spectrum of the surface profile is determined by discrete Fourier transform (DFT) computing with a fast Fourier transform (FFT) algorithm (see Appendix IV). The surface profile is denoted by $F(k)$ with k=0, 1, 2, . . ., $N-1$, where N is the number of samples in the surface profile, and the power spectrum of the surface profile is defined as:

$$Z(f_n) = \sum_{k=0}^{N-1} F(k\Delta l)\exp(-2\pi jk\Delta l f_n) \tag{VIII-1}$$

where n is an integer number, and f_n is a frequency component of the surface profile which represents the number of waves with a wavelength λ_n within a unit period of length:

$$\lambda_n = \frac{1}{f_n} = \frac{L}{n} \tag{VIII-2}$$

N is the total number of samples with the sampling length Δl taken within the measured length-period L of the surface profile, i.e.:

$$N = \frac{L}{\Delta l} \tag{VIII-3}$$

In order to prevent aliasing distortion, the sample rate f_{sample} must be chosen to be at the least twice the highest non-zero frequency component $f_{\max}$ contained in the surface profile according to the sampling theorem or Nyquist criterion, i.e.:

$$f_{sample} \geq 2 f_{\max} \tag{VIII-4}$$

Δl should be:

$$\Delta l \leq \frac{1}{2 f_{\max}} \tag{VIII-5}$$

In the present study, Δl is chosen to be 0.0002 mm which ensures an accurate representation of the surface profile with frequency content up to 5000mm^{-1}.

The power spectral density (PSD) is determined directly from the DFT. The periodgram $|Z(f_n)|^2$ is obtained by transforming the real data. This will yield N transformed points corresponding to N real data points. To minimize the distortion of the true spectrum due to Gibb's phenomenon, the spectral window corresponding to the Hamming lag window is applied to obtain the PSD. The Hamming window is operated on the frequency data by means of convolution, i.e.:

$$\mathrm{PSD}(f_0)=0.25(Z(f_p))^2+0.50(Z(f_0))^2+0.25(Z(f_s))^2 \tag{VIII-6}$$

where PSD(f_0) is the power spectral density at a particular frequency f_0, and f_p and f_s are the preceding and succeeding frequencies for f_0, respectively.

For the time-domain signal, such as cutting force signals in this study, the measured length L and the sampling length Δl, as mentioned above, are replaced by the measured time T and the sampling interval Δt, respectively, to analyze the spectral characteristics of the cutting force signal by PSD for this study.

Appendix IX Kistler 9252A

A **Kistler 9252A force transducer**, a quartz force sensor, is a 3-component force sensor F_x, F_y and F_z for measuring the three orthogonal components of a dynamic or quasi-static force being applied in any direction, which has a very extended measuring range, high stiffness and low cross talk.

Description

The force sensor contains 3 pairs of quartz rings which are mounted between two steel plates in the sensor housing. Two pairs of quartz are sensitive to shear and measure the force components F_x and F_y, while one pair of quartz sensitive to pressure measures the component F_z of a force applied to the sensor. The electrical charges proportional to the different components are channeled through electrodes to the corresponding connectors. The quartz packet is protected by tightly welded sensor housing (the stainless), having two fine-machined reference faces parallel to the y-axis. Consequently, these reference faces can be utilized to position the sensor and the coordinate system.

Mounting

Since the shear forces F_x and F_y are to be transmitted through static friction from the base and cover plate to the force sensor, the force sensor must be mounted under preload. The sensor is preloaded with a centered preloading bolt. Both reference faces are used to adjust the sensor. The technical data are shown in Table.III-1.

Electronics

Besides the force sensors, a three-component force measuring system also requires charge amplifiers for each channel, which amplify the electrical charge signals of the sensor and convert the signals into voltages exactly proportional to the acting force.

Table.III-1 Technical data for the Kistler 9252A sensor

<table>
<tr><td rowspan="2">Range</td><td>F_x, F_y</td><td>kN</td><td>-2.5~2.5</td></tr>
<tr><td>F_z</td><td>kN</td><td>-5~5</td></tr>
<tr><td rowspan="2">Overload</td><td>F_x, F_y</td><td>kN</td><td>-3</td></tr>
<tr><td>F_z</td><td>kN</td><td>-6</td></tr>
<tr><td>Threshold</td><td colspan="2">N</td><td><0.01</td></tr>
<tr><td rowspan="2">Sensitivity</td><td>F_x, F_y</td><td>pC/N</td><td>≈-8</td></tr>
<tr><td>F_z</td><td>pC/N</td><td>≈-4</td></tr>
<tr><td>Linearity</td><td colspan="2">%FSO</td><td>≤±1</td></tr>
<tr><td>Hysteresis</td><td colspan="2">%FSO</td><td>≤±0.5</td></tr>
<tr><td rowspan="3">Cross talk</td><td>$F_z \to F_x$, F_y</td><td>%</td><td>≤±1</td></tr>
<tr><td>$F_x \to F_y$</td><td>%</td><td>≤±3</td></tr>
<tr><td>F_x, $F_y \to F_z$</td><td>%</td><td>≤±3</td></tr>
<tr><td rowspan="2">Rigidity</td><td>K_x, K_y</td><td>N/μm</td><td>≈1000</td></tr>
<tr><td>K_z</td><td>N/μm</td><td>≈2600</td></tr>
<tr><td>Max. bending moment</td><td>M_x, M_y</td><td>Nm</td><td>±14</td></tr>
<tr><td>Operating temperature range</td><td colspan="2">^{o}C</td><td>-60~150</td></tr>
<tr><td>Temperature coefficient of sensitivity</td><td colspan="2">%/^{o}C</td><td>-0.02</td></tr>
<tr><td>Insulation resistance</td><td colspan="2">TΩ</td><td>≥10</td></tr>
<tr><td>Capacitance</td><td colspan="2">pF</td><td>≈30</td></tr>
<tr><td>Connector</td><td colspan="2">Type</td><td>10-32 UNF</td></tr>
<tr><td>Weight</td><td colspan="2">g</td><td>32</td></tr>
</table>

Appendix X Wyko 8000 Optical Profiling System

The **Wyko NT8000 Optical Profiling System** provides a rapid, easy and reliable approach to measuring and estimating different surfaces, such as step heights, surface roughness and surface topography, with non-contact 3D measurement from 0.1 nm to 8 millimeters, with sub-nanometer resolution.

The basic configurations:

The Wyko NT8000 Optical Profiling system is composed of several principle parts, which is organically combined together to work so as to offer information on the sample. The system contains:

(1) A integrated air table;

(2) A computer-controlled motorized x/y translational sample stage with 200mm computer-controlled w/encoders, mounted on the integrated air table in the range of 200mm, at the max. scan speed of 100µm/s;

(3) A Wyko Profiler head mounted on the computer-controlled z-axis within the max. range of 8mm and automated tip/tilt cradle;

(4) Various magnification objectives with automated field of view multiplies, mounted on a manual / motorized self-sensing turret;

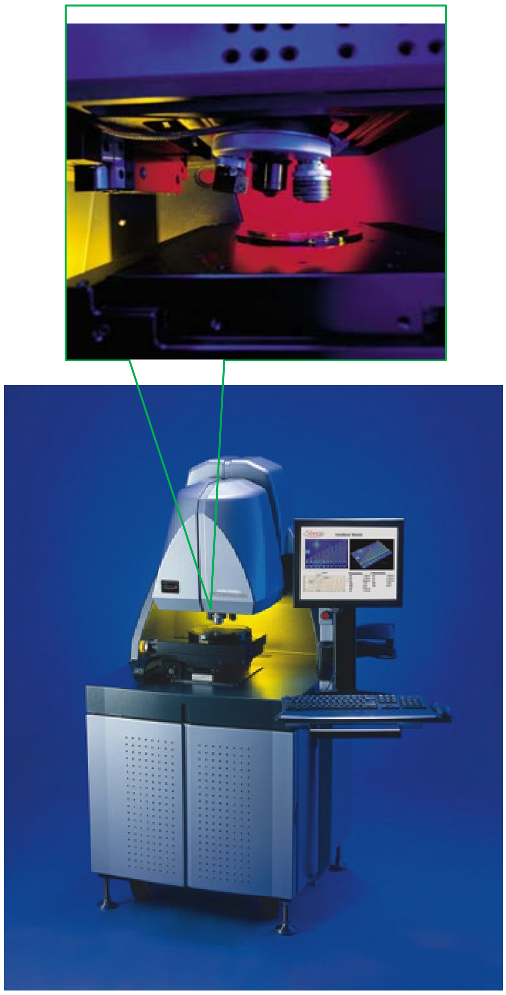

(5) An IBM-compatible computer, preloaded with Microsoft® Windows XP® and Wyko Vision software satisfying the autofocus, tip/tilt, stitching optional and self-calibrating to internal primary standard.

The Wyko Profiler

The key core of the Wyko NT8000 Optical Profiling system is the Modular Optics Assembly (MOA), containing a CCD camera and a Multiple Magnification Detector (MMD) with Field of View (FOV) lens. Objectives are attached to the bottom of the MOA on a turret. Light provided by an Illuminator box with an automatic filter assembly is channeled through the MOA by a fiber optic cable and is reflected to the objective by a beam splitter. Once the light reaches the objective, another beam splitter separates the light into two beams, the reference beam and the test beam. The reference beam is reflected from a super smooth reference mirror in the objective, while the test beam is reflected from the surface of the sample and back to the objective.

After the surface of the sample is at focus, the two light beams recombine and form an interference pattern of light and dark strips called fringes. The number of fringes depends upon the relative angle between the sample and the reference mirror. When the sample and the reference are parallel, only one large fringe can be observed. In this case, the fringes are said to be nulled. The interference pattern is received by the CCD camera and the signal is transferred to the computer, where it is processed by the Wyko Vision software, producing a graphical output display figuring out a contour map of the sample’s surface.

Measurement modes

There are two basic types of measurements available in the Wyko NT8000 Optical Profiling system.

Phase-shifting interferometry (**PSI**) a mechanical translation system precisely alters the optical path length of the test beam. Each optical path change causes a lateral shift in the fringe pattern. The shifted fringes are periodically recorded by the camera, producing a series of interferograms. Computerized calculations combine series of interferograms to determine the surface height profile.

Vertical scanning interferometry (**VSI**) an internal translator scans downward during the measurement as the camera periodically records frames. As each point on the surface comes into focus, the modulation on that point reaches a maximum, then tapers off as the translator passes through focus. By recording the height of the translator at maximum modulation, the system can determine the height of each pixel. The maximum scan depth for a VSI scan is 8mm.